ON THE MOCVD GROWTH OF ZnO

by

OLIVIER DEMENO PAGNI

Submitted in fulfilment of the requirements for the degree of

PHILOSOPHIAE DOCTOR

in the Faculty of Science at the University of Port Elizabeth

December 2004

Promoter: Prof A. W. R. Leitch

To my family – ndiyanithanda

ACKNOWLEDGMENTS

TABLE OF CONTENTS

Summary

Zinc oxide (ZnO) is a II-VI semiconductor material that offers tremendous potential as a light emitter in the blue-to-UV range. It has a wurtzite structure, and a direct band gap that can be tuned from 3.0 to 4.0 eV by alloying with Cd or Mg, respectively.

In this work, ZnO thin films were grown by metalorganic chemical vapor deposition (MOCVD) on *n*-Si 2 ° off (100), amorphous glass, *n*-GaAs (100), and *c*-plane sapphire substrates. Diethyl zinc (DEZn) and *tert*-butanol (TBOH) were chosen as precursors.

For the first time, Second Harmonic Generation Imaging was applied to the mapping of ZnO epilayers. The images obtained highlighted the polycrystalline character of the thin films, and provided insight as to the growth mode of ZnO on Si.

The influence of substrate temperature on the structural properties of the epilayers was investigated by X-ray diffraction and optical microscopy. Grain sizes as high as 54 nm were measured. The optimum temperature range for this system proved to be 450 – 500 °C.

The influence of the VI:II ratio during growth on the optical properties of the epilayers was studied by UV-vis-near IR spectroscopy. The lowest Urbach tail E_0 parameter was measured for material grown at a VI:II ratio of 18:1. The films' free electron concentration was shown to decrease by over two orders of magnitude, from 10^{19} to 10^{17} cm^{-3}, as the VI:II ratio increased from 10 to 60:1. This decrease in carrier concentration with rising VI:II ratio was paralleled to the surge at 12 K of a photoluminescence (PL) emission band characteristic of *p*-type ZnO.

The band gap energies extracted from room temperature transmission spectra ranged between 3.35 and 3.38 eV, in agreement with the value of 3.35 eV measured by room temperature PL.

Moreover, variable temperature PL spectra were recorded between 12 and 298 K on ZnO grown on Si. The 12 K spectrum was dominated by a donor-bound exciton (D°X) at 3.36 eV, while the 298 K scan displayed strong free exciton emission (FX) at 3.29 eV. The width of the D°X band proved to be as narrow as 7 meV. The intensity ratio between the room temperature near-band edge emission and the defect-related green band was as high as 28:1, highlighting the optical quality of the layers deposited in this work.

The electrical properties of the thin films were studied by Hall measurements (van der Pauw configuration), and a maximum room temperature mobility of 11 cm^2/Vs was recorded. Furthermore, a palladium (Pd) Schottky barrier diode on ZnO was fabricated. The barrier height and ideality factor were calculated from current–voltage measurements to be 0.83 eV and 1.6, respectively. The capacitance–voltage curve of the diode yielded a carrier concentration in the depletion region of $8 \bullet 10^{17}$ cm^{-3}.

This study has shown that the optical and electrical properties of ZnO depend strongly on the growth conditions employed. A suitable choice of growth parameters can yield high quality ZnO that may be used for various devices.

1. INTRODUCTION

Over the last half century, tremendous research has gone into understanding the principles governing the physics of wide-band gap semiconductors, as these materials are fitting for the development of photonic devices operating in the blue-to-UV range as well as for other opto-electronic applications. Consequently, the efforts of the semiconductor research community have focused on GaN, a III-V material that yielded the first blue light-emitting diode in the early 1990s. Other potential candidates include ZnSe, and 6H-SiC; unfortunately, ZnSe suffers from defect formation under high current drive, and SiC is known to generate weak light emission. On the other hand, there is a strong drive to study zinc oxide, the subject of this work, as its strong exciton binding energy of 60 meV means it yields even brighter emission than GaN ($E_x \sim 25$ meV). ZnO offers several other key advantages over GaN, one of them being a larger saturation velocity, thus making ZnO more desirable than GaN for high-speed devices. Having said that, the higher effective mass of ZnO explains its lower carrier mobility compared to GaN.

The endeavors of the semiconductor community have culminated in the recent development of a new family of nanostructures based on quasi-one-dimensional ZnO nanobelts (Wang, 2004). The allure of ZnO for nano-applications lies in positively charged (0001)-Zn and negatively charged $(000\bar{1})$-O surfaces, as they are responsible for a normal dipole moment, a discrepancy in surface energy, and spontaneous polarization along zinc oxide's *c*-axis. This spontaneous polarization in ZnO makes it a great tool to investigate piezoelectricity and polarization-induced phenomena at the nano-scale, thus paving the way for applications such as nanoscale sensors, transducers, or resonators. Furthermore, the fact that ZnO displays both semiconducting and piezoelectric properties means it is source to the largest family of nanostructures among all one-dimensional nanostructures, including carbon nanotubes (Wang, 2004).

Despite the progress recently made in the area of ZnO deposition and processing, there still remain severe challenges to the commercialization of ZnO devices, some of which will be addressed in this work. A major obstacle to overcome is the reproducible

1

production of p-type ZnO. The dearth of good p-type material has been explained by a lack of shallow-acceptor dopants, and by compensation by native donor defects. Furthermore, it is difficult to produce good Schottky contacts on ZnO. Nevertheless, the semiconductor community expects fast developments considering the various lessons learnt from the study of GaN since the early 1990s.

The focus of this thesis is the growth and characterization of ZnO thin films deposited by metalorganic chemical vapor deposition (MOCVD). The literature shows that ZnO layers have been deposited by all common techniques such as molecular beam epitaxy, pulsed laser deposition, and radio frequency sputtering. MOCVD is another well-known technique particularly helpful for large-area deposition and industrial applications. It hinges on the gas phase reaction of precursors, leading to the deposition of the semiconducting material on a substrate. Even though several reports on the MOCVD growth of ZnO epilayers have been published, crystal growers are still looking for a suitable oxygen precursor for the deposition of ZnO. In this work, the deposition and characterization of ZnO thin films obtained with *tert*-butanol (TBOH) as oxygen source is studied. While a handful of papers on the topic are available, TBOH remains overlooked by most research groups and this project aims, amongst other things, to display the merits of the TBOH oxygen precursor, as reflected in the properties of the ZnO thin films obtained.

A successful deposition procedure entails optimizing the growth parameters (substrate temperature, VI:II ratio during growth, etc.) in order to obtain the best possible surface morphology, structural, optical, and electrical properties. The link between these growth parameters and the sample properties therefore needs to be thoroughly monitored. Furthermore, the properties of a layer mirror the presence of defects in the material, and the activities of those defects within the sample must be understood. Consequently, one of the defects that will be carefully investigated here is the oxygen vacancy (V_O), a point defect that has recently been the center of extensive studies.

In the light of zinc oxide's potential applications, its optical and electrical properties need considerable attention. Since certain substrate materials are only suitable for particular characterization techniques, this project encompasses growth on Si, amorphous glass, GaAs, and c-plane sapphire substrates.

This thesis is organized as follows.

Chapter 2 depicts the basic properties of ZnO, and is vital to understanding the results presented here. It provides the reader an accurate description of the crystal structure, band structure, and band gap of ZnO. For the sake of completion, the latter section includes a paragraph on how to engineer the ZnO band gap by alloying with Cd or Mg. Finally a brief review of industrial applications based on ZnO illustrates the need to diligently study the ZnO system.

Chapter 3 focuses on the deposition of ZnO thin films by MOCVD. It begins with a timeline outlining the most important developments in the growth of ZnO by MOCVD. It continues with a description of the growth apparatus, a comparison of MOCVD with other growth techniques, and a discussion of the suitable substrates for this system.

To the author's knowledge, it is the first time that Second Harmonic Generation Imaging is performed on ZnO thin films, and chapter 4 presents the output from these measurements. The chapter starts with an explanation of the background theory pertaining to this fairly novel structural characterization method, followed by an account of the experimental apparatus in question. Section 4.3, the results section, is divided into three parts dedicated to growth on a particular substrate, namely Si, amorphous glass, and GaAs. A summary of the results is then given in section 4.4.

Chapter 5 focuses on the influence of one of the growth parameters, the substrate temperature, on the structural properties of a series of samples deposited on n-Si 2 ° off (100) substrates. X-ray diffraction spectra were recorded on all layers, and surface images of the thin films were taken by optical microscopy. There follows a

discussion of the variation of self-texture, tensile strain, grain size, preferred orientation quality, and surface morphology with substrate temperature.

Chapter 6 deals with the impact of another growth parameter, the VI:II ratio during growth, on the structural, optical, and dispersion properties of the thin films. All the layers studied here were grown on amorphous glass slides (fused silica) at the same substrate temperature, 450 °C. Besides X-ray diffraction measurements, the transmission spectra of the layers were recorded at room temperature, yielding the Urbach tail and band gap values of the layers. Analysis of the transmission and reflection spectra generated optical dispersion curves, which were fitted to Wemple and DiDomenico's single-oscillator model. A discussion of the band gap energies, in connection with the impact of the thermal mismatch strains on the band gap, closes the chapter.

Chapter 7 looks at the link between the photoluminescence properties of ZnO thin films deposited on n-GaAs (100) substrates and the following parameters: substrate temperature, VI:II ratio during growth, post-deposition annealing, insertion of a buffer layer, and TBOH purity. Transmission Electron Microscopy images and depth profiling by Auger Electron Spectroscopy provided additional information explaining the different results observed. Room temperature Hall measurements are also presented and compared to values reported in the literature.

Chapter 8 centers on variable temperature photoluminescence measurements performed on a ZnO thin film deposited on an n-Si 2 ° off (100) substrate. After a look at the background theory and experimental set up, the results section serves to identify the various peaks observed, as well as their thermal quenching behavior. Photoluminescence spectroscopy is indeed a versatile tool, as it provides the crystal grower a way of testing the optical quality of the material (section 8.3.3).

Having examined the optical properties of ZnO, the electrical properties of the thin films are investigated in chapter 9. The first part of the chapter provides the theory of the Hall effect, and an account of the scattering mechanisms known to affect the ZnO carrier

mobility. The variable temperature Hall system employed is depicted, and the transport properties of the thin films deposited on *c*-plane sapphire at room temperature and low temperatures are discussed. The second part of chapter 9 deals with the fabrication and characterization of a Pd Schottky barrier diode on a ZnO thin film grown on an n^+-GaAs 2 ° off (100) substrate. Current-voltage and capacitance-voltage curves are presented and analyzed.

Finally, chapter 10 sums up the results of this project, and lays out several areas that require further work.

2. THE BASIC PROPERTIES OF ZnO

The aim of this chapter is to outline the basic properties of zinc oxide. First of all, the crystal structure of ZnO will be discussed in detail. This encompasses a description of the ZnO crystal lattice and its lattice parameters. Furthermore, an in-depth presentation of the pressure dependence of the ZnO phases is given. This section is followed by an analysis of the band structure and optical band gap of ZnO, which is especially relevant considering the potential of ZnO as a light emitter in the blue-to-UV range. In addition, the band gap of ZnO can be engineered by alloying with Mg or Cd, and recent progress in this exciting field of research is depicted. Finally, some of the many applications of ZnO are described.

2.1   The crystal structure of ZnO

ZnO melts at 2250 K (Handbook of Chemistry and Physics, 1977) and belongs to the group of IIB-VIA binary semiconductors, a class of materials valuable for chief technological applications. Contrary to other IIB-VIA binary compounds that take on various metastable structures, ZnO crystallizes solely in the wurtzite phase at room conditions, as its sphalerite phase is only metastable. The wurtzite crystal (figure 2.1) is made of interpenetrating hexagonal close-packed sub-lattices of the anion (oxygen) and cation (zinc) displaced along the [0001] direction. It has a hexagonal unit cell, and fits in to the C_{6v}^{4} space group ($P6_3mc$, Z = 2), with two formula units per primitive cell, with all atoms occupying C_{3v} sites.

Every zinc atom in the wurtzite lattice is bonded by sp^3 covalent bonding to four oxygen atoms, which are located in the vertices of a slightly distorted tetrahedron. X-ray diffraction measurements have shown the Zn- and O-atoms along the c-axis to be 1.9915 ? apart at room temperature (Schulz and Thiemann, 1979). The distance separating them in the remaining directions is 1.9760 ? . The nature of the Zn-O bond has been studied in terms of atomic charge Q (number of outer-shell electrons), bond order W (Wiberg index), and atomic valence C. The Zn-O bond in bulk ZnO shows mixed covalent-ionic character, and has been proven to be less ionic than the bonds of other

common *s*-metal oxides. The Zn-O bond has a Wiberg index W (Zn-O) of 0.11e, a zinc valence of 0.47, and a total quantum chemical valence of 2.0 (Ermoshin and Veriazov, 1995).
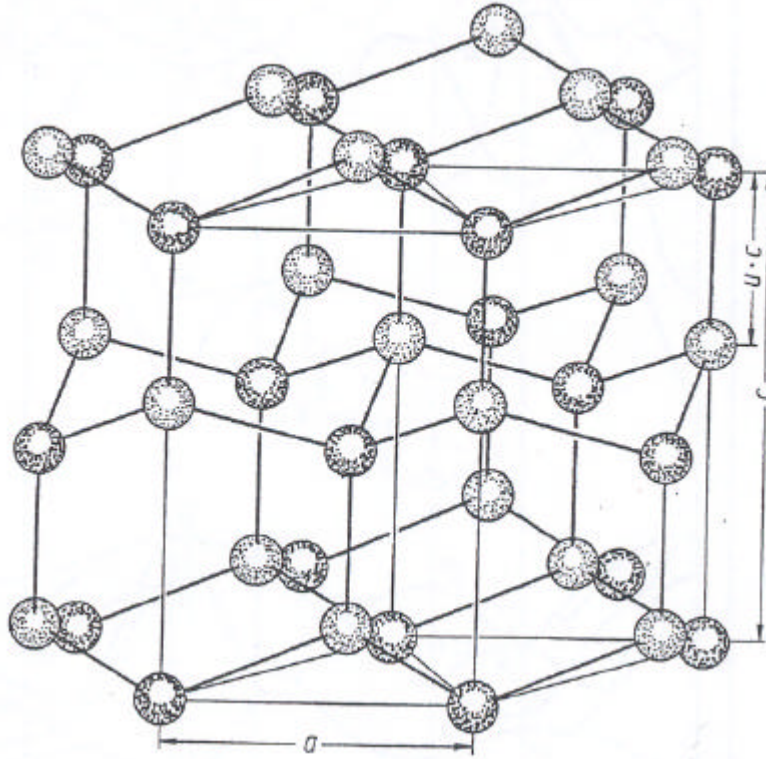
Figure 2.1: The ZnO crystal

The wurtzite lattice is characterized by three parameters, as opposed to one for a cubic unit cell; they are the basal plane lattice constant a, the uniaxial lattice constant c, and the internal coordinate u, which establishes the relative position of the anion and cation sub-lattices along the c axis. The literature reports room temperature values ranging from 3.2492 to 3.2503 ? for the a lattice parameter, and from 5.2031 to 5.2075 ? for c (Reeber, 1970). The considerable difference between the largest and smallest c values has been cleverly explained in 1961 by Mohanty and Azaroff. Their electron-density maps show that excess zinc atoms can enter the lattice interstitially, leading to an elongated

c- axis. In 1970, Reeber studied the temperature dependence of *a* and *c* from 4.2 to 296 K. He was able to fit a fourth-order polynomial to the experimental data he obtained for *a*:

$$a_T = 3.24853 - 1.0811 \bullet 10^{-5}T + 6.820 \bullet 10^{-8}T^2 - 6.109 \bullet 10^{-11}T^3 + 2.143 \bullet 10^{-14}T^4$$

His fit yielded a minimum *a* value at a temperature T_a of 93 K, in agreement with Ibach's work (1969). The accuracy of Reeber's fit for the temperature dependence of *c* did not enable him to determine a minimum for this parameter. Nevertheless, Ibach had previously measured a minimum value for *c* at a temperature T_c of 127 K. Reeber thus studied the thermal expansion behavior of his material by calculating the ratio of linear expansivity-minimum temperature (T_a and T_c) over the Debye temperature (θ_D). The negative thermal expansion of ZnO along the *a* axis ($T_a/\theta_D = 0.22$; $T_b/\theta_D = 0.31$) was in agreement with what had been found in other II-VI semiconductors. Furthermore, the variation of *a* and *c* with temperature should affect the molar volume of the material; and Reeber determined a change in molar volume of 0.17 % between room temperature and the minimum molar volume.

The third lattice parameter, *u*, has been quantified by X-ray diffraction experiments, yielding a value of 0.3820 at room temperature (Schulz and Thiemann, 1979); this reflects the distorted nature of the tetrahedron, as *u* = 0.375 in an ideal tetrahedral arrangement. The former value, *u* = 0.3820, sets the angle between the binding direction and the *c*-axis at 109.46 °.

An important structural property of the ZnO crystal is the phase change it undergoes, from hexagonal wurtzite to cubic rocksalt, when subject to high pressures (~ 9 GPa at room temperature). This transition results in an increased coordination number, from four to six, a volume decrease of approximately 17 %, and a change in symmetry (the rocksalt phase has F*m*3*m* symmetry). In 1993, Jaffe and Hess attempted to determine the total energy of ZnO as a function of unit cell volume by the *ab initio* all-electron Hartree-Fock linear-combination-of-atomic-orbitals method.

They fitted the Murnaghan equation,

$$E\left(\mathrm{V}\right)=E_0 - \frac{B_0 V_0}{B'-1}+\frac{B_0 V}{B'}\left[\frac{\left(V_0/V\right)^{B'}}{B'-1}+1\right]$$

to their total energy vs. volume curve, and obtained the following values for E_0, V_0, B_0 (the total energy, volume, and bulk modulus at zero pressure), and B' ($B' = d\mathrm{B}/d\mathrm{p}$):

	Wurtzite	Zinc blende	Rocksalt
E_0 (eV)	-5.658	-5.606	-5.416
V_0 (Å^3)	24.570	24.551	19.799
B_0 (GPa)	154.4	156.8	203.3
B'	3.6	3.6	3.6

Table 2.1: Total energy, volume, and bulk modulus of the pressure-dependent ZnO phases (after Jaffe and Hesse, 1993)

They calculated a transition pressure of 8.57 GPa, within experimental uncertainty of the reported values ranging between 9.0 and 9.5 GPa.

Karzel *et al.* (1996) furthered the understanding of the ZnO crystallographic transition by performing X-ray and [67]Zn-Mössbauer spectroscopy measurements at high external pressures. The lattice constants, bulk moduli, and volume changes of the ambient pressure and high-pressure phases are listed in the following table:

	Ambient pressure
Structure	Wurtzite
a (Å)	3.2496
c (Å)	5.2042
V_0 (Å^3)	23.796
	High-pressure
Structure	Rocksalt
a (Å)	4.271
V_{0H} (Å^3)	19.484
$1 - V_{0H}/V_0$	0.1813
	Parameters at the transition pressure $P_T^{\uparrow}$ when increasing pressure
$P_T^{\uparrow}$ (GPa)	8.7
$V(P_T^{\uparrow})/V_0$	0.957
$V_H(P_T^{\uparrow})/V_{0H}$	0.965
$1 - V_H(P_T^{\uparrow})/V(P_T^{\uparrow})$	0.175
	Parameters at the transition pressure $P_T^{\downarrow}$ when decreasing pressure
$P_T^{\downarrow}$ (GPa)	2.0
$V(P_T^{\downarrow})/V_0$	0.989
$V_H(P_T^{\downarrow})/V_{0H}$	0.991
$1 - V_H(P_T^{\downarrow})/V(P_T^{\downarrow})$	0.180

Table 2.2: Lattice properties of ZnO at ambient and high pressure (after Karzel *et al.*, 1996)

The volume change $1 - V_{0H}/V_0$ at the phase transition was approximately 18 % when extrapolating the parameters of the high-pressure phase to ambient pressure. At this point, the nearest-neighbor distance was seen to increase by ~ 8 %, while the next-nearest-neighbor distance decreases by ~ 6.5 %. All these changes could be reversed by releasing the pressure. It is worth mentioning that a strong hysteresis effect of the phase transition was observed. Furthermore, Karzel *et al.* investigated the variation of the electric-field gradient (EFG) in ZnO. The asymmetry parameter h of the EFG tensor is expected to be 0, since the Zn site in wurtzitic ZnO shows axial symmetry with respect to the *c*-axis. Nevertheless, they found h to increase to 0.3 at relatively mild pressures (< 0.1 GPa). This means that the wurtzite structure is considerably unstable against non-axial lattice distortions. Lastly, the ^{67}Zn-Mössbauer measurements yielded the *s*-electron density $r(0)$ at the ^{67}Zn nucleus. Unlike ZnSe, the $r(0)$ of ZnO remains low at high pressures, implying that ZnO retains its non-metallic character. The electrical conductivity of ZnO is therefore not expected to increase by applying high pressures.

The pressure dependence of the third lattice parameter, *u*, was probed in 1998 by Desgreniers. As previously mentioned, *u* depicts the relative position of the anion sublattice with respect to the cation sublattice along the *c*-axis of the wurtzite structure; the Zn atoms are placed at $\frac{1}{3}, \frac{2}{3}, 0$ and $\frac{2}{3}, \frac{1}{3}, \frac{1}{2}$, the O atoms at $\frac{1}{3}, \frac{2}{3}, u$ and $\frac{2}{3}, \frac{1}{3}, u + \frac{1}{2}$. The relationship between *u* and the ratio *c/a* is expressed as $uc/a = (3/8)^{1/2}$. Desgreniers found that *u* does not depart from the $uc/a = (3/8)^{1/2}$ relationship as wurtzitic ZnO becomes denser.

Having described the crystal structure of ZnO, a discussion of its band structure is found in section 2.2.

2.2 The band structure of ZnO

The band structure of a crystal, i.e. its energy-momentum (*E-k*) relationship, can be derived by solving the Schrödinger equation of an approximate one-electron problem (Sze, 1981)

$$\left[-\frac{\hbar^2}{2m}\nabla^2 + V(r)\right] \boldsymbol{f}_k(r) = E_k \boldsymbol{f}_k(r)$$

where $V(r)$ is a potential energy and $\boldsymbol{f}_k(r)$ the solutions of the Schrödinger equation. The Bloch theorem asserts that if $V(r)$ is periodic with the periodicity of the lattice, $\boldsymbol{f}_k(r)$ is of the form

$$\boldsymbol{f}_k(r) = e^{jk \cdot r} U_n(\mathbf{k}, \mathbf{r}) = \text{Bloch function}$$

where $U_n(\mathbf{k}, \mathbf{r})$ is periodic in $\mathbf{r}$ with the periodicity of the direct lattice, and n is the band index. For a given band index, it is adequate to only make use of $\mathbf{k}$'s in a primitive cell of the reciprocal lattice in order to identify the energy uniquely. The customary procedure is to employ the Wigner-Seitz cell in the reciprocal lattice; it is assembled by drawing perpendicular bisector planes in the reciprocal lattice from the chosen center to the nearest equivalent reciprocal lattice sites. This cell is called the first Brillouin zone. Hence, any momentum $\mathbf{k}$ in reciprocal space can be assigned a point in the Brillouin zone. In the case of a wurtzite crystal (figure 2.2), the Brillouin zone has three symmetry axes, $\Gamma - M$, $\Gamma - A$, and $\Gamma - K$. Γ, $2\pi/a$ (0, 0, 0), is the zone center.
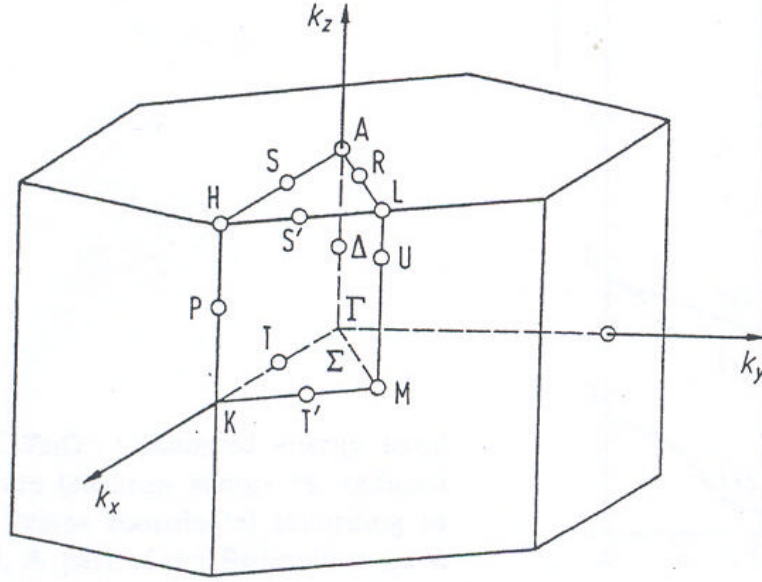
Figure 2.2: The Brillouin zone of ZnO

Over the years, several techniques aimed at theoretically studying the energy bands of solids have been developed. Schröer *et al.* (1993) courageously reported the first *ab initio* calculations of the band structure of ZnO by utilizing the local-density approximation (LDA); they calculated the lattice constants and electronic band structure of ZnO by solving the Kohn-Sham equations for non-local, separable, and norm-conserving pseudopotentials. Courageously, because ZnO is one of the worst candidates for pseudopotential description as both the O $2p$ and the Zn $3d$ orbitals are the lowest-lying orbitals of their respective symmetry type. Core electrons are therefore incapable of completely screening the nuclear charge, leading to tremendous strain in defining pseudopotentials and related wave functions. Nevertheless, they presented the following band structure and density of states (DOS) for ZnO. Around – 18 eV, they saw two *s* bands originating from the two O states in the unit cell. The next feature, from – 6.5 to –4 eV, consisted of 10 bands linked to the Zn $3d$ states. Subsequently, the O $2p$ states were responsible for the next group of six valence bands, while the lowest conduction bands came from the Zn $4s$ orbitals. Even though this work showed excellent agreement

between the theoretical and experimental lattice constants, it yielded a band gap of 0.23 eV, far from the experimental value of 3.3 - 3.4 eV (see section 2.3). This is because the LDA isn't able to correctly position the 3*d* levels; they emerge too close to the top of the valence band, and the coupling between the O 2*p* and Zn 3*d* orbitals is grossly overestimated. Vogel *et al.* (1995) obtained a more reasonable band gap energy, 3.77 eV, by incorporating a dominant self-interaction correction (SIC) to their LDA calculations. The *d* bands are shifted down in energy compared to the standard LDA method, resulting in a widened band gap. Additionally, the dispersion and bandwidth of the O 2*p* valence bands were considerably altered (figure 2.3).
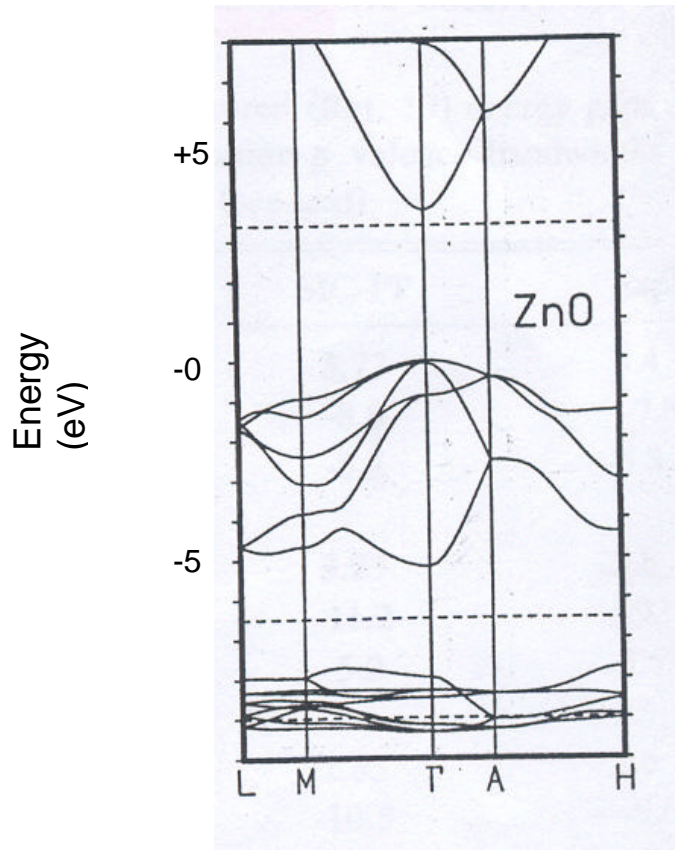
Figure 2.3: The band structure of ZnO (after Vogel *et al.*, 1995)

Furthermore, ZnO is known to have a direct band gap at room temperature. This is an important feature of the material that sets it apart from indirect semiconductors such as GaP. In direct semiconductors, electrons in the minimum of the conduction band and

holes at the top of the valence have equal momentum; this is not the case for indirect semiconductors. This means that interband transitions are highly probable in direct band gap semiconductors, and these interband transitions are known to be the chief radiative transition mechanism in such materials. On the other hand, the probability of interband transitions taking place in indirect band gap semiconductors is extremely low, since phonons or other scattering agents need to take part in the process in order to conserve momentum (Sze, 1981). This explains why direct band gap semiconductors such as ZnO are favored for light-emitting diodes and other opto-electronic applications, since no additional recombination centers need to be incorporated to improve the radiative processes.

Xu and Ching (1993) on their side delved into the effective masses, charge distributions and bonding patterns of ZnO by adopting the linear-combination-of-atomic-orbitals in the local-density approximation. They assessed the effective mass of the electrons in the conduction band (CB) and of the holes in the valence band (VB) from the band curvature of the ZnO crystal. The effective masses were highly anisotropic. The effective-mass components along the three symmetry axes are recorded in the following table:

	Conduction band edge	Valence band edge
ZnO crystal	0.37 ($\Gamma \rightarrow K$)	-4.31 ($\Gamma \rightarrow K$)
	0.28 ($\Gamma \rightarrow A$)	-1.98 ($\Gamma \rightarrow A$)

Table 2.3: Effective-mass components in units of electron mass along the three symmetry axes of ZnO (after Xu and Ching, 1993)

Several relevant observations were made from these calculations.
- The VB holes are much heavier than the electrons, which could lead to considerable optical nonlinearity in ZnO crystals
- The effective mass of the holes is more anisotropic than that of the electrons; this can be explained by the fact that the top of the valence band is correlated with the O p orbitals

- The effective mass of the electrons is less than 0.5; electrons should therefore control carrier transport in ZnO

- The smallest component of the electron effective mass is measured along the $\mathbf{k}_z$ direction; this may prove of importance in the construction of ZnO films and superlattices

- The effective mass of the holes is so high that conduction by holes is highly unlikely

Looking at the fractional ionic character (FIC) of ZnO, it is defined by the effective charges Q_{Zn}^* and Q_O^* as (Xu and Ching, 1993)

$$\text{FIC} = \left| Q_{Zn}^* - Q_O^* \right| / (Q_{Zn}^* + Q_O^*)$$

It ranges from 0 for a perfectly covalent compound to 1 for a 100 % ionic material. ZnO displayed a FIC of 0.70, compared to 0.95 for BeO and 0.56 for ZnS. Furthermore, the charge density along the Zn-O bond and the charge contour in a plane containing the Zn-O bond were plotted (figure 2.4).
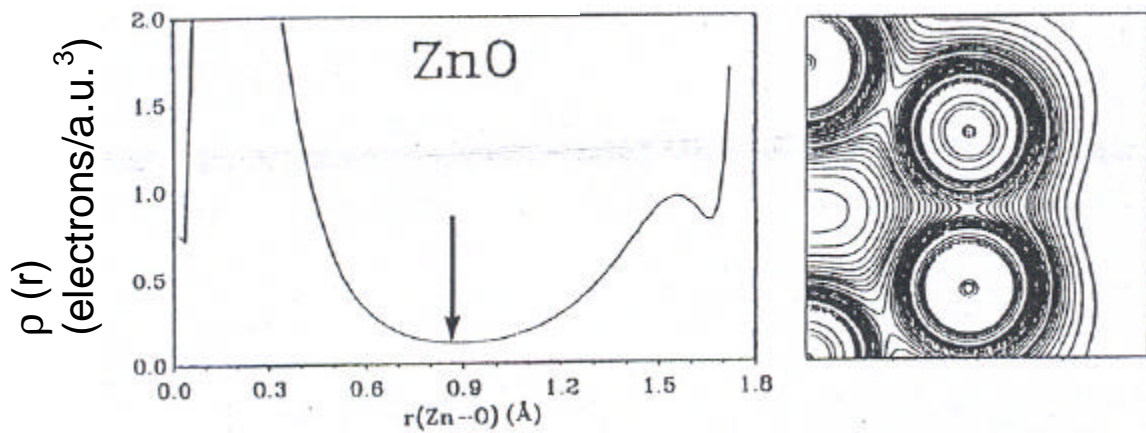
Figure 2.4: **Charge density along the Zn-O bond and charge contour in a plane containing the Zn-O bond (after Xu and Ching, 1993)**

The contour map highlights the boundary between Zn and O; this boundary then characterizes the effective radii r_{Zn} and r_O for the Zn and O atoms (the sum of r_{Zn} and r_O equals the Zn-O bond length).

	r_{Zn} (Å)	r_O (Å)	FIC
ZnO crystal	0.8855	0.9108	0.70

Table 2.4: Fractional ionic character and effective radii of Zn and O of ZnO (after Xu and Ching, 1993)

The ionic character of the Zn-O bond is also reflected in the large electronegativity difference between zinc and oxygen; zinc has an electronegativity of 1.65 Pauling units, compared to 3.44 for oxygen. Furthermore, the partial ionic character of ZnO is known to affect the polarity of the ideal (0001)-Zn and (000$\bar{1}$)-O surfaces; indeed, electrons at the (0001)-Zn surface are obliged to stay in the conduction band, causing a dearth of electrons at the valence band of the ideal (000$\bar{1}$)-O surface. This also means that the ideal Zn and O as-cleaved surfaces are metallic in nature (Kresse *et al.*, 2003). Finally, the ionic character of ZnO is also bound to affect the photoluminescence properties of the material; indeed, the material's ionicity is the reason why it displays remarkable exciton-phonon coupling, which is responsible for a broadening of the photoluminescence peaks observed at room temperature (Karpina *et al.*, 2004).

Having studied the band structure of ZnO, a discussion of the ZnO band gap is found in section 2.3.

2.3   The optical band gap of ZnO

Several groups have sought to measure the direct band gap E_g of ZnO at room temperature, resulting in a fairly broad range of values.

Beginning with thin films, values for E_g have been reported between 3.19 and 3.32 eV. Roth *et al.* (1981a) recorded the transmission and reflection spectra of their samples deposited by MOCVD and RF magnetron sputtering on glass substrates. They then calculated the band gap energy of ZnO using a model successfully tested on III-V compounds, where a Lorentzian broadening alters the square root dependence of the absorption coefficient; the band gap energy is easily gathered from the position of the point of maximum slope in the absorption spectrum. They obtained an E_g value of 3.28 eV.

Natsume *et al.* (1995), on the other hand, determined the E_g values of their CVD-grown thin films from transmission spectra alone; they reported different band gap values for different film formation temperatures. The smallest band gap energy, 3.19 eV, was measured at a growth temperature of 550 °C; the largest, 3.23 eV, was calculated for a sample deposited at 500 °C. The three samples considered were all grown on Pyrex glass substrates.

Srikant and Clarke (1997) worked on thin films grown on *c*- and *r*-plane sapphire, as well as on fused silica; their E_g results were obtained knowing that the absorption coefficient of a film is a parabolic function of the incident energy and the optical band gap. This generated E_g energies of 3.29, 3.32, and 3.24 eV for the samples grown on *c*-, *r*-plane sapphire, and fused silica, respectively.

While the disparity in thin film values can be explained in terms of factors such as strains and dopants, the various E_g values reported for single crystals, 3.1, 3.2, 3.3, and 3.4 eV (Liu *et al.*, 1992; Landolt-Bornstein, 1982; Gupta, 1990; Look, 2001) are intriguing. In order to clarify the situation, Srikant and Clarke (1998) performed spectroscopic

ellipsometry as well as other optical measurements on commercially supplied ZnO crystals; they concluded that the two lower values (3.1 and 3.2 eV) did not represent the conduction band-valence band transition, but reflected the presence of a deep donor level below the conduction band. Considering the evidence at hand, it seems appropriate to talk of an accepted band gap range of 3.3 – 3.4 eV. Furthermore, the band gap values measured in this study (see chapters 6 and 8) were found to range between 3.35 and 3.38 eV.

Moreover, the band gap of ZnO can be tuned by alloying with magnesium or cadmium, thus creating single-phased $Mg_xZn_{1-x}O$ and $Cd_yZn_{1-y}O$. The former has been shown to be a fitting material for the barrier layers of ZnO/(Mg,Zn)O superlattices because of its wider band gap (Ohtomo *et al.*, 1998), while a (Cd,Zn)O mixed crystal is known to alter the wavelength tunability of ZnO because of its narrower band gap.

We begin by discussing the (Cd,Zn)O system. Makino *et al.* (2001) have reported $Cd_yZn_{1-y}O$ band gap values of 3.0 eV for y = 0.07. One of the advantages of alloying ZnO with Cd is that the wurtzite phase of ZnO is going to be preserved when the rocksalt Cd is introduced, as the ionic radius of Cd^{2+} (0.74 Å) is close to that of Zn^{2+} (0.60 Å). Another advantage associated with Cd is that its maximum content (y = 0.07) proves much greater than the thermodynamic solubility limit (y = 0.02).

The alloying process is naturally going to affect the lattice constants of ZnO, and both the *a* and *c* constants monotonically increase with *y*. They can be fitted to polynomial functions (Makino *et al.*, 2001):

$$a = 3.252 + 0.143y - 0.147y^2$$
$$c = 5.204 + 0.956y - 5.42y^2$$

The band gap of $Cd_yZn_{1-y}O$ as a function of cadmium content is given as

$$E_g (y) = 3.29 - 4.40y + 5.93y^2$$

Makino *et al.* also found that the incorporation of Cd into the crystal led to changes in the PL properties of the material; the spectrum of $Cd_{0.07}Zn_{0.93}O$ displayed a low-energy shoulder absent at lower Cd content; this shoulder is indicative of a Cd-rich phase. Its density is however fairly low.

We now consider the (Mg,Zn)O system. The band gap of ZnO can be increased to 4.0 eV at room temperature by a Mg content corresponding to x = 0.33. Chen *et al.* (2003) reported the variation of the ZnO band gap with Mg content:

$$E_g(x) = 3.32 + 2.00x \qquad \text{for } 0 \le x \le 0.33$$

These two ternary alloys, (Cd,Zn)O and (Mg,Zn)O, are not only relevant individually, but the (Cd,Zn)O/(Mg,Zn)O (CZM) system is also important because by carefully picking the Cd and Mg concentrations, a CZM superlattice having perfect in-plane lattice match and a maximum barrier height of 0.9 eV can be developed (Kawasaki *et al.*, 1998). This is illustrated in figure 2.5; it can be seen that at x = 0.3 and y = 0.07 (for example), the (Cd,Zn)O/(Mg,Zn)O superlattice is perfectly lattice-mismatched.
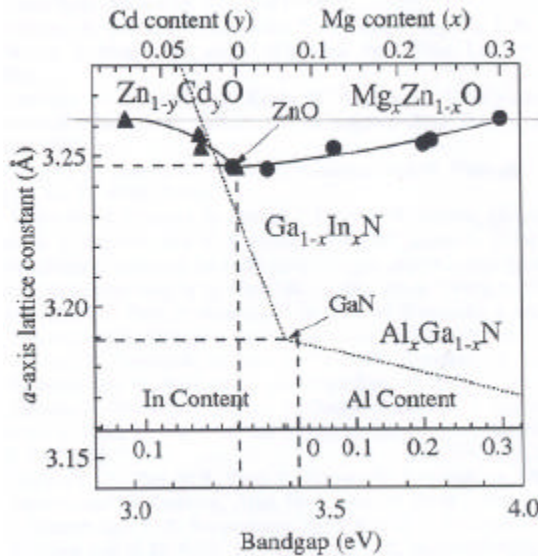
Figure 2.5: **Optical and structural properties of (Cd,Zn)O and (Mg,Zn)O alloys mapped out in a plane of a-axis length and room temperature band gap (after Makino *et al.*, 2001)**

On the other hand, the dashed curves representing the variation of the *a*-axis length of the (In,Ga)N and (Al,Ga)N alloys with band gap energy clearly shows that such in-plane lattice match is impossible for (In,Ga)N/(Al,Ga)N superlattices.

The CZM system has another advantage over (In,Ga)N/(Al,Ga)N superlattices. Indeed, a difference in lattice constant between a well and a barrier layer will generate strain and a piezoelectric field inside the well layers, thus complicating the superlattice's excitonic properties. Altogether, the attributes of the perfectly lattice-matched heterojunctions described above should open doors for their use as active layer in ZnO-based blue light-emitting diodes.

Finally, it is known that the band gap energies of semiconductors decrease with rising temperature; this phenomenon has been observed for most group IV, III-V, and II-VI materials, and is linked to the combined effect of thermal lattice expansion and electron-phonon interactions (Yu and Cardona, 1996). The variation of the ZnO band gap with temperature has been studied by several groups, and is further discussed in chapter 8, which deals with the optical characterization of ZnO epilayers.

2.4 Applications

Zinc oxide films have drawn tremendous attention as low cost transparent electrodes for thin film solar cells such as amorphous silicon (*a*-Si) or copper indium diselenide ($CuInSe_2$). ZnO-based films offer several advantages over commonly-used coatings made of In_2O_3:Sn or SnO_2:F (Jin *et al.*, 1988). Indeed, they are composed of cheap and abundant elements, in contrast to the pricey In-containing films. Furthermore, unlike Cd-containing films, they are harmless. Thirdly, they are more stable than SnO_2- and In_2O_3-based films in the presence of hydrogen plasma; this is particularly relevant to applications related to *a*-Si solar cells. Finally, they allow tailoring of the ultraviolet absorption, as the band gap of ZnO lies just at the end of the luminous spectrum. Additionally, the band gap of ZnO is smeared and shifted towards the UV by heavy doping. Hence, ZnO-based films can be utilized for UV protection. Additionally, Al-doped ZnO layers have been shown to have high luminous transmittance, high solar UV absorption, low thermal IR emission, and high electrical conductance, making them strong candidates for energy-efficient windows.

ZnO thin films have also enjoyed recognition for their role in magneto-optical (MO) disks (Carcia *et al.*, 1994). Pt/Co and Pd/Co multilayers (MLs) are known for their potential application as MO recording medium. It has been reported that depositing Pt/Co MLs on a ZnO layer results in increased perpendicular magnetic anisotropy energy (K_{eff}) and magnetic coercivity (H_c); both these characteristics are vital features of a recording medium. Since ZnO is transparent and has a modest refractive index, the Kerr rotation of Pt/Co and Pd/Co MLs is bolstered by optical interference with a thick ZnO layer. ZnO layers can therefore play a functional part in MO disks.

Another appealing feature of ZnO is its application to surface-acoustic-wave devices, which are created by using integrated circuit technology (Kino and Wagers, 1973). These devices require strongly piezoelectric materials (such as ZnO) that display weak acoustic losses; indeed, they are made of a thin film of piezoelectric material on top of the transducer, with a metal film deposited on top of the piezoelectric film. Excitation of the transducer leads to acoustic stresses in the piezoelectric film, thus exciting a surface wave

in the substrate. Theoretically, acoustic devices could be made on silicon or sapphire (upon which semiconductor devices could also be constructed), and it has been shown that the coupling coefficients of ZnO on sapphire are analogous to those obtained with LiNbO$_3$. Furthermore, broad bandwidth transducers made of ZnO on sapphire or silica are believed to be feasible.

Having looked at applications linked to zinc oxide's structural properties, the focus of the remaining paragraphs resides on the opto-electronic characteristics of the material. Green-blue and ultraviolet ZnO light-emitting diodes (LEDs) have already been reported (Akasaki *et al.*, 1991). Moreover, ZnO is an appropriate photoconductor in the UV range because of its large band gap and photoconductance. The photoresponse of ZnO comprises a swift and reproducible solid-state process [h$\nu \rightarrow$ h$^+$ + e$^-$, where h and e represent a hole and an electron respectively], and a slow process with a large response. This slow process consists of oxygen adsorption under dark conditions by trapping of an electron [O$_2$ (g) + e$^- \rightarrow O_2^-$], and desorption of O$_2$ by the capture of a photo-generated hole [h$^+$ + $O_2^- \rightarrow$ O$_2$ (g)]. In 2000, Liu *et al.* designed and tested a ZnO UV photodetector based on metal-semiconductor-metal circular structures. The device consisted of a 1μm thick ZnO:N layer grown on *r*-plane sapphire, with aluminium as contact metal. The device showed low frequency photoresponsivity (~ 400 A/W) at 5 V bias, and high response speed. The minority lifetime of the device was of the order of 1 μs. The rise and fall times were calculated to be 1 and 1.5 μs, using a high-speed pulse laser. These are encouraging results highlighting the importance of ZnO-based devices.

Most promising, however, was the report of room-temperature UV nanowire nanolasers in 2001 (Huang *et al.*, 2001). Under optical excitation, Huang *et al.* reported surface-emitting lasing action at 385 nm from self-organized, <0001> oriented ZnO nanowires on sapphire substrates. This opens a door to using ZnO in the areas of optical computing, information storage, and microanalysis. It is worth mentioning that the lasing action was monitored in the absence of any fabricated mirrors; in these nanowires, one end is the epitaxial interface between sapphire and ZnO, while the other end is the sharp (0001)

plane of the ZnO nanocrystals. Both of these can act as laser cavity mirrors. Additionally, a long lifetime of 350 ps was measured for these nanowires. While these nanowires were deposited by a simple vapor transport and condensation process, it is known that MOCVD is an ideal growth technique for the deposition of other low-dimensional structures such as whisker structures.

ZnO has certainly displayed its potential in recent years, but remains much less studied than GaN, another wide-band gap semiconductor ($E_g = 3.5$ eV). Nevertheless, ZnO displays several advantages over GaN (Look, 2001):

- It has an exciton binding energy of 60 meV, compared to 25 meV for GaN
- It has a native substrate
- It allows wet chemical processing
- It is more resistant to radiation damage than GaN

These additional features warrant a continued study of ZnO, and bring motivation to further the understanding of the material.

3. CRYSTAL GROWTH BY
METALORGANIC CHEMICAL VAPOR DEPOSITION

The aim of this chapter is to describe the technique by which the layers studied in this work were deposited. It begins with a timeline describing the development of the MOCVD growth of ZnO. This section is crucial, as the results already reported in the literature set the tone and determined the goals of this project. Consequently, the experimental details pertaining to the system employed in this study are depicted. There follows a comparison between MOCVD and other growth techniques, and the last section of this chapter explains which substrates are fitting for the heteroepitaxy of ZnO.

3.1 *History of growth*

One of the crucial decisions associated with designing an MOCVD growth system is the choice of precursors. The crystal grower also needs to optimize the growth parameters in order to obtain high-quality layers. This section provides a timeline of the progress made in these areas over the last twenty-five years.

3.1.1 Lau *et al.,* 1980

In 1980, Lau *et al.* deposited ZnO thin films on *r*-plane sapphire using the reaction between diethyl zinc (DEZn) and oxygen sources such as H_2O, CO_2, and N_2O. H_2 was selected as carrier gas. They assessed the role of the reactor geometry on the growth process; while a vertical gas flow system with substrate rotation offered uniform films in the $DEZn/N_2O$ system, it led to solid ZnO particles being blown onto the substrate in the case of H_2O, and spurious growth problems. Optimum growth was achieved with a horizontal reactor tube. Furthermore, they encountered obstacles linked to their choice of reagents. DEZn is an electron-deficient compound that effortlessly bonds with compounds having free electron pairs. Since organo-zinc complexes are formed even at low temperatures, they had to make the reactants meet as close as possible to the substrate, and design their reactor chamber accordingly. The reactor chamber had to be kept under low pressure (400 Torr) in order to enhance complex dissociation and the elimination of reaction products from the growth surface. They recorded a maximum growth rate of 5.1 μm/hr at 400 °C for the $DEZn/H_2O$ system, but added that the growth

rates had to be kept low in order to retain epitaxy and avoid the spurious growth of needles. They showed H_2 to be a poor carrier gas for ZnO growth, as the material proved highly unstable in a H_2 atmosphere at high temperatures.

3.1.2 Roth and Williams, 1981c

Roth and Williams furthered the work begun by Lau *et al.* by investigating the DEZn/O_2 system on Pyrex glass substrates, focusing on the variation of deposition rate and resistivity with substrate temperature. They encountered similar problems as Lau *et al.*, as DEZn and O_2 react spontaneously even at room temperature, causing the deposition of white ZnO powder on the reactor walls downstream of the reaction area. In fact, they had to connect to the oxygen inlet a quartz tube extending inside the reactor to ~2 cm in front of the substrate edge. They also had to reduce the reactor pressure below atmospheric to 76 Torr to play down gas-phase reactions affecting growth rate and film quality. The growth rate was found to increase for temperatures above 370 °C, reaching a maximum value of 2.4 μm/hr at 450 °C. The zinc to oxygen ratio in the film also changed above 370 °C, as the number of oxygen molecules incorporated in the grown film increased. The resistivity, however, displayed a minimum value ($8 \bullet 10^{-2}$ Ωcm) at 370 °C, which they paralleled to the maximum mobility (~4 cm^2/Vs) measured at 370 °C. They consequently stated that the variation of resistivity with growth temperature was linked to the competition between crystallization and degree of nonstoichiometry of the films.

3.1.3 Wright *et al.*, 1984

In an effort to avoid the premature reactions observed with powerful compounds such as H_2O and O_2, Wright *et al.* drew inspiration from the demonstrated growth of GaAs and InP using adducts; indeed, certain adducts can be transported to the deposition area near the substrate after *in situ* formation, thus steering clear of the white ZnO deposits mentioned previously. Consequently, oxygen-containing heterocycle compounds such as furan, tetrahydrofuran, and tetrahydropyran successfully led to the deposition of ZnO thin films on GaP and glass slides. This result seemed promising, as an inconsequential but slightly perceptible film occasionally appeared on the reactor walls upstream from the hot substrate. Nevertheless, the quality of the samples left much to be desired; the layers had a slight orange-peel texture, and hillock structures were visible on the surface images of

the thin films. These hillocks corresponded to Zn-rich islands. The ZnO layers displayed limited *n*-type conductivity, with resistivities averaging 10^{-1} Ωcm. Furthermore, the growth rates recorded paled in comparison to previous work; a peak value of 1.9 µm/hr was measured for growth with tetrahydropyran. Making matters worse is the fact that the mechanism of the reaction between dimethyl zinc and these heterocyclic compounds was unknown, inhibiting further progress.

3.1.4 Oda *et al.*, 1985

A breakthrough in the MOCVD growth of ZnO finally came in 1985 when Oda *et al.* carried the idea of adduct transport to grow ZnO thin films with DEZn and alcohols (R-OH). The addition of excess alcohol to DEZn is known to only displace one alkyl group to give alkyl zinc alkoxides of the form EtZn(OR), which act as active precursors to the ZnO thin film and decompose on the substrate with a negligible activation energy. Additionally, it has been proven that ZnO thin films grown with *i*-propanol and *tert*-butanol are not contaminated by carbon atoms from the precursors; this has been explained by the formation of a cyclic six-center transition state which proceeds, via abstraction of a ***b***-hydrogen, to eliminate methane and an alkene in order to form the desired ZnO.

Oda *et al.* tested methanol (MeOH), ethanol (EtOH), and *tert*-butanol (TBOH) as oxidizing agents. They set their DEZn and alcohol flow rates at 54 and 1300~9000 µmol/min, respectively, by adjusting the He carrier gas flow through the bubblers. They studied growth from 200 to 400 °C. They first noted that water is the most prevalent impurity in alcohols, and studied its impact on the adhesion of the films. ZnO films could easily be peeled from the substrates when alcohols containing less than 10^{-4} mole fraction of water were employed. On the other hand, adding a small amount of water to the alcohols caused the films to stubbornly stick to the substrates. X-ray diffraction spectra displayed a single peak corresponding to the (002) peak of ZnO. Of all the alcohols tested in their work, *tert*-butanol generated a crystalline layer at the lowest temperature (200 °C). TBOH also engendered the highest degree of *c*-axis orientation, which was mirrored in the columnar structure observed by scanning electron microscopy.

Importantly, Oda *et al.* suggested that the *n*-type conductivity of their samples was related to a degenerated donor level resulting from oxygen vacancies.

3.1.5 Hahn *et al.*, 1998

To the author's knowledge, it took thirteen years after the publication of Oda *et al.*'s article to witness further research on the MOCVD growth of ZnO using alcohols as oxidizing agents. In 1998, Hahn *et al.* reported on the MOCVD growth of ZnO using dimethyl zinc (DMZn), dimethyl zinc-triethylamine (DMZn-TEN), and *tert*-butanol as precursors. Layers were deposited on standard float glass at temperatures ranging from 260 to 410 °C. They varied the VI:II ratio during growth between 2 and 18:1, and the horizontal reactor chamber was kept at atmospheric pressure. They reported *c*-axis oriented ZnO thin films with grain sizes averaging 100 nm. They also noticed that layers deposited at a substrate temperature of 360 °C and at VI:II ratios less than 2:1 appeared brownish. The VI:II ratio during growth is a measure of the O-to-Zn ratio in the gas phase during the film deposition process; a low VI:II ratio therefore implies a low O-to-Zn ratio during growth. Hahn's finding seems to corroborate Gupta's work[1], as Gupta reported that oxygen deficiencies are responsible for the poor transparency and brownish color of samples deposited by electron-beam evaporation. Furthermore, Hahn *et al.* measured the electrical properties of their samples at room temperature. They reported mobilities ranging between 50 and 60 cm^2/Vs and resistivities between 0.07 and 0.3 Ωcm for samples deposited at a substrate temperature of 380 °C and a VI:II ratio during growth of 3.5:1. This is an outstanding result; the maximum mobility recorded in this work for samples grown on *c*-plane sapphire was 11 cm^2/Vs.

3.1.6 Sallet *et al*, 2002

In their paper, Sallet *et al.* focused on an aspect of film deposition scarcely mentioned in the literature: the impact of the cleanness of the reactor tube on a sample's surface morphology and orientation. ZnO samples grown after the silica deflector and susceptor had undergone thorough cleaning in a HCl:HNO$_3$ solution exhibited smooth surfaces together with the hexagonal crystalline symmetry characteristic of (0001) orientation. On the other hand, thin films deposited in an unclean environment showed a stacking of

---

[1] Vinay Gupta, PhD Thesis, University of Delhi

coalesced grains, and [01$\bar{1}$2] orientation. ZnO deposits on the reactor walls are liable to reduce by 50 °C the pyrolysis temperature of *tert*-butanol, which may in turn affect the morphology and orientation of the epilayer. In addition, these ZnO deposits may defile the sapphire surface during the heating step prior to film deposition. Furthermore, Sallet *et al.* characterized their samples by various techniques such as X-ray diffraction and photoluminescence spectroscopy. They measured a full-width at half-maximum for the ZnO (0002) 2θ peak of 0.3 ° and a *c*-axis length of 5.20 Å, close to the bulk value of 5.2066 Å (ASTM). The photoluminescence spectra recorded at 1.2 K were dominated by sharp near-band edge excitonic transitions. The width of these NBE peaks (< 3 meV) highlighted the optical quality of the material.

3.1.7 Oleynik *et al.*, 2003

In their work, Oleynik and co-workers deposited ZnO layers on *n*-Si (111) substrates covered by GaN templates. They opted for dimethyl zinc (DMZn) as Zn source, and *i*-propanol, acetone, and N_2O as oxidizing agents. The higher reactivity of DMZn compared to DEZn is explained by the difference in Zn-C bond strength (Smith, 1983). The bulk of this report centered on the surface attributes of the ZnO thin films, as studied by optical microscopy, scanning electron microscopy, and atomic force microscopy. With *i*-propanol, Oleynik *et al.* obtained their best layers at a substrate temperature and reactor pressure of 450 °C and 300 mbar (225 Torr), respectively, and a VI:II ratio during growth higher than 40:1. The samples consisted of hexagonal columns, highlighting the (0001) orientation of the crystals. They observed the presence of particles lodged on top of some hexagonal columns; these particles were found to etch away more slowly than the columns. They performed cathodoluminescence measurements on their layers, and correlated the surface morphology with the luminescence intensity. In fact, the strongest luminescence emerged from the edges and the top of the hexagonal columns. The CL emission was centered at a (A°, X) peak. The most striking result of this paper is the link between the oxygen precursor and the optical quality of the samples; layers grown with *i*-propanol and N_2O both displayed the (A°, X) peak, while no luminescence was measured from layers deposited with acetone as oxygen source.

3.1.8 Kirchner *et al.*, 2003

Kirchner *et al.* tackled the role of reactor pressure on the growth rate of their samples deposited with hydrogen as carrier gas, diethyl zinc (DEZn) as zinc source, and either *i*-propanol (*i*-PrOH) or *tert*-butanol (TBOH) as oxidizing agent. In both cases, the maximum growth rate was measured at a pressure of 400 mbar. At lower pressure, the mean-free path of the precursor molecules is too long for efficient adduct formation to take place. At higher pressures, parasitic reactions occur, causing a white, powdery fall-out in the case of *i*-PrOH, and brownish flakes with TBOH. These brownish flakes were not observed in this work, where TBOH was also chosen as oxidizing agent. Furthermore, the stability of the alkoxide adduct explained why the variation of growth rate with substrate temperature was different for *i*-PrOH and TBOH. The *i*-PrOH growth rate dropped suddenly at 380 °C, while the TBOH rate remained stable at 2.1 μm/hr from 380 to 510 °C. The alkoxide adduct formed with *i*-PrOH is believed to crack before this mass transport limited area of the growth rate curve is reached. Furthermore, disparities in optical quality surfaced in the 2.1 K photoluminescence spectra of the layers. Even though the PL spectra of *i*-PrOH and TBOH samples were both dominated by a donor-bound exciton peak, a considerable discrepancy in FWHM was observed: 1.1 meV for the TBOH layers, 4.5 meV for the *i*-PrOH samples. TBOH therefore seems to surpass *i*-PrOH as oxidizing agent for this system.

3.2 The MOCVD growth process

All the ZnO samples studied in this work were grown in a laboratory scale MOCVD system from *Crystal Specialties, Inc.* (figure 3.1) Since the system had previously served for the industrial growth of III-V compounds, a number of modifications had to be made.

The initial layers of this project were deposited with O_2 as oxidizing agent instead of *tert*-butanol, and the changes to the system reflect the peculiarities of such a powerful source (see section 3.1).

The fast switching manifold was removed, as DEZn and O_2 react even at room temperature. A *Thomas Swan* laboratory scale reactor tube (figure 3.2) able to handle 2x2 cm^2 substrates was fitted. This horizontal tube has a rectangular flat surface accommodating the susceptor, which supports the substrate. Graphite was chosen over molybdenum (Mo) as susceptor material, since Mo is known to react with O_2 to form molybdenum oxides. The susceptor makes an angle of 20 ° with the horizontal reactor floor; this configuration was preferred over a flat susceptor in an attempt to cause maximum impact of the gases onto the substrate. The original RF heating coil was replaced with a halogen lamp mounted outside the reactor, but below the susceptor. The substrate temperature was then monitored by a digital three-term PID controller, with a Ni-Cr/Ni-Al thermocouple embedded in the susceptor. A pressure gauge was also added to the system to monitor the reactor pressure.

The severity of the pre-reactions between DEZn and O_2 led to the use of *tert*-butanol as oxidizing agent; the results to be presented here stem from the work done with *tert*-butanol.

The group II precursor selected for this work was electronic grade diethyl zinc (DEZn), while *tert*-butanol (TBOH) served as oxidizing agent. The influence of the TBOH purity on sample quality was studied, and layers were deposited with electronic grade

(99.9999 % purity-6N) as well as 99.9 % pure (3N) TBOH. The choice of TBOH source (6N or 3N) will be clearly stated in each result chapter.

DEZn and TBOH form ZnO according to the following reaction:

$$(C_2H_5)_2Zn + (CH_3)_3COH \rightarrow \mathbf{ZnO} + CH_2{=}C(CH_3)_2 + CH_4$$
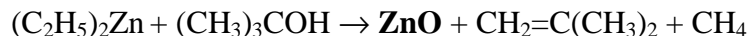
All the gases, the organometallic source (DEZn), and the oxidizing agent (TBOH) reached the reactor tube through individual lines. The TBOH line was wrapped with a heating coil in order to avoid the formation of TBOH crystals (TBOH melts at 25 °C). Valves located at the inlets of the reactor chamber enabled the gas flow to enter the reactor or the ventilating bypass system.

Electronic mass flow controllers regulated the flow of the reactants to the reactor chamber. Both the DEZn and TBOH sources were lodged in bubblers immersed in constant temperature baths. Argon gas (5N) flowed through the bubblers in order to pick up DEZn and TBOH vapor and acted as carrier gas to push the precursors, in the gas phase, to the reactor. A Micro Torr model PS 11-MC1-N filter from *SAES Pure Gas Inc.* was installed along the Ar line to further enhance its purity. The system was purged with nitrogen (N_2) when idle.

The temperature of the bath (T_{DEZn}) controls the vapor pressure of DEZn (P_{DEZn}) according to the following equation (Alfa Catalogue, 1978):

$$\log_{10}[P_{DEZn}(\text{Torr})] = 8.28 - \frac{2109}{T_{DEZn}}$$

The bath temperature was kept at 25 °C, yielding a DEZn vapor pressure of 15.95 Torr.

P_{DEZn}, in turn, establishes the DEZn flow rate (mol/min) by way of the ideal gas law:

$$n_{DEZn} = \frac{P_{DEZn}V_{DEZn}}{RT_{DEZn}}$$

where n_{DEZn} is the number of moles reaching the reactor tube per minute, and V_{DEZn} the volume of argon flowing through the DEZn bubbler per minute. V_{DEZn} in turn is determined by the mass flow controller.

The number of moles of TBOH carried to the reactor tube per minute (n_{OH}) can be calculated in similar fashion from the vapor pressure of TBOH, assuming that the argon flowing through the TBOH bottle is saturated with TBOH vapor. The TBOH bath was kept at 40 °C, where the TBOH vapor pressure is known to be 100 Torr (Handbook of Chemistry and Physics, 1977).

The VI:II ratio during growth is then defined as

$$\frac{n_{OH}}{n_{DEZn}} = \frac{TBOH\ flow\ rate\ in\ \textit{m}mol/\min}{DEZn\ flow\ rate\ in\ \textit{m}mol/\min} \qquad \text{...(3.1)}$$

After mixing, the gases are driven out of the reactor tube and through the pyrolysis furnace kept at 500 °C, where any remaining DEZn will be cracked. They are then expelled through the vent to atmosphere.

The DEZn flow rates used in this study ranged between 8 and 43 µmol/min (9 and 50 cc/min, respectively), while the TBOH rates varied between 215 and 1390 µmol/min (42 and 271 cc/min). The carrier gas flow rate was kept constant at 2000 cc/min. The VI:II ratio during growth was tuned between 10 and 90:1.

Figure 3.1: The MOCVD system

Ar

Ar filter

N_2

MFC

DEZn

Argon carrier

TBOH

VENT

Halogen lamp

Cracking Furnace

Pressure gauge

VENT

DEZn + Ar

Substrate

Thermocouple

TBOH

Halogen
lamp

Graphite
susceptor

VENT
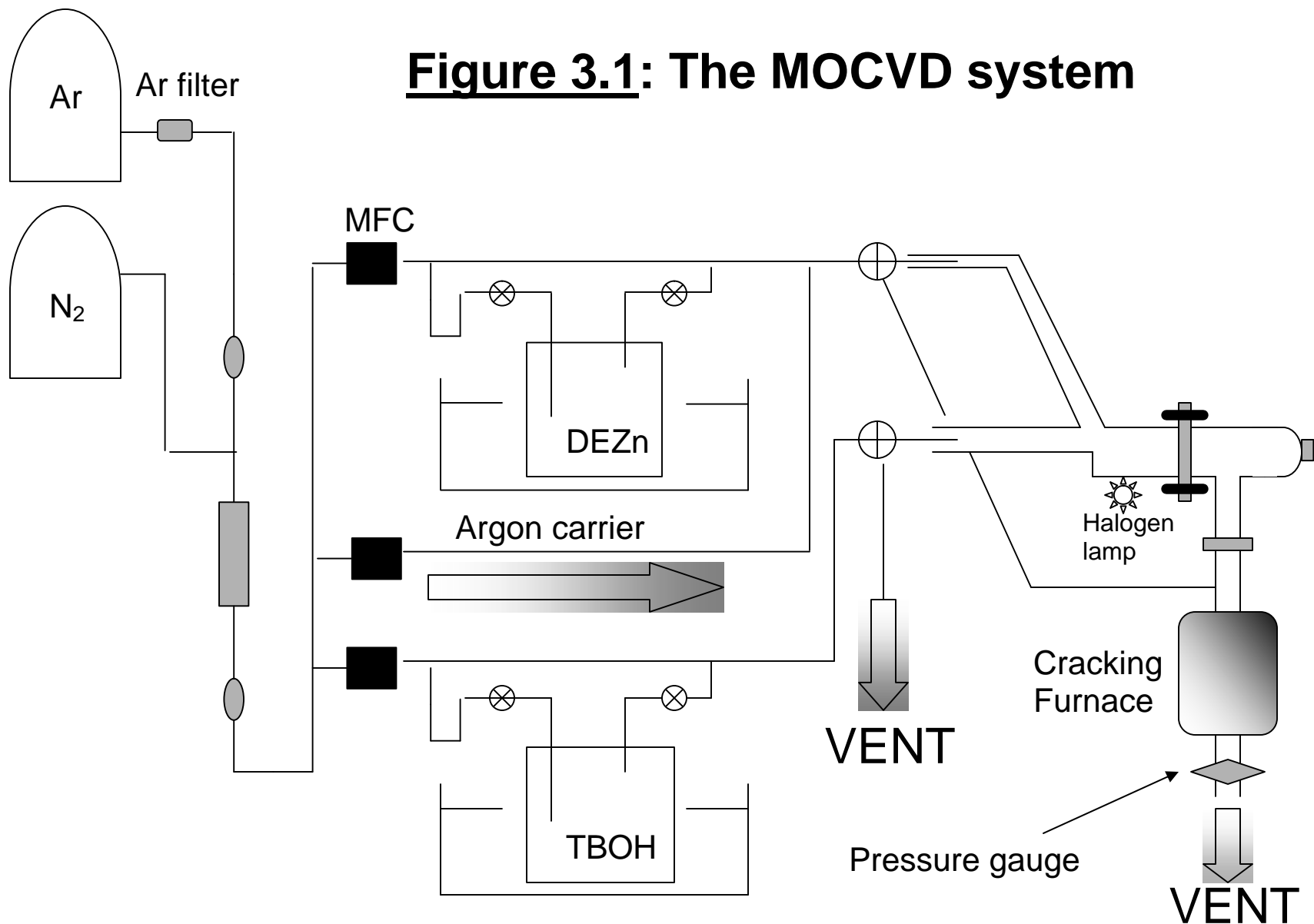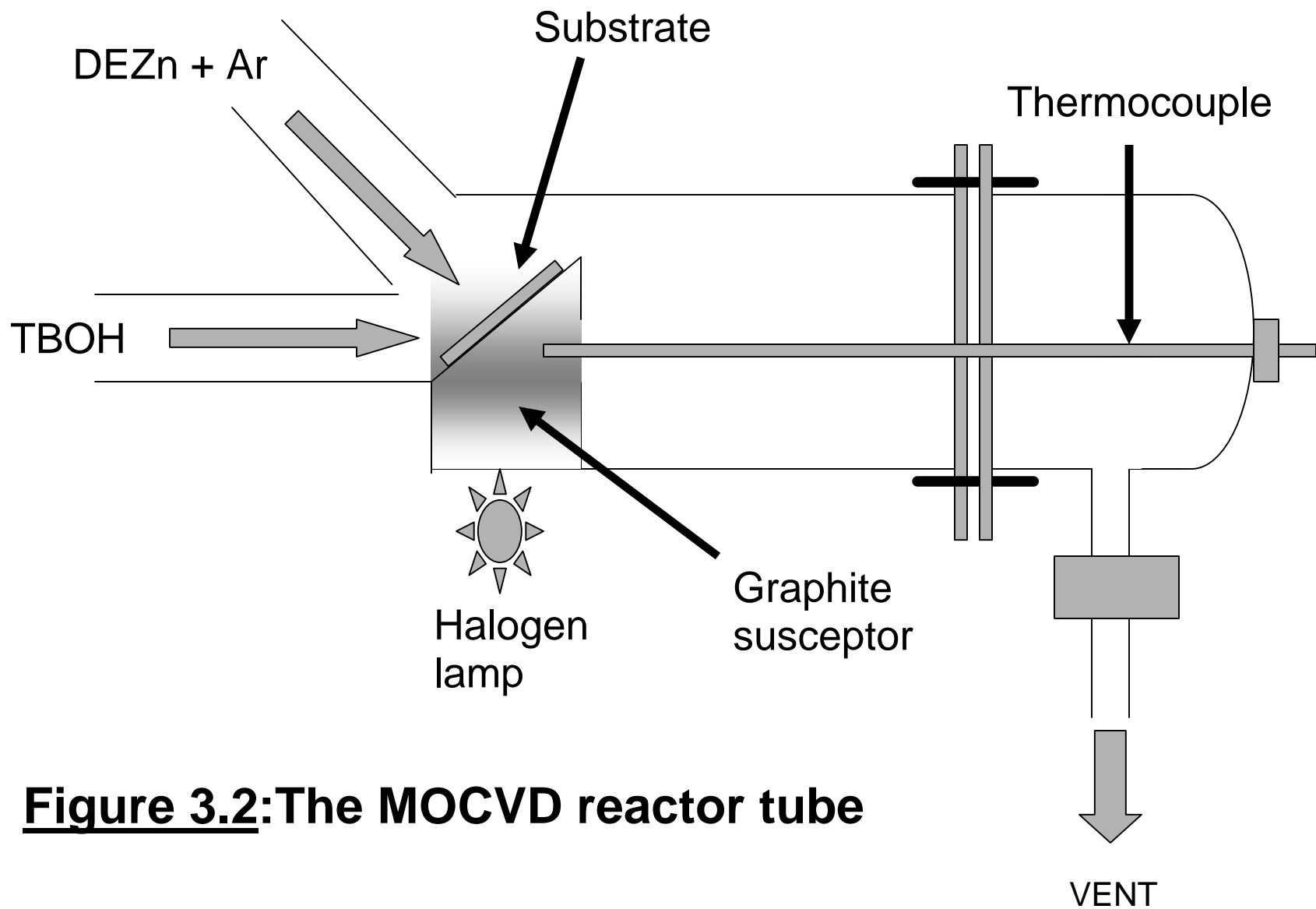
Figure 3.2:The MOCVD reactor tube

3.3 Comparison with other growth techniques

ZnO thin films have been grown over the years by several techniques. The aim of this section is to contrast these deposition methods with MOCVD, as well as provide an overview of sample quality in comparison with the material grown in this study.

Molecular beam epitaxy (MBE) is a well-known deposition method able to yield high-quality layers with abrupt interfaces and good control of thickness, doping, and composition (Cho, 1971). In MBE, the semiconductor precursors are found in the form of molecular beams, and are deposited onto a heated crystalline substrate to generate thin epitaxial layers. The molecular beams in question are usually made from thermally evaporated elemental sources. In order to obtain high-purity layers, it is vital to adopt extremely pure sources and to work in an ultra high vacuum (UHV) environment. On the other hand, semiconductor thin films can be deposited by MOCVD at atmospheric pressure. Another difference between MBE and MOCVD lies in the growth rates achieved, which are generally of the order of a few Å/s for MBE. This is illustrated by Ko *et al.*'s work (2000b). They grew ZnO films on epi-GaN predeposited on Al_2O_3 substrates by RF-plasma assisted MBE. GaN is a good template for ZnO growth on sapphire as it is closely lattice-matched to ZnO, yielding a lattice mismatch of only 1.8 % compared to 18 % for the ZnO/ Al_2O_3 system. They reported growth rates ranging between 0.4 and 0.75 µm/hr. Growth rates obtained in this study were as high as 5.0 µm/hr (see section 5.2.5) for growth on *n*-Si 2 ° (100) substrates. The optical quality of their layers was outstanding, as shown by their low temperature (10 K) photoluminescence spectra. They reported full-width at half-maximum values of 1.5 and 2.2 meV for the dominant near band edge (I_4 and I_2) emission bands. A full-width at half-maximum as narrow as 7 meV is reported in this study (see section 8.3.3). Having said that, the layer studied in section 8.3.3 was not grown on a buffer but directly on the Si substrate, which has a cubic diamond lattice. Introducing a buffer layer could reduce the 7 meV FWHM further.

The next two growth techniques are appealing because they have led to the deposition of *p*-type ZnO thin films.

Let us start with pulsed laser deposition (PLD). The concept behind PLD is simple. Short, high-energy laser pulses cause the evaporation of a target surface; this is followed by vapor condensation on a substrate, thus leading to a thin film having the same composition as the target. PLD is a versatile, cost-effective, and fast deposition technique generating high quality layers in less than fifteen minutes. Guo *et al.* (2001) took the PLD process a step further by using N_2O plasma to boost the oxidation of the Zn target, and to incorporate N in the ZnO film during the pulsed laser reactive deposition and plasma implantation process. This resulted in N acceptor doping, and *p*-type ZnO layers with carrier concentrations between 3 and $6 \bullet 10^{18}$ cm^{-3}, resistivities ranging between 2 and 5 Ωcm, and mobilities between 0.1 and 0.4 cm^2/Vs. They studied the structural properties of their samples by X-ray diffraction, and measured a FWHM of between 0.047 and 0.247 ° for the dominant ZnO (002) peak. The narrowest (002) peak recorded in this study was 0.17 °, within Guo *et al.*'s range.

Magnetron sputtering, on the other hand, works by removing a material from a solid cathode by bombarding it with positive ions emitted from a rare gas discharge. This transfer of momentum from impacting ions to surface atoms forms the foundation of sputter deposition. Sputtering leads to high quality, uniform films and like MOCVD is suitable for large-area deposition. Ye *et al.* (2003) adopted an idea similar to that described as Guo *et al.* (2001) and grew their films in an NH_3-O_2 ambient to incorporate N in the ZnO thin films. They reported a hole concentration of $3.2 \bullet 10^{17}$ cm^{-3}, a resistivity of 35 Ωcm, and a mobility of 1.8 cm^2/Vs. They also fabricated ZnO *p-n* homojunctions (*p*-N:ZnO/*n*-ZnO/*p*-Si), and obtained extremely high resistivities (10^7 $\Omega.cm$) for both the *p*- and *n*-type ZnO layers.

The next two deposition methods are mentioned because of their unconventional character, and because they are available at low-cost to the industry.

Zhenguo *et al.* (2003) have applied the *reactive deposition* technique to sublime zinc acetate dihydrate ($Zn(CH_3COO)_2•2H_2O$) onto a substrate, leading to ZnO thin films according to the following reaction:

$$Zn(CH_3COO)_2 \rightarrow ZnO + CO_2 + CH_3COCH_3$$
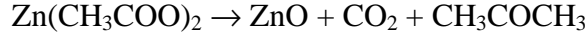
The ZnO thin films are thus deposited in a quartz tube evacuated to a base pressure of 10^{-3} Torr. The difference between zinc acetate dihydrate and the diethyl (or dimethyl) zinc chosen for MOCVD lies in its cost (zinc acetate dihydrate is cheaper than metal-organics), reactivity (zinc acetate dihydrate does not react with air or water), and toxicity (zinc acetate dihydrate is less toxic than DEZn). Zhenguo *et al.* reported that their films grown on glass displayed *c*-axis orientation, with a full-width at half-maximum of 0.30 ° for the XRD (002) peak. The most intriguing point observed from this study was the large range of electron concentrations measured, from $6.74•10^{12}$ to $1.86•10^{18}$ cm^{-3}, depending on the substrate and source temperature. The mobility values varied between 0.5 and 7.2 cm^2/Vs. The maximum room temperature mobility recorded in this study was 10.8 cm^2/Vs.

Furthermore, Basak *et al.* (2003) also employed zinc acetate dihydrate to deposit ZnO thin films with the *sol-gel* technique. Like the *reactive deposition* technique, the sol-gel method is known for its low operating cost. In the sol-gel method, zinc acetate dihydrate is first added to dehydrated isopropyl alcohol to prepare a solution, which is then mixed until it becomes transparent. The substrate is consequently coated using the drain coating method, and the film is dried in a hot oven. The thickness of the film obtained after repeating this coating and drying process ten times was only 300 nm. While the costs of growing thin films with the sol-gel method are low, the optical quality of the samples obtained leaves much to be desired. Figure 3.3 compares Basak *et al.*'s room temperature photoluminescence spectrum with a scan recorded in this work. The near-band edge emission of the sol-gel layer is weak compared to the defect-related visible band, and the samples deposited by MOCVD in this work are of much higher optical quality.
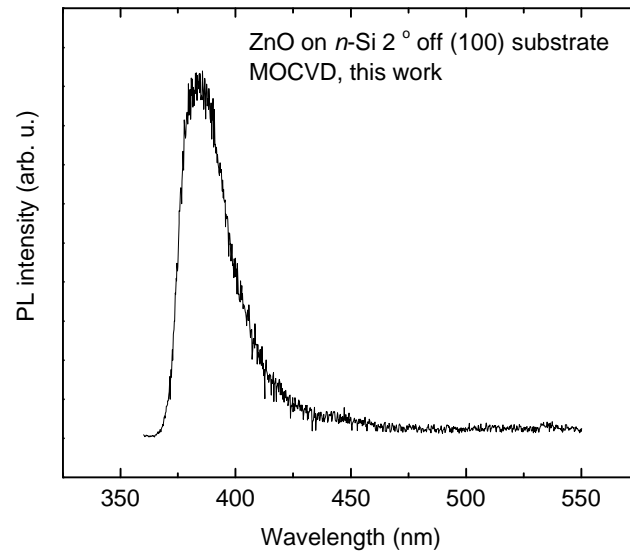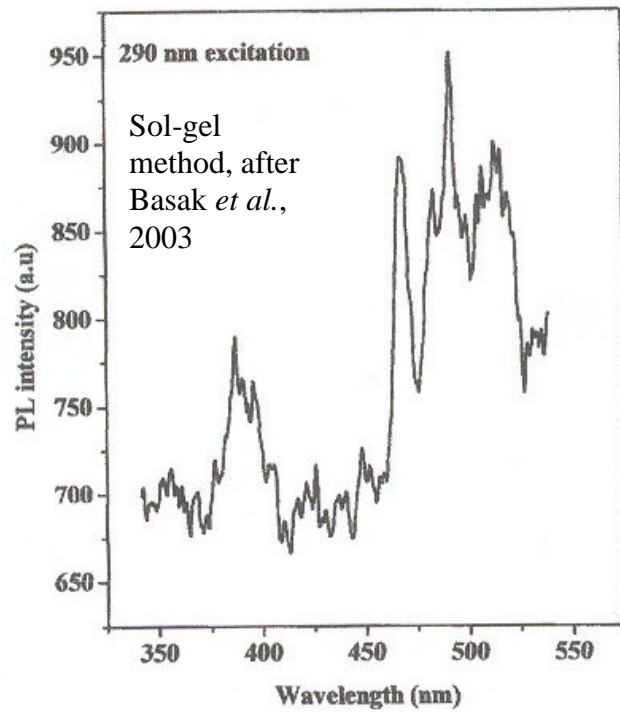
Figure 3.3: Room temperature photoluminescence spectra of ZnO samples deposited by the sol-gel method (top, after Basak *et al.*, 2003) and by MOCVD (bottom, this work)

3.4　Suitable substrates for the growth of ZnO

When working on a heteroepitaxial system, it is important to seek a low lattice mismatch between the epilayer and the substrate, as a large mismatch is likely to engender great residual strain and structural defects in the epilayer. GaN, with its wurtzite structure and similar lattice constants, seems an ideal and obvious substrate for ZnO growth. Regrettably, GaN does not have a native substrate; nevertheless, it has repeatedly been chosen as a buffer layer for the growth of ZnO (Ataev *et al.*, 2001).

On the other hand, *c*-plane sapphire ($a = 4.75$ Å, $c = 12.99$ Å) is one of the most commonly chosen substrates for growth and characterization of ZnO thin films. This is linked to the epitaxial relationship between ZnO and *c*-Al_2O_3 (Chen *et al.*, 1998). Indeed, the initial incommensurate growth of ZnO on *c*-Al_2O_3 takes place in a two-dimensional mode. Having said that, the $[2\bar{1}\bar{1}0]$ direction of ZnO then aligns itself with the $[1\bar{1}00]$ direction of *c*-Al_2O_3, while the $[1\bar{1}00]$ direction of ZnO follows the $[1\bar{2}10]$ direction of *c*-Al_2O_3. The 30 ° rotation of the ZnO orientation against the *c*-plane sapphire substrate is due to the ZnO lattice aligning itself with the oxygen sublattice in *c*-Al_2O_3. The resulting lattice mismatch is found to be 18 %. Additionally, *c*-axis growth is highly favored on *c*-Al_2O_3 (Gorla *et al.*, 1999). In fact, the $[0001]$ planes in the ZnO structure are Zn-terminated, while the $[000\bar{1}]$ planes end with O atoms. As previously mentioned, ZnO shows partial ionic character (section 2.1), leading to a partial and opposite charge on the $[0001]$ and $[000\bar{1}]$ planes. A net dipole therefore exists when the basal plane terminates the crystal; this causes the surface energy to diverge. By contrast, the $(11\bar{2}0)$ and $(10\bar{1}0)$ prismatic planes are nonpolar, since they have the same number of Zn and O atoms. The prismatic planes therefore have a lower surface energy than the basal plane, resulting in a strong growth rate along the *c*-axis.

As can be seen from figure 3.4, the difference in lattice constants between zinc oxide and common III-V substrates such as GaAs and InP is responsible for the large lattice

mismatch in the ZnO/GaAs and ZnO/InP systems. Nevertheless, these systems require appropriate study for the sake of industry.
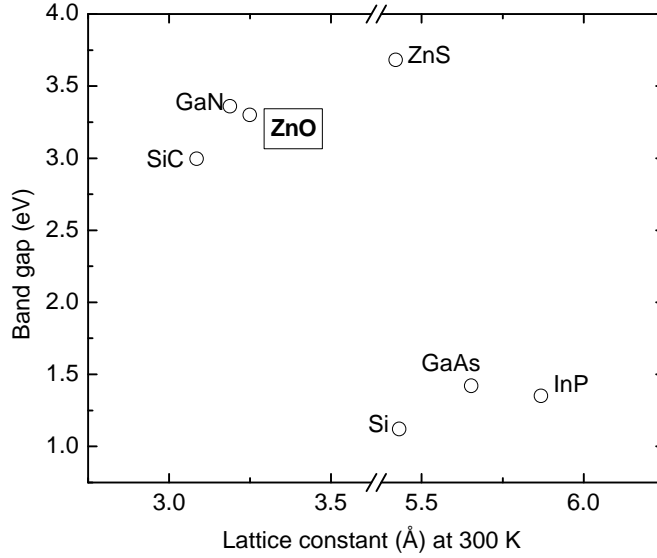
Figure 3.4: Variation of semiconductor band gap with lattice constant at 300 K

GaAs has a zincblende structure with a lattice constant of 5.6533 Å, and ZnO deposition on GaAs leads to a lattice mismatch of 19 %. This is an important growth system, as ZnO enhances the piezoelectric coupling of GaAs, therefore strengthening the use of GaAs for acoustic charge transport devices (Kim *et al.*, 1994a). On top of that, the ZnO film structure also enables the monolithic integration of SAW devices and GaAs electronics.

ZnO thin films have also been deposited on InP, which has a zincblende structure with a lattice constant of 5.8686 Å (Ramamoorthy *et al.*, 2001). The allure of InP lies in the possibility of creating *n*-ZnO/*p*-InP heterostructure solar cells for space applications; indeed, ZnO has been proven to behave as anti-reflection medium on InP.

Si is naturally relevant in the context of ZnO/Si junction solar cells. Even though Si has a cubic diamond structure with a lattice constant *a* of 5.4301 Å, it is a suitable substrate for the growth of ZnO as its thermal expansion coefficient ($3.6 \bullet 10^{-6}$ /°C) is close to that of ZnO ($4.0 \bullet 10^{-6}$ /°C) (Shimizu *et al.*, 1982). For the sake of comparison, GaAs and GaN

have thermal expansion coefficients of $6.93 \bullet 10^{-6}$ /°C and $3.17 \bullet 10^{-6}$ /°C, respectively (Kumar and Sastry, 2001; Morkoç, 1999). Furthermore, low resistivity ZnO layers displaying high optical transparency in the visible-to-infrared range, surface flatness, and good adherence to the substrate have been grown by chemical vapor deposition (CVD) on silicon. It has also been reported that introducing a Zn buffer layer on a Si (100) substrate strongly improves the crystal quality of the ZnO epilayer (Fu *et al.*, 1998b). This was attributed to the mismatch between the [$\bar{1}$100] direction of ZnO (5.63 Å) and $2x[\bar{1}2\bar{1}0]$ of Zn (5.33 Å) being only 5.4 %, while the mismatch between $3x[2\bar{1}\bar{1}0]$ of ZnO (9.75 Å) and 2x[0001] of Zn (9.9 Å) is a mere 1.5 %.

In the light of the complications stemming from a large lattice mismatch, several new materials have been suggested and tested as substrates for the growth of ZnO. $ScAlMgO_4$ (SCAM) is a pleasing substrate from the standpoint of lattice matching, as it offers a misfit of only 0.09 % (Makino *et al.*, 2002). SCAM is a natural superlattice composed of alternatively stacked layers of wurtzite (0001)-face $(Mg,Al)O_x$ and rocksalt (111)-face ScO_y; it has a hexagonal unit cell with lattice constants $a = 3.246$ Å and $c = 25.195$ Å. The literature mentions that layers deposited on SCAM have high carrier mobility (100 cm^2/Vs) and low residual carrier concentration (10^{15} cm^{-3}).

Opal substrates have also being investigated in the context of nanoheteroepitaxy (Ursaki *et al.*, 2004). Indeed, nanoheteroepitaxy has recently been put forward as a means of appreciably extending the thickness of pseudomorphic growth in mismatched systems; synthetic opal structures qualify as substrates for this technique as they are made of nanostructure-size patterns controlled by the diameter of their colloidal spheres. Initial results have verified the potential of opal substrates, and high quality, strain-free, optically active ZnO layers have already been reported.

As described in section 2.3, modulation of the ZnO band gap is fundamental to developing reliable heterojunctions for opto-electronic devices; it has been reported that the ZnO band gap can be adjusted from 3.0 to 4.0 eV by alloying ZnO with Cd and Mg,

respectively, forming $Cd_{0.07}Zn_{0.93}O$ and $Mg_{0.33}Zn_{0.67}O$ (Makino *et al.*, 2001). It is therefore necessary to find substrates that would be appropriate for the growth of the $Mg_xZn_{1-x}O$ and $Cd_yZn_{1-y}O$ alloys. Fortunately, the lattice constants of ZnO are only slightly disrupted by the alloying process. With Mg, *a* rises and *c* drops by approximately 1 % as *x* increases to 0.33. In the case of Cd alloying, the *a* lattice parameter increases from 3.25 to 3.26 Å and *c* shifts from 5.20 to 5.24 Å as *y* rises to 0.07. Alloying should not significantly affect the choice of substrate for the ZnO system.

In this study, ZnO thin films were deposited on four different substrates: *n*-Si 2 ° off (100), amorphous glass (fused silica), *n*-GaAs (100), and *c*-plane sapphire substrates. Certain characterization techniques cannot be applied to films deposited on certain substrates; Hall measurements cannot be performed on a ZnO sample deposited on a conducting substrate for example. This choice of substrates thus enabled the study of both the structural, optical, and electrical properties of ZnO epilayers.

4. SECOND HARMONIC GENERATION IMAGING

In recent years, great progress has been made in producing nonlinear optical waveguides from single crystals such as $LiNbO_3$, KTP, and $LiTaO_3$ for potential applications in integrated optics (Doumuki *et al.*, 1994; Guo *et al.*, 2000). Furthermore, the nonlinear properties of ZnO require proper consideration in order to maximize its function in UV optoelectronic devices. Unlike other structural characterization techniques such as atomic force microscopy, Rutherford backscattering, or reflection high energy electron diffraction, Second Harmonic (SH) Generation Imaging relies on the nonlinear optics of the sample probed, and several groups are currently studying the second harmonic efficiency of ZnO layers (Neumann *et al.*, 2004). In this work, SH mapping was applied to the surface study of ZnO thin films deposited on various substrates. While this characterization method has already been employed in the study of SiC polytypes, this is believed to be the first instance of ZnO epilayers investigated by SH mapping.

4.1   *Background theory*

In most SH experiments on semiconductor surfaces, a monochromatic beam (plane wave) of frequency *w* is incident upon the material, and generates a SH in reflection or transmission. ZnO has a non-centrosymmetric wurtzite structure, which displays broken inversion symmetry. Its second order non-linear polarization $\vec{P}^{(2)}$ (2ω) is therefore dominated by the electric dipole contribution $?^{(2)}_D$ of the second order optical non-linear susceptibility tensor according to the following equation,

$$\vec{P}^{(2)}(2\omega) = ?^{(2)}_D : \vec{E}(w)\,\vec{E}(w) \qquad\qquad \textbf{...(4.1)}$$

where $\vec{E}(w)$ is the electric field incident on the surface (Guyot-Sionnest and Shen, 1988). $?^{(2)}_D$ depends on the orientation and crystal structure of the sample, and has two independent components $?^{(2)}_{31}$ and $?^{(2)}_{33}$ in the Kleinmann approximation (Sipe *et al.*, 1987). During mapping experiments, the intensity of the reflected SH signal is monitored

while azimuthally rotating the sample about its *z*-axis. ZnO has been shown to display strong SH response, and is therefore an appropriate candidate for SH imaging.

4.2   Experimental procedure

The images presented here were taken at the *Laser Research Institute* of the University of Stellenbosch, South Africa[2].

The surface SH measurements were recorded with a commercial Ti:Sapphire oscillator from *Spectra Physics*. It is common practice to choose high-power pulsed lasers because of the low generation efficiency of surface SH. The laser pulse width (80 ± 5) fs and the repetition rate of 80 MHz were gauged by a custom built autocorrelator and a pulse train detector, respectively. A standard power meter from *Coherent* yielded a maximum pulse energy of 10.5 nJ. The spectral pulse composition, centered at a wavelength of 782.8 nm (1.59 eV), was recorded on a CCD array spectrometer from *Ocean Optics S1000*. Laser power fluctuations remained below the 3 % mark over the duration of the experiments.

Figure 4.1 shows the experimental setup utilized for SH imaging. The laser beam was aimed at the sample at an incident angle of 45 °. The spot size of (13 ± 2) μm at the focal point was established from the *z*-scan technique. The SH signal was split from that of the laser fundamental by a suitable set of cut-off filters, and recorded by a *Hamamatsu R760* photomultiplier tube. A computer automated data acquisition system together with lock-in amplifier and 500 Hz chopper enabled magnification of the signal to noise ratio. The samples were mounted on a computer controlled XY-stage. All measurements were taken in ambient air at room temperature. The samples were subjected to p-polarized excitation, where the incident electric field is in the plane of incidence (the $\hat{x} - \hat{z}$ plane).

---

[2] The author is indebted to Thorsten Scheidt of the Laser Research Institute for collecting the SH images and for fruitful discussions.

Figure 4.1: Experimental set-up for Second Harmonic Generation Imaging (after Scheidt *et al.*, 2004 - private communication)

M : mirror   F : filter   L : lens
P : polarizer   PMT : photomultiplier tube
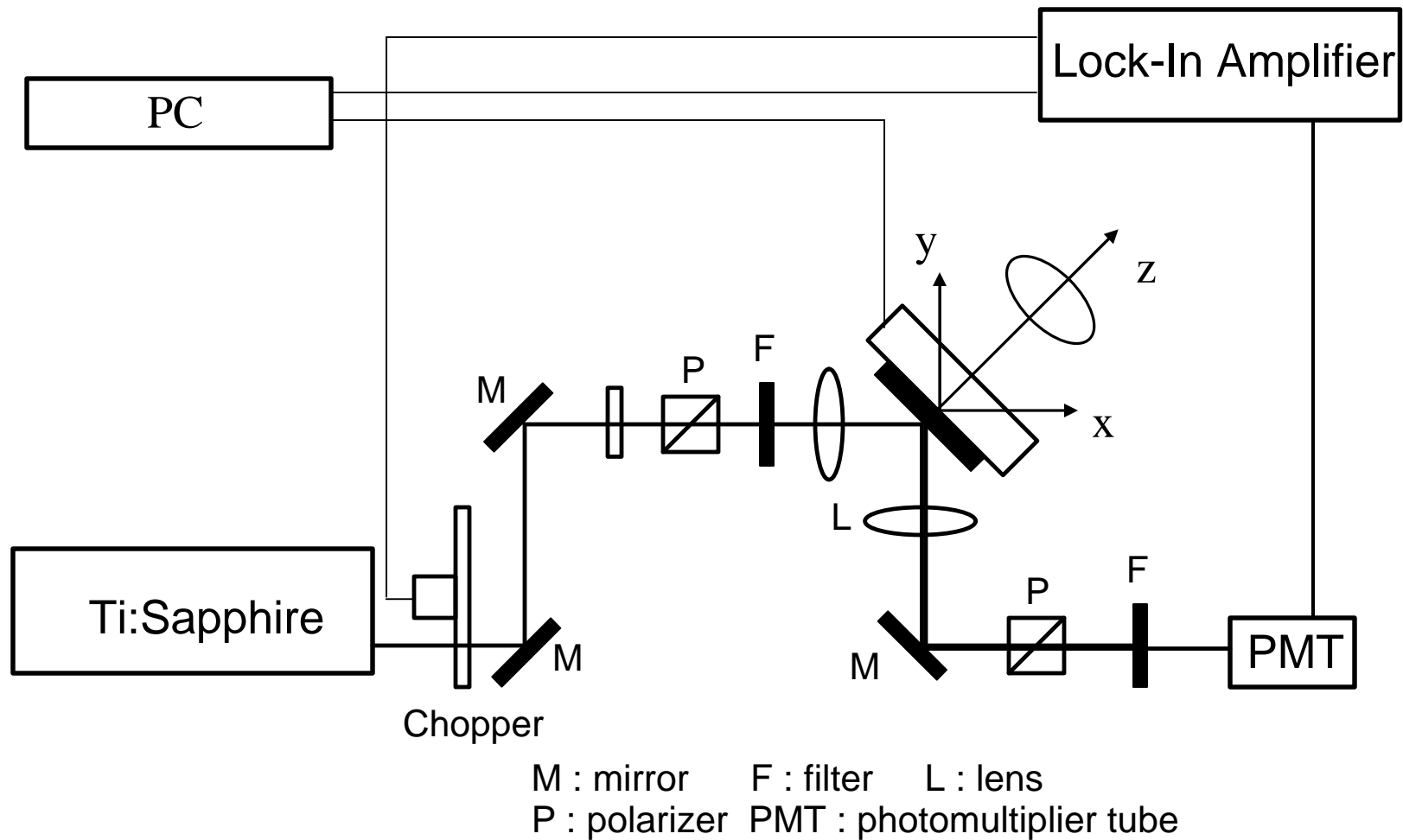
4.3   Results

The samples studied in this section are labeled according to their substrate and thickness in µm; S stands for *n*-Silicon 2 ° off (100), AG for amorphous glass, and G for *n*-GaAs (100). S5, for example, is a 5 µm thick sample grown on *n*-Si 2 ° off (100). Detailed information on the growth of the ZnO epilayer is available in chapters 5, 6, and 7.

4.3.1 Growth on *n*-Si 2 ° off (100) substrates

The second order nonlinear polarization $\vec{P}^{(2)}$ (2ω) of a sample is linked to its second order nonlinear susceptibility tensor $?\,^{(2)}_D$ according to equation 4.1. Moreover, $?\,^{(2)}_D$ determines the rotational anisotropy of the SH intensity, $I^{(2w)}(f)$, which is given in the electric dipole approximation by a truncated Fourier expansion (Lüpke, 1999)

$$I^{(2w)}(f) \propto \left| \overset{\leftrightarrow}{c}_D^{(2)} E^{(w)} E^{(w)} \right|^2 = \left| \sum_{m=0}^{3} a_m \cos m(f + f_m) \right|^2 I^{(w)^2} \qquad \text{...(4.2)}$$

with the complex a_m depending on the contributing elements of $?\,^{(2)}_D$ multiplied by Fresnel factors, where f and f_m are the sample azimuthal angle and the relative phases of the anisotropic a_m, and where $E^{(w)}$ and $I^{(w)}$ depict the electric field and intensity of the optical excitation at the fundamental frequency w. In order to test the presence of SH phenomena in this system, the variation of SH intensity with laser power of sample S5 is plotted (figure 4.2).
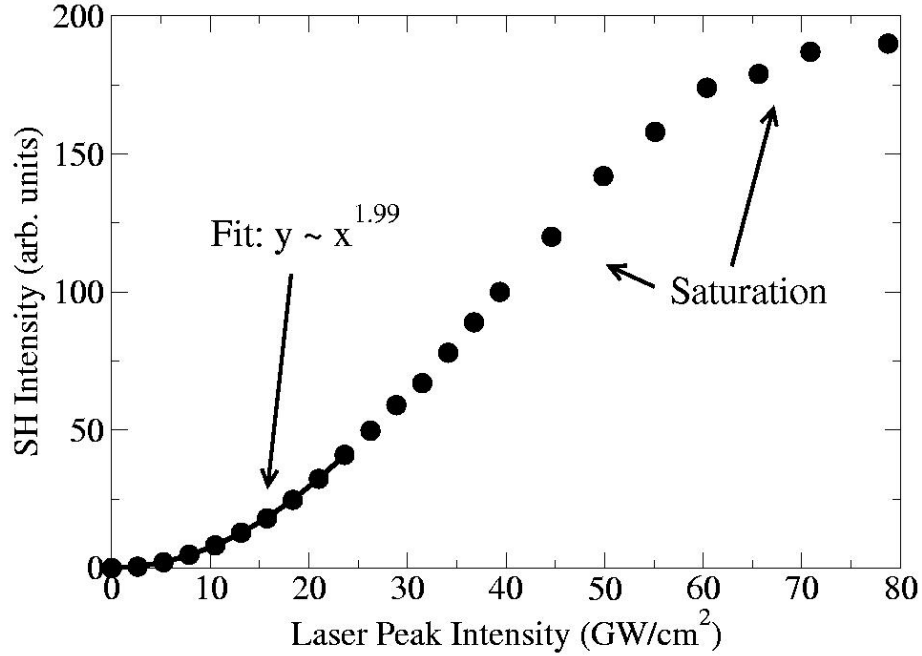
Figure 4.2: Variation of SH intensity with laser power

A polynomial curve is fitted to the experimental data points; it shows that the SH intensity and the laser power follow a square polynomial relationship. The fit matches the data up to 55 GW/cm^2, after which the SH intensity saturates at approximately 180 arb. units. Considering equation 4.2, which outlines the link between $I^{(2w)}$ and $I^{(w)}$, this initial result validates the SH measurements performed with the setup described above.

Next, the thickness dependence of the SH intensity is studied by applying SH imaging to samples S1, S5, and S10 (figure 4.3). Silicon has a centrosymmetric cubic diamond structure, and therefore adds no electric dipole contribution to its bulk second order optical susceptibility (Guyot-Sionnest, 1988; Sipe *et al.*, 1987). The SH response of the ZnO epilayer dominated the collected signal by an order of magnitude, and it wasn't necessary to correct the images for the SH derived from the Si substrate. All images display a sample area of 3x3 mm^2, and were recorded at equal incident laser intensity at the focal point of 12.5 GW/cm^2, with a step resolution of 30 μm.
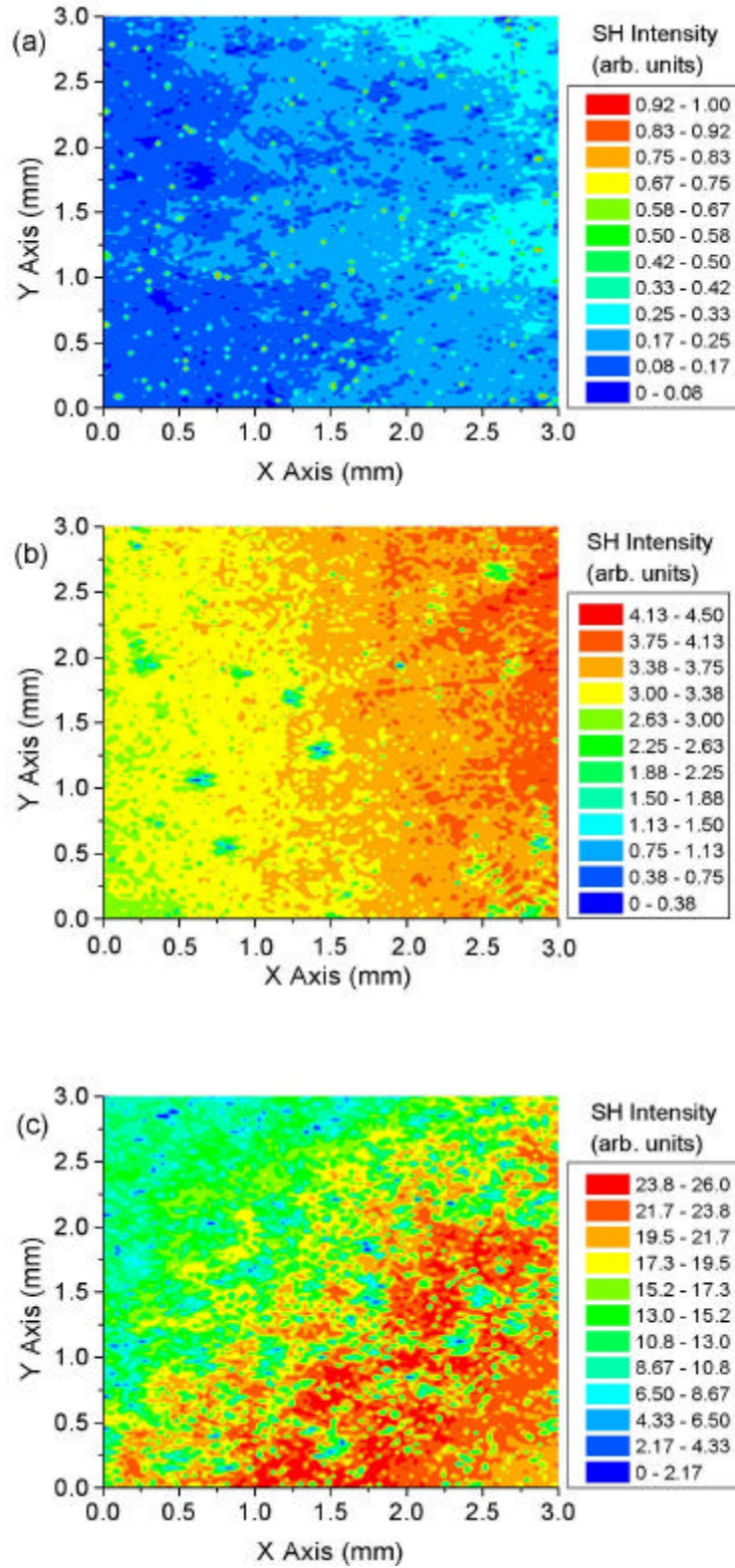
Figure 4.3: **Variation of SH Intensity with film thickness for (a) 1 mm (b) 5 mm (c) 10 mm ZnO films on Si substrates**

The pictures highlight a five-fold increase in SH intensity when the thickness climbs from 1 to 5 μm, followed by another similar boost as the thickness rises to 10 μm. This confirms that SH from a non-centrosymmetric medium such as ZnO probes the bulk of the sample, rather than the surface. Indeed, the induced nonlinear polarization of the bulk may be considered as the sum of sheets of polarization of the form

$$P^{(2w)} = \overset{\leftrightarrow(2)}{\boldsymbol{c}_D} E^w E^w \boldsymbol{d}(z - \boldsymbol{x})$$

where $\boldsymbol{x}$ represents the distance of the dipole sheet above the interface (figure 4.4).
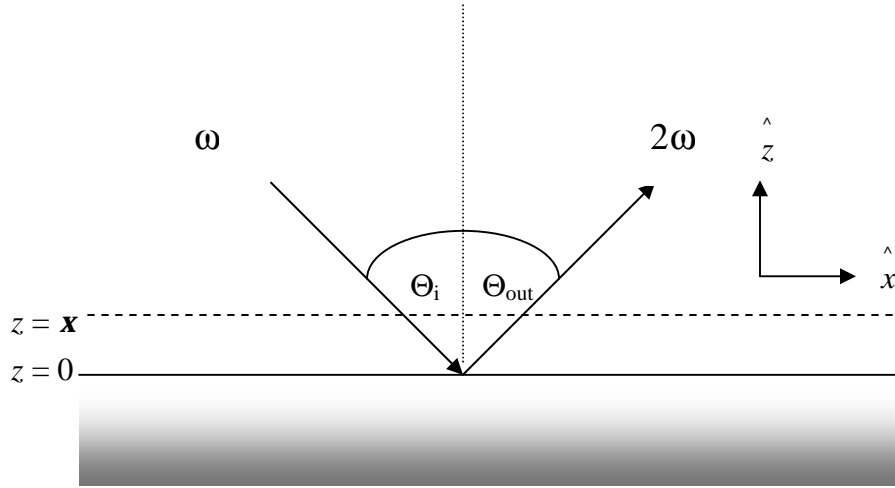
Figure 4.4: **Schematic representation of the interface at $z = 0$ and of a polarization sheet at $z = \boldsymbol{x}$ (after Lüpke, 1999)**

An increase in thickness leads to a boost in the number of polarization sheets on the sample, and therefore a higher SH signal.

Furthermore, figure 4.3 (a) highlights a spread of microcrystallites displaying a strong SH response across the sample. They appear green/yellow on the image. Under high magnification (figure 4.5), they are measured to be between 20 and 50 μm wide. These microcrystallites are randomly distributed across the sample, and may act as seeds during the growth process.
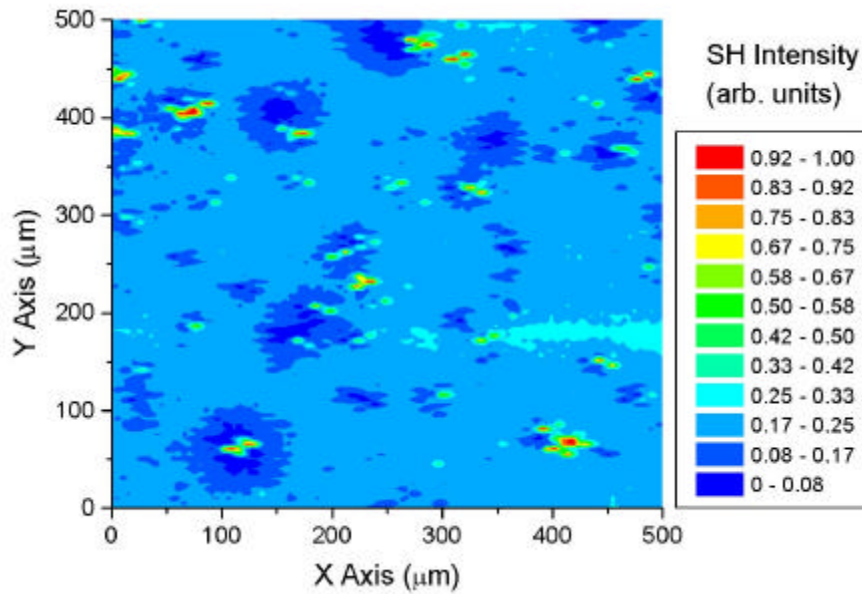
**Figure 4.5: SH image of 1 mm thick ZnO sample on Si,
under higher magnification**

Furthermore, the presence of these microcrystallites may be traced back to the MOCVD growth mechanism. The deposition of a thin film consists of several steps outlined in figure 4.6.
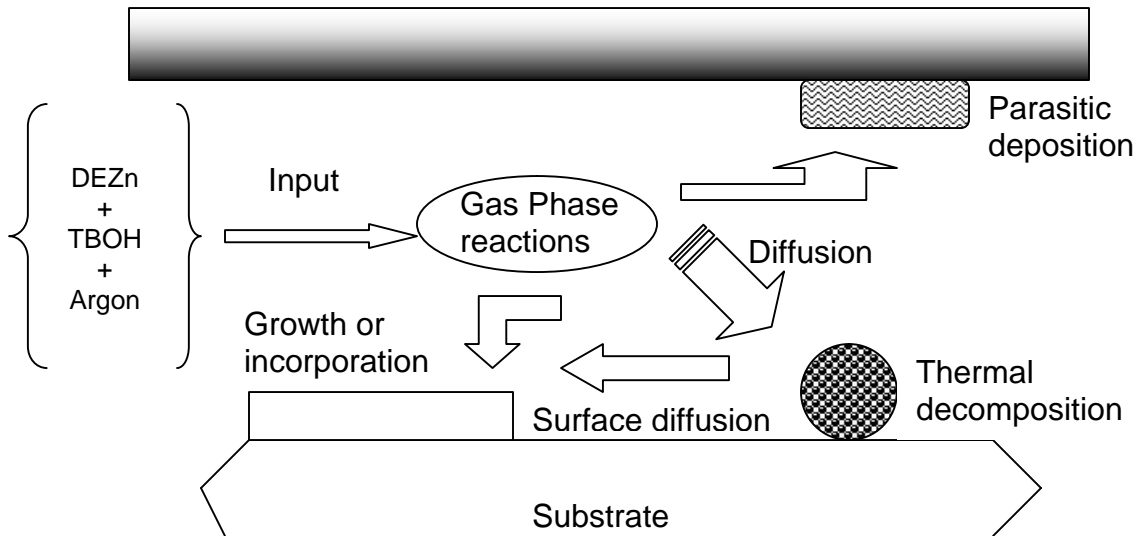
**Figure 4.6: Cross-section along the length of the reactor, illustrating
the MOCVD growth mechanism**

First of all, mass transport in the bulk gas flow regime takes place from the inlets of the reactor to the deposition zone. Gas phase reactions in the boundary layer then generate the formation of film precursors and by-products. The film precursors are consequently transported in mass to the growth surface, where they are adsorbed. Surface diffusion of the film precursors to the growth sites occurs, where surface chemical reactions lead to film growth. The microcrystallites observed in figure 4.5 probably spread across the substrate during the thermally activated diffusion process of the growth mechanism. Furthermore, these microcrystallites are likely to affect the homogeneity of the layers; indeed, they may generate the nucleation and coalescence of islands during growth, which may be indicative of the epitaxial *growth mode*.

Indeed, in a first-order approximation and assuming thermodynamic equilibrium, the growth morphology can be established from the balance of the various surface free energies involved according to the following expression (Bauer, 1958)

$$\Delta \boldsymbol{g}_{total} = \boldsymbol{g}_{ad} + \boldsymbol{g}_i - \boldsymbol{g}_s$$

where the sub indices *ad*, *i*, and *s* stand for adsorbate, interface, and substrate, respectively. Three different growth modes must be considered.

If $\Delta \boldsymbol{g}_{total} \leq 0$, the sum of $\boldsymbol{g}_{ad}$ and $\boldsymbol{g}_i$ is inferior or equal to $\boldsymbol{g}_i$, which means that the energetic cost of creating a substrate-adsorbate and an adsorbate-vacuum interface is less than the substrate surface free energy; substrate coverage is favored, and the deposit grows in a layer-by-layer manner. This is the *Frank-van der Merwe* growth mode (Frank and van der Merwe, 1949). In heteroepitaxial systems with a substantial lattice mismatch, like the ZnO/Si system studied here, the elastic strain energy amassed with increasing thickness must also be taken into account. Indeed, this fourth energy term is accountable for the break-up of the film into three-dimensional islands after the growth of a few atomic layers. This is the *Stranski-Krastanov* growth mode (Stranski and Krastanov, 1938). Finally, if $\Delta \boldsymbol{g}_{total} > 0$, the system aims to keep the substrate surface bare as long as possible whilst minimizing the exposed area of the deposit, thus generating the formation of 3-D islands. This is the *Volmer-Weber* growth mode (Volmer and Weber, 1926).

These three growth modes are illustrated in figure 4.7.
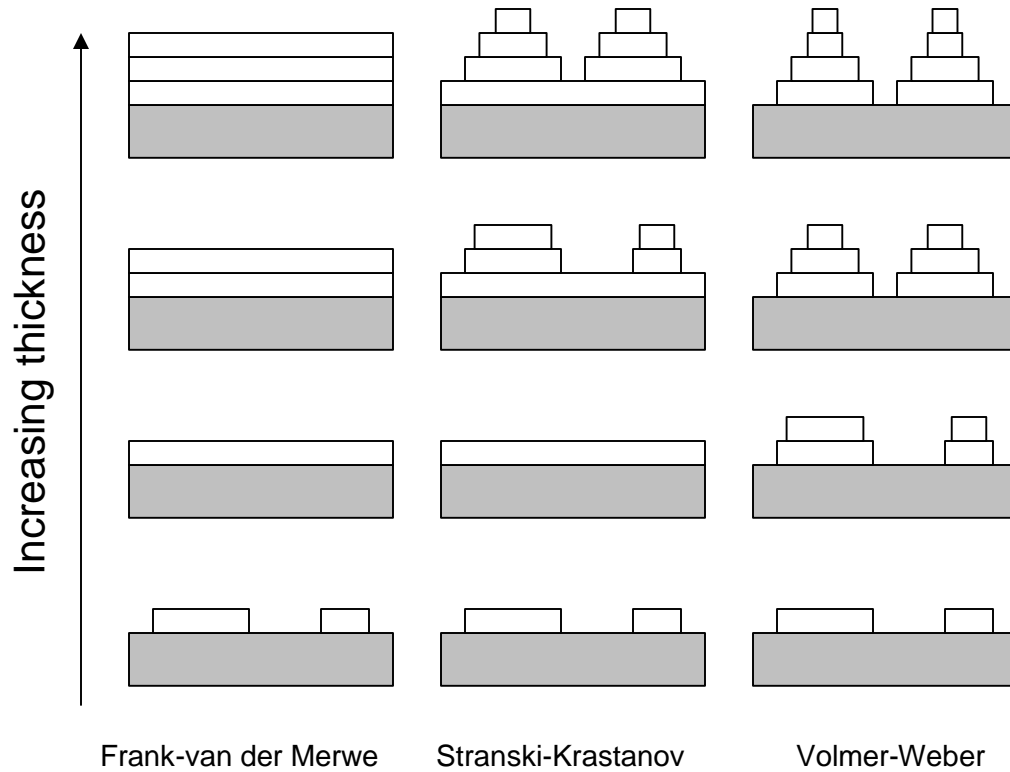
Figure 4.7: **Thermodynamical classification of epitaxial growth modes**

The presence of growth seeds on S1 is characteristic of the Stranski-Krastanov growth mode. The presence of 3-D structures was confirmed by looking at a cross-section micrograph of a sample deposited on Si (figure 4.8), which clearly displays the 3-D nature of the ZnO columns on Si. .
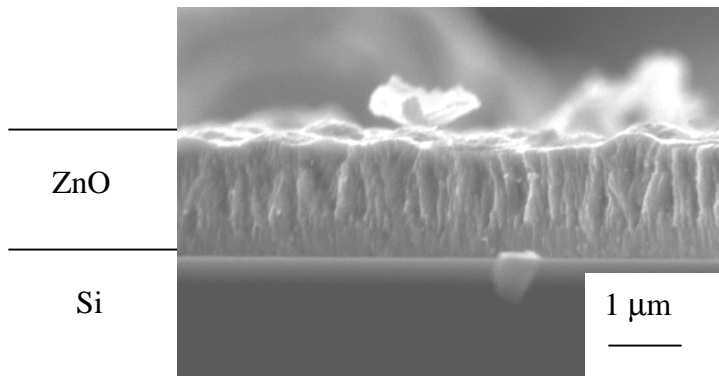
Figure 4.8: **Scanning Electron Microscopy micrograph of ZnO epilayer on Si substrate**

ZnO

Si

1 µm

The white particle at the Si/ZnO interface probably corresponds to a precipitate in the substrate. The Stranski-Krastanov growth of ZnO on Si has been observed by other workers using high-resolution ion beam analysis (Plachke *et al.*, 2001); this further validates the explanation presented here for the presence of microcrystallites scattered across the ZnO layer of sample S1.

The microcrystallites were, however, not observed on the thicker samples, S5 and S10; instead, the SH images revealed distinct macrostructures (figure 4.9).
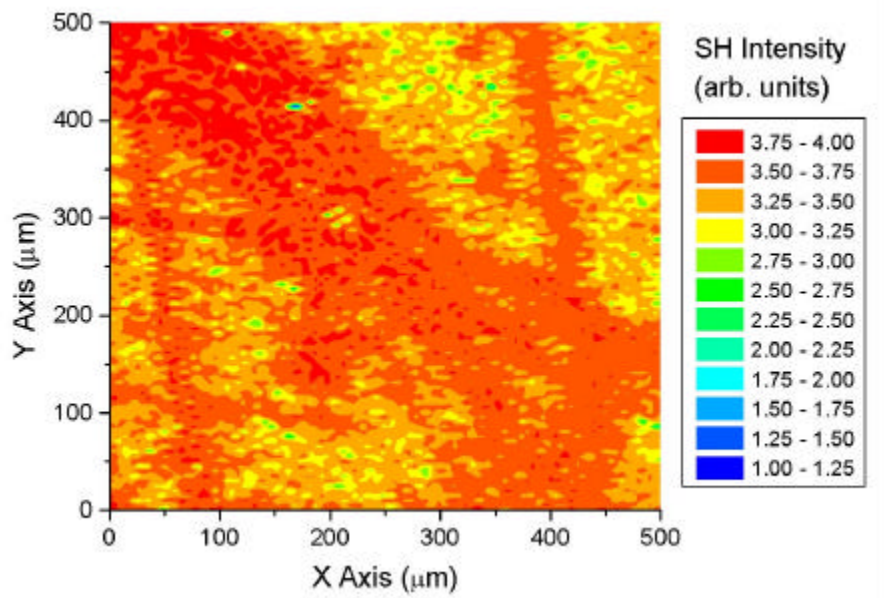
**Figure 4.9: SH image of 5 mm thick ZnO sample on Si,
under higher magnification**

It is worth mentioning that defects such as micropipes, microfacets, and crystalline inclusions may be studied by SH imaging. These defects are known to negatively affect the performance of devices. While it falls outside the scope of this particular study, the mapping of these films should be of importance to industry workers seeking to incorporate ZnO in silicon-based heterostructures.

Finally, the SH response of the layers is seen to depend on the sample position, highlighting the polycrystalline character of ZnO thin films deposited on Si (see chapter 5). This is expected, considering the large lattice mismatch between ZnO (wurtzite

structure) and Si (cubic diamond). Nevertheless, the layers showed fairly homogenous coverage; this may be due to the fact that Si and ZnO have similar thermal expansion coefficients ($3.57\bullet10^{-6}$ and $4.0\bullet10^{-6}$ /°C; Shimizu *et al.*, 1982). In incommensurate film/substrate systems (such as the ZnO/Si system), the lattice mismatch strains are usually relieved at the growth temperature via dislocation formation (Vincent, 1969). As these dislocation processes freeze out upon cooling, strains tend to be created as a result of difference in thermal expansion coefficient between the substrate and the film. The low thermal expansion mismatch of the ZnO/Si substrate ensures the reduction of these strains borne by the epilayer, which may enhance surface coverage and homogeneity.

4.3.2 Growth on amorphous glass slides

Figure 4.10 shows the images of two ZnO layers deposited on fused silica glass slides.
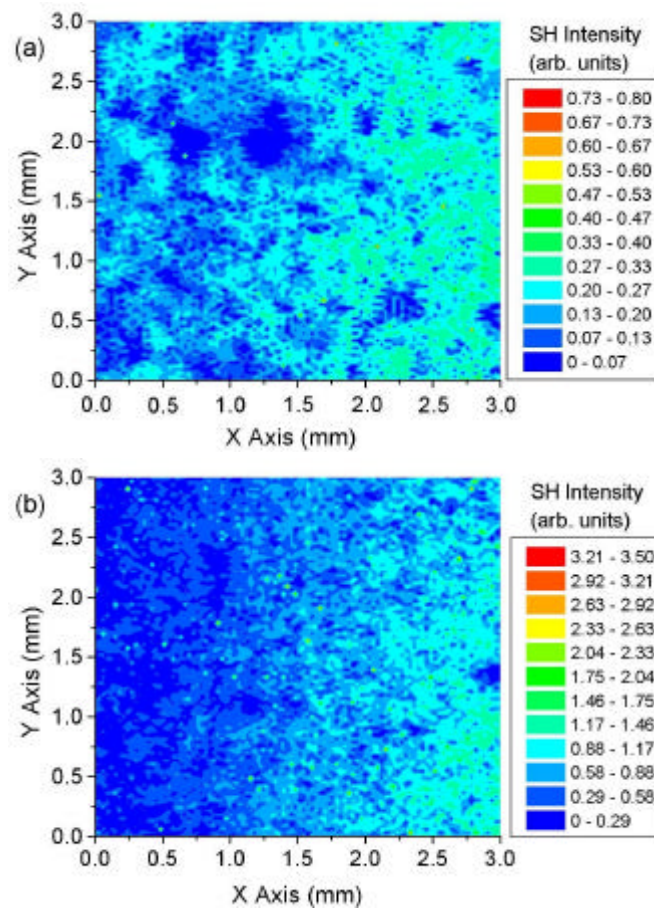
Figure 4.10: SH images of (a) 1 mm and (b) 5 mm thick ZnO
samples on amorphous glass

The glass slides give a weak SH response compared to the ZnO epilayer, enabling a direct analysis of the ZnO samples. The SH image of AG1 was recorded at an incident laser peak intensity of 25 GW/cm^2, that of AG5 at 12.5 GW/cm^2; both were recorded with a step resolution of 30 µm. Taking into account the laser intensity difference between the two scans and the fact that the SH signal is a quadratic function of the fundamental intensity ($I^{(2w)} \propto ((I^{(w)})^2)$), the SH intensity scale of figure 4.10 (a) was compensated by a factor of ¼; the signal amplitudes in figures 4.10 (a) and (b) therefore stand for comparison.

The right hand side of both AG1 and AG5 display a stronger SH response than the left hand side of each sample. This may be explained by the geometry of the reactor tube. Figure 4.11 schematically represents the flow of gases entering the reactor tube during deposition. A thorough description of the MOCVD reactor can be found in section 3.2.
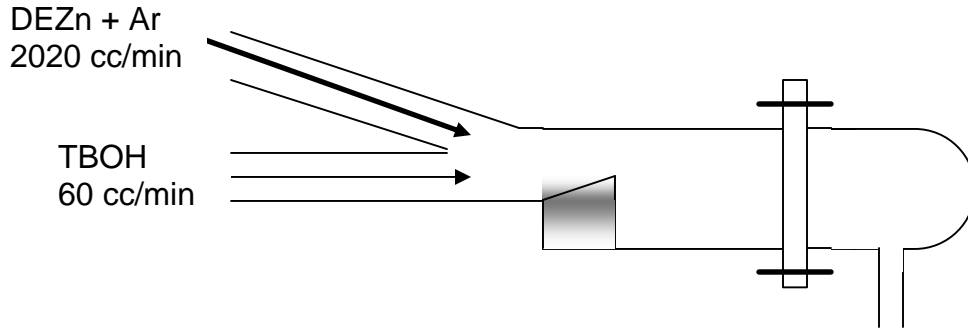
Figure 4.11: Horizontal side view of MOCVD reactor

The much larger gas flow originating from the DEZn/Ar inlet is likely to build a considerable side flux. This side flux is liable to affect the adsorption of film precursors on the substrate, which would explain the slight differences in crystallization across the substrate. Since DEZn and TBOH do not react at room temperature, the unevenness associated with this side flux may be remedied by adopting an MOCVD system with a fast switching manifold and a one-inlet reactor tube such as the one depicted in figure 4.12. This system would allow the DEZn, TBOH, and Ar to be mixed before entering the deposition zone; such a set-up would cancel the undesirable effects of a side flux. This

highlights one of the advantages of TBOH over other precursor sources such as O_2; its lack of reactivity at room temperature enables a flexible design of the MOCVD system to be implemented. Furthermore, the side flux also affected the ZnO/GaAs system, as can be seen in the next section.
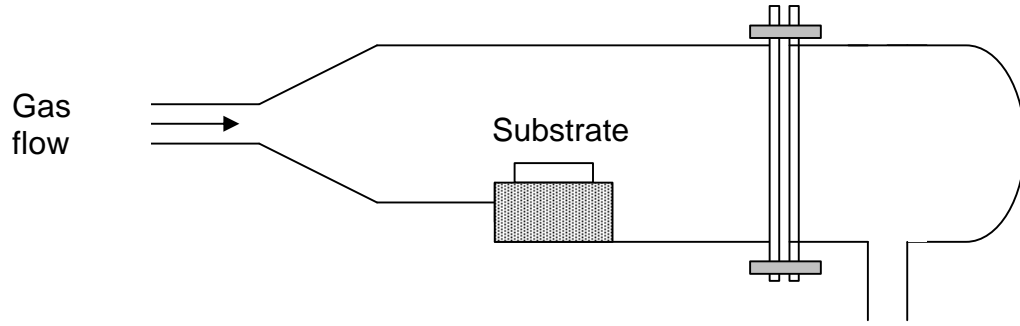
Figure 4.12: The horizontal *Thomas Swan* quartz reactor, as seen from the side

4.3.3 Growth on *n*-GaAs (100) substrates

Section 4.3.2 showed that the side flux associated with the reactor geometry is responsible for the varying SH response of the epilayer across the substrate. As further evidence, figure 4.13 shows the clear color gradient across ZnO samples deposited on GaAs.
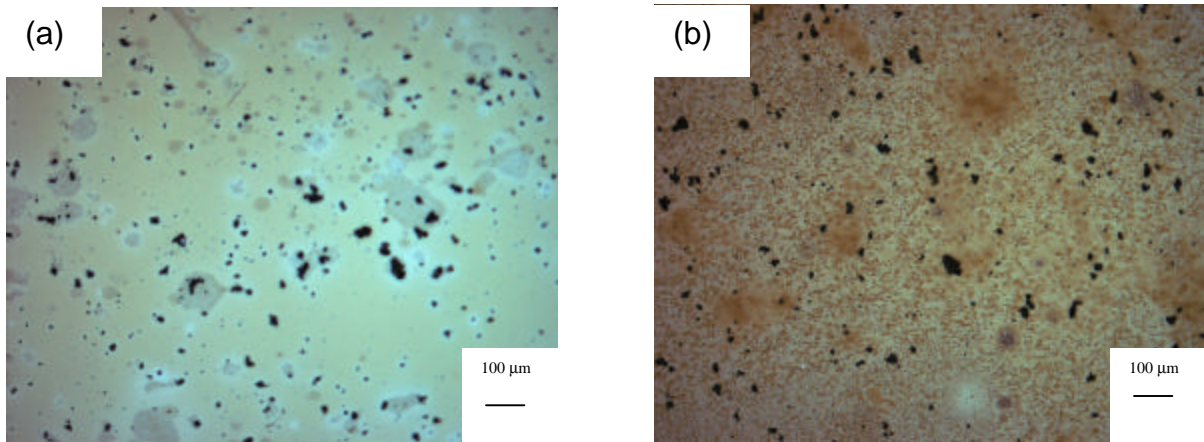
Figure 4.13: Optical micrographs showing the color gradient across a ZnO layer on GaAs; (a) represents the left half of the substrate, and (b) the right edge

These phase contrast (Nomarski) images were taken under the same illumination conditions. The right edge of the sample displays a pronounced yellow-brown color, and appears darker than the left half of the layer. It is possible that the side flux causes adsorbed Zn atoms to accumulate in crevices or other substrate defects that are shielded from O atoms. This explanation is bolstered by the fact that heating ZnO crystals in air is known to enhance its color, thus linking the color to oxygen vacancies (Srikant, 1998). Furthermore, it has been shown that highly oxygen deficient ZnO films deposited by electron-beam evaporation are brownish in color with poor transparencies (Gupta[3]).

Moreover, low-temperature photoluminescence spectra of the two halves of a ZnO layer on GaAs were recorded in order to test whether the color gradient across the layer affects the optical properties of the material. A description of the PL system can be found in section 8.2. The PL spectra of the two halves are found to be identical, and the color gradient across the ZnO sample on GaAs does not seem to be reflected in the photoluminescence properties of the material. An in-depth discussion of the photoluminescence properties of ZnO layers on GaAs is found in chapter 7.

Before looking at the SH images of samples grown on GaAs, it is important to mention that GaAs has a non-centrosymmetric zinc blende structure, and is expected to generate a SH response of the same order of magnitude as the ZnO epilayer. For the sake of comparison, a SH image of the GaAs substrate was taken, together with a plot of the variation of SH intensity with azimuthal angle (figure 4.14). Apart from a few minor impurities, the substrate shows a uniform and homogeneous SH response, which reflects the single crystalline character of the substrate. The plot of SH intensity with azimuthal angle, on the other hand, illustrates the rotational anisotropicity of GaAs.

---

[3] Vinay Gupta, PhD Thesis, University of Delhi
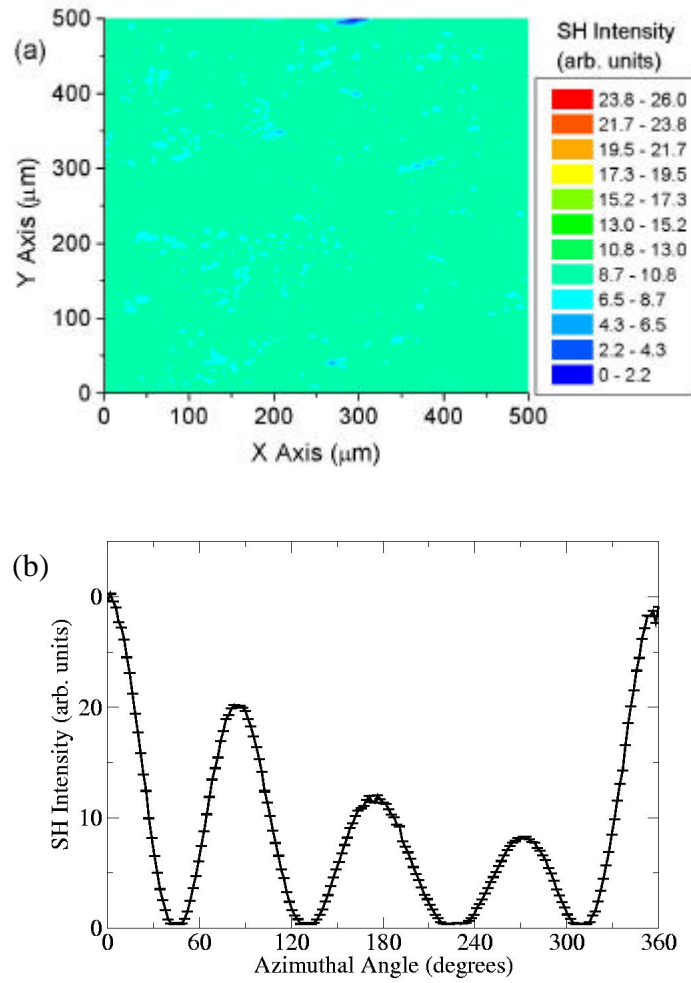
Figure 4.14: **(a) SH image of clean *n*-GaAs (100) substrate**
(b) Variation of SH intensity of *n*-GaAs (100) substrate with azimuthal angle

The SH images of the clean GaAs substrate and that of sample G5 are now compared in figure 4.15.
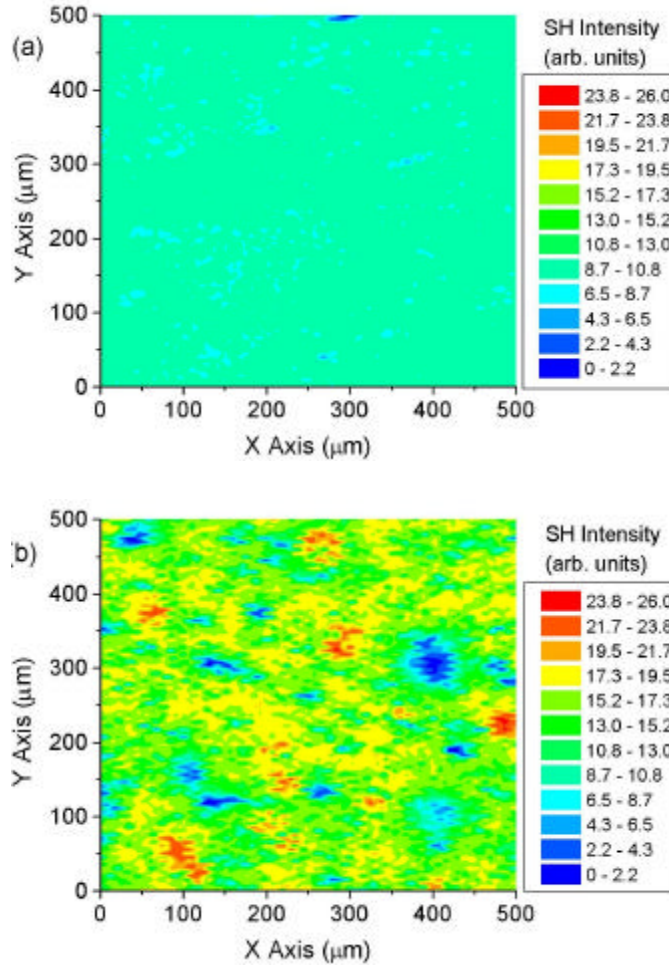
Figure 4.15: **(a) SH image of clean *n*-GaAs (100) substrate**

(b) SH image of 5 nm thick ZnO sample on *n*-GaAs (100)

The same color scale applies for both images. Figure 4.15 (b) highlights several areas, marked in dark blue, where the SH response of the underlying GaAs substrate is suppressed. They may correspond to amorphous ZnO stemming from an incomplete gas phase reaction between DEZn and TBOH. Moreover, these amorphous particles either absorb a substantial amount of the incident laser fundamental intensity, or quench the SH signal generated in the underlying GaAs substrate. The presence of these amorphous particles may partly explain why the photoluminescence properties of ZnO films grown on GaAs in this work are not as strong as those of ZnO thin films deposited on Si (see sections 7.2 and 8.3.3)

4.4   Summary

Second Harmonic Generation Imaging, a novel structural characterization technique, was used to generate images of ZnO thin films on n-Si 2 ° off (100), amorphous glass, and n-GaAs (100) substrates. Starting with Si, the variation of the SH intensity with laser power showed a square relationship until 55 GW/cm^2, after which the signal saturated. Furthermore, the thickness dependence of the signal intensity confirmed the polycrystalline nature of the thin films. The 1 μm thick sample displayed microcrystallites scattered across the substrate, which reflect the Stranski-Krastanov growth mode. On the other hand, the thicker samples showed the distinct presence of macrostructures; their nature and origin should be relevant to industry workers seeking to incorporate ZnO in silicon-based heterostructures. The samples deposited on amorphous glass highlighted a difference in SH response across the probed area, which may be traced to a large gas side flux due to the reactor geometry. Adopting a one-inlet reactor tube should solve the problems associated with the side flux. The impact of the side flux was also reflected in a color gradient across the samples grown on GaAs, and the yellow-brown part of the sample is possibly linked to a high concentration of oxygen vacancies. Having said that, the color gradient across the sample did not affect the photoluminescence properties of the ZnO on GaAs sample. In addition, SH images of the ZnO layers on GaAs betrayed the presence of amorphous ZnO particles, which may result from an incomplete gas phase reaction between the precursors. These amorphous particles may be partly responsible for the lower optical quality of samples deposited on GaAs compared to other substrates.

5. INFLUENCE OF SUBSTRATE TEMPERATURE ON STRUCTURAL PROPERTIES OF ZnO EPILAYERS

Silicon is the most studied semiconductor material, and the center of a vibrant industry. In the light of opto-electronic integration, it is important to appreciate the ZnO/Si system and know how to deposit the best possible ZnO thin films on silicon substrates. This chapter focuses on the influence of substrate temperature on the morphology and structural properties of ZnO epilayers.

5.1 Experimental procedure

5.1.1 Substrate preparation

A series of ZnO thin films was deposited on *n*-Si 2 ° off (100) substrates at growth temperatures ranging from 300 to 600 °C, keeping the VI:II ratio during growth constant at 18:1. The source materials were DEZn and 6N-purity TBOH. The 5x5 mm^2 substrates were obtained by cleaving 2-inch wafers with a diamond scriber. Prior to growth, the substrates were degreased in hot trichloroethylene (TCE), followed by rinsing in acetone, methanol, and deionized water. Dipping the degreased substrates in a dilute HF solution generated Si-H bonds and prevented the formation of a SiO_2 layer on top of the substrate. The reactor pressure was maintained at essentially atmospheric pressure for every growth run. A discussion of the flow and growth rates is found in section 5.2.6. The layers studied here are labeled according to their substrate temperature, i.e. Z300 was deposited at 300 °C.

5.1.2 X-ray diffraction

X-ray diffraction (XRD) spectra were recorded on all layers with a Philips PW 1729 generator using CuK_α radiation (λ = 0.154 nm). Table 5.1 shows allowed X-ray diffraction peaks for ZnO with their respective interplanar spacings *d* and Bragg angle 2θ.

Bragg angle 2θ (degrees)	Interplanar spacing d (Å)	Miller indices hkl	Relative intensity I/I_{MAX}
31.74	**2.82**	**100**	**71**
34.43	**2.60**	**002**	**56**
36.24	**2.48**	**101**	**100**
47.53	1.91	102	29
56.54	1.63	110	40
62.85	1.48	103	35
66.37	1.41	200	6
67.90	1.38	112	28
69.04	1.36	201	14
72.59	1.30	004	3
76.93	1.24	202	5
80.56	1.18	104	3
89.60	1.09	203	10
92.85	1.06	210	4
95.28	1.04	211	10
98.60	1.01	114	5
102.89	0.99	212	4
104.13	0.98	105	7
107.41	0.96	204	1
110.34	0.94	300	4
116.24	0.91	213	12
121.51	0.88	302	6
125.18	0.87	006	1
133.91	0.84	205	6
136.54	0.83	106	2
138.43	0.82	214	2
142.82	0.81	220	5

Table 5.1: Allowed X-ray diffraction peaks for ZnO, λ = 0.154 nm (after *Powder diffraction file, Joint Committee on Powder Diffraction Standards*)

The peaks observed in the XRD spectrum of bulk ZnO recorded for this study can be compared to the allowed peaks listed in table 5.1; as figure 5.1 shows, the spectrum of bulk ZnO is dominated by the (002) peak. The role of the (002) XRD peak in defining the concept of self-texture is further described in section 5.2.1.
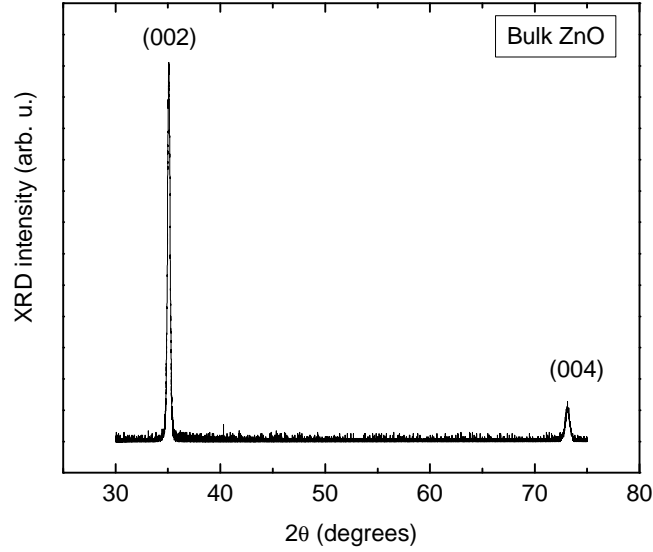
Figure 5.1: XRD spectrum of bulk ZnO

In order to assess the accuracy of the XRD system, the spectrum of a silicon standard was recorded (figure 5.2), and the peak positions and corresponding *d* and 2θ values compared to theoretical predictions (table 5.2).
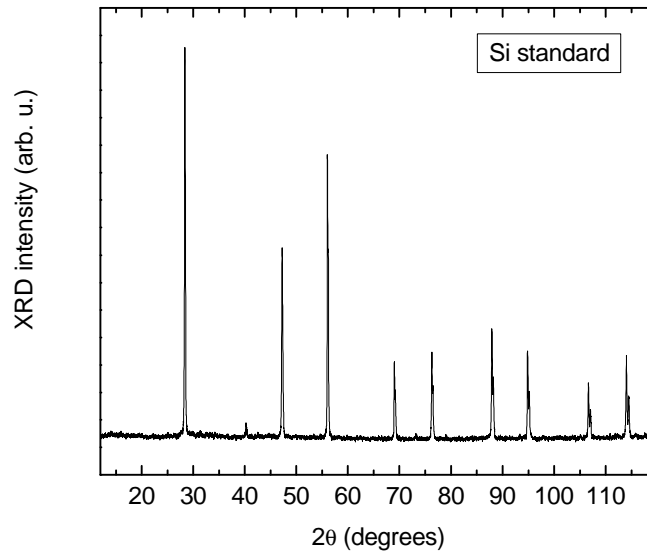
Figure 5.2: XRD spectrum of Si standard

Miller indices	Theoretical 2θ (degrees)	Experimental 2θ (degrees)	Error	Intensity ratio I/I$_{MAX}$
111	**28.418**	**28.385**	**-0.033**	**100**
220	**47.303**	**47.216**	**-0.087**	**50**
311	**56.1**	**56.03**	**-0.07**	**73**
400	69.168	69.015	-0.153	21
331	76.366	76.265	-0.101	24
422	88.052	87.901	-0.151	30
511	94.967	94.835	-0.132	24
440	106.725	106.578	-0.147	16
531	114.119	113.947	-0.172	23

Table 5.2: Theoretical and experimental XRD peak positions of Si standard, λ = 0.154 nm

As table 5.2 shows, the error in peak position clearly increases with rising Bragg angle 2θ, and the XRD peak positions of the ZnO epilayers deposited here were corrected appropriately.

5.2   *Results*

5.2.1 Self-texture

Before analyzing the XRD spectra recorded on this series of layers, it is necessary to give background information on the crystallization process and on the factors influencing film orientation.

One of the factors to consider when growing ZnO films on Si substrates is that ZnO nucleates on Si by atomic bonding and crystallizes hexagonally close-packed lattices on Si, which has a cubic diamond structure (Wu *et al.*, 2000). ZnO, with its hexagonal wurtzite structure, shows lattice constants *a* and *c* of 3.2498 and 5.2066 Å, respectively, while Si is characterized by a lattice constant *a* of 5.4301 Å. This illustrates why it is difficult to grow single crystal ZnO on Si, as the ZnO epilayer is inevitably strained due to the large lattice mismatch (Fu *et al.*, 1998b).

Nevertheless, the concept of self-texture plays a major role in determining the crystal quality of an epilayer. In a state of equilibrium, a film tends to grow with the plane of lowest surface free energy parallel to the surface; this is linked to the film's crystal structure. The ZnO crystal shows tetrahedral coordination due to sp^3 hybridization, with the direction of each apex parallel to the c-axis, [0001]. Fujimura and co-workers (1993) calculated the density of surface energy to be lowest for the (0001) plane (0.099 eV/Å^2), followed by (11$\bar{2}$0) (0.123 eV/Å^2), and (10$\bar{1}$0) (0.209 eV/Å^2). This explains why the (0001) textured film should be produced in the equilibrium state. This model is applicable where the atomic diffusivity is large at the outer surface of the growing film, but negligible inside the film (Knuyt *et al.*, 1995). In other words, only the energy of the outer film surface is considered in the energy minimization process, and the energy of the grain boundaries inside the film is ignored. The way a film evolves from its original random orientation (which depends on the properties of the substrate) to a self-textured film can be schematically depicted (figure 5.3) by considering that the outer film surface is taken as a plane divided into a large number of columnar regions (assuming constant total surface area).
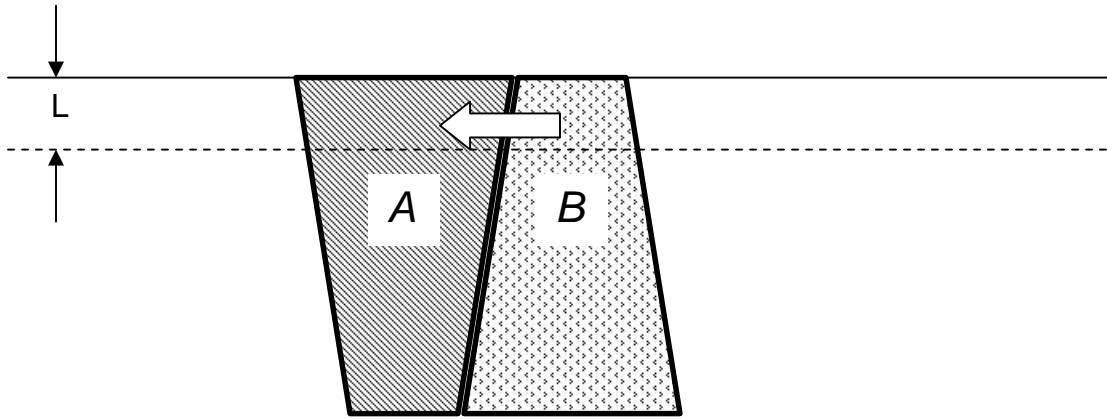
Figure 5.3: Schematic representation of columnar growth

(after Knuyt *et al.*, 1995)

If column *A* has a low surface energy, atoms of neighboring column *B* situated within a small layer of thickness L near the surface will want to jump towards column *A*. L is of the order of a near-neighbor atomic distance. This means that the grain boundary between

A and *B* will move during film growth, and column *A* (here corresponding to the (0001) plane) will prove more prominent than column *B* in the film's texture.

All the films grown in the range 300 – 600 °C are polycrystalline as demonstrated by their X-ray diffraction spectra. Nevertheless, significant differences in crystalline structure are observed depending on the growth temperature. Figures 5.4 and 5.5 show the X-ray diffraction spectra of ZnO samples Z300 and Z325.
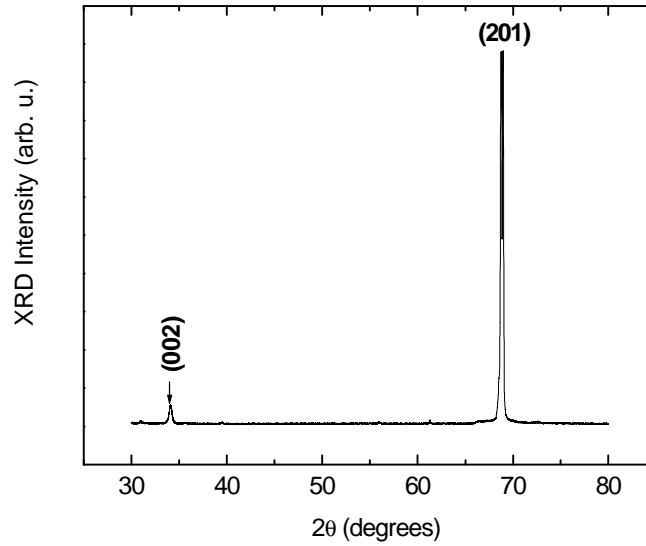
Figure 5.4: XRD spectrum of Z300
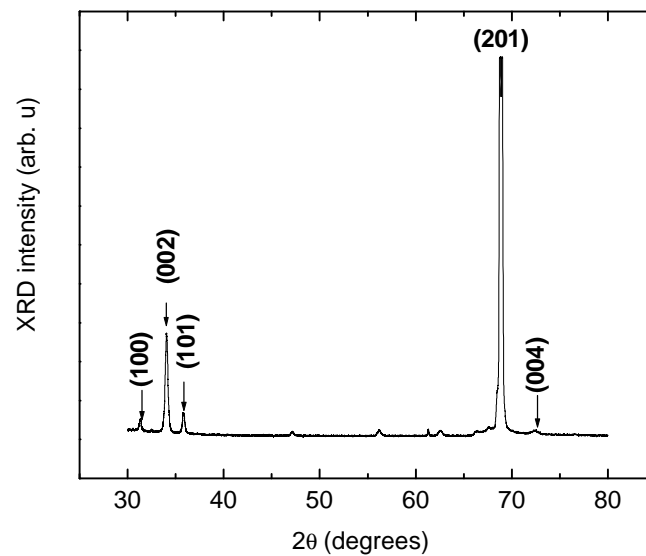
Figure 5.5: XRD spectrum of Z325

The spectra of Z300 and Z325 are dominated by a peak at 68.81 and 68.82 °, respectively. According to tables 5.1 and 5.2, it could either be the ZnO (201) peak or the Si (400) peak originating from incomplete substrate coverage. The peak assignment is made intricate by the fact that these peaks show similar relative intensities. Nevertheless, this peak has also been observed on ZnO samples deposited on GaAs substrates (figure 5.6), where no XRD spectrum is expected around 69 ° 2θ (table 5.3); the peak can therefore be attributed to ZnO rather than the Si substrate.
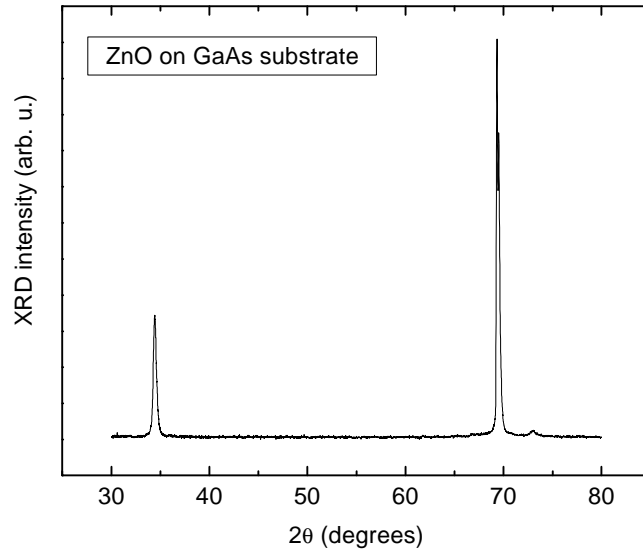
Figure 5.6: XRD spectrum of ZnO on GaAs

Bragg angle 2θ (degrees)	Interplanar spacing d (Å)	Miller indices hkl	Relative intensity I/I_{MAX}
27.33	3.26	111	100
31.56	2.83	200	< 1
45.32	2.00	220	35
53.74	1.70	311	35
66.05	1.41	400	6
72.85	1.30	331	8
83.72	1.15	422	6

Table 5.3: Allowed X-ray diffraction peaks for GaAs ($\lambda = 0.154$ nm)

Bragg angle	Interplanar spacing	Miller indices	Relative intensity
2θ (degrees)	d (Å)	*hkl*	I/I_{MAX}
90.11	1.09	333	4
100.82	1.00	440	2
107.39	0.96	531	2
118.97	0.89	620	4
126.55	0.86	533	2
141.38	0.82	444	4
153.23	0.79	711	2

Table 5.3 (cont'd): Allowed X-ray diffraction peaks for GaAs (λ = 0.154 nm; after *Powder diffraction file, Joint Committee on Powder Diffraction Standards*)

The XRD spectra of Z300 and Z325 (figures 5.4 and 5.5) do not show a strong (002) peak, the presence of which is indicative of a *c*-axis oriented film. This lack of *c*-axis orientation is attributed to the low substrate temperature. Indeed, the halogen lamp heating the substrate provides the thermal energy required to decompose the reactant gases into active species, which will then move to stable sites on the substrate surface (Kim and Kim, 1994b). Below 350 °C, these active species do not receive enough energy to migrate on the substrate to a low surface potential position. Consequently, the films do not display *c*-axis orientation. Nevertheless, figure 5.5 highlights the presence at 325 °C of the peak corresponding to the stable (101) plane, absent at 300 °C. More importantly, figure 5.5 clearly shows that the (002) peak is gaining in intensity compared to the other peaks, and hints at a change in preferred orientation. Indeed, the (002) peak dominates the XRD spectra of the films grown between 350 and 525 °C. Figure 5.7, the XRD spectrum of Z500, illustrates the point.
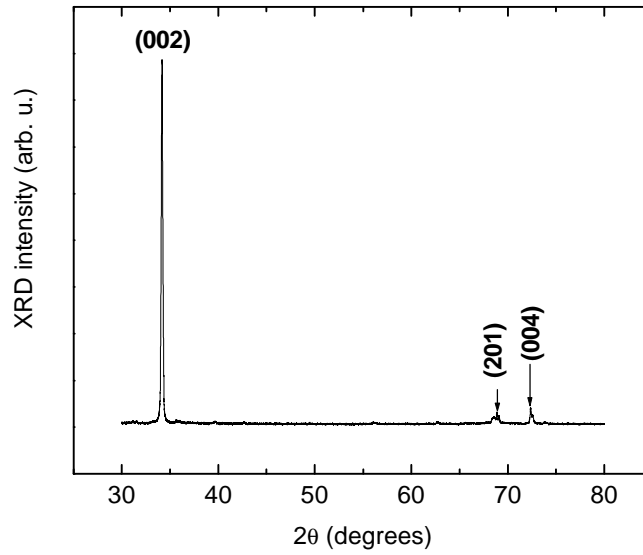
Figure 5.7: XRD spectrum of Z500

This is an encouraging result that certainly backs up the role of self-texture outlined earlier. Fujimura *et al.* (1993) observed a similar phenomenon for their films grown by RF magnetron sputtering. They reported that as the substrate temperature rose from room temperature to 500 °C, the texture of their ZnO films changed from $(11\bar{2}0)$ to (0001), thus reflecting an improvement in degree of *c*-axis orientation at higher substrate temperatures. Yan *et al.* (2004) also described for their samples deposited by plasma-assisted MBE an increase in the intensity of the (002) peak compared to the (101) peak with rising substrate temperature.

Nevertheless, above 525 °C, the films lose their *c*-axis orientation as can be seen in figure 5.8. This change in orientation may stem from an exceedingly fast reaction rate at high substrate temperatures that may hinder the crystallization process (Li *et al.*, 2003). In the light of the structural, optical, and electrical characterization of the samples, it appears that 450 – 500 °C proves the optimum growth temperature range for this system.

67
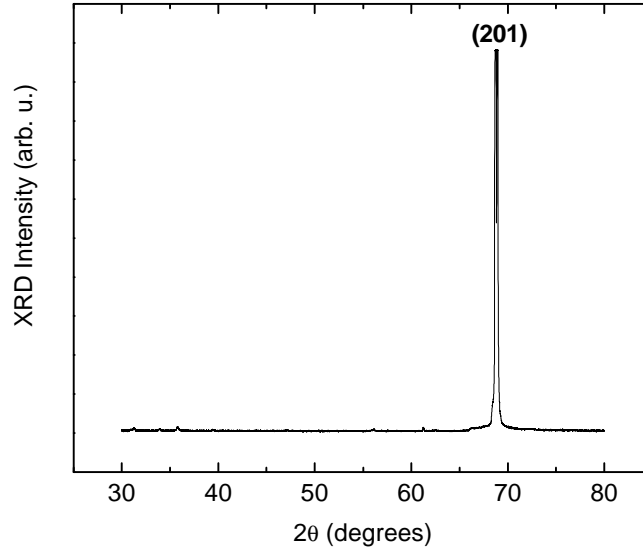
Figure 5.8: XRD spectrum of Z600

5.2.2 Tensile strain

The X-ray diffraction spectra are then used to calculate the lattice constant c of the ZnO epilayers. The lattice constants of a film can be calculated from the following expressions,

$$
\left\{
\begin{array}{l}
n\boldsymbol{\lambda} = 2d \sin\boldsymbol{\theta} \\[2mm]
\dfrac{1}{d_{hkl}^2} = \dfrac{4}{3}\dfrac{h^2 + hk + k^2}{a^2} + \dfrac{l^2}{c^2}
\end{array}
\right.
$$

where $\boldsymbol{\lambda}$ is the radiation wavelength, $\boldsymbol{\theta}$ the Bragg angle, d the interplanar spacing, and hkl the Miller indices of the plane of diffraction (Cullity, 1967). The XRD spectrum of a c-axis oriented film is dominated by the (002) plane. Since $h = k = 0$, and $l = 2$, it can be deduced that

$$
c = \frac{\boldsymbol{\lambda}}{\sin\boldsymbol{\theta}}
\qquad\qquad \text{...(5.1)}
$$

Compared to the bulk value of 5.2066 Å (ASTM) represented in figure 5.9 by a straight line, it is noted that all c-axis oriented films are elongated along the c-axis, with

68

compressive forces acting in the plane of the film. The error in the measurements is small, ± 0.003 Å, less than 0.1 %.
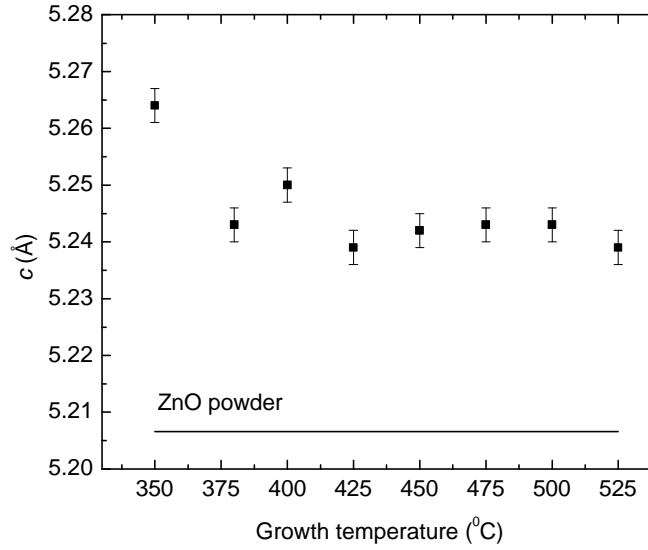
Figure 5.9: **Variation of lattice constant *c* with growth temperature; the straight line at *c* = 5.2066 Å represents the bulk value**

From there, it is possible to calculate the average uniform strain e_{zz} in the film, knowing that

$$e_{zz}(\%) = 100 \bullet \frac{c - c_0}{c_0} \qquad\qquad \textbf{...(5.2)}$$

where c_0 is the bulk value (Maniv *et al.*, 1982). Figure 5.10 shows how e_{zz} varies with substrate temperature. The highest strain (1.1 %) is measured at 350 °C. The value for e_{zz} then drops and remains fairly stable between 0.6 and 0.7 % in the range 380-525 °C; this indicates that the crystallization process is enhanced above 350 °C.
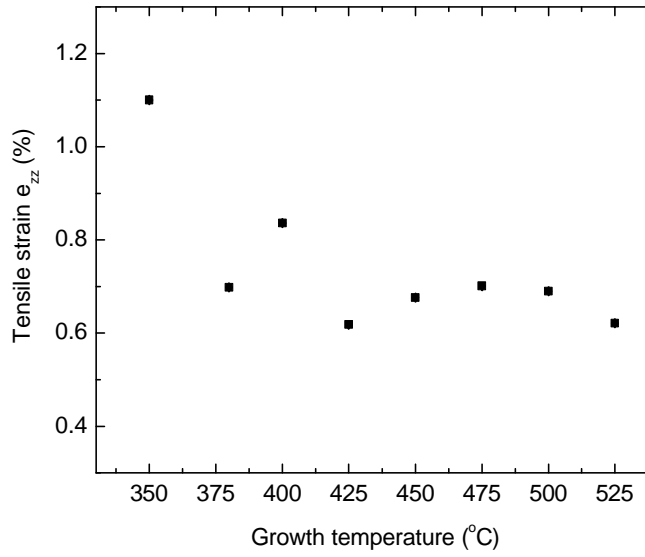
Figure 5.10: Variation of tensile strain with growth temperature

The stress s in the plane is now given by

$$s = [2C_{13} - (C_{11} + C_{12})C_{33}/C_{13}]e_{zz} \qquad \ldots(5.3)$$

where C_{ij} are the elastic stiffness constants of ZnO (Maniv *et al.*, 1982). C_{11}, C_{12}, C_{13}, and C_{33} are equal to $2.097 \bullet 10^{12}$, $1.211 \bullet 10^{12}$, $1.051 \bullet 10^{12}$, and $2.109 \bullet 10^{12}$ dyn/cm^2, respectively, at 25 °C (Bateman, 1962). The density of the films is also calculated since

$$r = \frac{M}{NV} \qquad \ldots(5.4)$$

where M is the sum of the atomic weights of the atoms in the unit cell, N Avogadro's number, and V the volume of the ZnO unit cell (Cullity, 1967).

In the case of a hexagonal unit cell,

$$V = \frac{\sqrt{3}a^2 c}{2} \qquad \ldots(5.5)$$

70

It was not possible to determine the lattice constant *a* because the X-ray spectra only display one peak between 350 and 525 °C; the parameter *a* is therefore assumed to be constant and equal to the bulk value of 3.2498 Å (ASTM). Table 5.4 summarizes the stress and X-ray determined density values of the *c*-axis oriented films. It can be seen that the direction of stress doesn't change with temperature, as all the films in this series are in a state of elongation. The lowest X-ray determined density is obtained at 350 °C, illustrating the underdense crystal structure found at low substrate temperatures (see section 5.2.6).

Growth temperature (°C)	Stress in plane σ (10^{10} dyn/cm^2)	X-ray determined density ρ (g/cm^3, ± 3E-3)
350	-4.99 ± 2.84E-3	5.61
380	-3.17 ± 1.81E-3	5.63
400	-3.79 ± 2.17E-3	5.63
425	-2.81 ± 1.61E-3	5.64
450	-3.06 ± 1.75E-3	5.64
475	-3.18 ± 1.82E-3	5.63
500	-3.13 ± 1.79E-3	5.64
525	-2.81 ± 1.61E-3	5.64

Table 5.4: Variation of stress in plane and X-ray determined density with growth temperature for ZnO films grown on *n*-Si 2 ° off (100) at a VI:II ratio of 18:1

Furthermore, Ong *et al.* (2002) have demonstrated that exciton transition energies in ZnO are linked to the film's strain. They solved the effective-mass **kxp** Hamiltonian and obtained the following expressions for the three exciton energies:

$$E_A = E_C^0 - E_{LH}^0 - E_b^{LH}$$

$$E_B = E_C^0 - E_{HH}^0 - E_b^{HH}$$

$$E_C = E_C^0 - E_{CH}^0 - E_b^{CH}$$

where E_C^0, E_{LH}^0, E_{HH}^0, and E_{CH}^0 are the conduction band and valence bands for light, heavy, and crystal-field split-off holes at $\mathbf{k} = 0$, and E_b^{LH}, E_b^{HH}, and E_b^{CH} correspond to binding energies for different holes. Figure 5.11 shows the variation of exciton transition energy with strain.
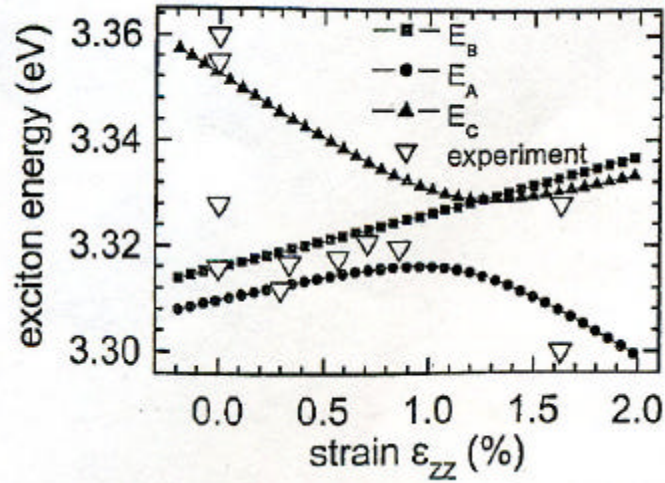
Figure 5.11: **Computed transition energies for A, B, and C excitons as a function of strain (after Ong *et al.*, 2002)**

Figure 5.11 shows that the strain in the films varies from 1.1 (Z350) to 0.6 % (Z425) depending on the substrate temperature. While the transition energies of the A exciton at these two strain values would be practically identical (within 1 meV), the B exciton of Z350 would appear at an energy 5 meV higher than that of Z425. On the other hand, the C exciton energy of Z425 would be 8 meV higher than that of Z350. This serves to illustrate how the tensile strain, and therefore the substrate temperature, would influence the optical characterization of ZnO thin films.

5.2.3 Grain size

Having studied the impact of the (002) peak position on the strain within the film, the full-width at half-maximum (FWHM) of the important peaks is measured. A full-width at half-maximum as low as 0.17 ° is obtained for the (002) peak of Z500. This marks an improvement compared to the FWHM of the bulk material shown in figure 5.1 (0.24 °),

and compared to values reported for ZnO films grown using other techniques such as magnetron sputtering (~ 0.4 °; Bachari *et al.*, 1999) and spray pyrolysis (~ 0.5 °; Studenikin *et al.*, 1998). It also outclasses the author's own FWHM values for samples grown using DEZn and O_2 as precursors (0.5 °), and the value reported in 2002 by Sallet *et al.* (0.3 °) who also worked on the DEZn/TBOH system. The FWHM of the (002) peak of the *c*-axis oriented films then serves to give the size of the grains and the preferred orientation quality of the (002) peak.

The grain size *D* is calculated using Scherrer's formula (Lim and Lee, 1999)

$$D = \frac{0.94 \bullet \mathbf{\mathit{l}}}{FWHM \bullet \cos\mathbf{\mathit{q}}} \qquad\qquad …(5.6)$$

where $\mathbf{\mathit{l}}$, *FWHM* , and $\mathbf{\mathit{q}}$ keep the same definition as in the previous sections of this chapter. Figure 5.12 represents the variation of grain size with growth temperature. Z300 and Z325 are not *c*-axis oriented, and the graph shows the grain size for the predominant (201) peak and for the (002) peak. It is found that while the (201) grains are larger than the (002) grains at 300 °C, the reverse is true at 325 °C. It is surprising to note that the films grown at 300 and 325 °C are (201) oriented, and not (112) or (101) oriented since the latter planes have a lower density of surface energy (Fujimura *et al.*, 1993). This may highlight the fact that at these low growth temperatures the films have not yet reached a state of equilibrium where the active species migrate on the substrate to find the most stable sites. The (002) grain size then increases from 350 to 380 °C and remains fairly stable until 525 °C, averaging 52 nm in that region. That average excludes the grain size of Z450, which is astonishingly low (34 nm). Another series of samples was grown at a later stage between 425 and 500 °C to test the reproducibility of this low grain size at 450 °C. It is found that the grain size and preferred orientation quality (see section 5.2.4) of samples deposited between 425 and 500 °C are practically identical. The low grain size of Z450 is therefore attributed to experimental error. At 550 °C, the film becomes (100) oriented and the (100) grains are larger than the (002) grains. A large drop in grain size follows at 600 °C, where the film returns to an unstable state.
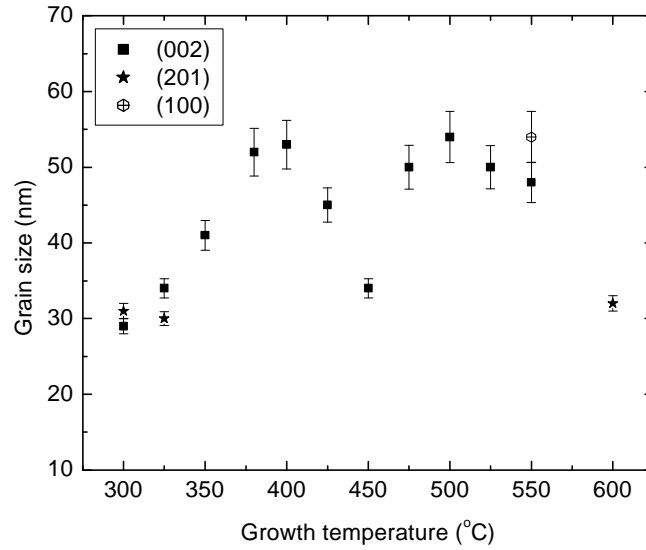
Figure 5.12: **Variation of grain size with growth temperature,
keeping the VI:II ratio during growth at 18:1**

All in all, the grain size is largest in the range 380 - 525 °C, indicating an improvement in the crystallization process compared to growth at other temperatures. This is in agreement with the study of the temperature dependence of the average uniform strain. It is essential to study the variation of the grain size with growth temperature for several reasons. First of all, the grain size helps define a strong or weak crystallization process. Secondly, the grain size and electrical properties of a film are linked (Lee *et al.*, 2003*)*. Indeed, carriers are scattered at grain boundaries, and carrier scattering leads to a decrease in carrier mobility. As the grain size increases, both the grain boundary density of a film and the scattering of carriers at grain boundaries will decrease. Consequently, the resistivity of films should drop with increasing grain size. Furthermore, Nan *et al.* (1999) discovered that the size of nanocrystalline grains could severely alter the electrical conductivity of their ZnO samples. Under applied *dc* voltages, they found that samples of grain size less than 20 nm displayed clear time dependent currents, which they attributed to space-charge-limited conductivity. The transient times they measured, i.e. times at peak current, were abnormally high, suggesting a high trap density in these samples. On the other hand, they reported that grains larger than 40 nm displayed ohmic behavior and the absence of space-charge-limited transient currents. As the substrate temperature

during the MOCVD growth of a ZnO layer considerably affects the film's grain size, it is also indirectly going to affect the film's conductivity. Looking at figure 5.12, it can be seen that samples deposited below 350 and above 550 °C are more likely to exhibit high trap densities and time dependent transient currents than samples grown within that temperature range.

5.2.4 Preferred orientation quality

The FWHM of the (002) peak now helps determine the preferred orientation quality of the (002) peak, POQ_{002}. The POQ_{002} is defined as

$$POQ_{002} = \frac{I_{002}/(FWHM_{002} \bullet ri_{002})}{\sum_{hkl} I_{hkl}} \qquad \dots(5.7)$$

where I_{002} is the actual intensity of the (002) diffraction line, $FWHM_{002}$ its full-width at half-maximum, and ri_{002} the relative intensity of the (002) line in a powder sample (D. Paraguay *et al.*, 2000). This empirical relationship is similar to the normalized integrated intensity outlined by Major and co-workers (Major *et al.*, 1986), but also takes into account the FWHM of the diffracting line. Figure 5.13 is a plot of POQ^*_{002}, which the author describes as the product of POQ_{002} and ri_{002}. The grain size and POQ^*_{002} follow the same trend as they both depend on the inverse of the FWHM. An increase in POQ^*_{002} is observed between 350 and 380 °C, after which it fluctuates little until 500 °C (except at 450 °C; see section 5.2.3). A three-fold decrease in POQ^*_{002} is then recorded between 500 and 525 °C. This is accompanied by the appearance of a large number of XRD peaks absent at 500 °C (figures 5.7 and 5.14).
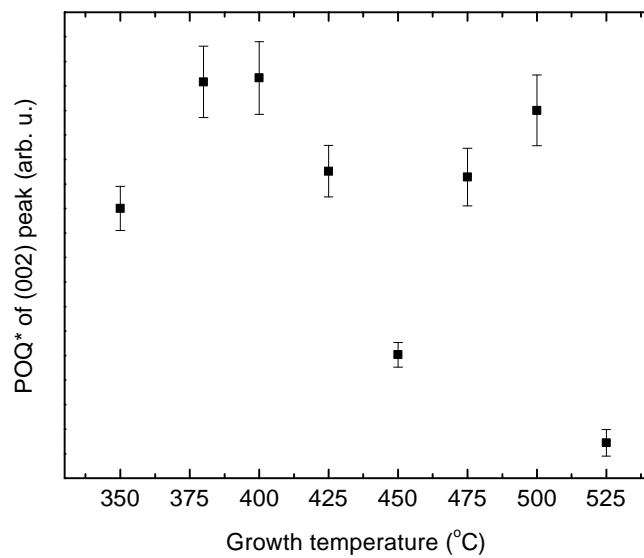
Figure 5.13: Variation of POQ^{*}_{002} with growth temperature
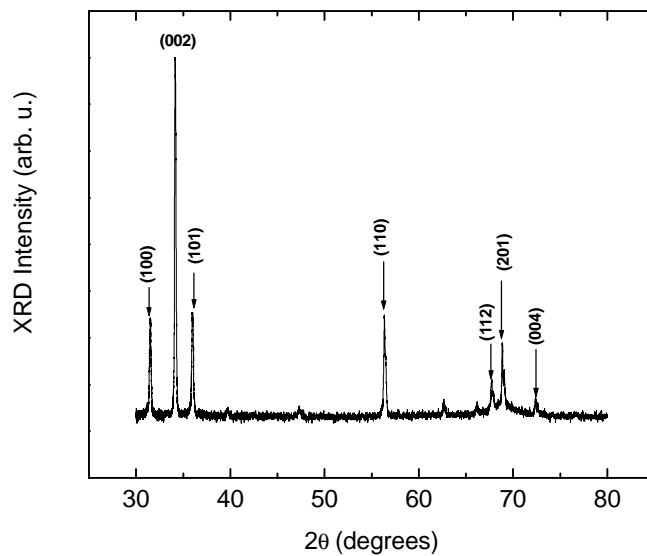
Figure 5.14: XRD spectrum of Z525

The relationship between good crystalline quality and large values of POQ_{002}^* needs to be emphasized. One of the factors that can influence the POQ_{002}^* is the number of nucleation centers, which in turn can cause the nucleation type to switch from homogeneous to heterogeneous, and thus lead to deterioration of crystalline quality. The classical homogeneous nucleation model is a simple model based on thermodynamics that assumes that growth occurs on defect-free surfaces. The reader is referred to the work of Venables (2000) for further information on nucleation mechanisms. The drop in POQ_{002}^* above 525 °C confirms that high temperature growth yields poor results.

5.2.5 Growth rates

The limiting factor in establishing the growth rate of this system is the DEZn flow rate, as deposition takes place with excess oxygen. The layers studied in this chapter were grown at a DEZn and TBOH flow rate of 43 and 770 µmol/min, respectively. The argon carrier gas flow rate was set at 2000 cc/min. The sample thickness was determined from cross-section images of the thin films taken by optical microscopy. Figure 5.15 shows the variation of growth rate with substrate temperature. The films' thicknesses were measured at 3 – 4 different points along the cross-section, and the error bars represent the accuracy of the measurements.
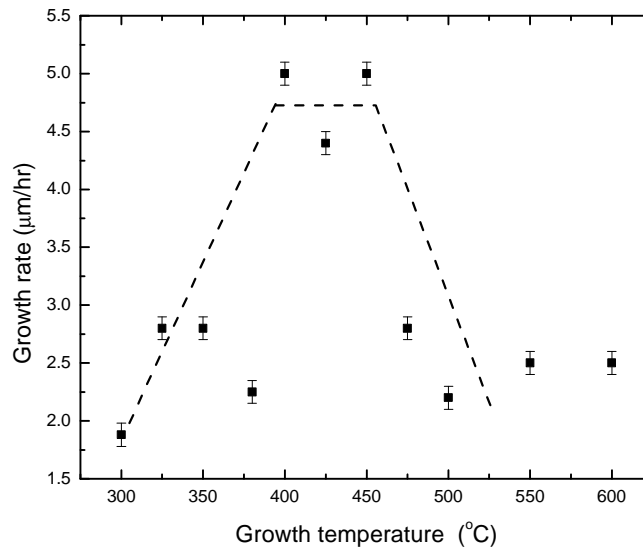
Figure 5.15: Variation of growth rate with growth temperature

The graph appears to be divided in three zones.

300-400 °C

The growth rate increases with increasing temperature. This means that the rate of deposition is controlled by mass transfer and reaction kinetics at or near the substrate surface. It is therefore defined by an activated process such as adsorption, surface diffusion, chemical reaction, or desorption. The activation energy associated with this process was calculated to be 0.3 ± 0.1 eV from the Arrhenius plot. Bang *et al.* (2003) grew ZnO thin films on GaAs by MOCVD using DEZn and O_2 as precursors, and reported an activation energy of 0.41 eV for the 300 – 400 °C temperature range. Furthermore, Ayouchi *et al.* (2003) measured an activation energy of 0.14 ± 0.01 eV for their films deposited by chemical spray pyrolysis on silicon.

400-450 °C

Here the growth rates are independent of temperature, and the highest growth rate (5.0 μm/hr) is recorded in this range. In this temperature range, the reaction kinetics are fast, and the growth process is limited by mass transfer of the reactants; the limiting factor is the concentration of reactants on the surface.

450-600 °C

A sharp decrease in growth rate is observed, and an activation energy of -0.8 ± 0.2 eV is calculated from the 450 – 500 °C data. This decrease can be traced back to the mechanism of the reaction between DEZn and TBOH. DEZn and TBOH molecules lead to the generation of ZnO via the formation of an intermediate alkylzinc alkoxide, $EtZnOMe_3$:

$$Et_2Zn + Me_3COH \rightarrow EtH + EtZnOMe_3$$
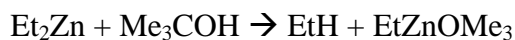
The decrease in growth rate can be explained by the fact that at high growth temperatures the alkylzinc alkoxide cracks in the gas phase before reaching the substrate surface. Kirchner *et al.* (2003) also reported a drop in growth rate but at a higher temperature, 510 °C. This may be due to the fact that they were working at 400 mbar, while the layers

studied here were deposited at essentially atmospheric pressure. Increasing the reactor pressure has the effect of reducing the mean free paths of the DEZn and TBOH precursor molecules. Although the precursor molecules may already have undergone cracking in the gas phase below 510 °C, the fact that Kirchner *et al.* were working at 400 mbar ensured that the precursor molecules could still reach the substrate surface and contribute to the formation of the ZnO thin film. Having said that, their reactor had a different geometry than the one used for this study, and this discrepancy may have also affected the growth rates.

5.2.6 Surfaces

The structure of a thin film depends on a sequence of morphological changes which take place as the layer thickens starting from discrete nuclei, and on grain boundary migration and recrystallization which may occur at the same time (van der Drift, 1967). Therefore, in addition to the relevant grain boundary energies, the growth process will hinge on the adatom adsorption probabilities, the density of surface states, and the adatom surface mobility. This explains why the impact of the substrate temperature on the structural properties of the epilayers should be reflected in the surface morphology of the samples. Figure 5.16 shows surface images of samples deposited at 350, 400, 450, and 550 °C. Each layer was grown for a period of 60 minutes, and all other growth conditions were kept constant.

ZnO layers on Si appear rough in comparison to thin films grown on GaAs (see sections 7.2.1 and 7.2.2). The is firstly attributed to the difference in film thickness; films grown on Si are 1.9 to 5.0 μm thick, while the largest film thickness on GaAs was 0.6 μm. Secondly, the disparity in surface morphology can be explained by the difference in substrate.
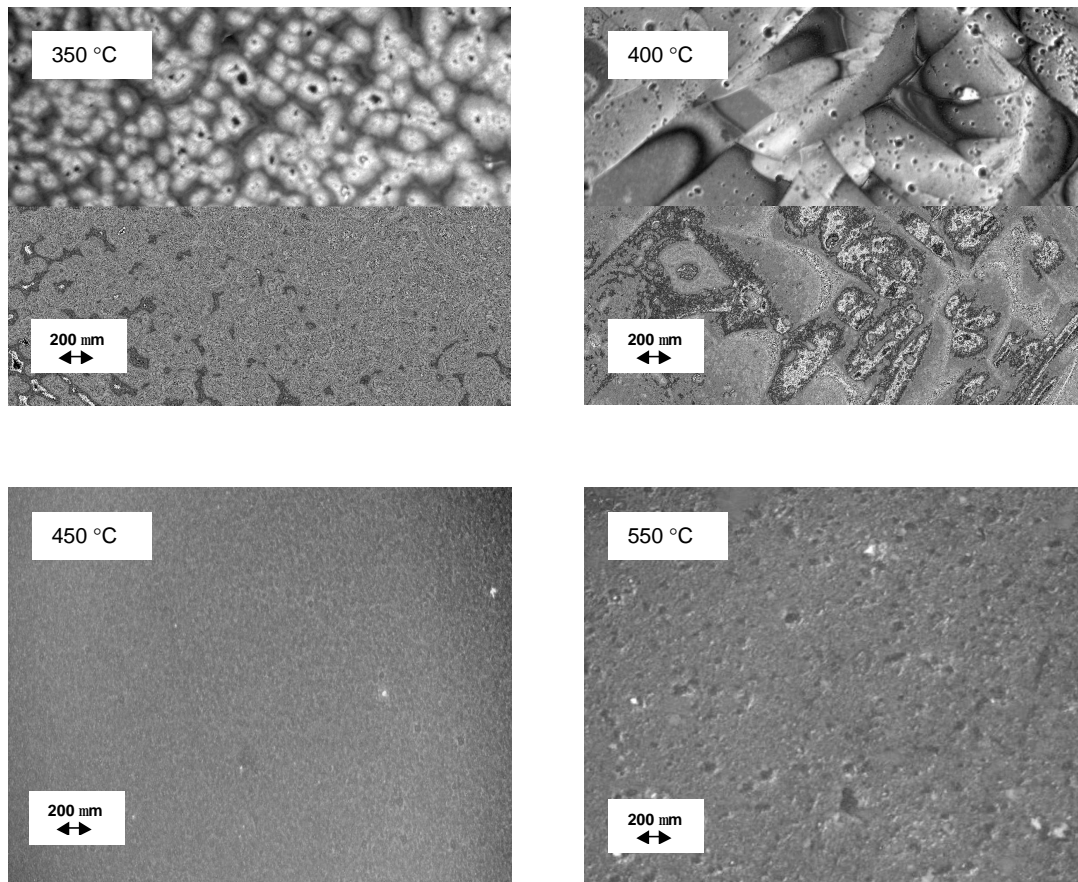
Figure 5.16: Optical micrographs of surfaces of ZnO layers deposited on
***n*-Si 2 ° off (100) at 350, 400, 450, and 550 °C**

As Figure 5.16 shows, the morphology of the ZnO layers deposited on Si is strongly dependent on substrate temperature. At 350 °C, the adatom surface mobility is low and the epilayer is made of tapered white crystallites separated by voids rather than grain boundaries. As a result, the film shows poor lateral strength and is underdense. Those intergrain voids begin to fill as the substrate temperature increases to 400 °C, and at 450 °C the sample displays a distinct surface structure made of smooth flat grains. At 550 °C, self-diffusion needs to be taken into account, and the film shows a loss of homogeneity compared to 450 °C. This may be due to the occurrence of sintering type coalescence at high growth temperatures, whereby the heating of the ZnO crystallites causes agglomeration of the grains to form larger particles and surface roughness.

The microstructures presented here are reminiscent of the 3-zone model proposed by Movchan and Demchishin (1969). Below 400 °C, the films show zone 1 behavior with underdense crystals and voids dividing the crystals. The size of the grains significantly rises in this zone. Between 400 and 500 °C, the films display a zone 2 surface morphology with densely packed grains and smooth, flat surfaces. This zone is expected to yield the best results for acousto-optic and acousto-electric applications of ZnO piezoelectric films. Above 500 °C, a type of sintering coalescence induces surface roughness, which is typical of zone 3 films.

5.3   Summary

The influence of growth temperature on the structural properties of a series of ZnO samples deposited between 300 and 600 °C was investigated. The self-texture, tensile strain, grain size, and preferred orientation quality were found to strongly depend on the substrate temperature. Layers grown between 350 and 525 °C were *c*-axis oriented, with the *c*-axis elongated and compressive forces acting in the plane of the film. The highest tensile strain (1.1 %) was measured for the film deposited at 350 °C; it then fluctuated between 0.6 and 0.7 % for layers grown between 380 and 525 °C. According to literature, this difference in strain should lead to shifts in exciton transition energies of several meV. The full-width at half-maximum of the (002) peak was measured for all samples; the narrowest FWHM (0.17 °) outclassed reported values for ZnO samples deposited by other techniques such as magnetron sputtering, spray pyrolysis, and by other workers using the DEZn/TBOH system. The variation of grain size with substrate temperature shows that films deposited below 350 and above 525 °C are more likely to display high trap densities and time dependent transient currents than films grown between those two temperatures. At a DEZn flow rate of 43 µmol/min, the growth rate was found to increase from 1.9 to 5.0 µm/hr between 300 and 400 °C, describing a mass transfer-limited growth process with an activation energy of 0.3 eV. From 400 to 450 °C, the growth rates remained practically constant. Above 450 °C, the growth rates decreased, and an activation energy of – 0.8 eV was obtained from the 450 - 500 °C data. The temperature dependence of the surface morphology of the ZnO layers was paralleled to Movchan and

Demchishin's 3-zone model. Below 400 °C, the surfaces showed a zone 1 morphology with poor lateral strength. The voids separating the crystals began to fill with increasing temperature, and from 400 to 500 °C the films exhibited smooth surfaces of densely packed grains characteristic of zone 2 surfaces. Above 500 °C, the surface images gave evidence of an increase in roughness typical of the sintering coalescence process that takes place in zone 3 layers as a result of high substrate temperature.

6. INFLUENCE OF VI:II RATIO DURING GROWTH ON STRUCTURAL, OPTICAL, AND DISPERSION PROPERTIES OF ZnO EPILAYERS

One of the obstacles currently being tackled by the ZnO community is the reproducible production of good *p*-type material. The task is made especially daunting by the fact that there remain several questions as to the nature of the defects causing *n*-type conductivity in undoped material. It has been reported that oxygen vacancies (V_O) act as shallow donors in ZnO, and are responsible for the intrinsic doping of ZnO together with zinc interstitials (Zn_i; Jin *et al.*, 2000). Furthermore, Kroger (1964) reports the energy level for the first ionization of oxygen vacancies to be $E_C - 0.05$ eV, where E_C refers to the bottom of the conduction band. On the other hand, Van de Walle's work (2001) advocates that oxygen vacancies cannot be considered a pool of free electrons in a stable manner. In addition, Look (2001) suggests that oxygen vacancies should be treated as deep donors, thus setting zinc interstitials as the main cause of *n*-type conductivity in ZnO. Look *et al.* (1999) also reported the zinc interstitial level to be 0.03 eV below the bottom of the conduction band. In an effort to shed some light on the problem, this chapter aims to quantify the effect of the VI:II ratio during growth, i.e. the amount of oxygen entering the reactor tube during deposition, on the properties of ZnO samples. A series of samples was deposited at four different VI:II ratios during growth on amorphous glass slides; their structural, optical, and dispersion properties are discussed.

6.1 Experimental procedure

The thin films were grown with DEZn and 3N-TBOH on fused silica slides at a substrate temperature of 450 °C. The DEZn flow rate was kept constant at 20 μmol/min for all growth runs, and growth rates between 1.6 and 2.0 μm/hr were measured. The growth time was set at 45 minutes for all samples, and the reactor chamber remained at essentially atmospheric pressure for all growth runs. The only parameter allowed to vary was the argon flow rate through the TBOH bottle. Four samples were grown at four different VI:II ratios: 10:1, 18:1, 35:1, and 60:1. The layers are labeled according to their

VI:II ratio during growth (i.e. Z10/1 was deposited at a VI:II ratio of 10:1). Table 6.1 provides the VI:II ratio during growth and thickness of each sample studied in this series.

Sample name	VI:II ratio during growth	Thickness (μm)
Z10/1	10:1	1.8
Z18/1	18:1	2.0
Z35/1	35:1	1.6
Z60/1	60:1	1.6

Table 6.1: VI:II ratio during growth and thickness of ZnO samples studied in this chapter

The structural properties of the layers were analyzed by X-ray diffraction (CuK$_\alpha$ radiation; $\lambda = 0.154$ nm). An error of ± 0.01 ° is associated with peak labeling.

The optical and dispersion properties of the layers were investigated by transmission and reflection spectroscopy. The transmission and reflection spectra were recorded with a *Shimadzu UV-3100* UV-vis-near IR spectrometer equipped with a PbS photoconductive cell as detector; this system is able to measure transmission, absorption, and reflection data from 190 to 3200 nm. There are different ways of measuring reflectance spectra; the scans presented in this work refer to the diffuse reflectance, as illustrated below:
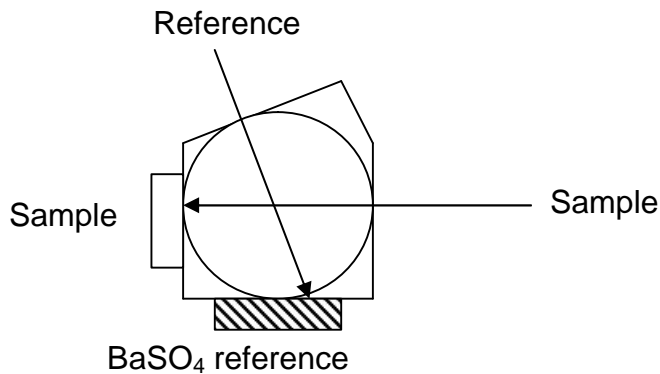
Figure 6.1: Experimental set-up for reflection measurements

6.2 Structural properties

6.2.1 X-ray diffraction

The XRD spectra of the four layers display a single dominant peak corresponding to the (002) plane of the ZnO lattice (figure 6.2). The signal-to-noise ratio of the spectrum presented here is less than what was observed in chapter 5 with ZnO on Si samples. This is attributed to the difference in film thickness (the samples grown on glass are thinner than those grown on Si), and to nature of the substrate (fused silica is an amorphous material). The samples are all highly c-axis oriented with the (002) plane parallel to the substrate. The (002) peak position of the samples doesn't however match the ZnO powder value of 34.42 °. This can be linked to the tensile strain produced within the film; when dealing with heteroepitaxy, the substrate chosen for growth has a direct bearing on the final state of strain in the film because it establishes the lattice mismatch and thermal expansion mismatch in the system. The (002) peak position of all four samples is less than that of ZnO powder, which shows that the films are in a uniform state of stress with tensile components parallel to the c-axis. The compressive forces at work in the layers are therefore acting in the plane of the film.
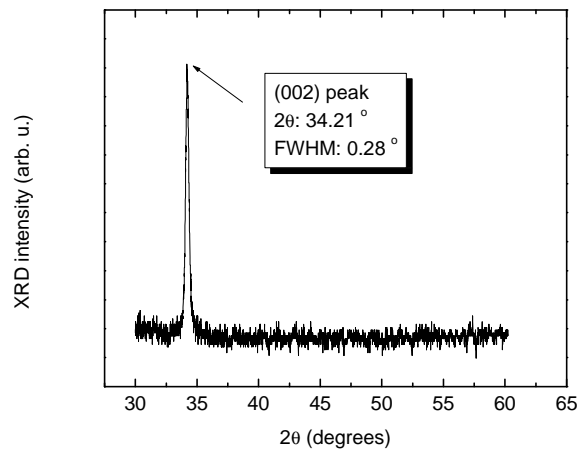
Figure 6.2: XRD spectrum of Z18/1

The angular peak position is found to increase from 34.16 to 34.24 ° as the VI:II ratio decreases, i.e. as less oxygen enters the system. The shift of the diffraction peak to larger

values has been previously associated in the context of annealing studies to the generation of oxygen or zinc vacancies in the crystal, as opposed to interstitials (Fu *et al.*, 1998a). In this case, it seems that decreasing the number of oxygen molecules allowed into the system has contributed to the generation of oxygen vacancies. This would explain the shift to a higher angular peak position as the VI:II ratio declines.

The lattice constant *c* is calculated for all samples according to equation 5.1 (table 6.2). The values yielded describe the *c*-axis as longer than that of ZnO powder. Just like the layers deposited on *n*-Si 2 ° off (100), the films' unit cell is elongated along the *c*-axis. The compressive forces responsible for the elongation clearly weaken as the VI:II ratio decreases, resulting in the shrinkage of the *c* value. Furthermore, the *c* value is used to determine the average uniform strain e_{zz} (equation 5.2) and the stress σ (equation 5.3) in the plane of the film. Logically, both the tensile strain and stress values sharply rise with increasing VI:II ratio.

The X-ray determined density of each film is calculated using equation 5.4. The lattice constant *a* could not be determined because the XRD spectra only showed one peak; it is therefore assumed to be constant and equal to the bulk value of 3.2498 Å (ASTM). The X-ray determined density shows a similar trend as the angular peak position; *r* increases with decreasing VI:II ratio, and the values obtained for Z10/1 and Z18/1 (5.646 and 5.642 g/cm^3) are closest to the ZnO powder data (5.674 g/cm^3; ASTM). The results obtained for the four samples fit well within the X-ray density range outlined for bulk ZnO (5.62 - 5.78 g/cm^3) (Heiland *et al.*, 1959).

The grain size *D* of the films is then evaluated using Scherrer's formula, equation 5.6. The grain size displays a different trend from the structural properties described earlier. The highest grain size (31 nm) is recorded for Z18/1, while Z60/1 exhibits the smallest grains (26 nm). When oxygen molecules are deficient in the chemical equilibrium of the reaction between DEZn and TBOH, an increase in TBOH flow rate will give the zinc precursors a better chance of reacting with the oxidizing agent. This would explain why $D_{Z18/1}$ overshadows $D_{Z10/1}$. On the other hand, excess oxygen in the system is likely to

engender the formation of oxygen gas within the film. This could lead to micro voids and other oxygen-related defects, which would hamper the formation of large ZnO grains in Z35/1 and Z60/1. The impact of these oxygen-induced defects can be seen on the surface images of ZnO samples deposited in similar conditions on n-GaAs (100) substrates (see section 7.2.2).

6.2.2 Summary: structural characterization

The influence of the VI:II ratio during growth on the structural properties of ZnO thin films was studied. Decreasing the VI:II ratio from 60:1 to 10:1 led the (002) XRD angular peak position to shift to higher values. This can be explained by the generation of oxygen vacancies in the crystal as less oxygen enters the reactor tube. The shift translated into a shrinkage of the ZnO c-axis, and a decrease in tensile strain along the c-axis. The largest grain size was measured at a VI:II ratio of 18:1.

Sample name	VI:II ratio	$2\theta_{002}$ (deg.) ($\pm\,0.01$)	c (Å) ($\pm\,0.003$)	Tensile strain (%)	Stress in the film (10^{10} dyn/cm^2)	X-ray Deter-mined density (g/cm^3) ($\pm\,0.003$)	Grain size (nm, ±1)
Z10/1	10:1	34.24	5.2321	0.49 $\pm$ 3E-4	-2.22 $\pm$ 1.27E-3	5.646	29
Z18/1	18:1	34.21	5.2366	0.58 $\pm$ 3E-4	-2.61 $\pm$ 1.50E-3	5.641	31
Z35/1	35:1	34.17	5.2432	0.70 $\pm$ 4E-4	-3.19 $\pm$ 1.83E-3	5.634	30
Z60/1	60:1	34.16	5.2440	0.72 $\pm$ 4E-4	-3.25 $\pm$ 1.86E-3	5.634	26
ZnO powder (ASTM)		34.42	5.2066	0	0	5.674	

Table 6.2: Summary of structural properties of ZnO samples on fused silica

6.3 Optical properties

6.3.1 Absorption coefficient, Urbach tail, band gap energies

Transmission spectra of the four ZnO samples were recorded at room temperature. They all reveal high transparency (>70 %) in the visible range (figure 6.3).
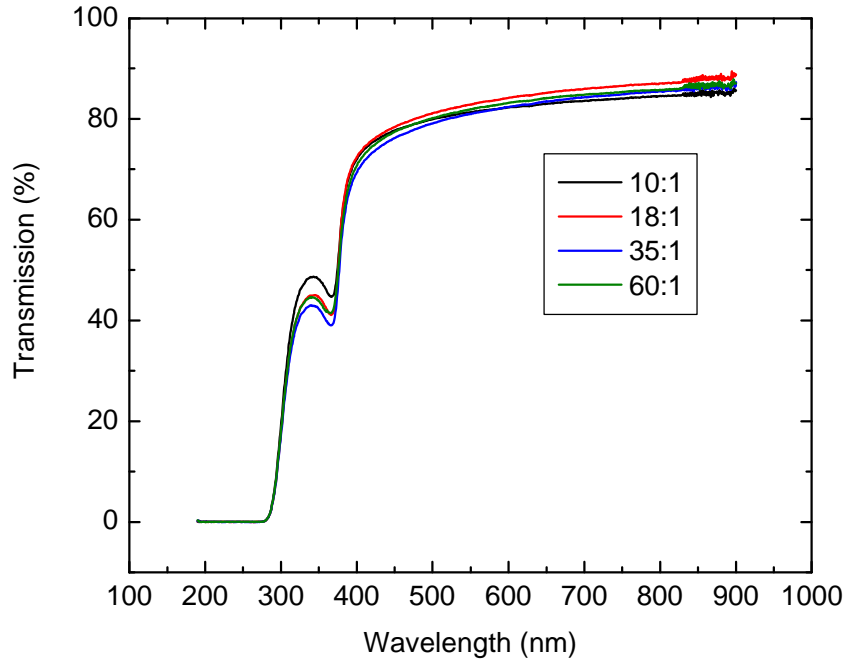
Figure 6.3: Room temperature transmission spectra of ZnO
samples Z10/1 – Z60/1

The transmission spectra are then used to calculate the absorption coefficient a of the samples. Indeed, the intensity of transmitted light (I) and the intensity of incident light (I_0) are related via the following equation

$$I = I_0 \exp(-at)$$

where t is the sample thickness. The transmittance T is then defined as I/I_0 (Kim *et al.*, 1997) and

$$a = \ln(1/T)/t \qquad \qquad \qquad \textbf{…(6.1)}$$

The four samples display a clear absorption peak at 365 nm due to a free exciton (figure 6.4). The presence of the free exciton peak at room temperature is closely related to film quality, and highlights the optical worth of these thin films.
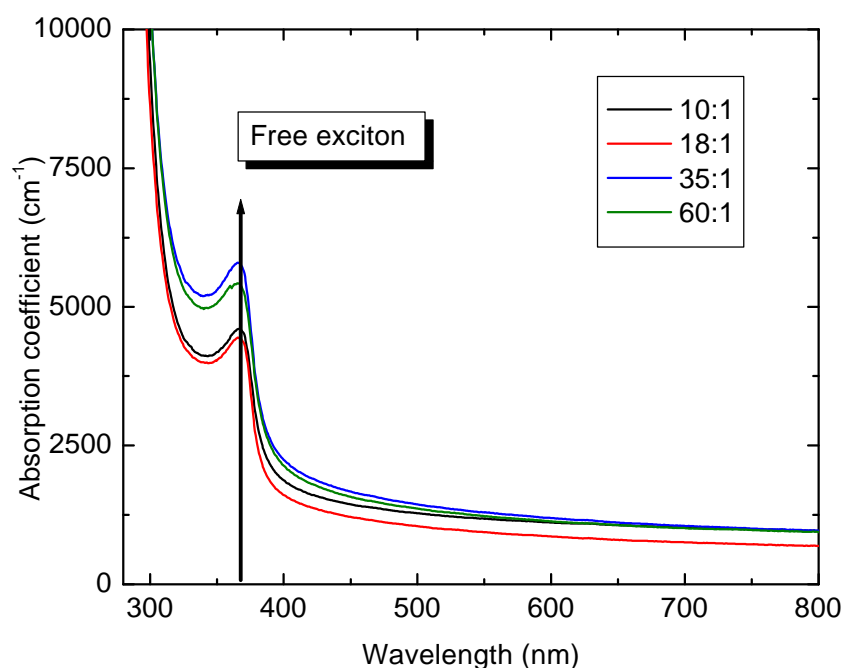
Figure 6.4: **Variation of absorption coefficient with VI:II ratio for ZnO samples Z10/1 – Z60/1**

Moreover, Z18/1 displays improved transparency throughout the visible range compared to the other three samples, as shown by the lower absorption coefficient in that range. This can be explained considering that the transmission is governed by three elements:

- oxygen deficiencies
- surface roughness
- impurity centers

Surface roughness and surface scattering affect the transparency of thin films because transmission is associated with grain size. Oxygen deficiencies are believed to affect the transmission properties of thin films, as layers deposited by electron-beam evaporation are brownish in color with poor transparencies (Gupta[4]). For the sake of comparison, the samples deposited on glass in this study were transparent in the visible range (see figure 6.3). As mentioned earlier, the angular peak position of the (002) peak in the XRD spectra continuously increases with decreasing VI:II ratio; this is explained by the formation of oxygen vacancies. The analysis of the variation of grain size with VI:II ratio

---

[4] Vinay Gupta, PhD Thesis, University of Delhi

also highlights the possible presence of oxygen gas and micro voids in the films grown at a VI:II ratio of 35:1 and 60:1. Hence, a large number of oxygen vacancies may explain the loss of light in Z10/1, while other oxygen-induced defects would account for the higher absorption coefficients of Z35/1 and Z60/1 compared to Z18/1. The influence of these oxygen-related defects on the surface morphology of ZnO thin films on GaAs substrates is presented in section 7.2.2.

The absorption coefficient values are then used to estimate the optical bandgap of the films. For a direct semiconductor like ZnO, the absorption coefficient a and the photon frequency n are related by the following relationship (Ye *et al.*, 2003)

$$\alpha^2 = A(\mathrm{h}\boldsymbol{n} - \mathrm{E_g}) \qquad\qquad \dots(6.2)$$

Linearly extrapolating the plot of α^2 vs. h$\boldsymbol{n}$ in the fundamental absorption region (figure 6.5) provided the $\mathrm{E_g}$ values reported in table 6.3.
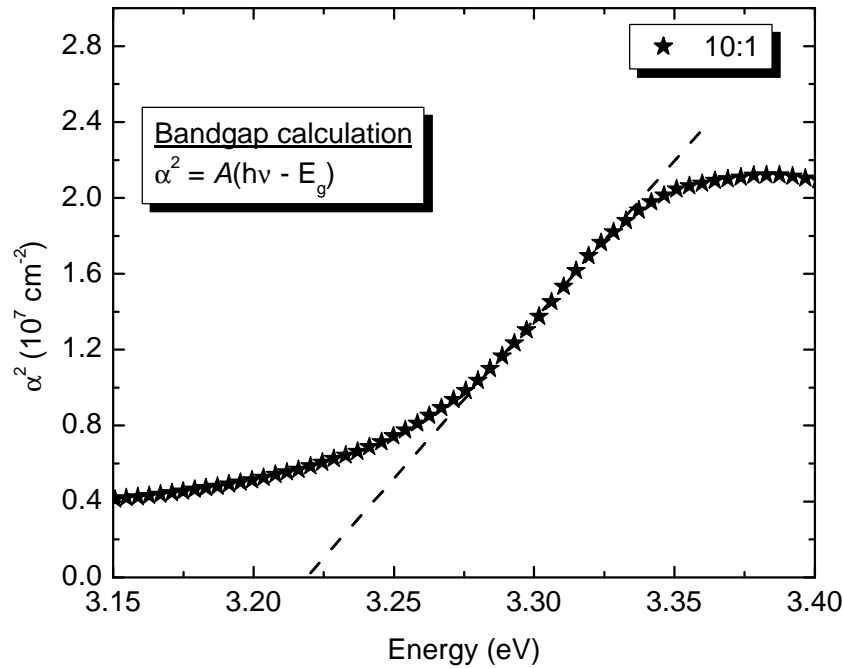
Figure 6.5: Band gap calculation for sample Z10/1

The highest E_g value (3.24 eV) is obtained for Z18/1, the lowest (3.21 eV) for Z60/1; furthermore, the band gap of all four samples is found wider than that of undoped material (3.20 eV; Landolt-Bornstein, 1982). The resolution of the instrument was 0.5 nm, which in the 3.20 – 3.30 eV range corresponds to an error of ± 4 meV. An in-depth discussion of the band gap values is found in section 6.4; it should be mentioned that of all the band gap energies reported for undoped ZnO (see section 2.3), Landolt-Bornstein's value was adopted because the carrier concentrations calculated with Landolt-Bornstein's band gap energy as reference closely matched the carrier concentrations obtained by Hall measurements on samples grown in similar conditions on *c*-plane sapphire substrates (see below). The widening of the bandgap when decreasing the VI:II ratio from 60:1 to 18:1 can be explained by Sernelius' effective mass model (Sernelius *et al.*, 1988). As the VI:II ratio drops, the number of oxygen vacancies is expected to rise. These oxygen deficiencies act as singly ionized donors and as the concentration of donors augments, the donor electrons generated tend to occupy the lowest states at the bottom of the conduction band (figure 6.6).

E_F

E_C

E_V
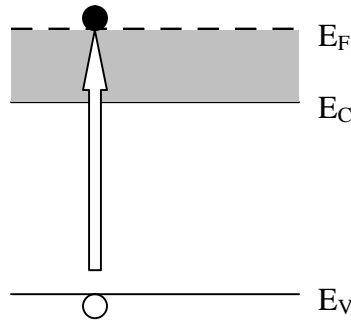
Figure 6.6: Conduction band filling due to heavy
***n*-type doping**

As a result of this band filling, absorption transitions cannot occur from the top of the valence band to the bottom of the conduction band anymore, and interband transitions correspond to the excitation of valence band electrons into empty states above the minimum of the conduction band. Consequently, the absorption edge shifts with the Fermi level to a higher energy. This is illustrated by the Burstein-Moss shift ΔE_g^{BM} (Wang *et al.*, 1996). In an *n*-type semiconductor, the absorption edge shift is given by

$$\Delta E_g^{BM} = (h^2/8\pi^2 m_{eff} e)(2\pi^2)^{2/3} n^{2/3} \text{ (eV)} \qquad\qquad \text{...(6.3)}$$

where m_{eff} is the reduced effective mass ($1/m_{eff} = 1/m_e + 1/m_h$), and n the carrier concentration. According to Pearton *et al.* (2003), the electron effective mass (m_e) and the hole effective mass (m_h) are equal to 0.24 and 0.59, respectively. Consequently, a blue shift in absorption edge is expected at higher carrier densities, i.e. at a higher density of oxygen vacancies. This was indeed the case: the absorption edge of Z60/1 and Z35/1 appears at 387 and 384 nm, respectively, while Z18/1 displays its absorption edge at 381 nm. Adopting the undoped band gap value of 3.20 eV (Landolt-Bornstein, 1982), the carrier concentrations of Z60/1, Z35/1, and Z18/1 are calculated to be $5.2 \bullet 10^{17}$, $2.7 \bullet 10^{18}$, and $4.2 \bullet 10^{18}$ cm^{-3} respectively. This implies that reducing the VI:II ratio during growth from 60 to 18:1 increased the carrier concentration by practically an order of magnitude. It is worth mentioning that these carrier concentrations are similar to those recorded by Hall measurements on ZnO layers deposited on *c*-plane sapphire in comparable conditions ($3.7 \bullet 10^{17}$ and $3.4 \bullet 10^{18}$ at a VI:II ratio during growth of 60 and 18:1, respectively; see section 9.4.2).

Conversely, the bandgap of Z10/1 did not fit the trend; it proved larger than the bandgap of Z60/1 but narrower than that of Z18/1 (3.22 eV for Z10/1, compared to 3.24 eV for Z18/1). This seems to contradict the XRD data presented in section 6.2.1, which indicates an increase in the donor concentration as the VI:II ratio decreases from 18 to 10:1. Nevertheless, it has been shown in various semiconductors that at high carrier densities, the energy gap (E_C-E_V) decreases due to the presence of a donor *band* rather than a discreet donor level. As the density of defects rises, the band structure of the crystal is perturbed by the potential of the defects as well as by the localized strains induced by the defects. At high densities, the perturbations overlap, and are liable to pull the bands down to lower energies. Since conduction band electrons have a smaller effective mass than valence band holes ($m_e/m_h = 0.41$; Pearton *et al.*, 2003), they will have a larger net effect on the conduction band, leading to the shrinkage of the energy gap (Stern and Talley, 1955). This describes a merging of the impurity band with the conduction band at

extremely high doping concentrations, thus leading to a semiconductor-metal transition and a swift decrease in band gap energy. Nevertheless, since the difference E_F - E_C between the Fermi level and the bottom of the conduction band is still increasing as the VI:II ratio during growth decreases from 18 to 10:1, the magnitude of the absorption edge shift is given by the sum of the two opposing factors (Pankove and Aigrin, 1962); while the band gap value of Z10/1 is still higher than that of undoped ZnO, the increase in ΔE_g is less than for Z18/1.

The carrier concentration of Z10/1 can now be calculated from Stern and Talley's impurity model (1955). They asserted that under certain approximations the energy levels of ordered impurities in semiconductors could be assimilated to the energy levels of metallic hydrogen. Indeed, the metallic hydrogen results can be extended to impurities in semiconductors according to the following conversion factor for the energy scale,

$$\frac{E_B}{e_B} = \frac{F}{f} = 13.60 \frac{m_c}{m} e^{-2} \qquad \qquad \text{...(6.4)}$$

where E_B and F represent the energy of the bottom of the $1s$ impurity band and the energy of the Fermi level at absolute zero, respectively, relative to the energy of the bottom of the conduction band. The parameters e_B and f have the same meaning, but for metallic hydrogen. Furthermore, m_c and m symbolize the effective mass at the bottom of the conduction band and the free electron mass; the factor e, on the other hand, is zinc oxide's dielectric constant. The latter is equal 8.5 according to Reynolds *et al.* (1965).

The shift of the band edge ΔE_g is then linked to the Fermi level by the following expression,

$$\Delta E_g = [1 + (m_c / m_v)](F - gkT) \qquad \qquad \text{...(6.5)}$$

where m_v is the effective mass near the top of the valence band, and $g = 4$ (Burstein, 1954). The Fermi level is calculated to be 0.118 eV above the bottom of the conduction band. Taking equation 6.4 into account and knowing that the radius of the unit sphere x_s is related to the donor concentration by the following equation (Stern and Talley, 1955),

$$x_s^{-3} = 6.2064 \bullet 10^{-25} (em/m_c)^3 n_D \qquad \text{...(6.6)}$$

where x_s is expressed in Bohr radii and n_D is the donor concentration in cm^{-3}, the donor concentration of Z10/1 is calculated from Stern and Talley's data for x_s^{-3} to be $9.4 \bullet 10^{19}$ cm^{-3}. It is fair to assume that most donors will be ionized at room temperature, and the carrier concentration can therefore be equaled to n_D. According to Mott (1974), the impurity and conduction bands merge when the carrier concentration exceeds $10 n_C$, where n_C is the conduction band density of states. Adopting $n_C = 5.9 \bullet 10^{18}$ cm^{-3} (Roth *et al.*, 1981a), the merge is taking place at $n = 5.9 \bullet 10^{19}$ cm^{-3}. The carrier concentration of Z10/1 is found superior to the merge threshold concentration, which justifies the use of Stern and Talley's model.

Considering that the free carrier concentration increases by two orders of magnitude as the concentration of oxygen vacancies rises, it is indeed tempting to associate the *n*-type conductivity of undoped ZnO with the presence of oxygen vacancies. This is in agreement with recent work by Tüzemen *et al.* (2003), who found that oxygen vacancies act as a source of free electrons at sample temperatures above 210 K. Below that temperature, the oxygen vacancy V_O will change its charge state to that of an inactive neutral charge state. Tüzemen *et al.* reported the thermal barrier required for an electron to go to the neutral charge state from the positively charged state to be 162 meV. They found the threshold temperature range to be 170 – 210 K.

After looking at the band gap energy and carrier concentration of the samples, the purity of the thin films is investigated by evaluating the near-band edge characteristics of the films. The Urbach tail is described by the following relationship (Pankove, 1965):

$$a \, (h\textbf{\textit{n}}) = \alpha_0 \exp(h\textbf{\textit{n}}/E_0) \qquad\qquad \textbf{...(6.7)}$$

$$\underline{\text{for } h\textbf{\textit{n}} < E_g}$$

The slope of the linear fit is used to calculate E_0 (figure 6.7). E_0 is an empirical parameter usually weakly dependent on temperature. E_0 has dimensions of energy and relates to the width of the localized states in the bandgap, but not to their energy position. E_0 has also been linked to the impurity concentration. Furthermore, it has been demonstrated that all defects, whether point, line or planar, bring about local electric fields that have an effect on band tailing (Redfield, 1963). Hence, E_0 is treated as a parameter that encompasses the influence of all possible defects. The lowest E_0 value (254 meV) is obtained for Z18/1. This further highlights the negative impact of the additional defect levels found in Z10/1 (E_0 = 338 meV), Z35/1 (312 meV), and Z60/1 (343 meV). Srikant and Clarke (1997) reported an E_0 value of 148.8 meV for a film deposited by laser ablation on fused silica, while Natsume *et al.* (1995) measured an E_0 as low as 80 meV for their samples grown by chemical vapor deposition on Pyrex glass. This implies that their samples are purer than the ones presented in this work. Nevertheless, it is worth mentioning that the samples studied here were deposited with low-purity *tert*-butanol; some of the defects are therefore not associated with the growth mechanism, but came straight from the oxygen precursor. Table 6.3 summarizes the sample properties determined from the transmission spectra.
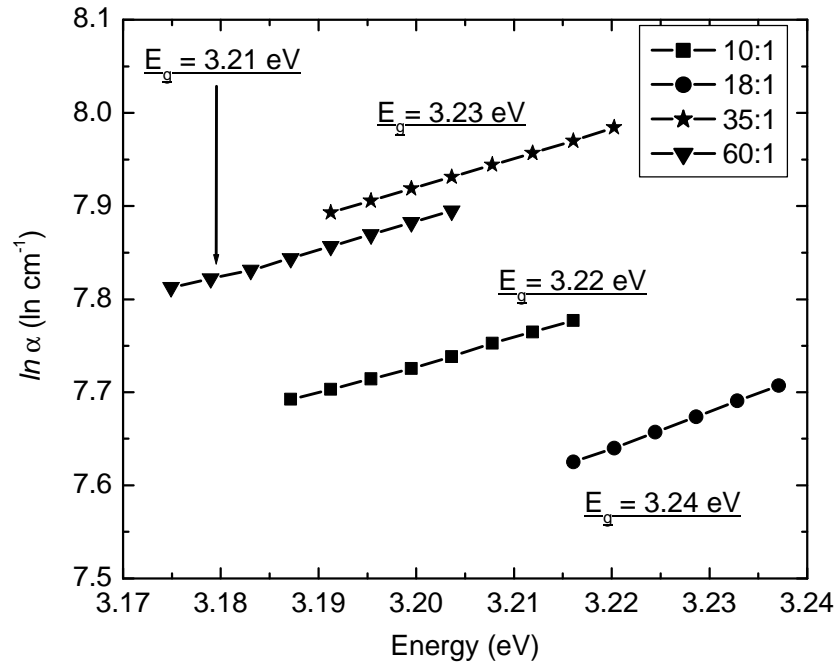
Figure 6.7: Variation of Urbach tail with VI:II ratio during growth

Sample name	Absorption edge (nm) (± 0.5)	E_g (eV)	Carrier concentration (cm^{-3})	Urbach tail E_0 parameter (meV)
Z10/1	385	3.22	$9.4 \bullet 10^{19}$	338 ± 5
Z18/1	381	3.24	$4.2 \bullet 10^{18}$	254 ± 2
Z35/1	384	3.23	$2.7 \bullet 10^{18}$	312 ± 2
Z60/1	387	3.21	$5.2 \bullet 10^{17}$	343 ± 9

Table 6.3: Summary of sample properties determined from transmission spectra

6.3.2 Optical dispersion: single-oscillator model

Several techniques have been developed in the last 40 years to determine the refractive index of a film at a particular wavelength. In this work, the refractive index is determined from the transmission and reflection spectra (Heavens, 1964). In this method, the optical constants of thin films are calculated from the measured values of reflection R (λ),

transmission T (λ), and thickness (t). The approach is to consider the reflection and transmission of light at the interface of the air/film/substrate (air multilayer) structures (figure 6.8), and express the results in terms of Fresnel coefficients.

$$n_0$$

$$n_1 - ik_1 \qquad t$$

$$n_2 - ik_2$$
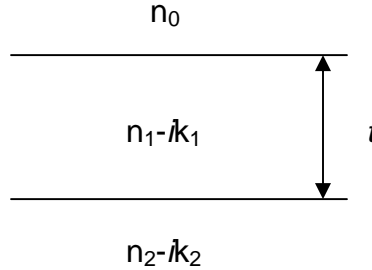
<u>Figure 6.8</u>: Schematic representation of absorbing film on transparent substrate

In this diagram, n_0 represents the refractive index of air, $n_1 - ik_1$ the complex refractive index of the absorbing layer (k being the layer's extinction coefficient), and $n_2 - ik_2$ that of the substrate. For a single absorbing film on a transparent substrate, the formulae relating the measured values at normal incidence of reflectance, transmittance, and thickness to the real and imaginary components of the refractive index n_1 and k_1 of the absorbing film are given by (Heavens, 1964)

$$R(1) = \frac{(g_1^2 + h_1^2)e^{2a_1} + (g_2^2 + h_2^2)e^{-2a_1} + A\cos 2g_1 + B\sin 2g_1}{e^{2a_1} + (g_1^2 + h_1^2)(g_2^2 + h_2^2)e^{-2a_1} + C\cos 2g_1 + D\cos 2g_1}$$

$$T(1) = \frac{n_2}{n_0} \frac{[(1+g_1)^2 + h_1^2][(1+g_2)^2 + h_2^2]}{e^{2a_1} + (g_1^2 + h_1^2)(g_2^2 + h_2^2)e^{-2a_1} + C\cos 2g_1 + D\cos 2g_1}$$

where $A = 2(g_1 g_2 + h_1 h_2)$, $B = 2(g_1 h_2 - h_1 g_2)$, $C = 2(g_1 g_2 - h_1 h_2)$, $D = 2(g_1 h_2 + h_1 g_2)$, and

$$g_1 = \frac{n_0^2 - n_2^2 - k_1^2}{(n_0 + n_1)^2 + k_1^2}, \quad h_1 = \frac{2n_0 k_1}{(n_0 + n_1)^2 + k_1^2},$$

$$g_2 = \frac{n_1^2 - n_2^2 + k_1^2}{(n_1 + n_2)^2 + k_1^2}, \ h_2 = \frac{-2n_2 k_1}{(n_1 + n_2)^2 + k_1^2},$$

$$a_1 = \frac{2\mathbf{p}k_1 t}{\mathbf{l}}, \ g_1 = \frac{2\mathbf{p}n_1 t}{\mathbf{l}}$$

These expressions lead to a continuous solution of n with $\mathbf{l}$, as shown in figure 6.9 for Z10/1.
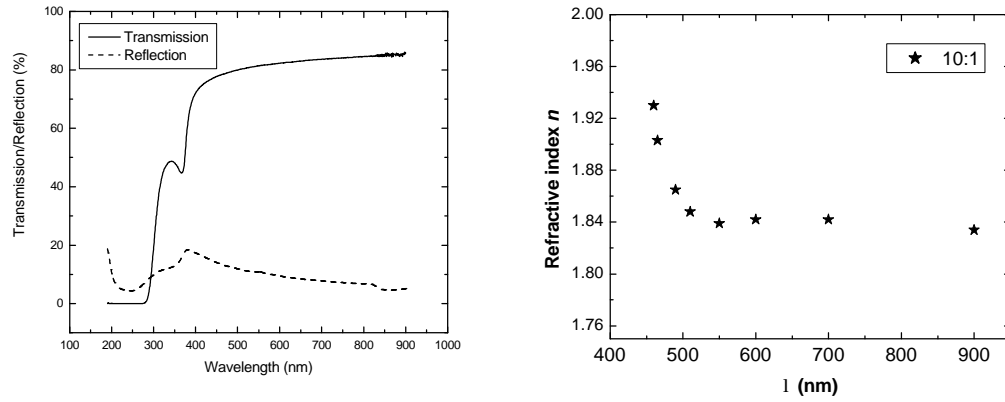
Figure 6.9: Transmission and reflection spectra, optical dispersion curve of Z10/1

The optical dispersion curves obtained are fitted to the single-oscillator model developed by Wemple and DiDomenico (1971). In their model, the optical dispersion curve is described by the following expression

$$n^2 - 1 = \frac{E_d E_{OSC}}{E_{OSC}^2 - (h\mathbf{n})^2} \qquad \qquad \textbf{...(6.8)}$$

where E_{0SC} is the single-effective-oscillator energy, E_d the dispersion energy, and hν the photon energy. E_d, the object of interest of this section, is a parameter that weighs the strength of interband optical transitions. The average oscillator strength is then given by

$$S_0 = \frac{E_d E_{OSC}}{(hc)^2} \qquad\qquad \textbf{...(6.9)}$$

while the average oscillator position, λ_0, is linked to the natural frequency of the particles, ν_0, by $\lambda_0 = c/\nu_0$. A plot of $1/(n^2 - 1)$ vs. $(h\nu)^2$ in the fundamental absorption region (figure 6.10) yields the E_d and E_{OSC} values reported in table 6.4.
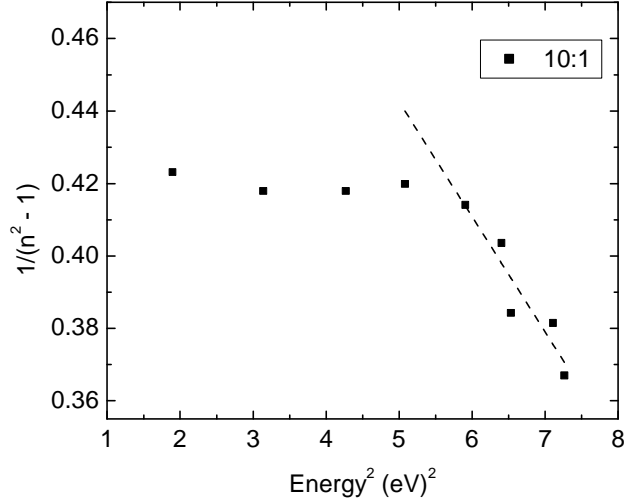
Figure 6.10: Single-oscillator-model: Z10/1

The experimental data reveals that both the interband optical transitions and the average oscillator strength are strongest in Z18/1.

Sample name	Optical dispersion: Single-oscillator model	
	E_d (eV)	E_{OSC} (eV)
Z10/1	7.23 ± 1.05	4.35 ± 0.96
Z18/1	9.25 ± 0.94	4.91 ± 0.72
Z35/1	7.30 ± 1.50	4.40 ± 1.36
Z60/1	5.67 ± 1.56	3.95 ± 1.75

Table 6.4: Summary of optical dispersion properties of ZnO samples

The E_d values measured here are somewhat lower than the values of 13.06 to 14.30 eV reported by Gupta and Mansingh (1996) for their samples deposited by sputtering on glass substrates. This probably reflects the high Urbach tail E_0 parameters of the samples presented here. Having said that, it should be mentioned that the variation of the strength of interband transitions with VI:II ratio seems to follow the observations made earlier; a low VI:II ratio during growth of 10:1 is responsible for an abundance of oxygen vacancies in the crystals, while micro-voids and other oxygen-induced defects are likely to appear at a VI:II ratio of 35 and 60:1. These defects are liable to disrupt the optical transitions in the material, and the strongest interband transitions are expected at a ratio of 18:1.

6.3.3 Summary: optical characterization

The influence of the VI:II ratio during growth on the optical and dispersion properties of ZnO thin films was studied. The measurements yielded the largest optical bandgap (3.24 eV) and the lowest Urbach tail E_0 parameter (254 meV) for the sample deposited at a VI:II ratio of 18:1. The carrier concentrations of Z60/1, Z35/1, and Z18/1 were calculated from the Burnstein-Moss shift; it was shown that decreasing the VI:II ratio during growth from 60 to 18:1 increased n by practically one order of magnitude, from $5.2 \bullet 10^{17}$ to $4.2 \bullet 10^{18}$ cm^{-3}. At a VI:II ratio of 10:1, the carrier concentration was calculated to be $9.4 \bullet 10^{19}$ cm^{-3} from Stern and Talley's method. Furthermore, the optical dispersion curves of the layers were plotted from the transmission/reflection method. They were fitted to Wemple and DiDomenico's single-oscillator model; it was found that the interband optical transitions are strongest in Z18/1. This confirms the role of oxygen-related defects on the optical quality of ZnO thin films.

6.4   Discussion of band gap energies

The band gap values of samples Z10/1 - Z60/1 were calculated in section 6.3.1 from the variation of the squared absorption coefficient with photon energy, and ranged from 3.21 eV for Z60/1 to 3.24 eV for Z18/1. As mentioned in section 2.3, the room temperature band gap energy of ZnO is believed to range between 3.30 and 3.40 eV. The discrepancy between thin film and single crystal values stems from the fact that the

variation of absorption coefficient with photon energy of a semiconductor thin film is linked to the presence of point defects, dislocations, impurities, grain boundaries, and the film's state of strain. Consequently, the absorption coefficient of a thin film is going to differ from that of a perfect, unstrained single crystal. The aim of sections 6.4.1 and 6.4.2 is to quantify the extent to which the thermal mismatch strains in the ZnO films is going to affect the calculated band gap.

6.4.1 Calculation of thermal mismatch strains in films

In incommensurate film/substrate systems, the lattice mismatch strains tend to be relieved at the growth temperature via dislocation formation (Vincent, 1969). Nevertheless, as dislocation processes freeze out during cooling, additional strains due to the difference in thermal expansion coefficient between the substrate and the film are generated. If the substrate is much thicker than the film, the substrate remains in essence stress-free and all strains are borne by the film. Furthermore, it can be assumed that the films investigated here are under plane stress condition, since they satisfy the thin film approximation (i.e. the lateral dimensions of the film are considerably larger than its thickness). The in-plane strains are then given by

$$\boldsymbol{e}_{ij}^{film} = \int_{T_{growth}}^{T_{RT}} (\boldsymbol{a}_{ij}^{film} - \boldsymbol{a}_{ij}^{substrate})dT \qquad\qquad …(6.10)$$

where $\boldsymbol{e}_{ij}$ and $\boldsymbol{a}_{ij}$ are the tensorial thermal strains and the thermal expansion coefficients of the film and substrate (Srikant and Clarke, 1997). It is necessary to know the epitaxial relationship between the film and substrate so as to gauge the in-plane thermal mismatch strains in the film because thermal strains are isotropic; this may be problematic in the present case, since there is no epitaxial relationship between ZnO and the fused silica substrate. Having said that, ZnO layers grown on fused silica are known to be textured, with the *c*-axis perpendicular to the substrate (Jin *et al.*, 1988). This was confirmed by the X-ray diffraction spectra taken on these samples (see figure 6.2). The high degree of *c*-axis orientation means that ZnO thin films on fused silica can be viewed as oriented thin films with random in-plane orientation. Furthermore, since the wurtzite crystal

101

structure is isotropic in the basal plane, the textured ZnO thin films on fused silica can be treated as c-axis oriented single crystals; the thermal mismatch strains can therefore be calculated from the thermal expansion coefficients of the ZnO film and the fused silica substrate. ZnO has a linear thermal expansion coefficient α_L of $8.63 \bullet 10^{-6}$ /°C (Kumar and Sastry, 2001); fused silica being amorphous has only one thermal expansion coefficient of $0.55 \bullet 10^{-6}$ /°C. Since the growth temperature was set at 450 °C, and the films were cooled to 25 °C after deposition, the two in-plane strains are calculated to be $3.43 \bullet 10^{-3}$. Moreover, the strains in all three directions need to be evaluated in order to work out the shift in the band gap with thermal mismatch strains. The out-of-plane strain is related to the in-plane strains from the plane stress condition, which states that

$$e_{out\,of\,plane} = -\frac{c_{1133} + c_{2233}}{c_{3333}} e_{in-plane}, \qquad \qquad \text{...(6.11)}$$

where c_{1133} and c_{3333} are the elastic stiffnesses of ZnO; they are equal to 105.1 and 210.9 GPa respectively (Landolt-Bornstein, 1982). The out-of-plane strain is therefore equal to $3.42 \bullet 10^{-3}$.

6.4.2 Influence of thermal mismatch strains on band gap energies

Having calculated the thermal mismatch strains in the films, it is now possible to quantify the effect of stress on the measured band gap. In order to do so, Pikus' linear approximation for the effect of stress on the optical spectrum of wurtzite-type crystals is adopted (Pikus, 1964). In this model, the band gap $E_g^{'}$ of a stressed material is described in terms of the unstrained band gap E_v^0 as

$$E_g^{'} = E_c^{'} - E_v^{'} = -E_v^{'} = -(E_v^0 + \Delta E_v^{'}) \qquad \qquad \text{...(6.12)}$$

where the position of the conduction band is considered the reference, E_v^0 is the unstressed position of the valence band, and $\Delta E_v^{'}$ represents the change in the position of

the valence band due to uniform bulk stresses. A decrease in the band gap energy will be reflected in a negative $\Delta E_{v}^{'}$ value, an increase in band gap energy will yield a positive $\Delta E_{v}^{'}$. Since the minimum energy transition is between the highest valence band $E_{v}(\Gamma_{7}^{u})$ and $E_{c}(\Gamma_{7})$ levels (figure 6.11), the position of $E_{v}(\Gamma_{7}^{u})$ is given (Pikus, 1964) in terms of the deformation potential as

$$\Delta E_{v}^{'}(\Gamma_{7}^{u}) = \boldsymbol{d}_{1} + \frac{\boldsymbol{d}_{2}}{2}\left\{1 + \frac{\Delta_{cf} - (\Delta_{so}/3)}{[(\Delta_{cf} - (\Delta_{so}/3))^{2} + 8(\Delta_{so}/3)^{2}]^{1/2}}\right\} \qquad \text{...(6.13)}$$

where Δ_{cf} is the crystal field splitting (42 meV) and Δ_{so} the spin orbital splitting (-5 meV). Furthermore, $\boldsymbol{d}_{1} = C_{1}\boldsymbol{e}_{zz} + C_{2}(\boldsymbol{e}_{xx} + \boldsymbol{e}_{yy})$ and $\boldsymbol{d}_{2} = C_{3}\boldsymbol{e}_{zz} + C_{4}(\boldsymbol{e}_{xx} + \boldsymbol{e}_{yy})$, where $\boldsymbol{e}_{xx}, \boldsymbol{e}_{yy}, \boldsymbol{e}_{zz}$ are the strains in the principal crystallographic directions and C_1, C_2, C_3, and C_4 zinc oxide's deformation potentials. C_1, C_2, C_3, and C_4 are respectively equal to –2.66, 2.82, -1.34, and 1.0 eV (Rowe *et al.*, 1968).
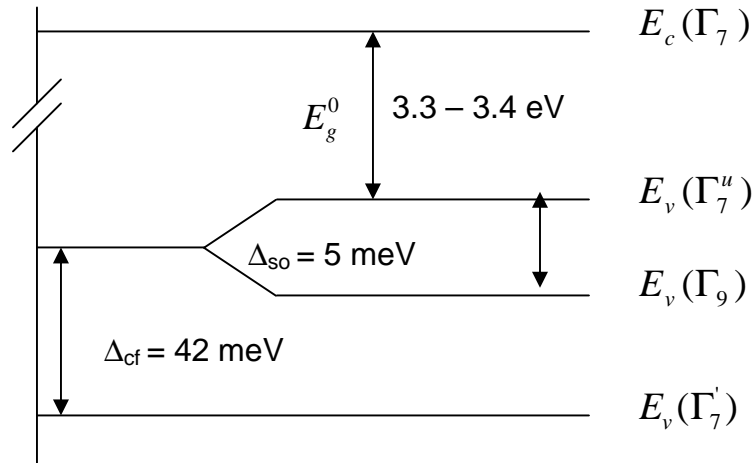
Figure 6.11: **Zinc oxide's upper energy levels**
(after Srikant and Clarke, 1997)

The thermal mismatch band shift in these samples is thereby calculated to be +39.8 meV. This indicates an increase in band gap energy of approximately 40 meV compared to

unstrained single crystals; this is intriguing because the maximum band gap value measured is 3.24 eV for Z18/1, 60 – 160 meV *below* the accepted band gap range of 3.30 - 3.40 eV. In order to clarify the situation, another parameter besides the influence of thermal strains on the band gap needs to be taken into account: *band bending*.

6.4.3 Band bending

If a considerable portion of the ZnO grains is depleted, a flat band description of the energy bands is no longer fitting, and the potential is found to vary throughout most of the grains. The potential can then be treated as periodic, as illustrated in figure 6.12:
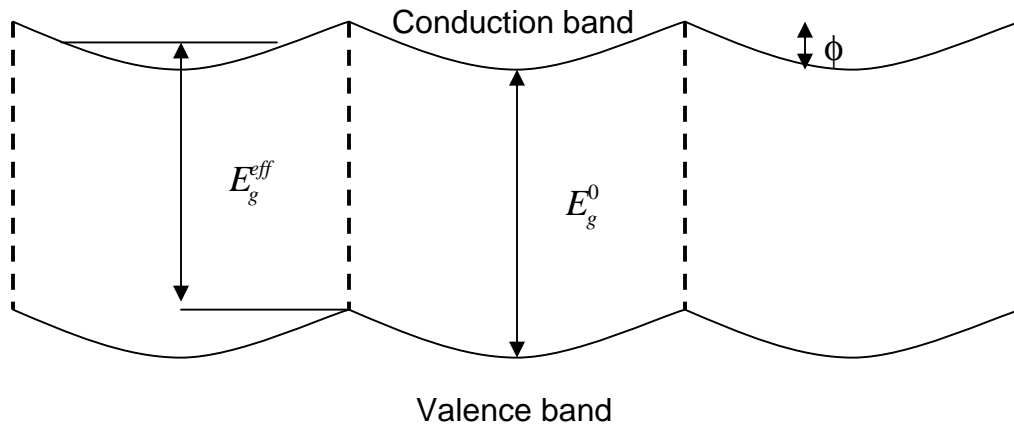
Figure 6.12: **Idealized 1D potential variation within grains (after Srikant and Clarke, 1997)**

The varying electrostatic potential leads to the generation of electric fields at the grain boundaries; these electric fields may engender optical transitions between the highest point of the valence band and the lowest point of the conduction. This would of course change the optical absorption edge and according to Döhler (1986), the effective band gap E_g^{eff} for compositionally modulated superlattices is

$$E_g^{eff} = E_g^0 - \boldsymbol{f} + \boldsymbol{x}_1 \qquad\qquad \textbf{...(6.14)}$$

where E_g^0 represents the undistorted band gap, ϕ the barrier height at the grain boundary, and ξ_1 the first quantized level of a 1D gas. In order to assess whether band bending does occur in these films, the effect of the grain boundary on conduction has to be discussed. It is in fact linked to the relationship between the grain sizes of the films and the Debye screening length L_D. (Orton and Powell, 1980).

The latter is given by

$$L_D = (ee_0 kT / e^2 n_D)^{1/2} \qquad \qquad \text{...(6.15)}$$

where e is zinc oxide's specific dielectric constant, e_0 the dielectric constant in vacuum, and n_D the donor concentration of the sample. If L_D is less than $D/2$ (D being the film's grain size), a potential barrier around each grain is generated due to band bending; this potential barrier is described by localized defect states in the forbidden-gap trapping majority carriers, thus creating depletion zones. The nature of these defect states at the boundary remains vague; they could stem from dangling or distorted bonds, or arise extrinsically from the segregation of impurities to the boundary. On the other hand, if L_D is larger than $D/2$, the conduction band can be considered flat, the potential barrier around the grains is nonexistent, and electron transport takes place without obstruction by grain boundaries. The electron concentrations of Z10/1, Z18/1, Z35/1, Z60/1 are calculated from Stern and Talley's method and the Burnstein-Moss shift (see section 6.3.1), and found equal to $9.4\bullet10^{19}$, $4.2\bullet10^{18}$, $2.7\bullet10^{18}$, and $5.2\bullet10^{17}$ cm^{-3}, respectively. Provided that most donors are ionized at room temperature, the donor concentration n_D is approximately equal to the electron concentration and for $e = 8.5$ (Reynolds *et al.*, 1965), L_D (Z10/1), L_D (Z18/1), L_D (Z35/1), and L_D (Z60/1) are respectively equal to 0.4, 1.7, 2.1, and 4.8 nm (table 6.5).

Sample name	Debye screening length L_D (nm)	Grain size D (nm)	$D/2$ (nm)
Z10/1	0.4	29	14
Z18/1	1.7	31	16
Z35/1	2.1	30	15
Z60/1	4.8	26	13

Table 6.5: Debye screening length and grain size of Z10/1 – Z60/1

As can be seen in table 6.5, $L_D < D/2$ for all samples; it is therefore necessary to take into consideration the effect of the grain boundary barriers created by band bending.

In order to quantify the band bending, the abrupt junction approximation needs to be adopted. This is appropriate, considering that the Debye length is smaller than the grain size. The next step consists of determining the rate-limiting step for electron transport across the grain boundaries. Transport across the potential barrier is made of three sequential steps: drift diffusion in the first depletion region, thermionic emission at the boundary plane, and finally drift diffusion in the second depletion region. Figure 6.13 schematically shows the conduction and valence bands, and the quasi-Fermi level in the vicinity of a grain boundary barrier (Evans and Nelson, 1991). In this diagram, V represents the voltage drop across the boundary, and E_b the appropriate Fermi level up to which boundary states are occupied. In addition, l_l and l_r represent the places where the space-charge regions terminate. In the thermionic limit, the quasi-Fermi level stays flat throughout the depletion regions; nevertheless, it would drop if drift-diffusion transport were important.
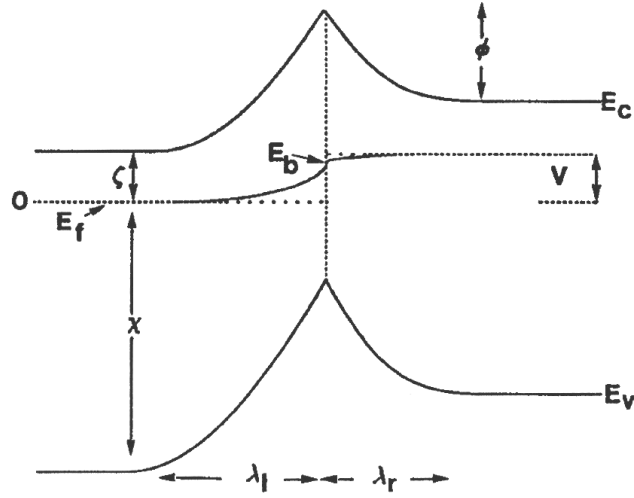
Figure 6.13: Schematic diagram of conduction (E_C) and valence (E_V) bands and quasi-Fermi levels E_f in the vicinity of a biased grain boundary (after Evans and Nelson, 1991)

Evans and Nelson calculated the crossover doping level (N_d^c), where the two transport mechanisms are equally important. It is given by

$$N_d^c = \frac{(1-c/2)^2 \, \bar{v} \, e}{8 e m^2 f_0} \qquad \qquad \text{...(6.16)}$$

where c is the fraction of thermionic flux from either side of the boundary which is trapped at the boundary, $\bar{v}$ the electron mean thermal velocity, e the permittivity of the semiconductor, m the carrier mobility, and f_0 the given zero-bias barrier height; they thus reported a crossover between the two transport mechanisms at a doping level of $3 \bullet 10^{14}$ cm^{-3}. If the doping level is two orders of magnitude higher than N_d^c, transport is best defined by the thermionic approximation; for doping levels two orders of magnitude lower than N_d^c, transport is described by the drift-diffusion approximation. Considering that the lowest carrier concentration measured here is of the order of 10^{17} m^{-3} (Z60/1), it is

safe to assume that thermionic emission is the rate-limiting step for electron transport across the grain boundaries of the samples studied in this chapter.

Furthermore, by assuming that all of the interface states are filled, meaning that there are no energy states above the Fermi level at the grain boundary, the interface charge can then be seen constant. Additionally, it is assumed that the potentials at all the grain boundaries are the same. These assumptions enable the abrupt junction model for electron transport across grain boundaries to be applied.

The Poisson equation can then be solved for the donor distribution in the vicinity of the grain boundaries; by applying the condition of charge neutrality, the barrier height is then given by (Srikant *et al.*, 1995b)

$$\boldsymbol{f} = \frac{eN_s^2}{2\boldsymbol{ee}_0 n} - \frac{kT}{e} \qquad \text{...(6.17)}$$

where N_s is the effective grain boundary trap density, and is equal to $2n\text{W}$ (n is the carrier concentration in the grain, and W the depletion width). Assuming a depletion width of 30 nm for films having a carrier concentration between 10^{17} and 10^{18} cm^{-3} (Vanheusden *et al.*, 1996a), the barrier height of Z60/1 is calculated to be 2.0 eV. From equation 6.14, this would give an effective band gap as defined by Döhler of 1.3 – 1.4 eV, which is clearly not realistic considering that the measured band gaps range between 3.21 and 3.24 eV (the correction associated with the quantization of levels is overlooked since it is minute compared to the band bending). While band bending might explain lower band gap values for samples displaying lower carrier concentrations (Srikant, 1995a), it cannot explain the lower band gap values observed on these samples.

6.4.4 Nature of measured transition

In order to elucidate the problem, a closer look was given at the nature of the transmission measurements that led to the band gap values reported here. Indeed, transmission spectroscopy probes the bulk of the crystal. Therefore, the low band gap

energies calculated from the transmission measurements may stem from the presence of a deep donor or acceptor level, thus engendering direct deep donor-valence band or conduction band-deep acceptor transitions appearing at energies lower than the actual band gap, E_c-E_v. This was tested by recording the infrared transmission spectra of the samples (figure 6.14).
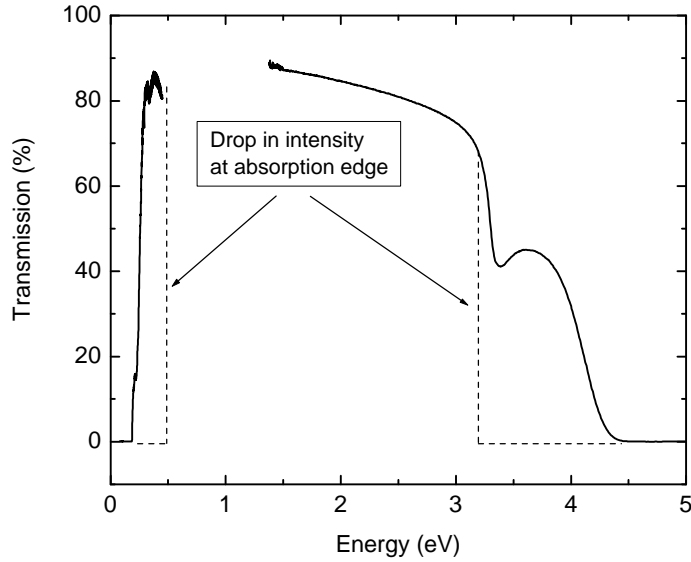
Figure 6.14: IR and UV-vis transmission spectra of Z10/1

All the films displayed sharp absorption at 0.18 eV, which is reminiscent of an intrinsic donor level measured by admittance spectroscopy 0.18 eV below the conduction band (Rossinelli *et al.*, 1985). It is now necessary to assess the number of carriers excited in the conduction band at room temperature from this possible donor level. The number n_0 of electrons promoted to the conduction band is given by

$$n_0 = \frac{2n_D}{1 + \sqrt{1 + (4n_D / \boldsymbol{b}N_c)\exp(E_d / kT)}} \qquad \text{...(6.18)}$$

where n_D is the number of donor levels of spin degeneracy $\boldsymbol{b}$ per unit volume ($\boldsymbol{b}$ = 2), and E_d the donor energy below the base of the conduction band, assuming that no other defect states exist (Blakemore, 1987). Assuming a donor density of $1 \bullet 10^{17}$ cm^{-3}, it is

found that 20 % ($2\bullet10^{16}$ cm^{-3}) of the donors are excited into the conduction band. This means that the valence band-donor level transition would feature more strongly than the valence band-conduction band transition in the calculation of the transition probabilities. This seems to be the case, as the drop in intensity at the absorption edge is larger in the IR than in the UV (figure 6.14).

The presence of this donor level is also mirrored in the reflection spectra of the samples; the theory of optical transitions in semiconductors predicts a reflection peak in the vicinity of a band edge (Wooten, 1972). Indeed, the reflection spectra of the samples (figure 6.9) display a reflection near the band edge, at 382.5 nm (3.18 eV). No peak was observed between 3.30 and 3.40 eV, where the band gap energy is expected. This confirms that the donor level-valence band transition dominated the transmission measurements. The corrected band gap values, taking into account the donor level 0.18 eV below the conduction band and the thermal mismatch strain shift of 0.040 eV, should therefore be corrected to 3.36, 3.38, 3.37, and 3.35 eV for Z10/1, Z18/1, Z35/1, and Z60/1, respectively. These values are close to the band gap energy of 3.35 eV measured by photoluminescence spectroscopy on a ZnO thin film on silicon (see section 8.3.2).

6.5   Conclusions

This study on the influence of the VI:II ratio during growth on the properties of ZnO thin films follows excellent work reported in the literature by other workers in the field. First of all, Choopun *et al.* (1999) performed Rutherford backscattering spectrometry/ion channeling measurements and atomic force microscopy scans on ZnO thin films deposited by pulsed laser deposition on *c*-plane sapphire substrates; they found links between the oxygen partial pressure and the structural and morphological properties of their samples. They measured the ratio of backscattered yield with the beam incident along the [0001] direction to that of a random direction (c_{min}), and reported that c_{min} near the surface region was greatly improved at low oxygen partial pressures (10^{-4} – 10^{-3} Torr) compared to high partial pressures (10^{-1} Torr). In other words, their films grown at low oxygen concentrations proved of better quality than the films grown

at high oxygen concentrations. They found that the defect densities near the interface was dependent on the oxygen pressure, and that the increase in c_{min} at high oxygen pressures meant that the films contained additional defects such as dislocations, low-angle grain boundaries, and interstitials. This result was reflected in this work too, as the Urbach tail E_0 of samples deposited at VI:II ratios of 35 and 60:1 proved larger than that of the sample grown at a ratio of 18:1. At low oxygen pressures, the layers of Choopun *et al.* (1999) also displayed 3-D growth features such as well-faceted hexagons, with a high density of atomic steps on the facets. They also reported a transition pressure (10^{-2} Torr) at which the samples showed smooth surfaces, and after which they were marred by high nucleation densities, irregular grains of different sizes, and increased surface roughness. Similarly, the VI:II ratio during growth of 18:1 appears to be a transition point in this system; indeed, the defect properties of the sample deposited at a ratio of 10:1 was dominated by an extremely high concentration of oxygen vacancies, while the films grown at 35 and 60:1 showed other oxygen-induced defects such as oxygen gas in the film. The impact of the VI:II ratio during growth on surface morphology is further studied in section 7.2.2. Choopun *et al.* then proceeded to suggest a two-step growth process, starting with the deposition of a nucleation layer grown at low oxygen pressures followed by the subsequent growth of the main layer at high oxygen pressures. It would be appealing to study such a two-step growth process for MOCVD growth.

Xiong *et al.* (2002) studied the impact of the O_2/Ar fraction in the feed of their reactive sputtering system, and found that at an O_2 fraction less than 55 %, their ZnO films displayed *n*-type conductivity, while at a fraction superior to 55 %, they obtained *p*-type material. The best hole concentration they measured was $9 \bullet 10^{17}$ cm^{-3}, with a resistivity of 3 Ωcm. This is an encouraging result in the light of the fabrication of ZnO-based *p* - *n* junctions. As will be seen in section 7.2.2, films deposited in this work at high VI:II ratios also began displaying photoluminescence properties associated with *p*-type ZnO.

Furthermore, this study has shown that the VI:II ratio during the MOCVD growth of ZnO with TBOH has a significant effect on both the structural and optical properties of ZnO. A low VI:II ratio will provoke an abundance of oxygen vacancies in the crystal lattice,

while a high VI:II ratio will cause the formation of oxygen gas and other oxygen-induced defects in the material. These defects are shown to affect the band gap, absorption edge, Urbach tail, and dispersion properties of the material.

The measured band gap increased from 3.21 to 3.24 eV as the VI:II ratio decreased from 60 to 35 to 18:1. This was explained by the Burnstein-Moss shift; the carrier concentration of these three samples was calculated to be $5.2 \bullet 10^{17}$, $2.7 \bullet 10^{18}$, and $4.2 \bullet 10^{18}$ cm^{-3}, respectively. The lesser widening of the Z10/1 band gap compared to the other three samples is attributed to a merging of the impurity band with the conduction band at high doping densities, thus giving rise to a semiconductor-metal transition and a swift decrease in band gap energy. The carrier concentration of Z10/1 was calculated to be $9.4 \bullet 10^{19}$ cm^{-3} from Stern and Talley's impurity model. It is seen that the carrier concentration can be varied over two orders of magnitude by carefully selecting the VI:II ratio during growth. This seems to corroborate Tüzemen *et al.*'s model (2003), who asserted that oxygen vacancies act as a source of free electrons at sample temperatures above 210 K.

The purity of the samples was investigated by determining their Urbach tail E_0 parameter. The lowest E_0 (254 meV) was calculated for Z18/1. The optical dispersion curves of the four samples were plotted and fitted to Wemple and DiDomenico's single-oscillator model; this highlighted that interband transitions were strongest in Z18/1, thus reflecting the impact of oxygen-related defects on the optical properties of ZnO layers.

Finally, the band gap values were discussed. The influence of the thermal mismatch strains on the optical spectrum was calculated to be + 40 meV. It was also found that the E_g values obtained from the transmission plots corresponded to a transition involving a deep donor level 0.18 eV below the conduction band and the valence band. The band gap values were consequently corrected, and considered equal to 3.36, 3.38, 3.37, and 3.35 eV for Z10/1, Z18/1, Z35/1, and Z60/1 respectively. These values are similar to the band gap energy of 3.35 eV measured by photoluminescence spectroscopy on a ZnO layer deposited on silicon (see section 8.3.2).

7. INFLUENCE OF GROWTH PARAMETERS ON PHOTOLUMINESCENCE PROPERTIES OF ZnO EPILAYERS

The fact that GaAs is a piezoelectric semiconductor has paved the way for its use in acoustic charge transport (ACT) devices. Nevertheless, depositing a strongly piezoelectric thin film like ZnO on top of the ACT-like structure could potentially improve gallium arsenide's piezoelectric coupling, which would have an effect on a variety of device properties such as lifetime, reliability, and size (Kim *et al.*, 1994a). Furthermore, the ZnO/GaAs structure is known to facilitate the monolithic integration of surface acoustic wave devices and GaAs electronics. These are some of the reasons why the deposition of ZnO epilayers on GaAs should be thoroughly investigated. Chapter 5 dealt with the relationship between the substrate temperature and the structural properties of the epilayers; amongst other things, chapter 6 handled the influence of the VI:II ratio during growth on the transmission properties of the ZnO epilayers. Chapter 7 now focuses on how the photoluminescence properties of the thin films vary with substrate temperature, VI:II ratio during growth, introduction of a buffer layer, and precursor purity.

7.1 Background theory and experimental procedure

The thin films examined in this work were grown at nominally atmospheric pressure on semi-insulating *n*-GaAs (100) substrates. Electronic grade (6N) TBOH was selected as oxidizing agent for all layers, except when comparing the influence of TBOH purity on the photoluminescence properties of the samples. The DEZn flow rate was kept at 15 μmol/min for all growth runs. A maximum growth rate of 0.8 μm/hr was measured at a substrate temperature of 450 °C. The growth time was set at 45 minutes, except otherwise mentioned. Samples T300 to T600 are labeled according to their growth temperature, keeping the VI:II ratio during growth constant at 18:1; samples S10 to S90 are named after their VI:II ratio during growth, keeping the growth temperature stable at 450 °C.

The structural properties of the samples were studied by X-ray diffraction, optical microscopy, Auger depth profiling, and both scanning and transmission electron microscopy. The SEM microscope employed was a Philips XL 30 model. Background information on Auger depth profiling and the TEM sample preparation is given in sections 7.1.1 and 7.1.2.

Photoluminescence spectra were recorded at both 12 and 300 K with a HeCd laser (λ_{ex} = 325 nm). An in-depth description of the photoluminescence spectroscopy set-up can be found in section 8.2.

Ohmic contacts were fabricated by soldering indium pads onto the samples. Indium was chosen because of the ease with which In contacts can be soldered onto samples, and because of the success In pads have found with other wide band gap semiconductors such as GaN (Molnar *et al.*, 1993). Hall effect measurements then yielded the room temperature resistivity, carrier concentration, and mobility of the films. The reader is referred to section 9.1.3 for experimental details.

7.1.1 Auger Electron Spectroscopy

The Auger spectra presented in this chapter were recorded at the Department of Physics of the *University of the Free State*, South Africa[5].

Auger spectroscopy is an important technique relying on the autoionization process within an excited atom. In the Auger effect, an incident electron causes photoemission of a core electron (electron 1, figure 7.1). Here, a 2 keV primary electron beam (SAM 590 PHI system) provided the initial photoemission. The electron vacancy (also called a hole) created in the core level by photoemission may then be neutralized by an electron moving down from an electron level of lower binding energy (electron 2). The quantum of energy ΔE, resulting from the difference in binding energy between the core hole and the down electron, may either exit the atom as a photon by a process of X-ray fluorescence or be

---

[5] The author is indebted to Prof H. C. Swart for performing the Auger measurements.

transferred to a third electron, which can then break out into the vacuum with a kinetic energy E_{KIN}. The kinetic energy of the third electron, the Auger electron, is given by

$$E_{KIN} = E_K - E_{L1} - E_{L_{2,3}} - f_{AES}$$

where $E_K - E_{L_1}$ is the energy available to the Auger electron from the down electron, and $E_{L_{2,3}} + f_{AES}$ the energy required to overcome the barrier to emission from within the atom.
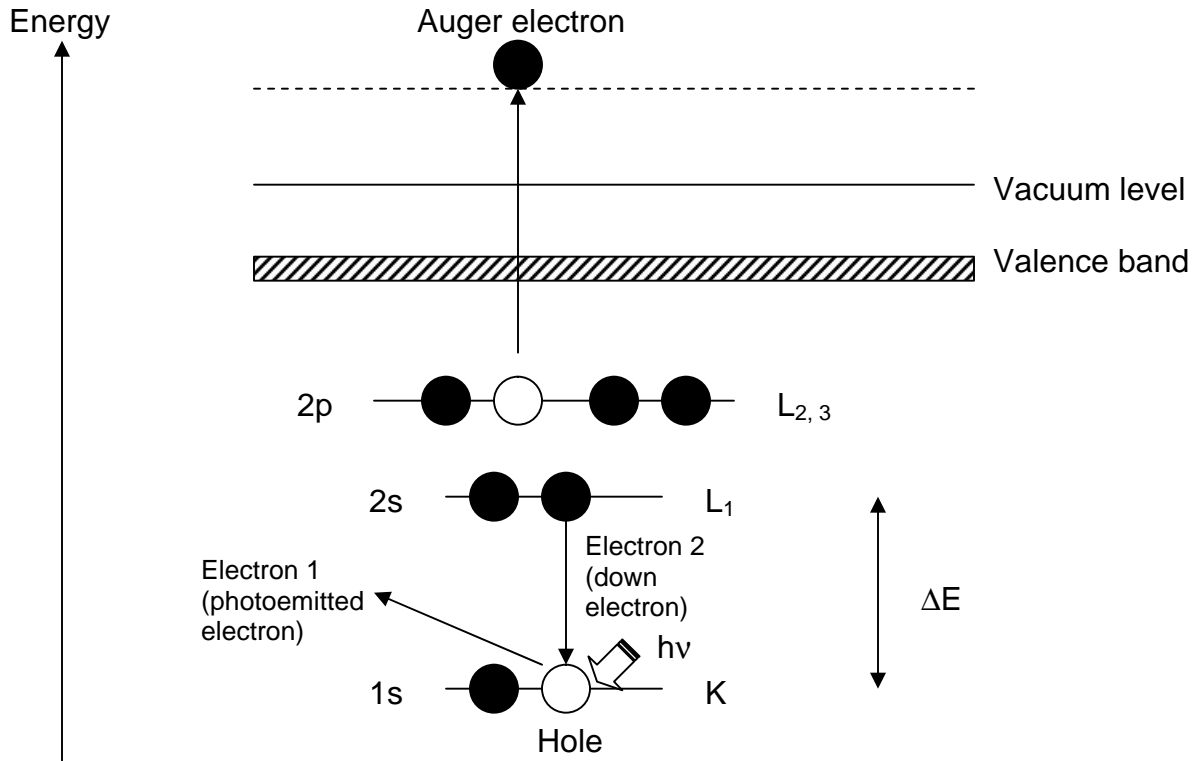

Figure 7.1: The Auger process

The kinetic energy of the Auger electron can now be applied to the identification of elements, as it is only dependent on the binding energies of electrons within the atom, and not on the energy of the incident radiation leading to the initial core hole. A typical AES spectrum then displays the electronic differentiation of the electron energy

distribution to yield a $dN(E)/dE$ curve. Another application of AES spectroscopy, depth profiling, consists of etching away layers of material by argon ion bombardment, thus enabling an incident electron beam focused on the Ar^+-bombarded area of the sample to generate Auger emission as a function of time and therefore depth. The depth profiling spectra recorded on ZnO are found in section 7.2.1.

7.1.2 Transmission Electron Microscopy

The cross-sections of two thin ZnO samples (20 nm) on n-GaAs (100) were studied by transmission electron microscopy[6]. Each sample was first thinned manually with 3M 1200 grit wet-and-dry paper for initial mechanical thinning, and then polished with Buehler Alpha Micropolish alumina paste of particle size 5 μm, 1 μm, and 0.5 μm consecutively. The next step consisted of gluing a copper grid to the sample, which was consequently degreased by boiling the sample in trichloroethylene (TCE), methanol, and ethanol. The sample was then rinsed in deionized water, and blown dry with nitrogen. While the copper grid covered one side of the sample, the other side was thinned further and polished in a similar fashion with alumina paste. The sample was again degreased, before undergoing argon ion milling in a Gatan precision ion polishing system, Model 691. The images were consequently taken with a Philips EM420 microscope operating at 120 kV.

7.2 Results

7.2.1 Substrate temperature

Figure 7.2 shows the variation of the 12 K photoluminescence spectra with growth temperature. The spectra have been offset for clarity. The spectra of T300 and T400 are dominated by a broad, defect-related blue-violet band, which is absent in T450, T500, and T600; raising the growth temperature means enough thermal energy is available for the adatoms to move to stable sites, and for impurities to relocate to grain boundaries. Furthermore, this improvement in mosaic structure will impact the formation of defects such as dislocations, vacancies, and interstitials in the crystal lattice, thus reducing the defect density inside the ZnO columns. As a result, the blue-violet band disappears. This

---

[6] The author is indebted to Kate Van Someren and Dr Pearl Berndt for the TEM work.

defect-related band may be due to the generation of Zn vacancies (V_{Zn}) from incomplete gas phase reactions at low growth temperatures; indeed, a violet band attributed to the recombination of a delocalized electron close to the conduction band with a deeply trapped hole in a V_{Zn}^{-} center has previously been observed on samples deposited by pulsed laser deposition (Wu *et al.*, 2001).
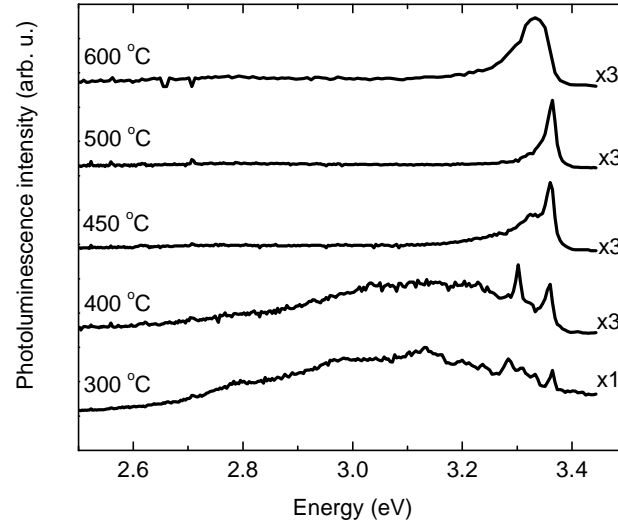
Figure 7.2: **Variation of 12 K photoluminescence spectra with growth temperature for ZnO thin films deposited at a VI:II ratio during growth of 18:1**

The effect of the enhanced adatom migration is also mirrored in the structural properties of the samples. First of all, a considerable improvement in surface coverage is observed when raising the substrate temperature from 300 to 450 °C (figure 7.3).
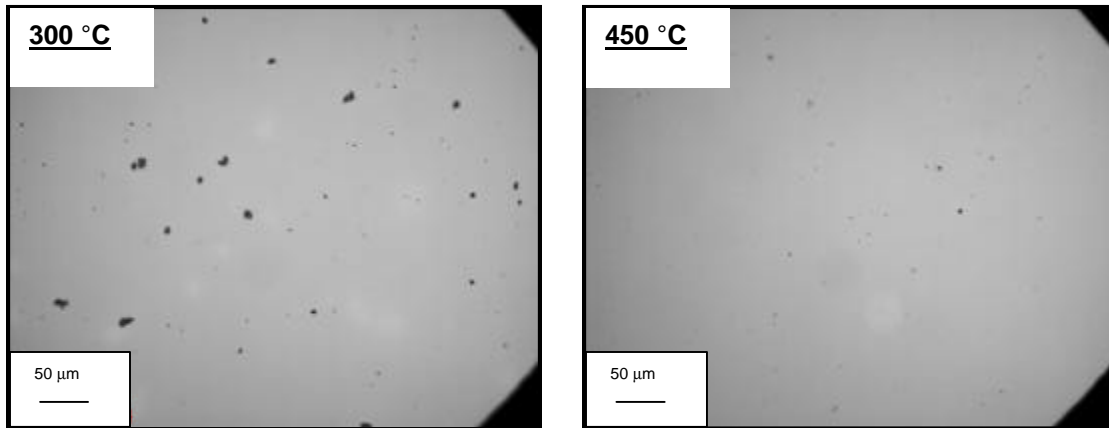
Figure 7.3: Optical microscopy images of ZnO samples T300 and T450

The surfaces of the ZnO samples grown on GaAs appear much smoother than the surfaces of the ZnO layers on Si (see section 5.2.6). This can be explained by the difference in substrate and by the fact that the ZnO thin films on GaAs are much thinner than the layers on Si.

Furthermore, X-ray diffraction revealed T300 to be amorphous, while T450 displayed a (002) peak at a 2θ angle of 34.81 °. Scherrer's formula (equation 5.6) yields a grain size value of 29 nm for T450. For the sake of comparison, Bang *et al.* (2003) reported a FWHM of ~ 0.35 ° for growth temperatures up to 450 ºC; the FWHM of the (002) peak of T450 was 0.30 °, an improvement compared to Bang *et al.*'s thin films.

The PL spectra of T450 and T500 at 12 K show two near-band edge (NBE) emissions at 3.36 eV and 3.32 eV. The former is due to a donor-bound exciton (D°X), while the precise nature of the latter is unknown at this stage; this emission could correspond to the DAP peak observed on samples deposited on *n*-Si 2 ° off (100) (see section 8.3.1). Furthermore, the large full-width at half-maximum of the NBE emission of T600 (80 meV) is indicative of increased defect concentration compared to T450 and T500 (30 and 25 meV, respectively). In order to assess the nature of these defects, Auger depth profiling was performed on thin samples (20 nm) grown under the same conditions as T450 and T600 (figure 7.4).
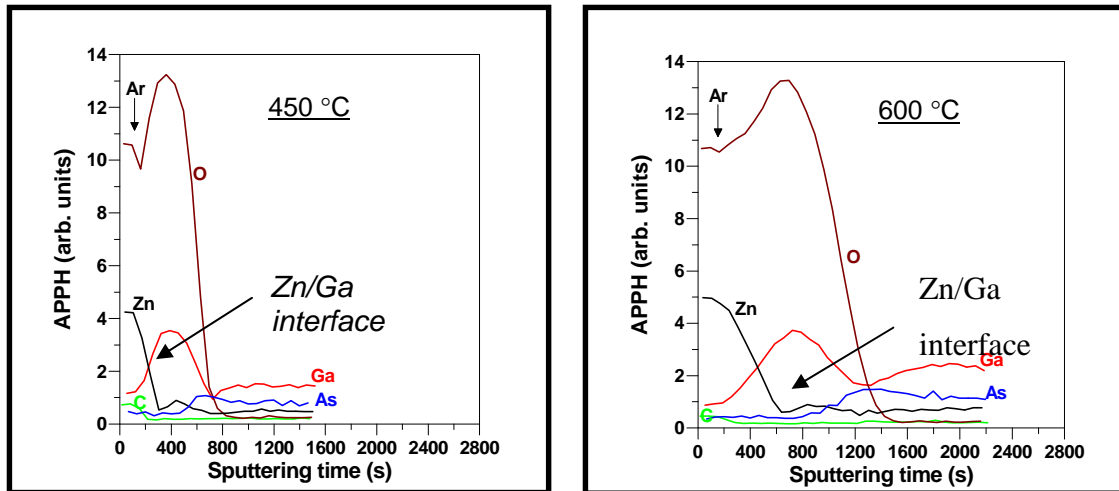
**Figure 7.4: Auger depth profiling of samples grown on
n-GaAs (100) at 450 and 600 °C**

The Zn/Ga interface, shown at the point where the Zn and O traces meet, is seen to significantly broaden as the temperature increases from 450 to 600 °C. Ga atoms are known to form shallow donors in the ZnO bandgap, and generate local strain and point defects in the crystal lattice (Ko *et al.*, 2000a). Additionally, at high Ga concentrations, impurity clusters or impurity-defect complexes may diminish the radiative efficiency of the samples (Swaminathan and Macrander, 1991). The broadening of the Zn/Ga interface may therefore account in part for the large FWHM of the NBE emission of T600.

Another element of answer explaining the large width of the NBE emission of T600 may come from the morphology study of T600 (figure 7.5). T600 displays non-uniform surface coverage compared to T450 and T500; this may be explained by the desorption of oxygen atoms at high growth temperatures.
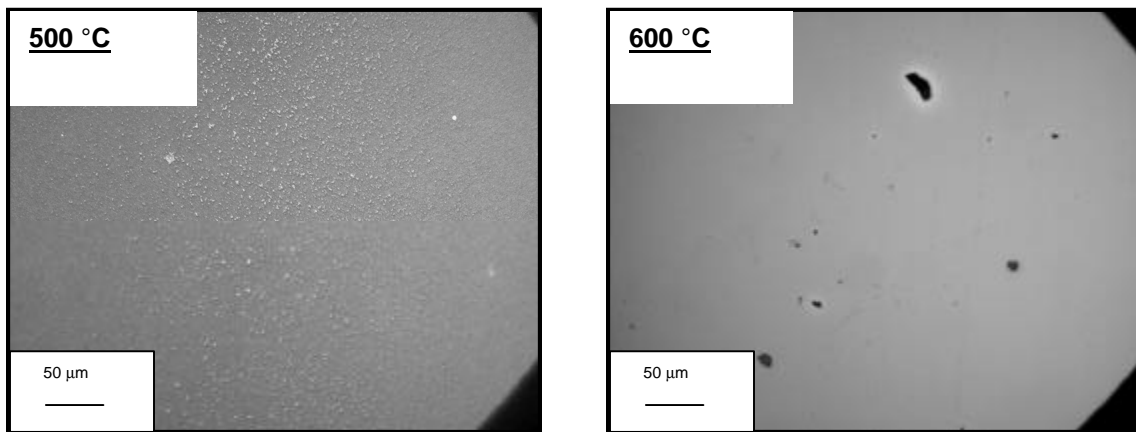
Figure 7.5: Optical microscopy images of ZnO samples T500 and T600

The energy-dispersive X-ray spectroscopy spectra of T500 and T600. were recorded in order to test this hypothesis. The quantification of the elements by atomic fraction clearly highlights a lower oxygen-to-zinc content in T600 (O : Zn = 3.3) compared to T500 (O : Zn = 5.4) (table 7.1). It should be mentioned, however, that the EDS spectra do not directly yield the film stoichiometry in this case. Indeed, if a few weight percent of a light element like oxygen is present in the sample, X-rays may be absorbed within the layer, and may not be detected. The element quantification by EDS therefore serves to compare

the oxygen-to-zinc ratio in the samples, not to give a quantitative analysis of the amount of zinc and oxygen in the films. The reader is referred to Williams and Carter (1996) for a detailed look at the statistics of energy-dispersive X-ray spectroscopy.

T500	Element	Weight fraction (%)	Atomic fraction (%)	T600	Element	Weight fraction (%)	Atomic fraction (%)
	O K	4.1	16.2		O K	2.3	9.6
	ZnL	3.1	3.0		ZnL	2.9	2.9
	GaL	44.9	40.6		GaL	44.5	42.6
	AsL	47.9	40.3		AsL	50.3	44.8

Table 7.1: EDS element quantification of ZnO layers T500 and T600 grown on _n_-GaAs (100) at a VI:II ratio during growth of 18:1

These additional defects are likely to lessen the optical quality of T600 compared to T450 and T500, and trigger a larger line width.

Having explained the difference in band width at different substrate temperatures, it should be mentioned that the width of the NBE peaks of the samples grown at 450 and 500 °C on semi-insulating _n_-GaAs (100) substrates (30 and 25 meV) are much larger than what is recorded for a sample deposited in similar conditions but at a slightly lower temperature, 425 °C, on _n_-Si 2 ° off (100) (7 meV). While the difference in growth temperature may partly explain this discrepancy, the larger line widths of the samples deposited on GaAs are believed to reflect the large lattice and thermal expansion mismatch of the ZnO/GaAs system compared to the ZnO/Si structure (see section 3.4). Having said that, the NBE peaks observed in this study are still much wider than what Ryu _et al._ (2000b) reported for their ZnO thin films deposited by pulsed laser deposition between 300 and 450 °C on GaAs. They reported bound exciton widths of less than 5 meV at 20 K. Furthermore, Second Harmonic Generation Imaging of ZnO samples deposited on GaAs in this work (see section 4.3.3) revealed the presence of amorphous

particles on the surfaces. These particles were absent on samples deposited on Si. These amorphous particles may further reduce the quality of the ZnO on GaAs layers compared to the ZnO on Si system.

7.2.2 VI:II ratio during growth

Figure 7.6 depicts the variation of the 12 K photoluminescence spectra with VI:II ratio during growth.
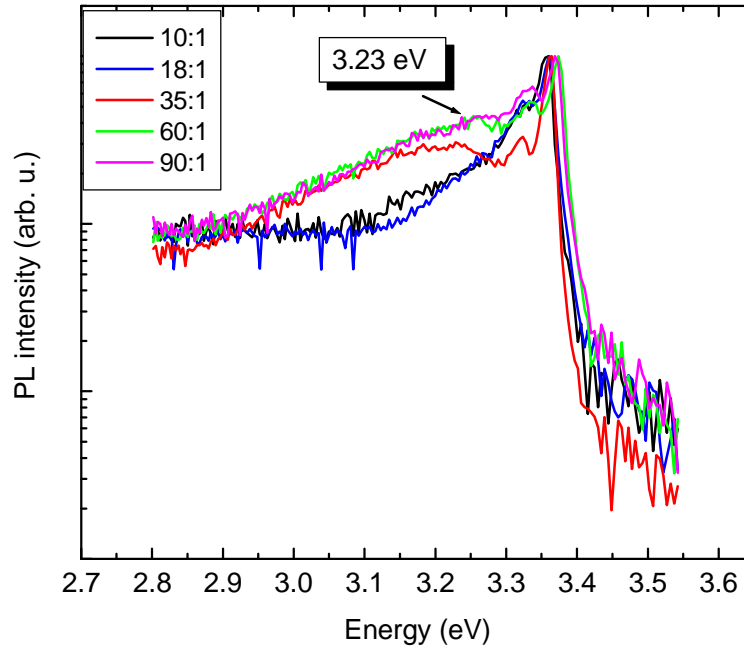
Figure 7.6: Variation of 12 K photoluminescence spectra with VI:II ratio during growth for ZnO thin films grown at 450 °C

They all display the prevailing D°X peak at 3.36 eV. Nevertheless, a major change is observed as the VI:II ratio during growth increases from 10 to 90:1. Indeed, we witness the appearance of a prominent emission band at 3.23 eV, which may be the donor-acceptor pair observed at 20 K in *p*-type ZnO on GaAs (Ryu *et al.*, 2000a). In other words, it seems that ZnO thin films begin to display a PL feature typical of *p*-type ZnO as the VI:II ratio during growth increases. As discussed in chapter 6, raising the VI:II ratio during growth from 10 to 60:1 leads to a reduction in the concentration of oxygen vacancies in the samples and a decrease in carrier concentration of two orders of

magnitude; oxygen vacancies acting as donors, these measurements seem to confirm that the *n*-type conductivity of ZnO is in part linked to the concentration of oxygen vacancies in the sample. While samples deposited at high VI:II ratios display a PL band characteristic of *p*-type ZnO at 12 K, their PL spectra are still dominated by the donor-bound exciton peak at 3.36 eV and Hall measurements reveal that layers deposited on *n*-GaAs (100) exhibit *n*-type conductivity.

Furthermore, the variation of the surface morphology with VI:II ratio of the samples deposited on *n*-GaAs (100) seems to reflect the presence of oxygen vacancies and other oxygen-related defects in ZnO (figure 7.7).
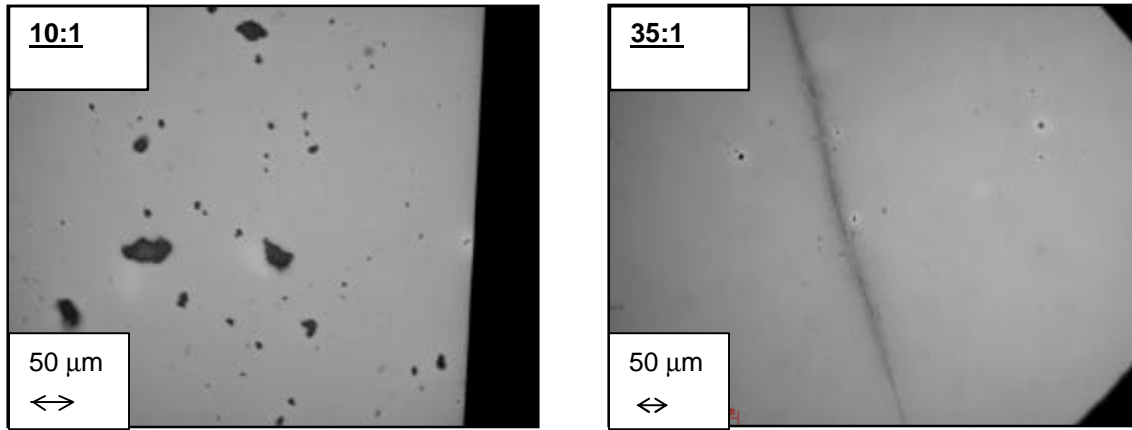
Figure 7.7: **Optical micrographs of ZnO samples S10 and S35, grown at 450 °C on *n*-GaAs (100) substrates; S10 shows incomplete surface coverage, while S35 exhibits the presence of microcracks**

A high concentration of oxygen vacancies at low VI:II ratios (10:1) is responsible for poor surface coverage, while choosing a VI:II ratio higher than 35:1 will lead to the formation of microcracks in the layers. A ratio of 18:1 brings about the optimum surface coverage (figure 7.3), and the VI:II ratio of 18:1 appears to be a transition ratio in this system.

Another intriguing observation can be made from figure 7.6. While the NBE emissions of samples S10, S18, and S35 peak at 3.36 eV, the NBE bands of samples S60 and S90 are

centered at 3.37 eV. Zhang *et al.* (2004) have reported a PL emission shoulder situated at 3.37 eV at 10 K; they attributed it to the A-free exciton. It was shown in chapter 6 that high VI:II ratios during growth cause the densities of residual donors such as oxygen vacancies and zinc interstitials to decrease. This in turn will induce a decrease in carrier concentration. It may be that while the large donor concentrations at low VI:II ratios inhibit free exciton recombination, the lower donor concentrations at VI:II ratios of 35, 60, and 90:1 may improve the optical purity of the samples to the point where free exciton recombination can even be detected at 12 K. Having said that, free exciton emission at low temperatures appeared as a shoulder in Zhang *et al.*'s thin films, rather than a dominant peak. Furthermore, it was shown in section 6.3.1 that the Urbach tail E_0 parameters of layers deposited on glass at ratios of 35 and 60:1 were considerably larger then the E_0 parameter of the sample grown at a ratio of 18:1, highlighting the presence of additional defects at high VI:II ratios. Further work is required to interpret the shift in peak position observed in figure 7.6.

7.2.3 Post-deposition annealing

Thermal annealing of thin films is a helpful method known to improve the quality of epitaxial layers, and several reports have documented the impact of post-deposition annealing on sample properties. Ogata *et al.* (2000), for example, reported that annealing their MBE-grown ZnO samples in O_2 at temperatures lower than the growth temperature (780 °C in their case) reduced the electron carrier density by an order of magnitude, from $2.4 \bullet 10^{18}$ to $2.5 \bullet 10^{17}$ cm^{-3}. They attributed this result to a decreasing concentration of residual donors. This result can be paralleled to work presented in chapter 6 of this thesis, where increasing the VI:II ratio during growth from 10 to 60:1, thereby decreasing the concentration of oxygen vacancies, led to a reduction in carrier concentration of over two orders of magnitude. Furthermore, Uesugia *et al.* (1997) reported that thermal treatment of their ZnSe on GaAs samples displayed improved, flat surfaces after thermal treatment. This is believed to stem from enhanced migration of atoms on the surface as a result of post-deposition annealing (Ogata *et al.*, 2002). On the other hand, this study focuses on the influence of post-deposition annealing on the photoluminescence properties of the ZnO epilayers.

Figure 7.8 shows the 12 and 300 K PL spectra of a sample grown at 500 °C, before and after annealing for 45 minutes at 600 °C in argon. The growth time of this sample was 180 minutes as opposed to 45 minutes for all the other samples studied in this chapter. The increased growth time was implemented in an effort to enhance the diffusion of As atoms from the GaAs substrate into the epilayer. This diffusion process is believed to occur at substrate temperatures equal to or higher than 450 °C (Ryu *et al.*, 2000b).

At 12 K, the spectra show a five-fold increase in emission intensity after annealing. The luminescence efficiency h is dependent on the probability of radiative (W_R) and nonradiative (W_{NR}) transitions taking place, according to (Ni *et al.*, 2001)

$$h = W_R/(W_{R+}W_{NR}) \qquad\qquad …(7.1)$$

Annealing is likely to reduce the number of lattice and surface defects responsible for nonradiative centers, thus inducing restructuring of the crystal lattice. As a result, W_{NR} falls, and h rises.

Annealing also leads to an increase in the relative intensity of the peak located at 3.31 eV compared to the D°X peak at 12 K. The 3.31 eV emission is likely to be the acceptor-bound exciton (A°X) recorded in *p*-type ZnO on GaAs, as annealing is believed to generate the diffusion of As acceptor levels from the substrate into the epilayer (Ryu *et al.*, 2000a).

Additionally, annealing also induces the surge of an emission band at approximately 3.22 eV, which may correspond to the DAP band in *p*-type ZnO mentioned earlier. The 3.31-eV peak did not feature strongly in T500 (figure 7.2). This may be because the growth time of T500 was only 45 minutes, compared to 180 minutes for this sample; the low growth time of T500 may explain why few As atoms diffused into its epilayer.
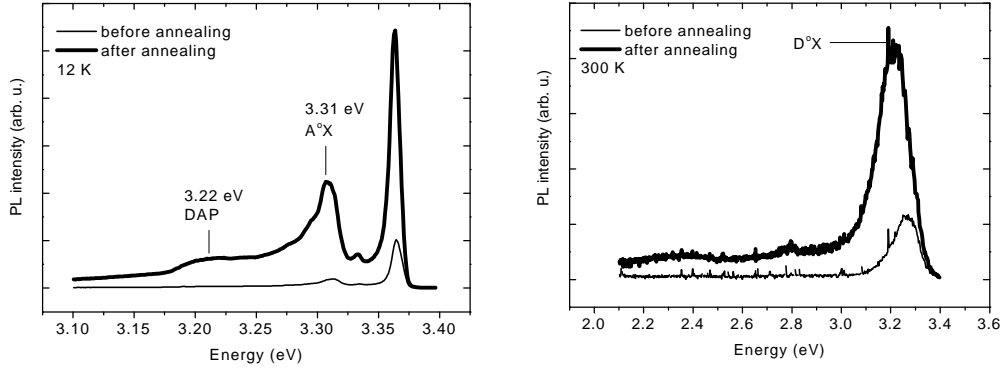
Figure 7.8: **12 K and 300 K photoluminescence spectra before and after annealing, for ZnO layer grown on *n*-GaAs (100) at 450 °C at a VI:II ratio during growth of 18:1**

The 300 K spectrum of the non-annealed sample displays a single NBE emission band at 3.27 eV. This band has also been observed by Bang *et al.* (2003) for their ZnO samples on GaAs substrates, and has been attributed to a donor-bound exciton (D°X). It should be mentioned that their MOCVD-grown samples only displayed weak NBE emission at a growth temperature of 500 °C; the NBE band only became prominent at growth temperatures greater than 600 °C. A couple of additional points need to be raised.

First of all, the position of the D°X peak at 300 K shifts from 3.27 to 3.22 eV after annealing. This is probably linked to a change in band gap induced by quantum confinement. The band gap is given by

$$E_g \approx E_{g0} + h^2\pi^2 m_{eff}/D^2 - 1.8e^2/\varepsilon D \qquad \qquad \textbf{...(7.2)}$$

where E_{g0} is the bandgap of bulk ZnO, *D* the particle size, $1/m_{eff} = 1/m_e + 1/m_h$ (m_e and m_h corresponding to the electron and hole effective masses), and ***e*** zinc oxide's dielectric constant (Ni *et al.*, 2001). Attempts to record XRD spectra on this sample were unfruitful, so it was decided to grow layers in identical conditions on *c*-plane sapphire to measure an eventual change in grain size after annealing. An increase in grain size of 14 meV was measured after annealing (*D* jumped from 22 to 36 nm) nm; this would lead to a decrease

125

in band gap energy of 65 meV according to equation 7.2. This is fairly close to the 50-meV-shift in D°X peak position observed in the ZnO on *n*-GaAs (100) sample.

Secondly, the optical quality of a thin film can be gauged by the full-width at half-maximum of the D°X peak, as well as by the intensity ratio between the NBE and the deep level (DL) bands (see section 8.3.3). The precise nature of the deep level band is still subject to discussion, even though researchers agree it is associated with defects in the material (see section 8.3.3). The FWHM of the D°X peak is seen to increase from 128 to 148 meV after annealing; the I_{UV}:I_{DL} ratio remained practically constant at 13:1 after treatment. The larger FWHM of the D°X peak may reflect the diffusion of As atoms induced by annealing previously discussed. Bang *et al.* (2003) reported the FWHM of the D°X for ZnO samples deposited between 600 and 720 °C. The NBE emission at 600 °C was 126 meV, close to the FWHM of the sample investigated here (128 meV). The FWHM then saturated at 117 meV for the thin films grown at higher temperatures. The fact that films of similar optical quality are obtained in this study at lower growth temperatures is encouraging, as high growth temperatures are known to generate poor epilayer surfaces as a result of film desorption and sintering type coalescence (see section 5.2.6). The main difference between the system used by Bang *et al.* and the one employed here is the choice of precursors: Bang *et al.* worked with oxygen gas (O_2), while TBOH was selected by the author for this study. This further confirms the quality of TBOH as oxidizing agent for the MOCVD growth of ZnO. Kumano *et al.* (2000) reported a room temperature full-width at half-maximum of 120 meV for their samples deposited on GaAs substrates by molecular beam epitaxy. This further confirms the high optical quality of the samples deposited in this project.

Having investigated the influence of annealing on the room temperature photoluminescence properties of the layers, let us turn our attention briefly to the electrical properties of the samples. It was found indispensable to anneal the In ohmic contacts in order to measure the Hall voltage of the samples. Indeed, the contact resistance exceeded 50 kΩ before annealing. Annealed samples, on the other hand, display *n*-type conductivity with carrier concentrations of the order of 10^{18} cm^{-3}, in

harmony with Bang *et al.*'s measurements (Bang *et al.*, 2003). Having said that, Hwang *et al.* (2003) reported that annealing their samples at 600 °C in vacuum led to *p*-type ZnO as a result of As diffusion from the GaAs substrate. The difference in conductivity between their samples and the ones studied here seems to lie in the annealing ambient.

A maximum room temperature mobility of 7 cm^2/Vs on annealed material was recorded here at a growth temperature of 450 ºC. The same sample had a resistivity of 0.7 Ωcm. At the same growth temperature, the mobility reported by Bang *et al.* was approximately 20 cm^2/Vs.

7.2.4 TBOH purity, low-temperature buffer layer

This first section deals with the influence of *tert*-butanol purity on sample quality. A 2.4 μm thick layer was grown at 500 °C with 99.9 %-pure (3N) TBOH, as opposed to the electronic grade TBOH (6N) used so far. Like the layers deposited with 6N-TBOH (see figure 7.8), the 300 K photoluminescence spectrum of the 3N-layer is dominated by a D°X emission band, and displays weak deep level luminescence. Having said that, the 3N-sample showed a larger FWHM, 151 meV, compared to the sample deposited with electronic grade TBOH (128 meV). 3N-TBOH has a higher water content than electronic grade TBOH, and contains a higher percentage of metals such as Al and Cu; these impurities may be responsible for the larger FWHM. Nevertheless, 3N-TBOH presents itself as a cheap oxidizing agent for the MOCVD growth of ZnO and unlike other affordable sources such as H_2O or CO_2, it doesn't react violently with DEZn, thus foiling the formation of white precipitates on the reactor walls. Furthermore, as will be seen in chapter 9, layers deposited with 3N-TBOH on *c*-plane sapphire substrates are found electrically active, displaying reasonable mobility values.

Finally, the impact of a low-temperature buffer on sample quality was examined.
The oxidation of GaAs surfaces in the initial stages of growth is known to generate amorphous oxide layers because of the volatile nature of the associated arsenic oxides (Tarsa *et al.*, 1993). The latter inhibit the growth of the epitaxial ZnO layer, and introducing a ZnO buffer layer between the GaAs substrate and the ZnO thin film would

thwart the formation of these amorphous oxides. Furthermore, a ZnO buffer layer would also assist in accommodating the lattice mismatch between the GaAs substrate and the epilayer, which would result in less structural defects compared to an non-buffered sample. The introduction of a buffer layer has proven an efficient way to improve crystal quality in other systems as well; in the case of GaN for example, an AlN buffer layer has been shown to promote lateral growth of GaN, and supply nucleation sites with low orientation fluctuation (Amano *et al.*, 1988).

The approach here was to grow two samples, one with a buffer and another without, in order to compare their TEM cross-sectional images. The buffered sample was deposited following a two-step growth process. The *n*-GaAs (100) was first heated to 300 °C for ten minutes, after which a ~ 10 nm ZnO buffer layer was deposited. The substrate temperature was then increased to 450 °C, and allowed to stabilize at that temperature for another ten minutes. This *in-situ* anneal of the buffer layer should lead to optimal diffusion of the buffer layer on the substrate. A thin (~ 20 nm) ZnO layer was then grown at 450 °C on top of the ZnO buffer.

Figure 7.9 shows the TEM cross-sectional images of the buffered and non-buffered samples. The ZnO/GaAs interface of the non-buffered sample is seen to be uneven. Additionally, the substrate of the non-buffered film reveals the presence of etch pits absent in the buffered sample. It cannot at this stage be deduced whether these interface pits are empty or filled with material. In contrast, the buffered layer had a clean interface, and showed no sign of substrate pitting or erosion. The buffer layer also improved the adhesion properties of the layer compared to the non-buffered sample. Besides, the non-buffered layer shows evidence of a region of lesser electron transparency. It also seems to include a considerable concentration of planar defects, as well as randomly oriented crystallites. Quenching these defects may therefore sensibly enhance the optical properties of ZnO samples grown on GaAs. Indeed, the FWHM of the room temperature NBE emission band of thicker samples decreased from 151 to 139 meV after insertion of the buffer layer.

50 nm

No
buffer

50 nm

With
buffer
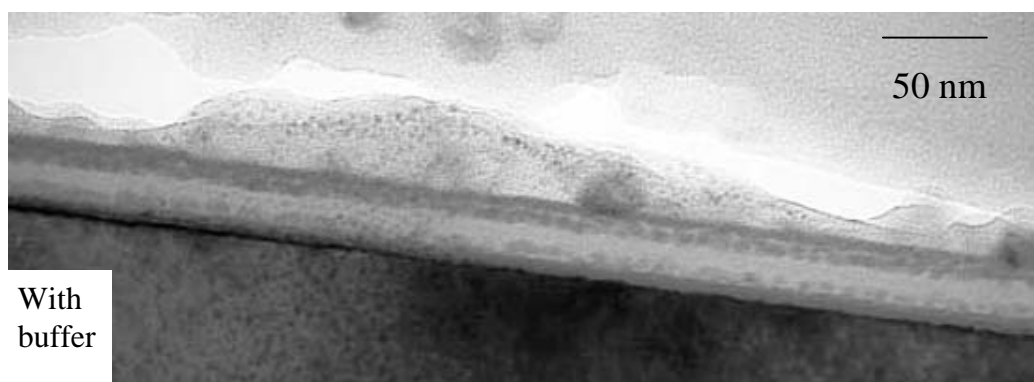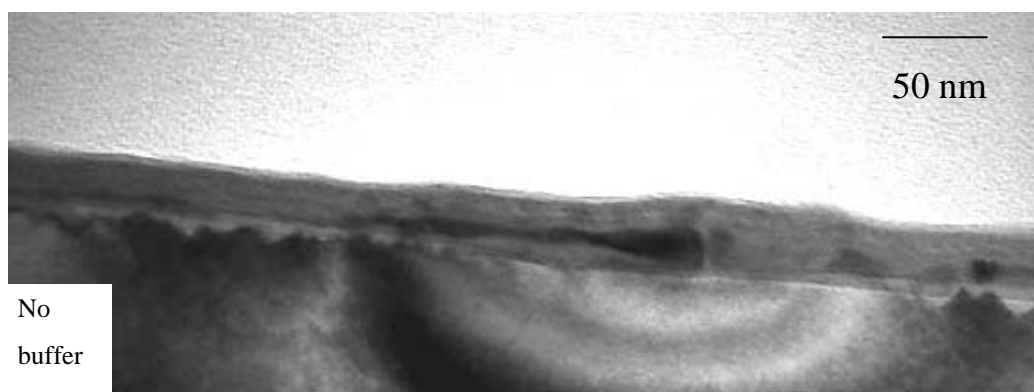
Figure 7.9: TEM images of non-buffered and buffered ZnO thin films
grown at 450 °C on *n*-GaAs (100) substrates

This study follows a publication by Yan *et al.* (2004), who studied the influence of a low-temperature buffer on the properties of samples deposited on Si (111) by plasma-assisted molecular beam epitaxy. They also reported a decrease in the FWHM of the room temperature ultraviolet band from 89 to 72 meV. Additionally, they noticed a difference in the origin of the UV band depending on the presence or absence of a buffer layer. The UV band of the non-buffered layer peaked at 3.277 eV, and was attributed to a bound exciton. The bound exciton only appeared as a shoulder at 3.270 eV in the buffered layer, and was overshadowed by free exciton emission at 3.310 eV. In other words, they found that the free exciton peak could only be observed in the buffered sample. This doesn't seem to be the case in the samples investigated here, as no additional peak or shoulder was observed on the buffered sample compared to the non-buffered layer.

7.3 Summary

ZnO thin films have been successfully grown on *n*-GaAs (100) substrates. The optical properties of the samples depended strongly on the substrate temperature and VI:II ratio during growth. Below 400 °C, the 12 K photoluminescence spectra were dominated by a broad, defect-related blue-violet band. From 450 to 600 °C, they showed a strong peak at 3.36 eV due to a donor-bound exciton. The large width of the excitonic emission of the sample deposited at 600 °C (80 meV) can be attributed to a broadening of the Zn/Ga interface at high substrate temperatures since Ga atoms are known to form shallow donor levels in the ZnO band gap, as well as to the desorption of oxygen at high growth temperatures. Samples deposited at 450 and 500 °C displayed FWHM values at 12 K of 30 and 25 meV, respectively.

Increasing the VI:II ratio during growth from 10 to 90:1 led to the surge of an emission band at 3.23 eV, which may be the DAP band reported for *p*-type ZnO on GaAs. This implies that increasing the VI:II ratio during growth causes ZnO thin films to display photoluminescence properties associated with *p*-type ZnO. This confirms the results obtained from the study of the influence of the VI:II ratio during growth on carrier concentration (section 6.3.1), which showed that the free electron concentration could be reduced by two orders of magnitude when increasing the VI:II ratio from 10 to 60:1.

A full-width at half-maximum of 128 meV for the dominating donor-bound exciton band at room temperature is reported, together with a $I_{UV}:I_{DL}$ ratio of 13:1.

The influence of post-deposition annealing on the films' photoluminescence properties was studied; annealing a ZnO sample at 600 °C for 45 minutes in argon increased the photoluminescence intensity by a factor of five, and led to an increase in FWHM of the UV band of 20 meV. It also generated a redshift in NBE emission peak of 65 meV, which was attributed to quantum-confinement-induced band gap narrowing.

Furthermore, it was indispensable to anneal the samples in order to measure a Hall voltage. Inversion of conductivity as a result of As diffusion was however not observed; annealed samples displayed *n*-type conductivity with a carrier concentration of the order of 10^{18} cm^{-3}. A maximum mobility of 7 cm^2/Vs was obtained.

The optical quality of samples deposited with 6N- and 3N- TBOH was studied. The FWHM of the UV band of the 3N layers displayed a larger FWHM (151 meV), which may reflect the higher water content and metal concentration in the 3N source. Having said that, the absence of the defect-related ZnO green band together with good electrical properties (chapter 9) leads to the conclusion that 3N-TBOH may be used as a cheap oxygen precursor for the MOCVD growth of TBOH.

Finally, the structural and optical properties of the samples could be improved by depositing an amorphous ZnO buffer layer under the main layer. The buffered layer studied exhibited an improved NBE full-width at half-maximum (139 meV) compared to the non-buffered sample. Furthermore, the buffer inhibited the formation of erosion pits, and led to improved adhesion properties.

8. OPTICAL CHARACTERIZATION OF ZnO EPILAYERS: VARIABLE TEMPERATURE PHOTOLUMINESCENCE MEASUREMENTS

In the light of the desire to use ZnO for opto-electronic devices, it is vital to assess the optical quality of the samples deposited in this work. The aims of this chapter are to report on the variable temperature photoluminescence (PL) properties of a ZnO thin film deposited on an *n*-Si 2 ° off (100) substrate, compare the nature of the observed emission bands with other reports, and quantify the sample's purity at room temperature by measuring the intensity ratio between the ultraviolet near-band-edge emission and the defect-related ZnO green band. The chapter begins with a discussion of the theory of photoluminescence spectroscopy and a description of the experimental set-up. The results section comprises a discussion of the spectrum recorded at 12 K, a look at the thermal quenching behavior of the PL bands, and an analysis of the room temperature spectrum.

8.1   *Background Theory*

Photoluminescence spectroscopy is a non-destructive technique able to detect impurities that produce radiative recombination processes. When recording PL spectra, the sample studied is excited with an optical source, usually a laser whose energy $h\nu$ is higher than the semiconductor band gap E_g. This leads to the generation of electron-hole pairs (*ehp*) that recombine by one of several mechanisms. The energy of the photons emitted after excitation therefore depends on the nature of the recombination processes involved. Figure 8.1 schematically describes common radiative transitions observed by photoluminescence.
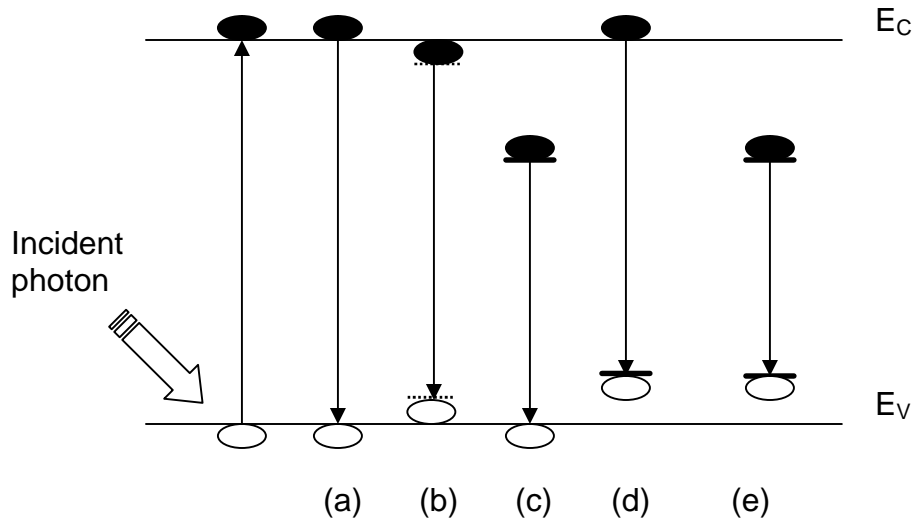
Figure 8.1: **Radiative transitions observed by photoluminescence spectroscopy (after Schroder, 1998)**

Band-to-band recombination, depicted in figure 8.1 (a), is the most frequently occurring process at room temperature; on the other hand, it rarely takes place at low temperatures in materials with small effective masses due to large electron orbital radii and thermal quenching effects. Excitonic recombination, (b), represents a bound electron-hole pair in a hydrogen like state. The *free exciton* (FX) has energy slightly less than the band gap energy required to generate a separated electron-hole pair. In fact, a photon emitted by free exciton (FX) recombination has energy

$$E = E_g - E_x \qquad\qquad \text{...(8.1)}$$

where E_x is the exciton binding energy (60 meV in the case of ZnO). Knowing the exciton binding energy enables one to accurately determine the band gap from the energy of the free exciton recombination. In doing so, however, distinguishing free excitonic emission from other excitonic or impurity-related lines is crucial. Furthermore, a free hole can combine with a neutral donor to form a positively charged excitonic ion, or *donor-bound exciton* (D°X*)*, as illustrated in figure 8.1 (c). Similarly, a free electron can combine with a hole on a neutral acceptor to form an *acceptor-bound exciton*, A°X (d).

132

Finally, an electron on a neutral donor can recombine with a hole on a neutral acceptor; this is called donor-acceptor pair recombination (DAP), and is illustrated in figure 8.1 (e).

The Coulombic interaction between donors and acceptors results in the modification of the DAP emission line energy E, and

$$E = E_g - (E_A + E_D) + q^2 / \pmb{e}\pmb{e}_0 r$$

where r is the distance between donor and acceptor, and $\pmb{e}$ the dielectric constant of the material. Thus, for higher concentrations of impurities, r will decrease and the DAP transition will shift to higher energies.

8.2 Experimental procedure

The PL spectra presented in this work were recorded on a scanning PL system schematically depicted in figure 8.2. The system employs a closed cycle cryostat, permitting measurements from 4.2 to 300 K. The samples investigated are fastened to the sample holder in the cryostat with vacuum grease, and are excited by the 3250 Å line of a HeCd laser. The laser beam passes through a filter, and is then subjected to a chopper. The beam is consequently focused perpendicularly onto the sample surface after being reflected off a variable position mirror. The mirror is linked to an x-y motion controller, making it possible to position the laser anywhere on the sample surface. The emitted luminescence then backtracks the signal up to the position mirror where it is deflected. It then passes through a high pass filter that removes the reflected laser beam. The photoluminescence is dispersed by a 0.5 m SPEX 1870 spectrometer, and detected by a water-cooled photomultiplier tube (PMT). The output from the detector is finally amplified by a lock-in amplifier interfaced to a computer where the PL spectrum is viewed and analyzed. The HeCd laser yielded a maximum power of 20 mW, which could be reduced by inserting optical density filters between the chopper and the position mirror.
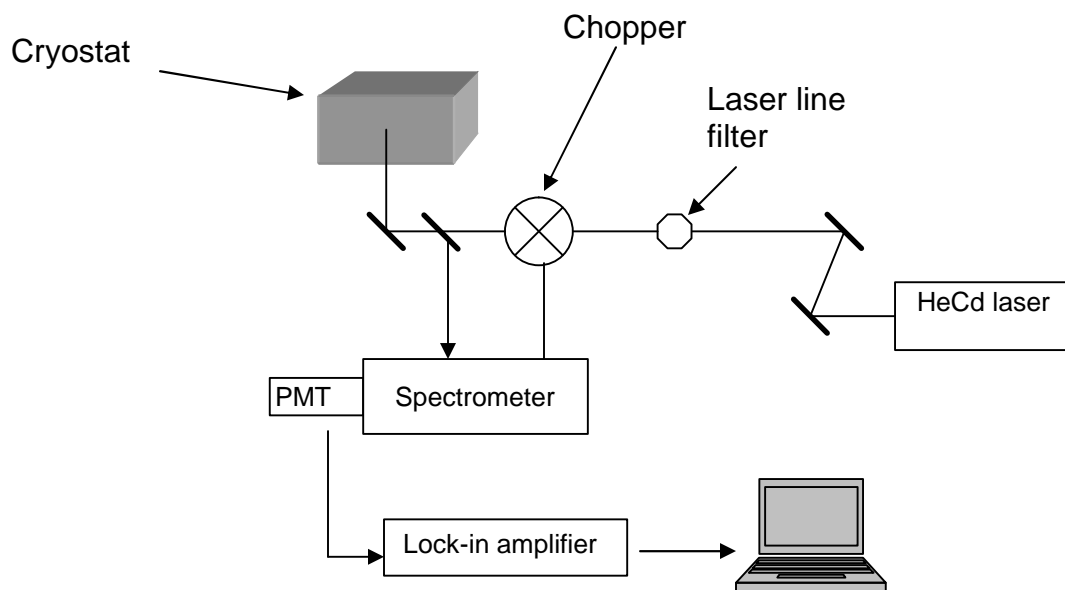
Figure 8.2: Experimental set-up for photoluminescence spectroscopy

8.3 Results

8.3.1 Peak identification

The sample investigated (Z425) was grown at 425 °C on an *n*-Si 2 ° off (100) substrate, and had a thickness of 4.4 μm; it was one of the thin films deposited in the study of the influence of substrate temperature on the structural properties of ZnO, and was grown following the procedure outlined in chapter 5.

Figure 8.3 shows the 12 K photoluminescence spectrum of Z425. The spectrum consists of four distinct emission bands at 3.36, 3.32, 3.25, and 3.17 eV. The 3.36 eV emission band is commonly observed in ZnO epilayers, and is attributed to a neutral donor-bound exciton (D°X). A group of donor-bound excitons around 3.36 eV has been previously reported (Reynolds *et al.*, 1998). These D°X lines are believed to represent impurity or defect pairs of different separations or orientations. The intriguing thing mentioned by Reynolds *et al.* is that when annealed in Ar or air at 800 ºC or above, all of the D°X lines seem to merge into one line at 3.357 eV. This line may represent the isolated impurity or

134

defect. The 3.36 eV line has been extensively studied in the literature, and has been labeled I_4. It has also been reported in a different study that the I_4 emission at 3.363 eV is greatly dampened when the sample is annealed at 600 °C, the temperature at which hydrogen is known to leave the lattice (Look, 2003). The I_4 emission can also be restored by exposure to hydrogen plasma (Strhemechny *et al.*, 2003), which suggests that I_4 corresponds to an exciton bound to a hydrogen donor. Furthermore, Hofmann *et al.* (2002) reported that this hydrogen donor level is located 35 meV below the conduction band minimum. On the other hand, Look *et al.* (1999) reported the presence of a zinc interstitial donor level (Zn_i) at approximately the same energy. The identity of the donor level involved in the I_4 emission therefore remains unknown.
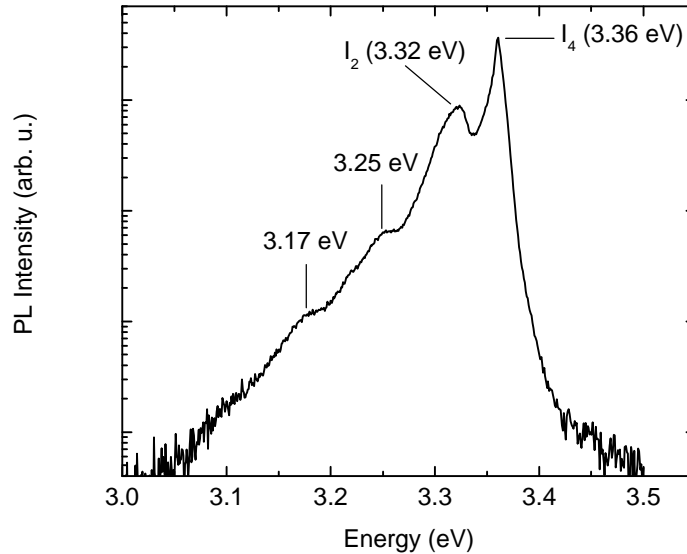
Figure 8.3: 12 K photoluminescence spectrum of Z425

Furthermore, the nature of the 3.32 eV peak (also named I_2) remains controversial. It has been detected in high quality ZnO epitaxial films (Ko *et al.*, 2000c; Yamamoto *et al.*, 2001), nano-crystalline thin films (Zhang *et al.*, 2001), and ZnO rods (Zhang *et al.*, 2003). Different recombination channels have been suggested for this band. It has mostly been attributed to the LO phonon replica of the free exciton (Ko *et al.*, 2000c; Yamamoto *et al.*, 2001), but it has also been reported that neutral acceptor-bound exciton (A°X) emission may be found in that spectral range (Look *et al.*, 2002; Chen and Fujita, 2002).

Wang and co-workers (2002), in contrast, have labeled it a donor-acceptor pair. The first step in establishing the origin of the 3.32 eV emission at 12 K in Z425 is to study the laser dependence of the peak position (figure 8.4).
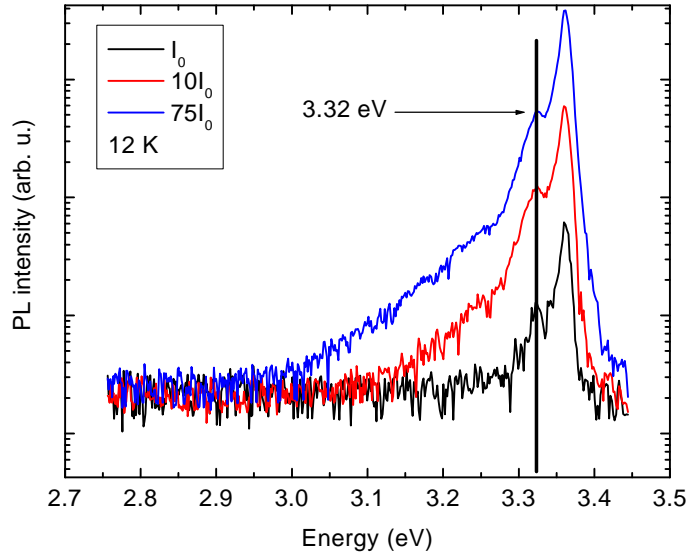
Figure 8.4: Laser dependence of 3.32 eV emission band for ZnO thin film on *n*-Si 2 ° off (100)

The laser power was varied over practically two orders of magnitude, and the position of the 3.32 eV peak is found to be independent of laser power. This would indicate that the band is not a donor-acceptor pair. Indeed, it has been shown for heavily-doped material that the peak energy w_p of the DAP band is blueshifted with increasing laser intensity I_{ex} following the exponential relationship $I_{ex} \propto \exp(w_p/b)$, where b is a parameter dependent on the film's compensation ratio (Yu, 1977). This dependence can be traced to a random distribution of the impurity potential, which induces the formation of potential wells of energy $\sim b$ linked to the impurity-occupied lattice sites. As a result, electron-hole pairs localized in these wells recombine through nearby impurity site tunneling. These wells become increasingly saturated as I_{ex} rises, and the DAP luminescence shifts to higher energies. Having said that, the peak shift may be fairly minute; Ursaki *et al.* (2004) for example reported an upward shift of 4 meV per laser power order of magnitude. Considering that an error of ± 2 meV is associated with the assessment of peak position in this system, further studies are required to conclusively rule out the DAP option for

this band. In order to shed light on the matter, the temperature dependence of the 3.32 eV peak position was investigated (figure 8.5).
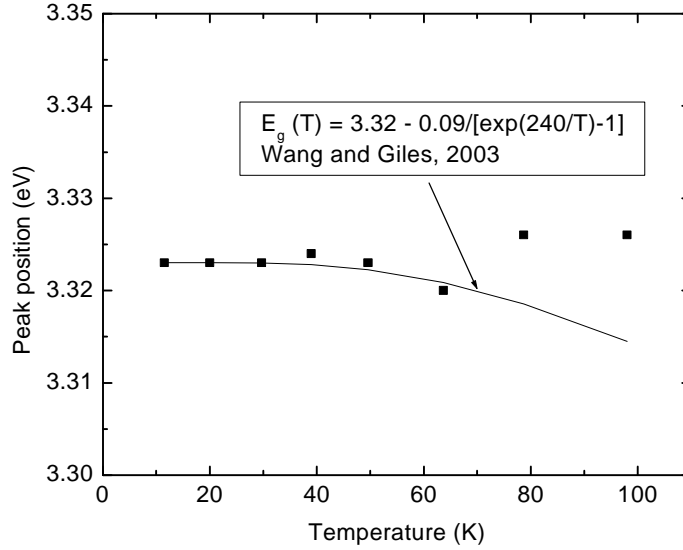
**Figure 8.5: Temperature dependence of 3.32 eV band
peak position**

The experimental data is fitted to the temperature dependence of the ZnO band gap obtained from Wang and Giles (2003). It is known that the band gap energy E_g of semiconductors decreases with increasing temperature. This red shift of the fundamental band gap energy is due to the combined effect of thermal lattice expansion and electron-phonon interactions (Allen and Cardona, 1981). Several expressions have been developed to model the temperature dependence of the band gap. Here, the following semi-empirical relationship is adopted:

$$E_g(T) = E_g(0) - \frac{a_{BE}q_{BE}}{\exp(q_{BE}/T)-1} \qquad \qquad \textbf{…(8.2)}$$

where $q_{BE} = \hbar\nu/k_B$ represents an effective phonon temperature, and a_{BE} the high-temperature slope of the E_g (T) curve (O'Donnel and Chen, 1991). The experimental data was fitted to Wang and Giles's curve (2003), with

$$E_g(T) = E_g(0) - \frac{0.09}{\exp(240/T)-1}$$
...(8.3)

The position of the 3.32 eV emission follows the temperature dependence of the band gap up to about 65 K; above 65 K the measured energy is higher than expected from the fit. This is typical of a donor-acceptor pair (DAP) band evolving towards a free electron-neutral acceptor eA^o due to donor ionization.

Furthermore, the variation of the difference in energy ΔE between the band gap energy and the peak position was plotted (figure 8.6). The 3.32 eV emission is seen to move towards the band gap with increasing temperature at a rate of approach of 1.43kT, which is close to the expected value of 2kT for a DAP band (Eagles, 1960). This seems to indicate that the 3.32 eV emission is indeed due to a donor-acceptor pair, in agreement with Wang *et al.* (2003).
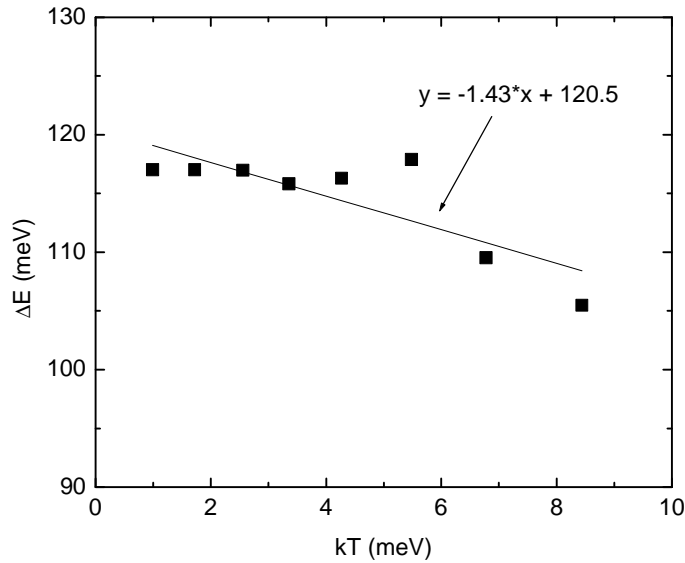
Figure 8.6: **Variation with temperature of energy difference between band gap and peak position**

Returning to figure 8.3, the remaining emission bands at 3.25 and 3.17 eV can safely be assigned to longitudinal optical (LO) phonon replica of the DAP band, as the energy difference between the DAP and each of them is respectively one and two times the

energy of the $A_1(LO)$ phonon in wurtzite ZnO (72 meV). These two emission bands therefore originate from first- and second-order Raman scattering (Ursaki *et al.*, 2004). Indeed, resonant Raman scattering from solids can be detected if the energy of the incoming or scattered photons matches real electronic states in the material; furthermore, multiphonon scattering processes have been reported for bulk ZnO (Scott, 1970), ZnO films (Zhang *et al.*, 2001), and ZnO nanowires (Ng *et al.*, 2003).

In order to more accurately characterize the donor and acceptor levels involved in these transitions, it is necessary to find out the energy of the band gap at low temperatures. This was achieved by studying the thermal quenching behavior of the lines.

8.3.2 Thermal quenching of emission bands

As the cryostat temperature rises, the $D^\circ X$ and DAP lines seen in figure 8.3 decrease in intensity and merge as a result of the thermal ionization of excitons and the thermal activation of nonradiative recombination mechanisms. In fact, the spectra show a single emission band from 125 K onwards (figure 8.7).
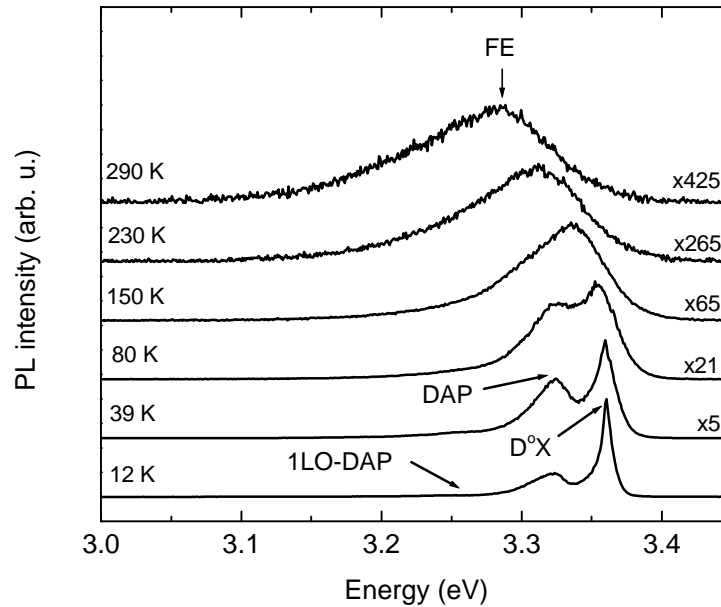
Figure 8.7: **Variable temperature PL spectra of ZnO sample Z425 grown on *n*-Si 2 ° off (100) at 425 °C**

In order to determine the nature of this single UV band, the variation of its intensity with temperature is investigated.

Under injection, the population governing a PL transition is linked to the following expression,

$$\frac{\partial n}{\partial t} = G - \frac{n}{t_R} - \frac{n}{t_{NR}} \qquad \qquad \text{...(8.4)}$$

where n is the density of the minority carrier or exciton concerned, G the generation rate, and t_R and t_{NR} radiative and nonradiative lifetimes (Leroux *et al.*, 1999). Nonradiative recombination rates tend to be thermally activated, whether they embody the depopulation of the level or the activation of a nonradiative recombination center. Nonradiative recombination rates can therefore be described by an Arrhenius-type equation,

$$t_{NR} = t_0 \exp(E_A / kT) \qquad \qquad \text{...(8.5)}$$

Under steady state, and because PL intensities are proportional to n / t_R, the variation of PL intensity I with temperature is given by

$$I(T) = \frac{I_0}{1 + A \exp(-E_A / kT)} \qquad \qquad \text{...(8.6)}$$

where I_0 is the PL intensity at 0 K, and A a constant equal to t_R / t_0. Figure 8.8 shows the thermal quenching of the intensity of the D°X line and of the single UV band. The fit yielded an activation energy of 57 ± 2 meV for the single UV band, which is close to the reported exciton binding energy of 60 meV (Look, 2001). The activation energy of the D°X band was found to be 7 ± 0.6 meV. The single UV band can therefore be assigned to

140

a free exciton. This free exciton was dominant all the way to room temperature, where it peaked at 3.29 eV.
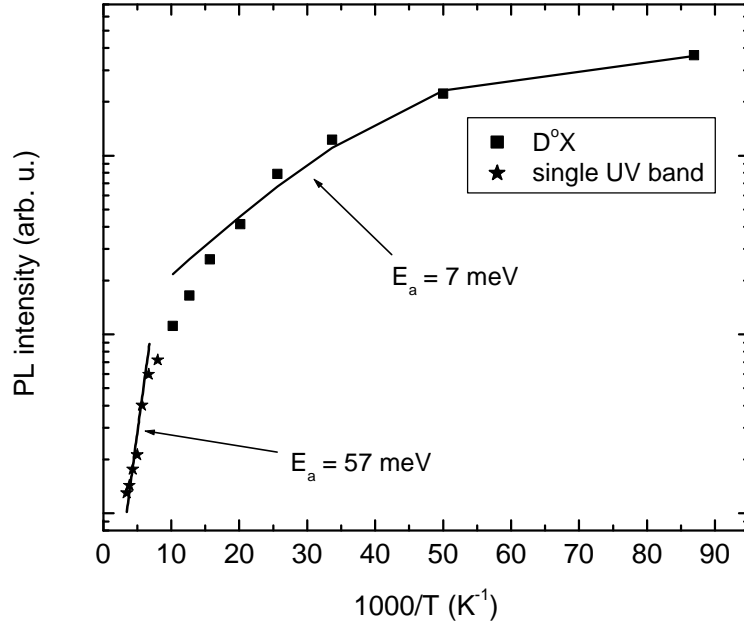
Figure 8.8: Thermal quenching of DX line and single UV band

With the experimentally determined binding energy of 57 meV, the room temperature band gap energy is given by equation 8.1, and equal to 3.35 eV. This is within the band gap range of 3.35 - 3.38 eV calculated on the samples deposited on fused silica (see section 6.4.4).

In order to verify that free exciton radiatiave recombination is the dominant origin of the observed luminescence at room temperature, the variation of PL intensity with excitation power was plotted (figure 8.9). The PL intensity is seen to be linearly dependent on the excitation power, with a slope of 0.98.

Recombination of free excitons can be described by

$$dx/dt = -\boldsymbol{g}_{radx}x - \boldsymbol{g}_{nrx}x \qquad\qquad ...(8.7)$$

141

where x is the exciton density, $\boldsymbol{g}_{radx}$ the radiative recombination rate, and $\boldsymbol{g}_{nrx}$ the nonradiative decay rate (Fouquet and Siegman, 1985).
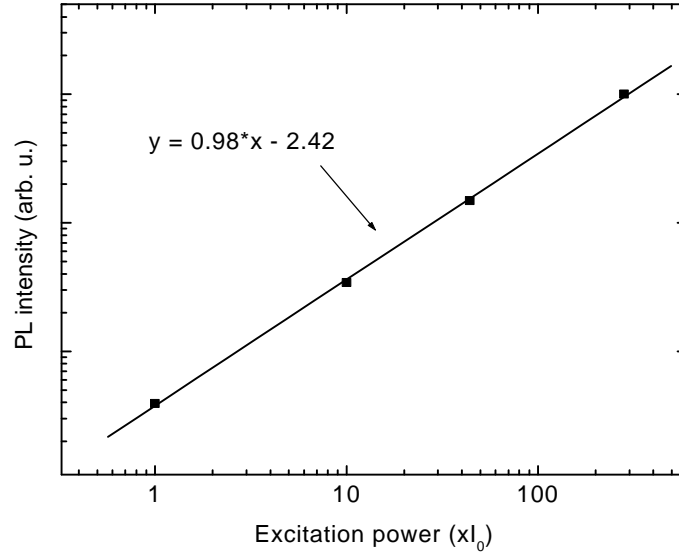
Figure 8.9: **Variation of room temperature FX (3.29 eV) emission intensity with excitation power**

The photon emission rate P is then given by

$$dP/dt = \boldsymbol{g}_{radx} x \qquad\qquad \text{...(8.8)}$$

and free exciton recombination exhibits exponential photoluminescence decay. Furthermore, Fouquet and Siegman showed that $P \propto I_{ex}$ for free exciton recombination; the measured slope of 0.98 ± 0.15 (log scale) for the PL intensity vs. laser power graph therefore confirms that free exciton emission is indeed the prevailing origin of the observed luminescence at room temperature. This is explained by the thermal stability of ZnO, which in turn is linked to its high exciton binding energy of 60 meV. If free carriers played an important role, the slope would approach 2, as $P \propto I_{ex}^2$ for free carrier bimolecular recombination.

The variation of the FX peak position with temperature (figure 8.10) was also found to follow the temperature dependence of the band gap as outlined by Wang and Giles (2003).
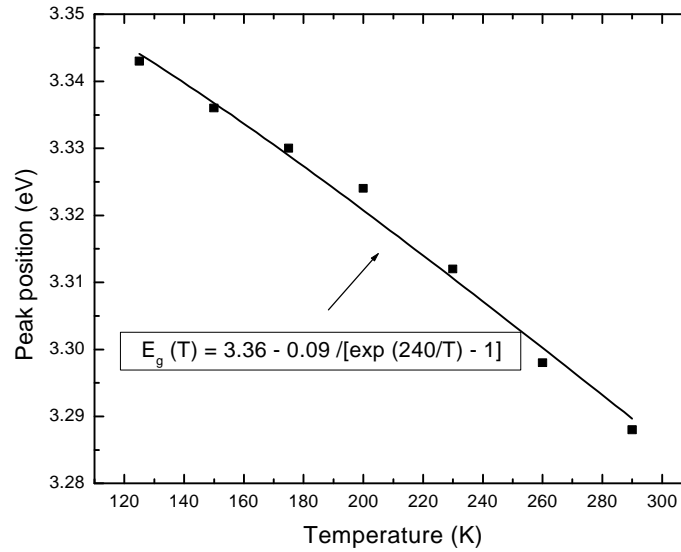
Figure 8.10: **Temperature dependence of FX peak position of ZnO sample Z425 grown on *n*-Si 2 ° off (100) at 425 °C**

The FX peak position values can now serve to obtain the band gap energy values throughout the temperature range. First of all, the band gap energy between 125 and 300 K is deduced from equation 8.1, taking the exciton binding energy to be 57 meV (figure 8.11).
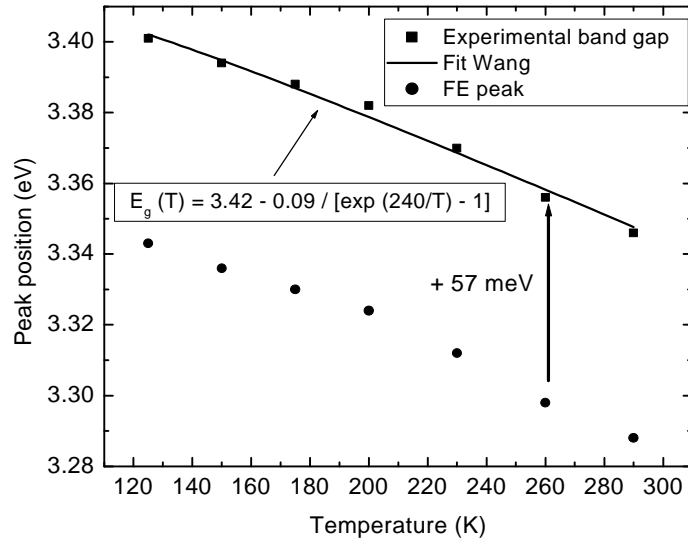
Figure 8.11: **Temperature dependence of FX peak position and of experimentally determined band gap of sample Z425**

It is then fitted to Wang and Giles's equation to obtain the band gap values at low temperatures (figure 8.12).
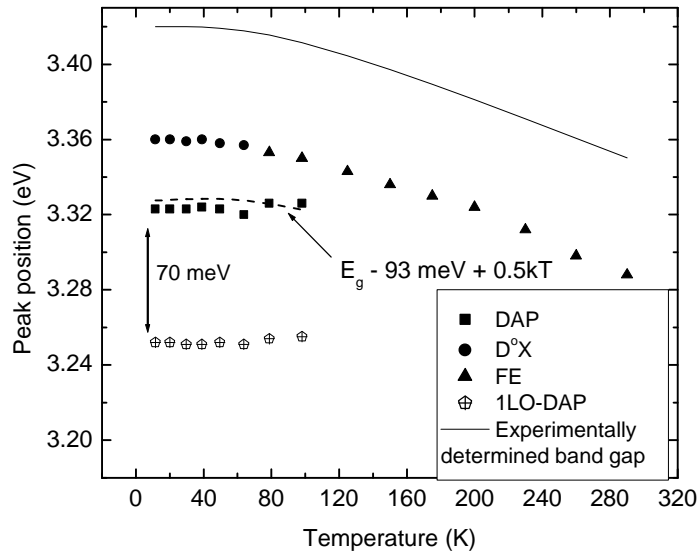
Figure 8.12: **Temperature dependence of D°X, DAP, 1LO-DAP, FX, and experimentally determined band gap**

Having studied the temperature dependence of the FX peak position between 125 and 300 K (figure 8.11), the fit of the temperature dependence of the FX peak position is extended to lower temperatures (figure 8.13). The fit is found to coincide within experimental error with the position of the dominant peak at 80 and 100 K. This means that the dominant peak observed at 80 and 100 K probably corresponds to the free exciton; it can thus be deduced that most shallow donors are ionized above 65 K. This is in agreement with the temperature dependence of the DAP peak position (figure 8.5), which implied that the DAP band had developed to a free electron-neutral acceptor complex above 65 K.
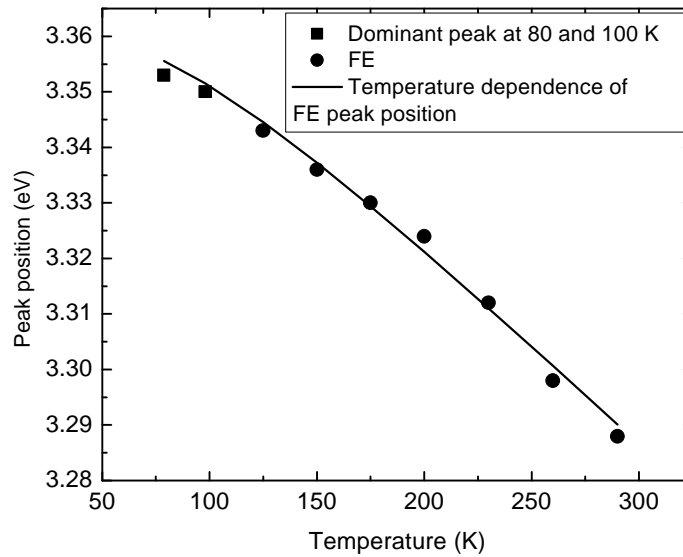
Figure 8.13: Nature of dominant emission band at 80 and 100 K

The depth of the acceptor can be estimated from the free electron-neutral acceptor data points at 80 and 100 K (figure 8.12). Knowing that a free-to-bound transition moves closer to the band edge with increasing temperature at a rate of kT/2 (Eagles, 1960), the acceptor depth is found to be 93 ± 2 meV. This is a reasonable value, knowing that the two shallow donors reported in the ZnO literature are found 30-40 and 60-70 meV below the conduction band (Look *et al.*, 2003). Both these donor levels should therefore be depleted before the acceptor level 93 meV above the valence band, and the emission

bands observed at 80 and 100 K are indeed due to a free exciton and a free electron-neutral acceptor complex.

8.3.3 Optical quality of sample

One of the reasons why photoluminescence spectroscopy is a powerful tool is the fact that it allows an accurate determination of the optical quality of a semiconductor thin film. Indeed, the optical purity of a material is, amongst other things, linked to the presence of band tails. The random distribution of charged impurities is known to result in potential fluctuations of the band edges. This causes the band edges to vary spatially, and states with energy below the unperturbed conduction band edge or above the unperturbed valence band edge are called tail states. These tail states considerably alter the density of states in the vicinity of the band edge (figure 8.14), and will lead to a broadening of PL peaks.
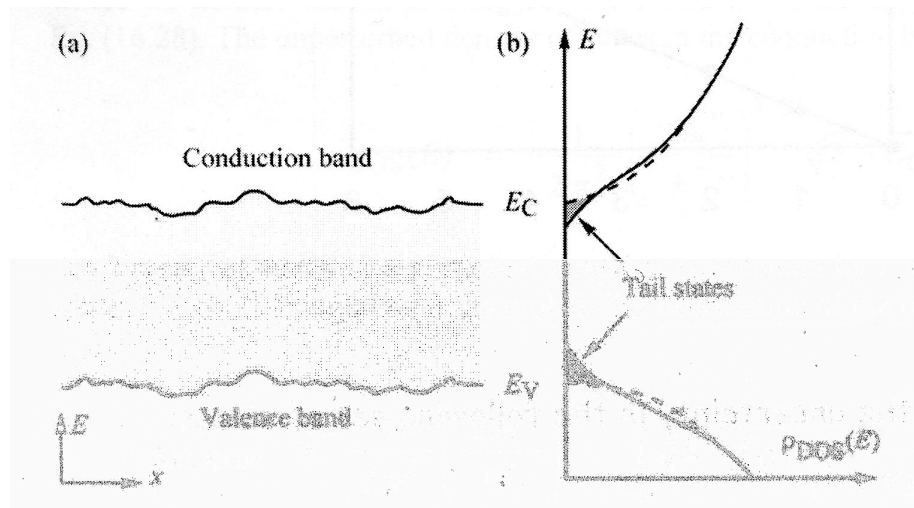
Figure 8.14: **(a) Spatially fluctuating band edges caused by random distribution of impurities (b) Resulting densities of states in the conduction and valence band with tail states extending into forbidden gap (after Schubert, Rensselaer Polytechnic Institute)**

The full-width at half-maximum of the D°X band at 12 K was 7 meV, an outstanding result considering the large lattice mismatch between ZnO and Si. It may be noted that FWHM values of 25 – 30 meV were measured for similar layers grown on GaAs

substrates (see section 7.2.1). The FX emission band at room temperature was 104 meV wide, which is excellent compared to values reported for bulk ZnO (109 meV; Suscavage *et al.*, 1999) or ZnO on sapphire (117 meV; Chen *et al.*, 1998). Again, in section 7.2.3, it was shown that the FWHM of the PL band at 300 K was 128 meV for ZnO grown on GaAs substrates. The smaller FWHM values recorded for the ZnO samples grown on Si as opposed to GaAs reflect the low thermal expansion mismatch of the ZnO/Si system (see section 3.4).

Furthermore, the ratio between the intensity of the UV band and that of the ZnO green band reveals additional information about the purity of the material. Most workers agree that the green band is related to defects in the material, but its precise origin remains controversial. Vanheusden *et al.* (1996b) have attributed it to the singly ionized oxygen vacancy level, while Liu *et al.* (1992) believe it is linked to zinc and oxygen interstitials (Zn_i and O_i). Assuming a relationship between the ZnO green band and the GaN yellow band, Reynolds *et al.* (1997) suggested that the green band results from the recombination of a shallow donor and a deep level.

The following radiative recombination mechanisms have also been suggested (Xu *et al.*, 2003):

- A transition from deep donor levels ($V_O Zn_i$) to the valence band
- A transition from shallow donor levels (Zn_i) to shallow acceptor levels (V_{Zn} and O_i)

The latter is not likely, however, as the ZnO green emission is broad and deep states are known to generate broad bands. Figure 8.15 shows the room temperature PL spectrum of Z425 with the green band located at approximately 2.4 eV. The spectrum yields an $I_{UV}:I_{DL}$ ratio of 28:1, which is superior to previously reported values for MOCVD-grown material (5:1, Bethke *et al.*, 1987; 3:1, Gorla *et al.*, 1999). Wang and co-workers (2003) reported a ratio of 24:1 for their MOCVD-grown samples on Si, similar to what is presented here.
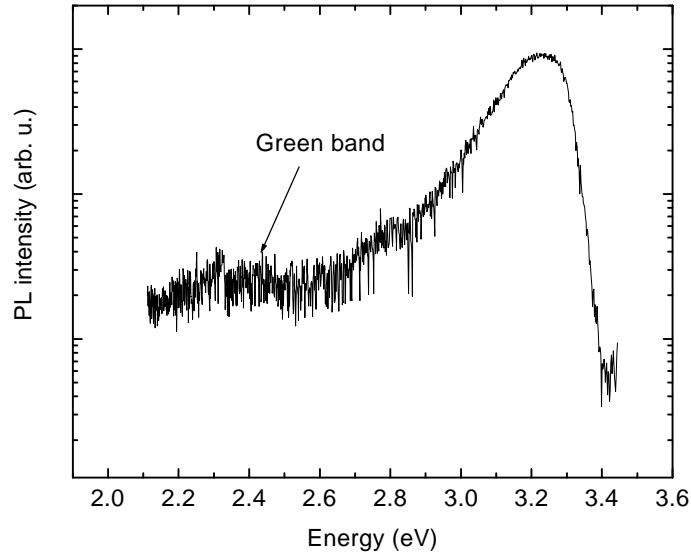
<u>Figure 8.15</u>: Room temperature PL spectrum of Z425

Considering that the room temperature band gap of ZnO is calculated to be 3.35 eV (see figure 8.7) and the green band is centered at 2.4 eV, the energy difference between the two, 950 meV, can correspond to that of a deep donor or deep acceptor, or a combination of the two. Xu *et al.* (2003) calculated the density of states of the oxygen vacancy-zinc interstitial complex ($V_O Zn_i$); they found that two of the defect states of the complex are located 1.0 and 1.2 eV below the conduction band minimum, making them deep donor levels. Furthermore, they found that two states associated with the O_{Zn} (oxygen on a zinc site) defect are located 1.0 and 1.5 eV above the valence band minimum, making them deep acceptor levels. In the light of the energy difference between the band gap and the green band measured here (950 meV), it appears that both the $V_O Zn_i$ complex and the O_{Zn} defect may indeed be associated with the ZnO green band.

8.4   Summary

Variable temperature photoluminescence spectra were recorded on a 4.4 μm thick ZnO sample deposited on an *n*-Si 2 ° off (100) substrate. At 12 K, the spectrum revealed four emission bands at 3.36, 3.32, 3.25, and 3.17 eV which are believed to correspond to a donor-bound exciton (D°X), a donor-acceptor pair (DAP), and the 1LO- and 2LO-

phonon replica of the DAP band. The 3.32 eV peak is believed to be a DAP because of the temperature dependence of its peak position, and because of the rate of approach at which it moves towards the band gap. The fact that the power dependence of the peak position did not match that of a DAP band is explained by experimental error. It would however be necessary to vary the laser power over three or four orders of magnitude to obtain definite results as to the nature of the 3.32 eV band.

The emission bands are found to decrease in intensity and merge with increasing temperature as a result of the thermal ionization of excitons and the thermal activation of nonradiative recombination mechanisms. Most shallow donors seem to be ionized above 65 K, and the two photoluminescence bands observed at 80 and 100 K are believed to correspond to a free exciton and a free electron-neutral acceptor complex. The temperature dependence of the ZnO band gap enabled an assessment of the acceptor depth from the position of the eA^0 complex; the measured acceptor depth of 93 meV is reasonable considering that the shallow donors in ZnO are believed to be 30 - 40 and 60 - 70 meV below the conduction band.

From 125 K onwards, the PL spectrum showed a single UV band corresponding to free exciton emission. Its binding energy was calculated to be 57 meV. At room temperature, the free exciton peaked at 3.29 eV, thus yielding a band gap energy of 3.35 eV. This is similar to the band gap values calculated on the ZnO samples deposited on fused silica (3.35 – 3.38 eV).

The width of the D°X band was measured to be 7 meV at 12 K, a great result considering the large lattice mismatch between ZnO and Si. At room temperature, the dominant FX band was 104 meV wide, and the intensity ratio between the UV band and the defect-related green band was 28:1. The latter reflects the optical quality of the samples deposited in this study compared to other MOCVD-grown ZnO thin films.

9. ELECTRICAL CHARACTERIZATION OF ZnO EPILAYERS

This chapter deals with the electrical characterization of ZnO thin films. The first part of the chapter focuses on Hall measurements performed between 300 and 80 K on ZnO samples grown on *c*-plane sapphire substrates, as the carrier concentration, mobility, and conductivity data obtained help identify the transport properties of the samples. The second part of the chapter covers the fabrication of a Pd Schottky barrier diode on a ZnO thin film deposited on an n^+-GaAs 2 ° off (100) substrate.

Part I: The Hall effect

9.1 Background Theory

The electrical properties of ZnO thin films are investigated by the Hall effect (van der Pauw technique), which yields the carrier type, concentration, mobility, and conductivity of semiconductor materials. The Hall effect relies on the principle that charge carriers are subjected to a Lorentz force ($\vec{F} = q\,\vec{v}\,x\,\vec{B}$) when a current flow and a magnetic field perpendicular to the current are applied at the same time to the semiconductor thin film. This Lorentz force leads to charge separation and an electric field $\vec{E}_H$ (called Hall field) given by (Thomas, 1986)

$$\vec{E}_H = R_H (\vec{J}\,x\,\vec{B}) \qquad \qquad \text{...(9.1)}$$

where R_H is the Hall coefficient, $\vec{J}$ the current density, and $\vec{B}$ the applied magnetic field (figure 9.1).
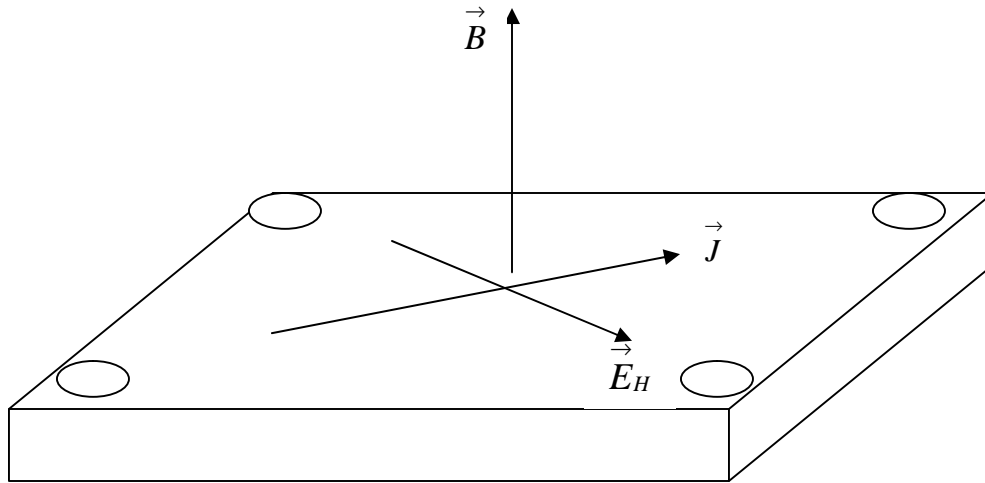
Figure 9.1: Magnetic field, Hall field, and current density in the Hall effect

Another electric field, $\vec{E}$, needs to be taken into account in addition to the Hall field; it stems from the motion of the charges in the magnetic field, and will be equal to $\vec{E}_H$ at equilibrium. This means that

$$R_H(\vec{J} \times \vec{B}) = -\vec{v} \times \vec{B}$$

where $\vec{v}$ is the velocity of the charge carriers. Since

$$\vec{J} = ne\,\vec{v}$$

the Hall coefficient R_H is described by

$$R_H = r_H(-1/ne) \text{ for } n\text{-type material} \qquad \textbf{...(9.2)}$$
$$R_H = r_H(1/pe) \text{ for } p\text{-type material} \qquad \textbf{...(9.3)}$$

where *n* and *p* correspond to the free carrier concentration of an *n*- or *p*-type semiconductor, and r_H the Hall scattering factor. The parameter r_H depends on the material in question, the carrier type, the dominant scattering mechanism, the temperature, and the magnitude of the magnetic field. In general, r_H is taken to be equal to 1 (Pierret, 1987). The Hall coefficient is then linked to the Hall voltage V_H by

$$R_H = \frac{V_H t}{iB} \qquad \qquad \text{...(9.4)}$$

where *t* is the thickness of the sample investigated, and *i* the current applied across the sample (Thomas, 1986). The Hall coefficient and the film's carrier concentration can therefore be calculated by applying a magnetic field and current to a sample of known thickness.

It should be mentioned that several factors are likely to alter the measured Hall voltage in an experiment; these factors are associated with the contact geometry, contact quality, and thermal gradients in the sample due to current traveling through the material. Fortunately, these error-inducing effects can be minimized by working with small currents, by taking measurements over a short period of time, and by adopting the van der Pauw technique (van der Pauw, 1958). The latter entails reversing the applied magnetic field through all possible contact combinations in order to measure the Hall voltage V_H.

Having obtained the Hall voltage, it is now possible to measure the Hall mobility, which gauges how easily carriers within a semiconductor travel. The mobility $\boldsymbol{m}$ is inversely proportional to the amount of scattering in the semiconductor (Pierret, 1987), and is given by

$$\boldsymbol{m} = 1/ne\boldsymbol{r} \qquad \qquad \text{...(9.5)}$$

where n is the carrier density of an n-type material like ZnO, and r its resistivity. The latter is described by (Schroder, 1998)

$$r = \frac{ptR}{\ln 2} \qquad \ldots(9.6)$$

where R is the average resistance, given by

$$R = \frac{R_A + R_B}{2}$$

with $R_A = V_{kl} / I_{ij}$, and $R_B = V_{jk} / I_{il}$ (figure 9.2). In these expressions, I_{ij} is the current passed between contacts i and j, and V_{kl} the voltage measured across contacts k and l.
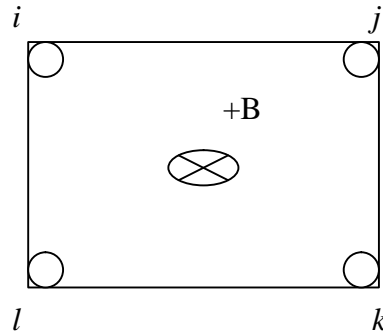
Figure 9.2: Annotation of ohmic contacts on sample

Unfortunately, R_A and R_B usually differ as a result of different contact size, geometry, and position. Nevertheless, Newton's iterative method is known to correct this problem; starting with a trial solution, successive approximations are derived from the expression (Weider, 1976)

$$r_{n+1} = r_n - \frac{r_n^2(a + b - 1)}{pt(aR_A + bR_B)}$$

where

$$a = \exp\left(\frac{-ptR_A}{r_n}\right), \text{ and } b = \exp\left(\frac{-ptR_B}{r_n}\right)$$

The precise film resistivity can be obtained by iterating this expression until it converges (five iterations are usually sufficient).

Having calculated the film resistivity r, the conductivity s is simply given by

$$s = 1/r \hspace{8cm} …(9.7)$$

9.2 Scattering mechanisms in ZnO

The motion of charge carriers in a material is given by Boltzmann's transport equation, which establishes the link between the changes in the carrier distribution (occupied energy states) and the forces that push the carriers to a nonequilibrium state. The mobility m of the carriers is then described by

$$m = \frac{e\langle t \rangle}{m*}$$

where e is the electron charge, $\langle t \rangle$ the average relaxation time, and $m*$ the effective mass of the charge carriers (Chen, 2000). The carrier mobility will therefore hinge on the drift velocity and the mean free path of the charge carriers, since they will influence the relaxation time of the carriers. Furthermore, these two parameters depend on the mechanisms by which the carriers are scattered; it is therefore important to understand the dominant scattering mechanisms defining the upper limit of mobility. Figure 9.3 gives an outline of the various scattering mechanisms found in semiconductors (Look, 1989). A brief discussion of some of the notions introduced in this figure, and their impact on carrier transport in ZnO, follows.
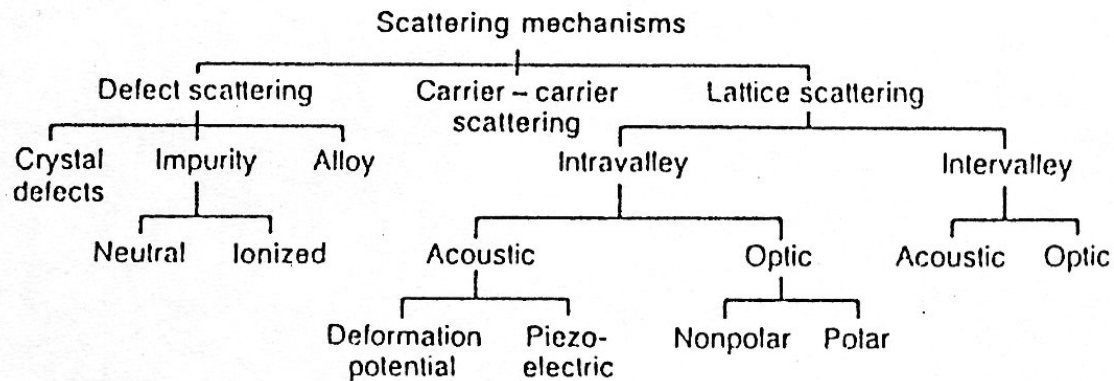
Figure 9.3: Scattering mechanisms in semiconductors
(after Look, 1989)

Lattice scattering, also known as *phonon scattering*, stems from the fact that crystals have a finite temperature, causing atoms to vibrate around their equilibrium lattice sites. These lattice vibrations result in phonons (quantized lattice vibrations) displaying different energies.

Intravalley acoustic phonon scattering refers to scattering of carriers within the same energy valley, by acoustic phonons. It can be divided into two sub-categories: deformation and piezoelectric potential. In the case of *deformation potential*, the acoustic-mode lattice vibrations generate modifications in lattice spacing, which will lead to variations in the band gap from point to point. On the other hand, the *piezoelectric potential* sees the introduction of a second potential and an internal electric field as a result of atomic displacements. This mechanism takes place in crystals lacking a center of symmetry.

Furthermore, *intravalley optical phonons* branch out into two types of scattering mechanisms, *polar* and *non-polar*. *Polar optical phonons* are associated with the formation of dipole moments resulting from the vibration of ionic charges on the atoms undergoing optical-mode lattice vibrations. The maximum mobilities of lowly doped ZnO single crystals are believed to be limited by scattering at polar optical phonons

(Look *et al.*, 1998). According to Morkoç (1999), the mobility linked to polar optical phonon scattering can be described by

$$m_{pop} \approx \frac{T^{1/2}}{(m*)^{3/2}}$$

Non-polar optical phonons, on the other hand, induce a perturbing potential through local variations in the band gap. It is not however as strong as other lattice scattering mechanisms.

Intervalley scattering refers to carriers interacting with a phonon having large momentum; the carrier is then scattered to another valley of same energy. Intervalley scattering becomes more intense with increasing temperature. Nevertheless, it is not believed to be one of the dominant scattering mechanisms in ZnO at room temperature.

Carrier-to-carrier scattering needs to be taken into account for highly doped material, and must certainly be considered in the ZnO samples studied here since carrier concentrations ranged between $1.2 \bullet 10^{17}$ and $3.4 \bullet 10^{18}$ cm^{-3}. Scattering between electrons and holes can usually be neglected since large concentrations of electrons and holes are unlikely to be found at the same point in a semiconductor. On the other hand, electron-electron and hole-hole scattering may disturb the distribution of momentum among the carrier types, and will reflect on other scattering mechanisms. While ionized impurity scattering (see below) is believed to be the dominant scattering mechanism in doped ZnO, electron-electron scattering is partly responsible for the discrepancy between mobilities measured experimentally and mobilities determined theoretically from theories of ionized impurity scattering (Fischetti, 1991).

While the scattering mechanisms previously mentioned are going to influence the transport properties of ZnO to some extent, the dominant scattering mechanisms of this material are found in the third class of scattering mechanisms, *defect scattering*. Mobility vs. temperature data (Young *et al.*, 2000) has confirmed that *neutral impurity scattering*

is the dominant scattering mechanism in undoped ZnO, and *ionized impurity scattering* in doped material.

Consider an electron passing close to a neutral atom; in *neutral impurity scattering*, momentum can be transferred through a process in which the free electron exchanges with a bound electron on the atom (Look, 1989). This mechanism is especially important at low temperatures, where a considerable number of donors or acceptors is neutralized by carrier freeze-out. As the temperature falls, the number of neutral impurity centers will increase, thereby decreasing the carrier mobility (Askerov, 1994).

In *ionized impurity scattering*, dopant impurities scatter carriers through their screened Coulomb potential; this mechanism is predominant at low temperatures in any semiconductor. For a non-degenerate semiconductor, the mobility limited by ionized impurity scattering exhibits a distinct temperature dependence $\boldsymbol{m} \sim T^{3/2}$. On the other hand, a degenerate material will see its carrier mobility being practically independent of temperature (Li, 1993).

There seems to be disagreement in the literature concerning the influence of grain boundaries on the transport properties of ZnO. Reviews dealing with transparent conducting oxides such as ZnO briefly state that carrier transport in these materials is limited by ionized impurity scattering or by grain barriers (Chopra *et al.*, 1983). Young *et al.* (2000) used spectroscopic ellipsometry data to model optical mobilities in their ZnO thin films; they found that their modeled values agreed with dc Hall mobilities, which give a description of *inter-grain*, as opposed to *intra-grain*, mobilities. Their conclusion was backed up by the absence of a grain boundary barrier height, as determined by Ghosh *et al.* (1991) by temperature-dependent resistivity data. On the other hand, Srikant *et al.* (1995b) described the transport properties of their ZnO samples in terms of transport across grain boundaries. Furthermore, the room temperature data to be presented in section 9.4.2 will show that electrical transport across grain boundaries can explain the observed increase in mobility with carrier concentration for concentrations less than $3.7 \bullet 10^{17}$ cm^{-3}.

9.3 Experimental procedure

9.3.1 Description of apparatus

The Hall system described here enables measurements to be performed from approximately 300 to 20 K. Having said that, the data presented here was recorded between 300 and 80 K. The home-built Hall system comprises a cryostat, Helium compressor, switch/control unit, current source, voltmeter, magnet power supply, and temperature controller. The various elements of the system are connected to a computer displaying the measured values. The following section outlines the technical details relevant to the system.

The samples were placed in a *Quantum Technology* cryostat, which was cooled with a *Cryomech* model GB 220 closed-cycle compressor; helium gas was delivered to the cold head from a model CP 415 compressor package. The cryostat was evacuated with a *Varian* rotary and diffusion pump system before cooling. The system was kept at a pressure of the order of $4 \bullet 10^{-3}$ Pa during measurements.

The sample temperature was measured with a *Lake Shore Cryotronics* model 331 temperature controller, together with a TG-120 calibrated AlGaAs diode temperature sensor. The latter displays an error of less than 0.25 K for magnetic fields under 50 kG and temperatures above 4 K, according to the manufacturer. The sample and the temperature sensor were mounted on a solid oxygen-free high conductivity copper rod (OFGC), in order to avoid a temperature discrepancy between the sample and the sensor. An IEEE-488 GPIB interface provided the link between the temperature controller and the computer.

An *Oxford instruments* N100 electromagnet produced the magnetic field applied to the sample. The current for the magnet came from a *KEPCO 75-8M* dc power supply interfaced to the computer. All the measurements were taken with a 5 kG magnetic field.

The current through the sample originated from a *Keithley* model 244 programmable current source. This model can deliver a current ouput between 20 nA and 101 mA, with a minimum step of 5 nA. It complies to voltages up to 105 V in 1 V increments.

Finally, the Hall voltage was read from an *Agilent 34401A* digital multimeter, which can pick up voltages ranging from 100 nV to 300 V.

9.3.2 Overview of samples investigated

The samples studied in this section were all grown on *c*-plane sapphire at 450 °C; only the VI:II ratio during growth was varied. 3N-TBOH was selected as oxidizing agent. All samples but one were grown following the two-step growth process described in section 7.2.4. Table 9.1 outlines the sample names together with their growth parameters.

Sample name	Growth temperature (°C)	VI:II ratio during growth	Low temperature buffer	Thickness (μm)
H50	450	18:1	Yes	2
H58	450	18-35:1[7]	No	2
H61	450	60:1	Yes	2
H62	450	90:1	Yes	2
H63	450	70:1	Yes	2

Table 9.1: Overview of ZnO samples studied in this chapter

9.4   Results

9.4.1 Ohmic contact resistance

Indium contacts were soldered onto the samples in order to measure their electrical properties by the Hall effect. Indium was chosen because it is known to form good ohmic

---

[7] Due to technical problems, the VI:II ratio during growth of sample H58 could not be accurately determined. This has, however, no bearing on the results presented in this chapter.

contacts on ZnO (Hutson, 1957). Having soldered the In pads, the first task consisted of assessing the metal contact quality. Indeed, for this experimental set-up, it is required to have a two-terminal resistance R in the kΩ range in order to measure a Hall voltage. This is because the Hall system is equipped with a 10 V battery; a two-terminal resistance of the order of 1 MΩ would yield a current of 10 μA, which is far too low for such measurements. It is indeed recommended to work with currents higher than 200 μA. Moreover, high two-terminal resistances are likely to generate strong noise during the measurements.

The two-terminal resistances of the samples are found to be in the MΩ range irrespective of the growth parameters (VI:II ratio, buffer or no buffer), making it impossible to measure the Hall voltage of as-grown, unannealed, samples. This is surprising, as Look *et al.* (1998) managed to perform Hall measurements on bulk ZnO with non-annealed In contacts (although localized heat was apparently supplied using an In-soldering device). The samples were consequently annealed in argon for 15-minute intervals at 600 °C. A striking difference was noticed between H58, a non-buffered sample grown at a VI:II ratio of approximately 25:1 (see section 9.3.2), and H50, a buffered layer deposited at a VI:II ratio of 18:1. After annealing H58 for one hour, a two-terminal resistance of 55 kΩ was measured; an improvement of three orders of magnitude compared to the resistance measured before annealing. Nevertheless, a 15-minute anneal was sufficient to reduce the two-terminal resistance of H50 to 1 kΩ. This confirms the results from the GaAs work presented in this thesis (section 7.2.4), which describe the positive impact of a low-temperature buffer layer on sample quality. In the case of ZnO on *c*-plane sapphire, the improvements in surface quality may be due to the formation of a thin surface layer of $ZnAl_2O_4$ resulting from a reaction-diffusion process between the ZnO buffer and the Al_2O_3 substrate. This polycrystalline $ZnAl_2O_4$ layer has been shown to alter the nucleation and growth of GaN on *c*-plane sapphire by enhancing the wetting of the surface by the laterally growing $ZnAl_2O_4$ after the initial three-dimensional nucleation, and by providing an improved lattice match to the GaN (Gu *et al.*, 2000). Similar results would be expected for the ZnO on *c*-plane sapphire system. It should be mentioned that the slight difference in VI:II ratio during growth between H50 and H58 is not likely to

greatly affect the two-terminal resistances of In contacts on ZnO; non-buffered ZnO layers systematically displayed higher two-terminal resistances than buffered thin films.

Having obtained reasonable two-terminal resistances, it is then required to test the ohmicity of the In contacts. Figure 9.4 shows the two-terminal current-voltage curve of H62 after annealing.
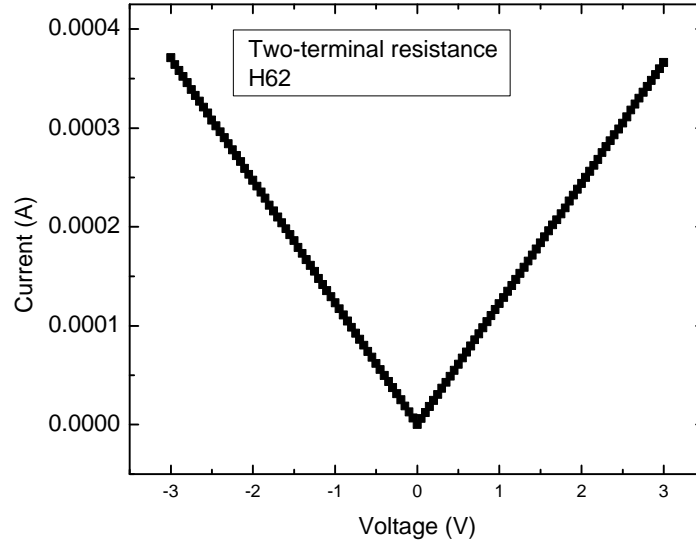
Figure 9.4: **Two-terminal current voltage curve of H62 after annealing**

The curve clearly displays the linear current-voltage characteristics of ohmic contacts, validating the choice of In pads for ZnO samples. For the sake of completion, it should be mentioned that while few reports dealing with low-resistance ohmic contacts on ZnO have been published, a couple of other metal combinations have already been tested. Kim *et al.* (2002) have reported low-resistance Ti/Al ohmic contacts on undoped ZnO; they attributed the success of the Ti/Al metallization to the formation of an intermediate phase of Al_3Ti. Prior to that, Kim *et al.* (2000) had reported on high-quality Ti/Au contacts on ZnO. These Ti/Au contacts were deposited by electron beam evaporation, which can lead to sample damage as explained in section 9.5. In that respect, soldering is more advantageous than e-beam evaporation.

9.4.2 Room temperature transport properties

The influence of the VI:II ratio during growth on the carrier concentration and mobility of ZnO thin films was investigated by growing a series of samples on *c*-plane sapphire at different VI:II ratios during growth; all the samples were grown at 450 °C with the two-step growth process involving a buffer layer deposited at 300 °C. After growth, the contacts were annealed for 15 minutes at 600 °C so as to reduce the two-terminal resistance. All samples displayed *n*-type conductivity, and figure 9.5 shows the variation of carrier concentration with VI:II ratio during growth.

The carrier concentrations of H50 ($3.4 \bullet 10^{18}$ cm^{-3}) and H61 ($3.7 \bullet 10^{17}$ cm^{-3}) are similar to the carrier concentrations measured by the Burnstein-Moss shift on samples grown at the same VI:II ratios on glass slides ($4.2 \bullet 10^{18}$ and $5.2 \bullet 10^{17}$ cm^{-3}, respectively; see section 6.3.1). The carrier concentration of these samples is seen to decrease by over an order of magnitude when the VI:II ratio during growth is increased from 18 to 90:1, highlighting a lower concentration of donors at high VI:II ratios.
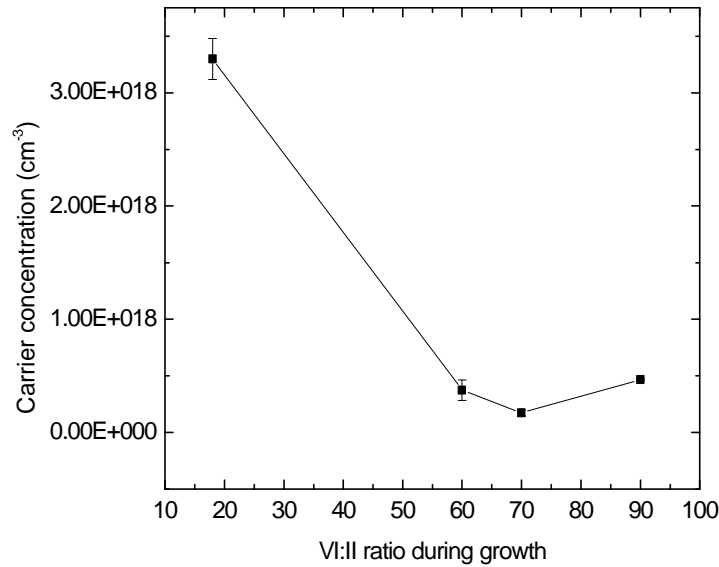
Figure 9.5: **Variation of carrier concentration with VI:II ratio during growth for ZnO on *c*-plane sapphire substrates**

ZnO is known to display room temperature *n*-type conductivity even without doping because of a deviation from stoichiometry caused by defects such as zinc interstitials and

oxygen vacancies (Ma *et al.*, 2003). Increasing the VI:II ratio during growth from 18 to 90:1 causes a decrease in oxygen vacancies, which in turn will reduce the carrier concentration as can be seen in figure 9.5.

Furthermore, the relationship between the carrier mobility and the carrier concentration is plotted in order to assess the impact of scattering mechanisms on carrier mobility (figure 9.6; the data of H58 is included).
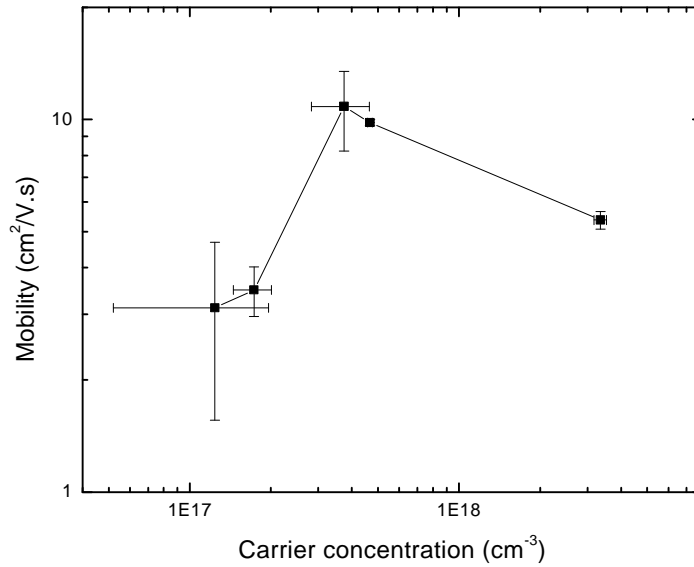
Figure 9.6: Variation of carrier mobility with carrier concentration

Each measurement was taken four to five times, and the error bars were calculated from the average results. The carrier mobility is first seen to increase with carrier concentration until about $n = (3 - 4) \bullet 10^{17}$ cm^{-3}; it then decreases for higher concentrations. The increase in mobility with carrier concentration can be explained in terms of the established principles of electron transport in polycrystalline semiconductors having potential barriers at grain boundaries (Orton and Powell, 1980). When modeling the thin film conductivity, defects are considered localized at the grain boundaries, and behave as traps for the majority carriers in the neighboring grains (Seager and Castner, 1978). The electrons trapped by the defects proceed to create a negative charge at the grain boundaries, which leads to a space-charge region in the grains because of the buildup of counterions having a positive charge, the donor atoms. Consequently, a potential barrier

that looks like a back-to-back Schottky barrier is generated at the grain boundaries; this potential barrier is going to hinder the transport of electrons when a voltage is applied to the polycrystalline material. Furthermore, the conductivity of polycrystalline materials with barriers at the grain boundaries is known to depend on the electron mean free path, the width of the depletion region, the grain size, the carrier concentration, and the density and energy of the interface states. The electron mean free path is given by

$$l_e = \left(\frac{h}{2q} \right) \left(\frac{3n}{p} \right)^{1/3} m \qquad \qquad \text{...(9.8)}$$

where n and m are the material's carrier concentration and mobility (Pei *et al.*, 2001). Table 9.2 gives the carrier concentration, mobility, and electron mean free path of the samples investigated. The mean free paths of the samples are two orders of magnitude smaller than the grain size of the samples (table 9.2). This suggests that the abrupt junction approximation is valid for this system.

Following the reasoning of section 6.4.3, the Debye length of the films is given in table 9.2; in each case, the Debye length is inferior to the grain size, which further validates the use of the abrupt junction approximation for these thin films.

Sample name	Carrier concentration (cm^{-3})	Mobility (cm^2/V.s)	Electron mean free path (nm)	Debye length (nm)	Grain size (nm)
H50	$(3.4 \pm 0.2) \bullet 10^{18}$	5.4 ± 0.3	0.16	2	21
H58	$(1.2 \pm 0.7) \bullet 10^{17}$	3.1 ± 1.6	0.03	9	17
H61	$(3.7 \pm 0.9) \bullet 10^{17}$	10.8 ± 2.6	0.16	6	26
H62	$(4.7 \pm 0.09) \bullet 10^{17}$	9.8 ± 0.2	0.15	5	20
H63	$(1.7 \pm 0.28) \bullet 10^{17}$	3.5 ± 0.5	0.04	9	24

Table 9.2: Carrier concentration, electron mean free path, Debye length, and grain size of ZnO samples studied in this chapter

Solving Poisson's equation, the barrier height f and carrier mobility m are described by the following expressions,

$$f = \frac{eN_s^2}{2ee_0 n} - \frac{kT}{e} \qquad \qquad \text{...(9.9)}$$

$$m = m_0 \exp\left(-\frac{f}{kT}\right) \qquad \qquad \text{...(9.10)}$$

where $m_0 = qv_d D'/8kT$, $D' = D + D_1$, v_d being the electron's drift velocity, and D_1 the grain boundary thickness (Srikant *et al.*, 1995b). As the carrier concentration increases from $1.2 \bullet 10^{17}$ to $3.7 \bullet 10^{17}$ cm^{-3}, the barrier height f drops, thus causing the carrier mobility m to increase according to equation 9.10 (as seen in figure 9.6).

While the mobility of H50 ($n = 3.4 \bullet 10^{18}$ cm^{-3}) is measured higher than the mobilities of H58 ($n = 1.2 \bullet 10^{17}$ cm^{-3}) and H63 ($n = 1.7 \bullet 10^{17}$ cm^{-3}), it is also found smaller than the mobilities of H61 ($n = 3.7 \bullet 10^{17}$ cm^{-3}) and H62 ($n = 4.7 \bullet 10^{17}$ cm^{-3}). This cannot be explained by the electron transport principles depicted by equations 9.9 and 9.10. As mentioned in section 9.2, ionized impurity scattering is believed to be one of the factors limiting the mobility values of doped ZnO. Shockley (1950) derived an expression describing the relationship between mobility m, impurity charge Z, and electron density n_e for ionized impurity scattering:

$$m^{Sh} = \frac{3(e\,e_0)^2 h^3}{Z^2 m^{*2} e^3} \left\{ \ln\left[1 + \left(\frac{3^{2/3} p^{1/3} e_r e_0 h^2 n^{1/3}}{2m_{eff}\, e^2}\right)^2\right]\right\}^{-1} \qquad \qquad \text{...(9.11)}$$

where e is the relative static permittivity, and m_{eff} the effective mass. The mobility is therefore seen to be inversely proportional to the impurity charge. In an attempt to describe the mobilities of their heavily doped germanium samples, Dakhovskii *et al.* (1971) suggested that clusters of impurities may act as scattering centers with a charge Z_C

superior than the individual impurity's charge Z. The presence of impurity clusters may be responsible for the drop in mobility measured for concentrations larger than $3.7 \bullet 10^{17}$ cm^{-3}. Indeed, as n rises above that threshold concentration, the presence of impurity clusters begins to be felt by the carriers, leading to a decrease in mobility according to equation 9.12. It therefore appears that below $3.7 \bullet 10^{17}$ cm^{-3}, carrier mobility is dominated by electron transport across grain boundaries. Furthermore, for $n > 3.7 \bullet 10^{17}$ cm^{-3}, an appreciable concentration of impurity clusters may be formed; this leads to stronger ionized impurity scattering, and a mobility lower than expected. Having said that, the fact that the Debye length of H50 ($n = 3.4 \bullet 10^{18}$ cm^{-3}) is less than twice its grain size suggests that band bending must indeed be taken into account for this sample. It may be that the mobility of H50 is determined by a combination of electron transport across grain boundaries and ionized impurity scattering. Additionally, it should be mentioned that the sample pool employed for this study was rather small; this investigation should be furthered with additional layers in order to confirm the trend.

Before looking at variable temperature conductivity measurements, let us compare the mobilities of these samples with the mobilities of n-type layers grown on semi-insulating GaAs during this project, and other literature values (table 9.3). Firstly, ZnO layers grown in this work on c-plane sapphire and semi-insulating GaAs display similar mobilities; this probably reflects the similar lattice mismatch of these two growth systems. Secondly, the mobilities measured in this work are considerably smaller than what Look *et al.* (1998) reported for bulk material. On the other hand, the mobilities reported here are similar to what has been published in the literature for material grown both by MOCVD and by other techniques. This highlights the electrical quality of the material, in line with its optical quality as observed by photoluminescence (see section 8.3.3). Furthermore, it should be mentioned that despite the number of workers studying ZnO, reported mobility values have not significantly improved in the last twenty-five years. This may imply that there exists a physical limitation hindering the development of thin films having mobilities larger than $40 - 60$ cm^2/Vs (Ellmer, 2001).

MOBILITY (cm^2/Vs)				
This work: *c*-plane sapphire substrates	This work: semi-insulating GaAs substrates	Bulk ZnO	MOCVD	Other growth techniques
3 - 11	**4 – 7**	205 (Look *et al.*, 1998)	0.7 – 31.1 (Ma *et al.*, 2003)	0.47 – 7.2 (reactive deposition; Zhenguo *et al.*, 2003)
			50 – 60 (Hahn *et al.*, 1998)	8.0 – 16.8 (magnetron sputtering; Subramanyam *et al.*, 2000)
			2 – 6 (Roth and Williams, 1981b)	10 – 40 (reactive evaporation; Jin and Ying, 1993)

Table 9.3: Summary of mobilities measured in this work compared to literature values

9.4.3 Variable temperature conductivity measurements

The mechanism of the conduction of electrons in ZnO above room temperature is reported to be the transfer of electrons excited from zinc interstitial donor levels into the conduction band. Nevertheless, few reports describe the low-temperature conductivity properties of ZnO (Natsume *et al.*, 1992; Natsume *et al.*, 1995). The aim of this section is to identify and describe the nature of the conduction mechanism of MOCVD-grown ZnO samples.

Figure 9.7 shows the temperature dependence of the conductivity of H50 and H62 between 80 and 290 K.
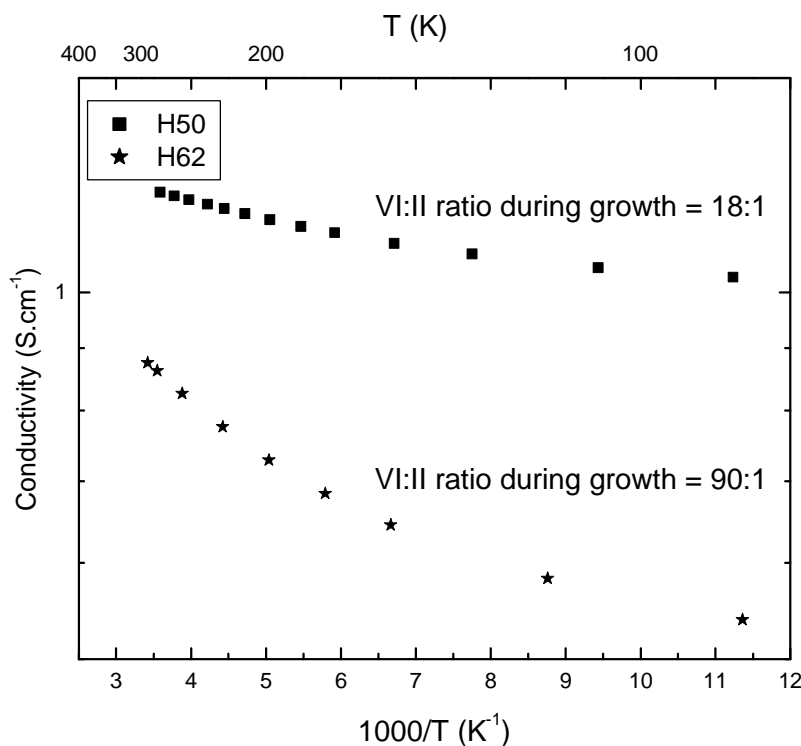
Figure 9.7: **Variation of electrical conductivity of samples H50 (VI:II = 18:1) and H62 (VI:II = 90:1) with reciprocal temperature**

First of all, H50 displays a higher conductivity (i.e. lower resistivity) than H62 throughout the temperature range studied. Following the discussion of carrier concentration vs. VI:II ratio (see figure 9.5), it is clear that H50 contains a larger density of donor defects increasing the conductivity. Furthermore, the room temperature resistivities of H50 and H62 (0.83 and 1.14 Ωcm, respectively) are similar to reported values for thin films of $1 - 10$ Ωcm (Look, 1998).

Moreover, it appears that the two curves display different temperature dependences. The data can be divided into two temperature ranges: the high temperature range from 290 to 169 K, and the low temperature range from 169 to 80 K; the following discussion deals with electrical conduction in the two temperature ranges separately.

Electrical conduction between 290 and 169 K

In the high temperature range, an Arrhenius plot can be fitted to the conductivity data due to the band conduction of carriers (figure 9.8).
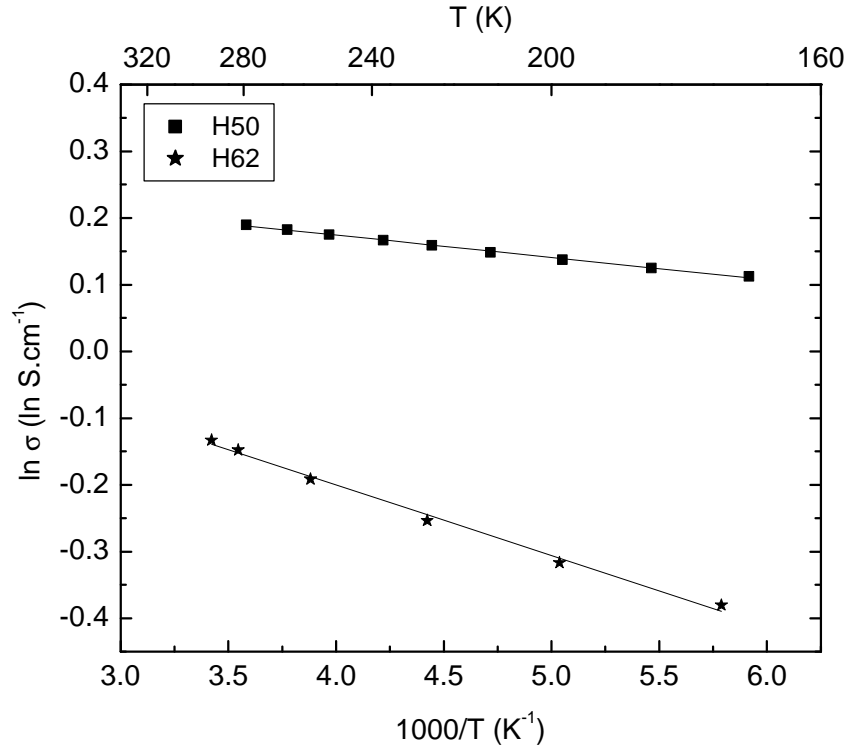
Figure 9.8: **Variation of electrical conductivity of H50 and H62 with reciprocal temperature from 290 to 169 K**

The activation energies E_a of the curves are found to be 2.9 ± 0.1 meV for H50, and 9.1 ± 0.4 meV for H62. Since the donor will be located at an energy $E_d = 2E_a$ below the conduction band (Natsume *et al.*, 1995), the donor energy in H50 and H62 is found to be 6 and 18 meV respectively. The latter is similar to the donor energy reported by Natsume *et al.* for a sample deposited at 575 °C by chemical vapor deposition (20 meV). Natsume *et al.* (1995) attributed the donor level to zinc interstitials in the light of XPS spectra previously recorded. This seems a fair assumption, considering that Look *et al.* (1999) reported from high-energy electron irradiation experiments the presence of the interstitial Zn_i (or a Zn_i-related defect) 30 meV below the conduction band. Furthermore, the low

donor energy of H50 seems to betray the beginning of the formation of an impurity band merging with the conduction band (see section 6.3.1).

Having calculated the activation energies for conduction in this range, let us continue by looking at the effect of the grain boundaries on the films' conduction properties. As described in section 9.4.2 and in table 9.2, the Debye length of both H50 and H62 is less than half the film's grain size, which implies that a potential barrier is created around each grain due to band bending. The impact of grain boundaries on a film's transport properties has been studied by Roth and Williams (1981b) in terms of the material tunneling constant E_{00} given by

$$E_{00} = 18.5 \bullet 10^{-12} (n / m_e e)^{1/2} \qquad \qquad \textbf{...(9.12)}$$

where n is the impurity concentration and m_e the effective mass of the electron. They showed that if $E_{00} \leq kT$, the carrier mobility $\boldsymbol{m}$ is limited by thermionic emission of electrons over the grain boundary barriers. On the other hand, if $E_{00} \geq kT$, the mobility is limited by thermal field emission of electrons through the grain boundary barriers. The tunneling constants of H50 and H62 are calculated to be 22 and 8 meV, respectively; this means that the mobility of carriers in both H50 and H62 at room temperature is limited by the thermionic emission of electrons over the grain boundary barriers. This result confirms the description of barrier height and mobility of sections 9.4.2, where thermionic emission is assumed for solving Poisson's equations for the abrupt junction approximation. Roth and Williams (1981b), on the other hand, found that the mobility of their CVD-grown samples was limited by both thermionic and thermal-field emissions of electrons at room temperature.

Having identified that carrier transport across grain boundaries is limited by thermionic emission in these samples, another mechanism must be taken into account at lower temperatures since thermal excitations of electrons around the Fermi level are not

frequent below 170 K. This is the object of the next section. Table 9.4 summarizes the results obtained from 290 and 169 K.

Sample name	Carrier concentration (cm^{-3})	Activation energy E_a (meV)	Donor energy (meV)	Tunneling constant E_{00} (meV)	Carrier transport across grain boundaries limited by…
H50	$3.4 \bullet 10^{18}$	2.9 ± 0.1	6	22	Thermionic emission
H62	$4.7 \bullet 10^{17}$	9.1 ± 0.4	18	8	Thermionic emission

Table 9.4: Conductivity data between 290 and 169 K for ZnO samples H50 and H62

Electrical conduction between 169 and 80 K

In order to identify the type of conduction observed in this temperature range, it is necessary to call on the classification system created by Hausmann and Teuerle (1972) for an In-doped ZnO single crystal. Their classification system is based on the ratio between the mean distance r between nearest donors in ZnO, and their effective mean radius a^*. The mean distance r is defined as

$$r = \left(\frac{4\boldsymbol{p}n_d}{3} \right)^{-1/3} \qquad \qquad \text{…(9.13)}$$

where n_d is the donor concentration; the effective Bohr radius is then given by

$$a^* = \frac{0.53\boldsymbol{e}m}{m_e} \qquad \qquad \text{…(9.14)}$$

They identified three types of conduction depending on the r/a^* ratio.

- If $r/a^* > 5$, electrical conduction is described by band and nearest-neighbor hopping between isolated donor levels

- If $2 < r/a^* < 5$, variable-range hopping between localized states of an impurity band takes place

- If $r/a^* < 2$, metallic conduction is prevailing because of the overlap between the impurity and conduction bands

The r/a^* ratio is found equal to 2.5 for H50 and 4.8 for H62. It appears that in both cases the conductivity is best described by variable-range hopping between localized states, although the r/a^* values border on metallic conduction and nearest-neighbor hopping, respectively. Charge transfer by hopping is different from conventional solid state conduction processes in that the transfer takes place in a localized energy region within the energy gap of the material, and not in the conduction band (Hill, 1971). Mott (1969) proposed the following expression for conduction due to variable-range hopping:

$$s = s_{h0} \exp\left[- (T_0 / T)^{1/4}\right] \qquad \qquad ...(9.15)$$

where

$$s_{h0} = \frac{3e^2 v_{ph}}{(8 p k)^{1/2}} \left[\frac{N(E_F)}{aT}\right]^{1/2} \qquad \qquad ...(9.16)$$

and

$$T_0 = \frac{l a^3}{k N(E_F)} \qquad \qquad ...(9.17)$$

In these expressions, v_{ph} corresponds to the phonon frequency at Debye temperature, $N(E_F)$ is the localized state density for electrons at the Fermi level, a the inverse localization length of wave function for a localized state, and l a dimensionless constant. The phonon frequency and l are respectively equal to 10^{13} s^{-1} and 16 (Natsume et al., 1995). From equations 9.15 – 9.17,

$$s = \frac{3e^2v_{ph}}{(8pk)^{1/2}} \left[\frac{N(E_F)}{aT}\right]^{1/2} \exp\left(-\frac{T_0}{T}\right)^{1/4} \qquad ...(9.18)$$

and

$$sT^{1/2} = \frac{3e^2v_{ph}}{(8pk)^{1/2}} \left[\frac{N(E_F)}{a}\right]^{1/2} \exp\left[-\left(\frac{T_0}{T}\right)^{1/4}\right] \qquad ...(9.19)$$

Finally,

$$\ln(sT^{1/2}) = -\left(\frac{T_0}{T}\right)^{1/4} + \frac{3e^2v_{ph}}{(8pk)^{1/2}} \left[\frac{N(E_F)}{a}\right]^{1/2} \qquad ...(9.20)$$

A plot of $\ln(sT^{1/2})$ vs. $T^{-1/4}$ should therefore yield a straight line. This is indeed the case for both H50 and H62, as shown in figure 9.9.
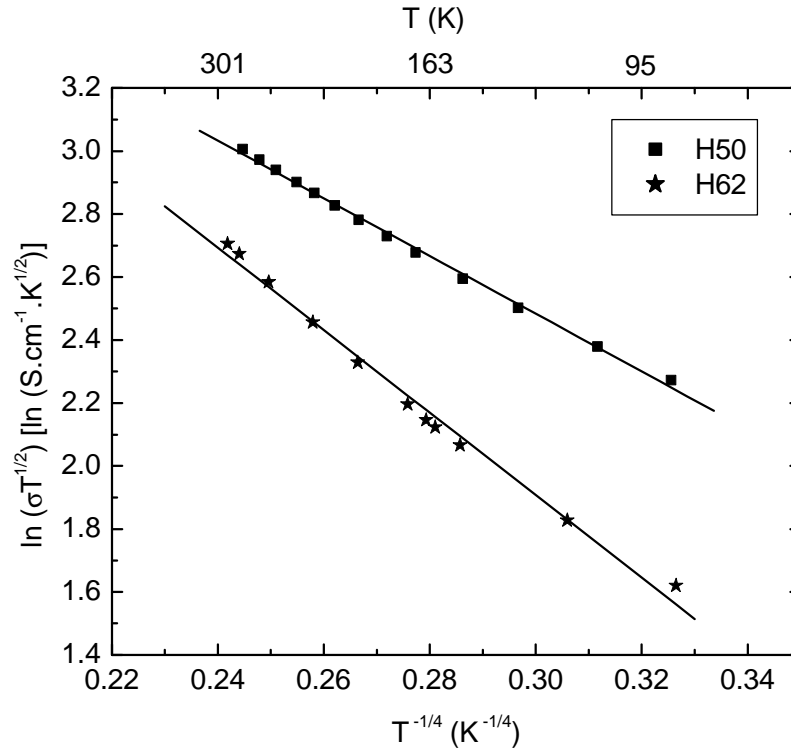
Figure 9.9: **Variable-range hopping conduction, H50 and H62**

173

It can be seen that variable-range hopping accurately describes the temperature dependence of the conductivity of both H50 and H62 from 80 to 290 K, which confirms that this conduction mode indeed takes place in this temperature range.

The inverse localization length of wave function for a localized state a and the localized state density for electrons at the Fermi level $N(E_F)$ can now be calculated from the slope m and y-axis intercept c of the $\ln\left(sT^{1/2}\right)$ vs. $T^{-1/4}$ curve as

$$a = \frac{2m^2 k \exp(c)}{3e^2 n_{ph}} \sqrt{\frac{2p}{l}} \qquad \text{...(9.21)}$$

$$N(E_F) = \frac{l a^3}{m^4 k} \qquad \text{...(9.22)}$$

The average incremental energy, or hopping energy, W can now be calculated together with the radial distance required for an incremental energy W, since (Mott, 1969)

$$R = \left(\frac{9}{8pakTN(E_F)}\right)^{1/4} \qquad \text{...(9.23)}$$

$$W = \frac{3}{4pR^3 N(E_F)} \qquad \text{...(9.24)}$$

The calculated values of a, $N(E_F)$, R, and W at 150 K are reported in table 9.5.

Sample name	a ($\bullet 10^5$ cm^{-1})	$N(E_F)$ ($\bullet 10^{17}$ cm^{-3}.eV^{-1})	R ($\bullet 10^{-6}$ cm)	W ($\bullet 10^{-3}$ eV)
H50	3.5 ± 0.4	1.2 ± 0.5	2.9 ± 0.5	8.7 ± 7.9
H62	13.3 ± 2.3	148 ± 96	1.09 ± 0.18	12.5 ± 14.2

Table 9.5: a, N(E$_F$), R, and W for H50 and H62 at 150 K

Furthermore, there are two requirements set by Mott for variable-range hopping:

αR must be superior (>>) to 1, and W must be larger (>>) than kT. In the case of H50, αR is equal to 1.01, and W (8.7 meV) is slightly less than kT (13 meV at 150 K). This probably reflects the fact that H50 is a borderline case of conduction between variable-range hopping and metallic conduction. Nevertheless, the good fit of figure 9.9 seems to indicate that variable-range hopping plays a role in the conduction properties of H50. In the case of H62, on the other hand, αR is equal to 1.45, and W (12.5 meV) is practically equal to kT at 150 K. While αR is considerably higher for H62 than for H50, the W value of H62 still doesn't surpass the thermal energy kT at 150 K. It can be concluded from figure 9.9 that variable-range hopping indeed influences the conduction properties of H62. The low W value of H62 probably reflects the fact that with a r/a^* ratio of 4.8, H62 presents itself as a borderline case between variable-range hopping and nearest-neighbor hopping.

Furthermore, the presence of the impurity band can be paralleled with the Urbach tail measurements done on sample Z18/1, a sample deposited on fused silica at the same VI:II ratio as H50, 18:1 (see section 6.3.1). Davis and Mott (1970) have shown that disordered and amorphous materials produce localized states extending in the band gap. The Urbach tail E_0 parameter of Z18/1 was calculated to be 254 meV, which implies that the localized states extend 254 meV into the band gap from near the edge of the conduction band. These states will turn to localized states as they approach the band gap, thus ensuring variable-range hopping conduction between the localized states of the impurity band in H50 and H62 at low temperatures.

9.5   Summary: Hall effect measurements

The transport properties of ZnO thin films grown on *c*-plane sapphire were studied by the Hall effect (van der Pauw configuration). The two-terminal resistance of the In pads serving as ohmic contacts was found to improve with the insertion of a low-temperature buffer layer, and after annealing at 600 °C in argon.

The dependence of the carrier mobility with carrier concentration was plotted. For $n < 3.7 \bullet 10^{17}$ cm^{-3}, the mobility increases with carrier concentration; this was explained in

terms of electron transport across grain boundaries. Furthermore, the mobility at $n = 3.4\bullet10^{18}$ cm^{-3} is seen higher than the mobilities at $n = 1.2\bullet10^{17}$ and $1.7\bullet10^{17}$ cm^{-3}, but lower than the mobilities at $n = 3.7\bullet10^{17}$ and $4.7\bullet10^{17}$ cm^{-3}; this may be attributed to large concentrations of impurity clusters impacting the mobility according to ionized impurity scattering. Having said that, band bending was calculated to indeed take place at $n = 3.4\bullet10^{18}$ cm^{-3}, and the mobility for n > $3.7\bullet10^{17}$ cm^{-3} may be defined by the combination of electron transport across grain boundaries and ionized impurity scattering.

Variable temperature conductivity measurements between 290 and 80 K were presented for two samples having different carrier concentrations (H50, $3.4\bullet10^{18}$ cm^{-3}; H62, $4.7\bullet10^{17}$ cm^{-3}). Arrhenius plots between 290 and 169 K yielded donor energies of 6 and 18 meV, respectively; the latter is fairly close to the reported zinc interstitial energy of 30 meV, while the former betrays the formation of an impurity band at high carrier concentrations. The conductivity data between 169 and 80 K showed that the conductivity of H50 and H62 was best described by variable-range hopping, and the corresponding Mott parameters were calculated. The presence of impurity bands was paralleled to the Urbach tail E_0 parameters measured for samples deposited in this work on glass slides.

Part II: Pd Schottky barrier diode

9.6   Experimental procedure

The Pd Schottky barrier diode (SBD) was fabricated on a ZnO sample deposited on an n^+-GaAs 2 ° off (100) substrate with the same two-step growth process outlined in section 7.2.4. The sample thickness was estimated to be 2 µm. The sample was cleaned following the same procedure used for substrate degreasing: 2 x boiling in high purity trichloroethylene, 2 x boiling in high purity acetone, 2 x boiling in high purity methanol, rinsing in 18 MΩ deionized water, and drying in nitrogen flow. The low resistance back contact was then fabricated by soldering indium (In) with an iron set at 450 °C.

Palladium (Pd) was chosen as Schottky contact for this diode. It is known that chemical reactions between the metal and the semiconductor and diffusion of the metal into the semiconductor are bound to impact the formation of Schottky contacts. This is much more striking in II-VI semiconductors than in III-V materials (Brillson, 1982). Aluminium would therefore be inappropriate for the ZnO system, as it would react with the oxygen atoms in ZnO to generate a large concentration of dissociated zinc cations, resulting in low n-type barrier heights (Sheng *et al.*, 2002). An inert metal such as Au, Ag, Pt, or Pd would be more preferable.

The literature only reports a handful of articles dealing with the fabrication of SBDs on ZnO. While a couple of publications dealing with Au and Ag have been published (e.g. Polyakov *et al.*, 2003 and Coppa *et al.*, 2003), the author could only find one report of Pd SBD on ZnO (von Wenckstern *et al.*, 2004). This provided further incentive to investigate the Pd SBD on ZnO.

The melting point of Pd is 1554 °C. Pd dots of radius $0.25 \bullet 10^{-3}$ m were evaporated through a shadow mask onto the ZnO/n^+-GaAs structure by resistive heating. Resistive heating offers a strong advantage over electron-gun metallisation; despite the presence of a baffle aiming to redirect most electrons escaping from the magnetic field when using

the e-gun, there may still be a fraction of electrons impinging onto the sample during the metallization process, thereby damaging it. Such sample damage would of course not occur with resistive heating. Figure 9.10 schematically represents the SBD fabricated for this investigation.
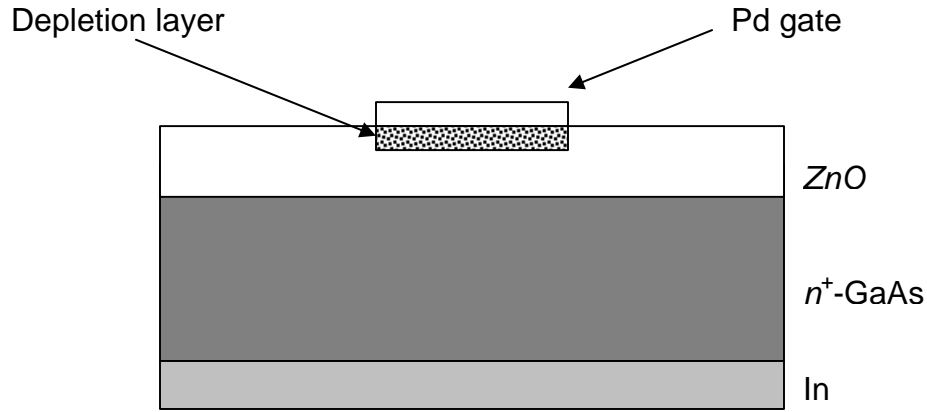
Figure 9.10: Pd SBD on ZnO/n^+-GaAs

Four gates were evaporated onto the ZnO sample. They proved to be of equal worth; the results to be presented in sections 9.7 and 9.8 are therefore representative of all four gates.

9.7   Ideality factor and barrier height

The height of the barrier that an electron faces when traveling from the metal to the semiconductor is called the effective barrier height ϕ_B. Assuming that thermionic emission prevails, the transport of carriers over the top of the barrier of height ϕ_B is described by (Schroder, 1998)

$$I = \left[AA^*T^2 \exp\left(-\frac{q\boldsymbol{f}_B}{kT}\right)\right]\left(\exp\frac{qV}{kT} - 1\right) \qquad \text{...(9.25)}$$

where I is the diode current, A the diode area, q the electron charge, k Boltzmann's constant, T the absolute temperature, V the applied bias, and A^* the effective Richardson constant given by

$$A^* = 4\pi q m^* / h^3 \qquad \text{...(9.26)}$$

According to Sze (1981), A^* is equal to 32 $\text{Acm}^{-2}\text{K}^{-2}$ for ZnO. It should however be noted that an experimental value of A^* has yet to be reported.

Equation 9.25 can be simplified, since the –1 term can be ignored for $V \gg 3kT/q$ (Sze, 1981). Equation 9.25 then yields

$$\ln I = \left[\frac{q}{kT}\right]V + \left[-\ln(AA^*T^2)\frac{q\mathbf{f}_B}{kT}\right] \qquad \text{...(9.27)}$$

A plot of $\ln I$ vs. V should therefore yield a straight line of gradient m equal to q/kT. This only holds if the saturation current $I_s = AA^*T^2\exp\left(-\frac{q\mathbf{f}_B}{kT}\right)$ is independent of the applied bias V for V larger than a few kT/q. Furthermore, this will only take place if ϕ_B is independent of the external bias, as outlined by the pure thermionic emission model. In reality, factors such as non-ideal carrier transport mechanisms are bound to cause deviations from theory, and the impact of these factors is carried over to the experimental data by adding a dimensionless parameter called the ideality factor n. The thermionic current-voltage relationship of a SBD is then given by

$$I = \left[AA^*T^2\exp\left(-\frac{q\mathbf{f}_B}{kT}\right)\right]\left(\exp\frac{qV}{nkT}-1\right) \qquad \text{...(9.28)}$$

and the ideality factor n is related to the slope m of the $\ln I - V$ curve by

$$n \equiv \frac{q}{kT}\frac{\partial V}{\partial(\ln I)} = \frac{q}{kT}\left(\frac{1}{m}\right) \qquad \text{...(9.29)}$$

Finally, the barrier height at zero bias conditions can be determined by extrapolating the $\ln I - V$ cuve to $V = 0$. The following expression is obtained:

$$\ln I = \ln I_S = -\ln\left(AA^*T^2\right)\frac{qf_B}{kT} \qquad \text{...(9.30)}$$

which leads to

$$f_B = \frac{kT}{q}\ln\left(\frac{AA^*T^2}{I_S}\right) \qquad \text{...(9.31)}$$

Figure 9.11 shows the room temperature current-voltage curve of the Pd SBD on ZnO/n^+-GaAs.
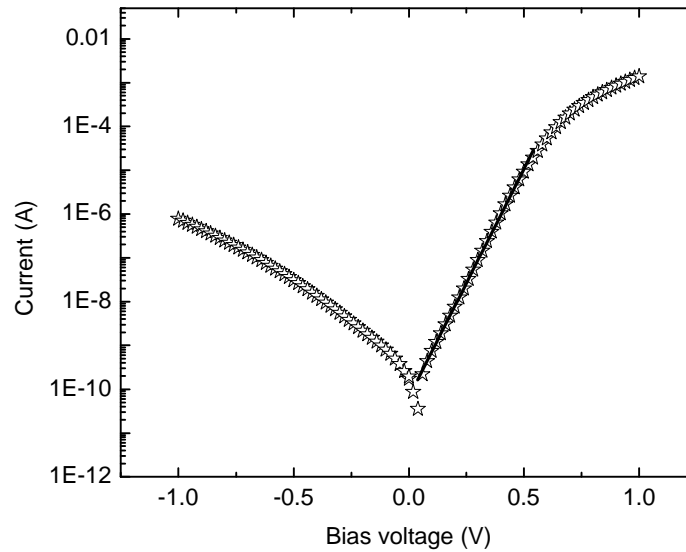
Figure 9.11: **Current-voltage curve of Pd SBD on ZnO/n^+-GaAs**

The plot shows a linear relation between current and voltage over five orders of magnitude; the deviation from linearity for voltages larger than 0.5 V is attributed to series resistance. The linear fit between 0.08 and 0.50 V yields an ideality factor of 1.6 ± 0.2, and a barrier height of 0.83 eV. Table 9.6 summarizes the reported ideality factors

and barrier heights for SBDs on ZnO. As can be seen from table 9.6, the ideality factor measured here (1.6 ± 0.2) falls well within reported values for SBDs on ZnO, and is close to the value reported by von Wenckstern *et al.* (1.4) for their Pd SBDs on ZnO thin films. These idealities do not, however, match ideality factors for GaN, where idealities as low as 1.002 have been reported (Tracy *et al.*, 2003). The high idealities of SBDs on ZnO can be explained by the prevalence of tunneling, the impact of interface states, or the influence of deep recombination centers (Polyakov *et al.*, 2003).

ZnO is an ionic semiconductor, and the Schottky-Mott model should therefore serve to explain the barrier formation and barrier height of the material (Kurtin *et al.*, 1969). The barrier height is then given by the difference between the metal work function and the semiconductor electron affinity. A barrier height of ~ 1.02 eV is therefore expected for the Pd/ZnO SBD, since Pd has a work function of 5.12 eV, and ZnO an electron affinity of 4.1 eV (Liang *et al.*, 2001). The barrier height measured here (0.83 eV) is lower than the theoretical value, but close to von Wenckstern *et al.*'s reported barrier heights (0.79 and 0.84 eV). The difference between theory and experiment has also been attributed by Polyakov *et al.* to the presence of interface defect states.

METAL	IDEALITY FACTOR	BARRIER HEIGHT (eV)	COMMENTS REFERENCE
Ag	1.33	0.83	TF; Sheng *et al.*, (2002)
	1.6 – 1.8	0.68 – 0.69	B; Polyakov *et al.* (2003)
	1.4	0.76	TF; von Wenckstern *et al.*, 2004
	1.5	0.76	SC; von Wenckstern *et al.*, 2004
	> 2	-	SC wafers; Coppa *et al.*, 2003
	1.86	0.67	plasma-cleaned wafers; Coppa *et al.*, 2003
	1.6 – 1.8	0.64 – 0.65	B; Polyakov *et al.* (2003)
	2.7	-	PC; Fabricius *et al.*, 1986
Ni	1.7	-	SC; von Wenckstern *et al.*, 2004
Pd	**1.4**	**0.79**	**TF; von Wenckstern *et al.*, 2004**
	1.75	**0.84**	**SC; von Wenckstern *et al.*, 2004**
Pt	1.704	0.613	TF; Ip *et al.*, 2004

Table 9.6: Reported ideality factors and barrier heights for SBDs on ZnO
(TF = thin films, SC = single crystals, PC = polycrystalline samples, B = bulk material)

9.8　Carrier concentration

The carrier concentration of a semiconductor may be obtained from the capacitance – voltage measurements of a Schottky barrier diode. Consider a SBD on an n-type semiconductor with doping density n_D. A dc bias V applied to the SBD will generate a space charge region of width W. The capacitance C is obtained by superimposing a small-amplitude ac voltage on the dc voltage V, and the differential capacitance of the space charge region is

$$C = \frac{dQ_S}{dV} \qquad \qquad \text{...(9.32)}$$

where Q_S is the semiconductor charge. In order for overall charge neutrality to hold, the charge increment dQ_m added to the metal contact as the ac voltage rises must be counterbalanced by an equal and opposite charge increment dQ_S, where (Schroder, 1998)

$$dQ_S = qAn_D(W)dW \qquad \qquad \text{...(9.33)}$$

This is accurate if the electron and hole concentrations are assumed to be zero in the space charge region, and if the acceptor concentration is taken to be zero for an n-type semiconductor. Additionally, all donor levels are taken to be ionized at the measurement temperature (room temperature in this case).

The charge increment dQ_S is then generated by enlarging the width of the space charge region by an amount dW. Combining equations 9.32 and 9.33, the following expression is obtained,

$$C = \frac{dQ_S}{dV} = qAn_D(W)\frac{dW}{dV} + qAW\frac{dn_D(W)}{dV} \qquad \qquad \text{...(9.34)}$$

The differential $\dfrac{dn_D(W)}{dV}$ is set equal to zero as it is assumed that the doping density is constant over the distance dW, or cannot be derived from the capacitance-voltage method; equation 9.34 can therefore be simplified to

$$C = \frac{dQ_S}{dV} = qAn_D(W)\frac{dW}{dV} \qquad \qquad \textbf{...(9.35)}$$

Furthermore, if the reverse bias SBD is taken to be a parallel plate capacitor,

$$C = \frac{ee_0 A}{W} \qquad \qquad \textbf{...(9.36)}$$

where e is the dielectric constant of the semiconductor and e_0 the permittivity of vacuum. Equation 9.36 can then be differentiated with respect to voltage to give

$$n_D(W) = \frac{C^3}{qee_0 A^2 dC/dV} \qquad \qquad \textbf{...(9.37)}$$

which yields

$$n_D(W) = -\frac{2}{qee_0 A^2 d(1/C^2)/dV} \qquad \qquad \textbf{...(9.38)}$$

The doping density of the semiconductor can thus be calculated by inserting the slope of the $1/C^2$-V linear plot into equation 9.38. Figure 9.12 shows the capacitance voltage and $1/C^2$-V curves of the Pd SBD.
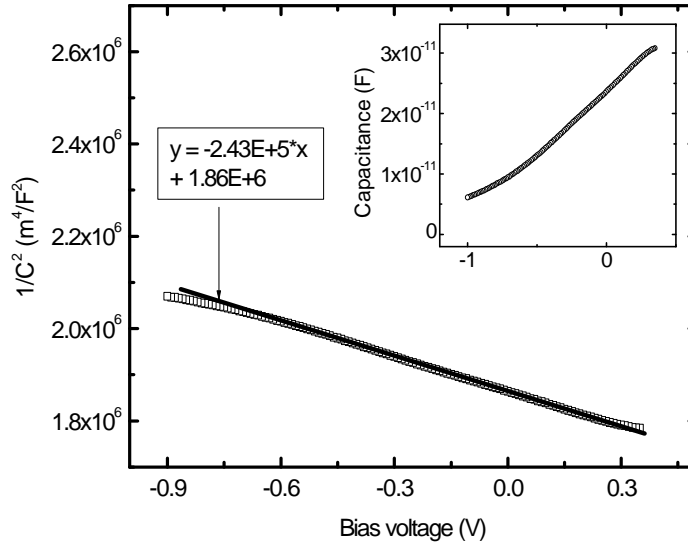
Figure 9.12: Capacitance-voltage and $1/C^2$-V curves for Pd SBD

The effective carrier concentration of the sample is calculated to be $7 \bullet 10^{17}$ cm^{-3}, in close agreement with the carrier concentration obtained from Hall measurements on a sample deposited on *c*-plane sapphire in similar conditions ($8 \bullet 10^{17}$ cm^{-3}).

9.9   Summary: Pd Schottky barrier diode

Pd Schottky contacts of radius $0.25 \bullet 10^{-3}$ m have been successfully evaporated by resistive heating on a ZnO/n^+-GaAs structure. The resulting Schottky barrier diode was characterized by current-voltage and capacitance-voltage measurements. The current-voltage curve of the diode displayed the rectifying attributes of the Pd contact, and yielded barrier height and ideality values of 0.83 eV and 1.6, respectively. These results are similar to literature values for SBDs on ZnO. From the $1/C^2$ - V curve, the effective electron concentration of the depletion region was calculated to be $(8 \pm 0.8) \bullet 10^{17}$ cm^{-3}, in close agreement with the carrier concentration obtained from Hall measurements ($7 \bullet 10^{17}$ cm^{-3}).

10. Conclusions and Further Work

Conclusions

ZnO thin films have been successfully deposited by metalorganic chemical vapor deposition on several different substrates using diethyl zinc and *tert*-butanol as zinc and oxygen precursors, respectively. The emphasis of the work rested on the influence of the growth parameters on the sample properties, which were studied by a variety of techniques.

To the author's knowledge, this is the first investigation of the growth process of ZnO epilayers by Second Harmonic Generation Imaging, a novel structural characterization technique employed to generate sample images. ZnO thin films deposited on *n*-Si 2 ° off (100), amorphous glass, and *n*-GaAs (100) substrates were probed. Beginning with the ZnO on Si system, the thickness dependence of the SH signal originating from the epilayers proved their polycrystalline nature. Furthermore, a 1 μm thick sample displayed microcrystallites scattered across the substrate; these microcrystallites are believed to act as seeds during film growth, and are characteristic of the Stranski-Krastanov growth mode. Moreover, the images of thicker samples exhibited distinct macrostructures, whose nature and origin should be relevant to industry workers seeking to incorporate ZnO in silicon-based heterostructures. Furthermore, the images of samples grown on amorphous glass revealed differences in SH response across the probed area; this is believed to stem from a gas side flux associated with the reactor geometry. The impact of the side flux was also seen in optical micrographs of ZnO samples grown on GaAs, as the images displayed a clear color gradient across the epilayer surface. The yellow-brown edge of the samples may be attributed to a high concentration of oxygen vacancies. Adopting a single inlet horizontal reactor tube should quench the impact of the side flux on surface homogeneity. Finally, the ZnO on GaAs surfaces revealed the presence of amorphous particles, which are believed to stem from incomplete gas phase reactions between the precursors. These amorphous particles may be partly responsible

for the lower quality of ZnO samples grown on GaAs compared to Si as revealed by photoluminescence spectroscopy.

The influence of substrate temperature on the structural properties of ZnO thin films grown on Si substrates was investigated by growing a series of layers between 300 and 600 °C on n-Si 2 ° off (100) substrates, recording their X-ray diffraction spectra, and taking optical micrographs of their surfaces. The self-texture, tensile strain, grain size, and preferred orientation quality of the samples were found to greatly depend on the growth temperature. Thin films deposited between 350 and 525 °C displayed the favorable c-axis orientation, with the c-axis perpendicular to the substrate and elongated, and with compressive forces acting in the plane of the film. The full-width at half-maximum of the dominant (002) peak was found to be as narrow as 0.17 °, an improvement compared to literature values for ZnO layers grown both by MOCVD and by other techniques. The films' grain size averaged 52 nm from 350 to 525 °C, reflecting the high structural quality of the samples. The variation of growth rate with substrate temperature could be divided into three zones. The growth rate increased from 1.9 to 5.0 µm/hr as the temperature rose from 300 to 400 °C; in this region, film growth was controlled by mass transfer and reaction kinetics. An activation energy of 0.3 eV was calculated from the Arrhenius plot. The growth rate then remained stable from 400 to 450 °C; in this region, film growth was limited by the concentration of reactants at the surface. The growth rate then decreased above 450 °C as a result of the reaction intermediates cracking in the gas phase before reaching the substrate surface. A negative activation energy of – 0.8 eV was calculated from the 450 to 500 °C data. Furthermore, the temperature dependence of the surface morphologies of the layers was paralleled to Movchan and Demchishin's three-zone model. Below 400 °C, the surfaces exhibited a zone 1 morphology characterized by poor lateral strength. The voids separating the crystals began to fill with increasing temperature and from 400 to 500 °C, the films displayed smooth surfaces of densely packed grains characteristic of zone 2 surfaces. Above 500 °C, the surfaces showed an increase in roughness typical of the sintering

coalescence process that takes place in zone 3 layers as a result of high substrate temperatures. The optimum growth temperature range is concluded to be 450 – 500 °C.

Moreover, the influence of the VI:II ratio during growth on the structural and optical properties of ZnO thin films deposited on amorphous glass slides was investigated, for a series of layers grown at VI:II ratios of 60, 35, 18, and 10:1. The position of the (002) peak observed by X-ray diffraction was seen to shift to higher values with decreasing VI:II ratio; this can be explained by a higher concentration of oxygen vacancies at low VI:II ratios. The largest grain size (31 nm) was measured at a VI:II ratio of 18:1. The band gap energies of the four samples were calculated from the transmission curves, and found to be 3.21, 3.23, 3.24, and 3.22 eV at VI:II ratios of 60, 35, 18, and 10:1, respectively. The increase in band gap energy as the VI:II ratio decreased from 60 to 18:1 was attributed to the Burnstein-Moss shift; the corresponding carrier concentrations were calculated to be $5.2 \bullet 10^{17}$, $2.7 \bullet 10^{18}$, and $4.2 \bullet 10^{18}$ cm^{-3}, respectively, in close agreement with carrier concentrations obtained by Hall measurements on samples grown on *c*-plane sapphire. The band gap energy shift, in reference to undoped ZnO, of the film deposited at a ratio of 10:1 was lower than expected, and betrayed the merging of the impurity band with the conduction band. The carrier concentration of this sample was calculated from Stern and Talley's impurity model, and found to be $9.4 \bullet 10^{19}$ cm^{-3}; the carrier concentration is therefore seen to increase by over two orders of magnitude as the VI:II ratio during growth decreases from 60 to 10:1. This seems to corroborate a model suggested in 2003 by Tüzemen *et al.;* they asserted that oxygen vacancies act as a source of free electrons at sample temperatures above 210 K.

Furthermore, the influence of the substrate on the band gap energies was studied. Considering that the films were deposited at a substrate temperature of 450 °C, it was calculated that the thermal mismatch strains lead to an increase in band gap of 40 meV. Moreover, the nature of the transition observed by the transmission measurements was investigated; it was found that the band gap energies calculated correspond to a transition between a donor level located 0.18 eV below the conduction band and the valence band. Taking into account the influence of the thermal mismatch strains described above, the

band gap energies were corrected and given as 3.35, 3.37, 3.38, and 3.36 eV at VI:II ratios of 60, 35, 18, and 10:1, respectively. These values are similar to the band gap energy of 3.35 eV calculated by photoluminescence spectroscopy on a sample deposited on an *n*-Si 2 ° off (100) substrate.

Furthermore, the purity of the samples was studied by calculating the Urbach tail E_0 parameter from the absorption coefficient curves. The lowest E_0 parameter (254 meV) corresponding to the purest sample was obtained for the thin film deposited at a VI:II ratio of 18:1. The higher E_0 parameter of the layer deposited at a VI:II ratio of 10:1 (338 meV) was explained in terms of an extremely high concentration of oxygen vacancies, while the large E_0 parameters of the layers grown at VI:II ratios of 35 and 60:1 (312 and 343 meV, respectively) were attributed to the formation of oxygen gas, micro voids, and other oxygen-related defects in the material. These micro voids were apparent on the surfaces of samples deposited at high VI:II ratios on *n*-GaAs (100) substrates.

The influence of both the substrate temperature and the VI:II ratio during growth on the sample properties was also reflected in the photoluminescence spectra of ZnO layers grown on *n*-GaAs (100), recorded at 12 and 300 K. Beginning at 12 K, the scans of samples deposited at 300 and 400 °C were dominated by a broad, defect-related, blue-violet band that may be linked with the presence of zinc vacancies in the material. At 450 and 500 °C, the spectra showed a strong donor-bound exciton (D°X) peak at 3.36 eV. The width of the band was 30 and 25 meV at 450 and 500 °C, respectively. The sample grown at 600 °C, on the other hand, exhibited a much wider band (80 meV); depth profiling performed by Auger spectroscopy betrayed a broadening of the Zn/Ga interface at 600 °C compared to lower growth temperatures. These Ga atoms were partly responsible for the larger band, as they are known to create donor levels in the ZnO band gap. Furthermore, energy-dispersion X-ray spectroscopy proved that the sample grown at 600 °C had a lower oxygen content than the layers deposited at lower temperatures; this further reduced the optical quality of the sample grown at 600 °C.

Following the reduction in electron concentration with increasing VI:II ratio observed on ZnO samples deposited on glass slides, it was seen that the 12 K photoluminescence spectra of layers grown on *n*-GaAs (100) at high VI:II ratios (35:1 and above) displayed a band at 3.23 eV absent at lower VI:II ratios. This emission band is believed to correspond to the donor-acceptor pair (DAP) band observed on *p*-type ZnO films deposited on GaAs substrates by other workers. The intensity of this DAP band relative to the D°X band also strongly increased after high-temperature annealing in argon, as a result of As diffusion from the substrate into the epilayer. Nevertheless, layers grown on *n*-GaAs (100) displayed *n*-type conductivity. A maximum room temperature mobility of 7 cm^2/Vs was measured. Furthermore, the influence of the purity of the *tert*-butanol (TBOH) source on the room temperature spectra was tested; both the samples grown with 6N- and 3N-TBOH displayed a strong single emission band at 3.27 eV due to a donor-bound exciton. The width of the NBE band of the 3N-sample was 151 meV, compared to 128 meV for the 6N-layer. The larger width of the NBE band of the 3N-sample reflects the presence of the impurities found in the source. Nevertheless, the defect-related ZnO green band was weak in comparison to the D°X band in both samples, a sign of strong optical quality. This suggests that 3N-TBOH can be used as a cheap oxidizing agent for the MOCVD growth of ZnO thin films. Finally, the structural and optical properties of the samples could be improved by depositing an amorphous ZnO buffer layer under the main layer. The buffered layer grown with 3N-TBOH exhibited an improved NBE full-width at half-maximum (139 meV) compared to the non-buffered sample (151 meV). This improvement was paralleled to the improved cross-section of the buffered layer compared to the non-buffered sample, as shown by transmission electron microscopy images. Indeed, the buffer inhibited the formation of erosion pits, and led to improved adhesion properties.

Having studied the impact of various growth parameters on the quality of ZnO thin films, their optical and electrical properties were systematically studied by variable temperature photoluminescence and Hall measurements. Variable temperature photoluminescence spectra were recorded and a sample deposited at 425 °C on *n*-Si 2 ° off (100). At 12 K, the spectra showed four emission bands at 3.36, 3.32, 3.25, and 3.17 eV assigned to a

donor-bound exciton (D°X), donor-acceptor pair (DAP), and the 1LO- and 2LO- phonon replica of the donor-acceptor pair. The bands decreased in intensity and merged with increasing temperature, and emission from a free exciton and a free electron-neutral acceptor complex (eA°) dominated the PL spectra from 80 to 100 K. From the position of the eA° band, it appears that the acceptor level is located about 93 meV above the valence band, an acceptable value considering that the shallow donors in the ZnO band gap are believed to be 30 - 40 and 60 – 70 meV below the conduction band. From 125 K onwards, the photoluminescence spectra displayed a single emission band due to a free exciton. The width of the free exciton band and the intensity ratio between the ultraviolet band and the defect-related green band at room temperature were 104 meV and 28:1, respectively, confirming the high quality of the films grown in this work.

Hall measurements were performed on samples deposited at 450 °C on c-plane sapphire substrates. The two-terminal resistances of the indium contacts soldered onto the samples could be strongly reduced by introducing a low-temperature buffer between the substrate and the main epilayer. It was nevertheless necessary to anneal the contacts at 600 °C in argon in order to obtain resistances in the kΩ range. The room temperature transport properties of the samples were studied, and the graph of mobility vs. carrier concentration plotted. The increase in mobility with carrier concentration for $n < 3.7 \bullet 10^{17}$ cm^{-3} was explained in terms of transport across grain boundaries. The carrier mobility at $n = 3.4 \bullet 10^{18}$ cm^{-3} was lower than expected. This was attributed to the formation of impurity clusters, and therefore enhanced ionized impurity scattering at high carrier concentrations. The transport properties of this sample may be determined by a combination of electron transport across grain boundaries and ionized impurity scattering. The electrical conduction properties between 290 and 80 K of two ZnO thin films deposited on c-plane sapphire were investigated. The Arrhenius plot of the conductivity data between 290 and 169 K yielded a donor energy of 18 meV, smaller than the literature values of 30 – 40 meV. The donor level in question is believed to originate from zinc interstitials. The conductivity data between 169 and 80 K revealed that the conduction properties of samples of concentration $4.7 \bullet 10^{17}$ and $3.4 \bullet 10^{18}$ cm^{-3}

were at least partly described by variable-range hopping between localized states; the corresponding Mott parameters were calculated.

Finally, a Pd Schottky barrier diode was fabricated on a ZnO thin film deposited on n^+-GaAs 2 ° off (100). A barrier height of 0.86 eV and an ideality factor of 1.6 were calculated from the measured current–voltage curve. Capacitance–voltage measurements yielded a carrier concentration in the depletion region of $8 \bullet 10^{17}$ cm^{-3}.

Further work

Having established the worth of *tert*-butanol as oxidizing agent and having thoroughly described the properties of the ZnO thin films deposited in this work, there nevertheless remain several challenges requiring further attention.

The variable temperature photoluminescence spectra of a ZnO layer on *n*-Si 2 ° off (100) were studied. The spectrum recorded at 12 K displayed a strong emission band at 3.32 eV, which was attributed to a donor-acceptor pair from the temperature dependence of its peak position and peak energy. Nevertheless, the experimental set-up at hand only allowed a study of the laser dependence of the peak position over two orders of magnitude, which is insufficient to conclude with absolute confidence that this band originates from a donor-acceptor pair transition. It would be beneficial to advance this study by employing a laser exhibiting a higher excitation power. Furthermore, the depth of the acceptor involved in this donor-acceptor pair transition was found to be approximately 93 meV; this is a reasonable value, as it makes the acceptor deeper than the shallow donors commonly found in ZnO. Nevertheless, the nature of the acceptor could not be deduced from the photoluminescence spectra, and further work is required to discover its origin.

The influence of the VI:II ratio during growth on sample properties has been investigated, and it was found that the samples' free electron concentration can be decreased by two orders of magnitude by increasing the VI:II ratio from 10 to 60:1; furthermore, layers

deposited at high VI:II ratios began displaying photoluminescence properties associated with *p*-type ZnO. Nevertheless, the layers still showed *n*-type conductivity; the next step in trying to achieve *p*-ZnO should involve introducing a dopant such as As or N during growth. Ion implantation should also be tested.

A Pd Schottky barrier diode was successfully fabricated on a ZnO sample grown on n^+-GaAs 2 ° off (100). The ideality factor and barrier height measured agreed well with literature values, which warrants the further use of palladium for SBDs on ZnO. On the other hand, the leakage currents observed were too high to perform deep level transient spectroscopy measurements on as-grown material. Exposing the SBDs to hydrogen plasma may reduce the leakage currents by several orders of magnitude, thus enabling DLTS measurements to be performed. Further work would also entail optimizing the sample quality from the experience acquired so far in this project, and testing other metals to improve the diodes.

Finally, ZnO can serve as transparent window for solar cells, and collaboration with research centers that are investigating the fabrication of solar modules in South Africa may result in improved efficiencies and reduced operating costs.

The future of ZnO is bright. Opportunities seldom knock twice – now is the time to give our best, and to give it lavishly.

REFERENCES

Akasaki I., Amano H., Yito M., and Mramatsu K., *J. Luminesc.* **48/49** (1991) 666

Alfa Catalogue, *Organometallics for Electronics*, Ventron Corporation, USA, 1978

Allen P. B. and Cardona M., *Phys. Rev. B* **23** (1981) 1495

Amano H., Akasaki I., Hiramatsu K., Koide N., and Sawaki N., *Thin Solid Films* **163** (1988) 415

Askerov B. M., *Electron Transport Phenomena in Semiconductors*, World Scientific, Singapore, 1994

Ataev B. M., Lundin W. V., Mamedov V. V., Bagamadova A. M., and Zavarin E. E., *J. Phys.: Condens. Matter.* **13** (2001) L211

Ayouchi R., Martin F., Leinen D., and Ramos-Barrado J. R., *J. Cryst. Growth* **247** (2003) 497

Bachari E. M., Baud G., Ben Amor S., and Jacquet M., *Thin Solid Films* **348** (1999) 165

Bang K.-H., Hwang D.-K., Lim S.-W., and Myoung J.-M., *J. Cryst. Growth* **250** (2003) 437

Basak D., Amin G., Mallik B., Paul G. K., and Sen S. K., *J. Cryst. Growth* **256** (2003) 73

Bateman T. B., *J. Appl. Phys.* **33** (1962) 3309

Bauer E., *Z. Kristallogr.* **110** (1958) 372

Bethke S., Pan H., and Wessels B. W., *Appl. Phys. Lett.* **52** (1988) 138

Blakemore J. S., *Semiconductor Statistics*, New York : Dover Publications, 1987

Brillson L. J., *Surf. Sci. Rep.* **2** (1985) 295

Burstein E., *Phys. Rev.* **93** (1954) 632

Carcia P. F., Li Z. G., and van Kesteren H. W., *Thin Solid Films* **246** (1994) 126

Chen Y., Bagnall D. M., Koh H. –J., Park K. –T., Hiraga K., Zhu Z., and Yao Y., *J. Appl. Phys.* **84** (1998) 3912

Chen M., Pei Z. L., Wang X., Yu Y. H., Liu X. H., Sun C., and Wen L. S., *J. Phys. D: Appl. Phys.* **33** (2000) 2538

Chen J. and Fujita T., *Japan. J. Appl. Phys.2* **41** (2002) L203

Chen J., Shen W. Z., Chen N. B., Qiu D. J., and Wu H. Z., *J. Phys.: Condens. Matter.* **15** (2003) L475

Cho A., *J. Vac. Sci. Technol.* **8** (1971) S31

Choopun S., Vispute R. D., Noch W., Balsamo A., Sharma R. P., Venkatesan T., Iliadis A., and Look D. C., *Appl. Phys. Lett.* **75** (1999) 3947

Chopra K. L., Major S., and Pandya D. K., *Thin Solid Films* **102** (1983) 1

Coppa B. J., Davis R. F., and Nemanich R. J., *Appl. Phys. Lett.* **82** (2003) 400

Cullity B.D., *Elements of X-ray diffraction*, Addison-Wesley Pub. Co., 1967

Dakhovskii I. V., Polyanskaya T. A., Samoilovich A. G., and Shartsev Y. V., *Sov. Phys.-Semicond.* **4** (1971) 1857

Davis E. A. and Mott N. F., *Phil. Mag.* **22** (1970) 903

D. Paraguay F., Morales J., L. Estrada W., Andrade E., and Miki-Yoshida M., *Thin Solid Films* **366** (2000) 16

Desgreniers S., *Phys. Rev. B* **58** (1998) 14102

Döhler G. H., *IEEE J. Quantum Electron.* **QE-22** (1986) 1682

Doumuki T., Tamada H., and Saitoh M., *Appl. Phys. Lett.* **65** (1994) 2519

Eagles D. M., *J. Phys. Chem. Sol.* **16** (1960) 76

Ellmer K., *J. Phys. D: Appl. Phys.* **34** (2001) 3097

Ermoshin V. A. and Veriazov V. A., *Phys. Stat. Sol. (b)* **189** (1995) K49

Evans P. V. and Nelson S. F., *J. Appl. Phys.* **69** (1991) 3605

Fabricius H., Skettrup T., and Bisgaard P., *Appl. Opt.* **25** (1986) 2764

Fischetti M. V., *Phys. Rev. B* **44** (1991) 5527

Fouquet J. E. and Siegman A. E., *Appl. Phys. Lett.* **46** (1985) 280

Frank F. C. and van der Merwe H. J., Proc. Roy. Soc. London, Ser. A **198** (1949) 205

Fu Z.-X., Guo C.-X., and Liao G.-H., *Chin. Phys. Lett.* **15** (1998) 457 (a)

Fu Z., Lin B, Liao G., and Wu Z., *J. Cryst. Growth* **193** (1998) 316 (b)

Fujimura N., Nishihara T., Goto S., Xu J., and Ito T., *J. Cryst. Growth* **130** (1993) 269

Ghosh S., Sarkar A., Chaudhuri S., and Pal A. K., *Thin Solid Films* **205** (1991) 64

Gorla C. R., Emanetoglu N. W., Liang S., Mayo W. E., Lu Y., Wraback M, and Shen H., *J. Appl. Phys.* **85** (1999) 2595

Gu S., Zhang R., Sun J., Zhang L., and Kuech T. F., *Appl. Phys. Lett.* **76** (2000) 3454

Guo L., Yang S., Yang C., Yu P., Wang J., Ge W., and Wong G. K. L., *Appl. Phys. Lett.* **76** (2000) 2901

Guo X.-L., Tabata H., and Kawai T., *J. Cryst. Growth* **223** (2001) 135

Gupta T. K., *J. Am. Ceram. Soc.* **73** (1990) 1817

Gupta V. and Mansingh A., *J. Appl. Phys.* **80** (1996) 1063

Guyot-Sionnest P. and Shen Y. R., *Phys. Rev. B* **38** (1988) 1985

Hahn B., Heindel G., Pschorr-Schoberer E., and Gebhardt W., *Semicond. Sci. Technol.* **13** (1998) 788

Handbook of Chemistry and Physics, 57th ed., 1977

Hausmann A. and Teuerle W., *Z. Phys.* **257** (1972) 299

Heavens O. S., *Optical properties of thin solid films*, Dover New York, p. 74, 1964

Heiland G., Mollow E., and Stockmann F., *Sol. State Phys.* **8** (1959) 191

Hill R. M., *Phil. Mag.* **24** (1971) 1307

Hofmann D. M., Hofstaetter A., Leiter F., Zhou H., Henecker F., Meyer B. K., Orlinskii S. B., Schmidt J., and Baranov P. G., *Phys. Rev. Lett.* **88** (2002) 5504

Huang M. H., Mao S., Feick H., Yan H., Wu Y., Kind H., Weber E., Russo R., and Yang P., *Science* **292** (2001) 1897

Hutson A. R., *Phys. Rev.* **108** (1957) 222

Ibach H., *Phys. Status Solidi* **33** (1969) 257

Ip K., Heo Y. W., Baik K. H., Norton D. P., Pearton S. J., Kim S., LaRoche J. R., and Ren F., *Appl. Phys. Lett.* **84** (2004) 2835

Jaffe J. E. and Hess A. C., *Phys. Rev. B* **48** (1993) 7903

Jin Z. – C., Hamberg I., and Granqvist C. G., *J. Appl. Phys.* **64** (1988) 5117

Jin B. J., Bae S. H., Lee S. Y., and Im S., *Mat. Sci. Eng. B* **71** (2000) 301

Karpina V. A., Lazorenko V. I., Lashkarev C. V., Dobrowolski V. D., Kopylova L. I., Baturin V. A., Pustovoytov S. A., Karpenko A. Ju., Eremin S. A., Lytvyn P. M., Ovsyannikov V. P., and Mazurenko E. A., *Cryst. Res. Technol.* **39** (2004) 980

Karzel H., Potzel W., Köfferlein M., Schiessl W., Steiner M., Hiller U., Kalvius G. M., Mitchell D. W., Das T. P., Blaha P., Schwarz K., and Pasternak M. P., *Phys. Rev.* B **53** (1996) 11425

Kawasaki M., Ohtomo A., Shiroki R., Ohkubo I., Kimura H., Isoya G., Yasuda T., Segawa Y., and Koinuma H., *Extended Abstracts of the 1998 International conference on Solid State Devices and Materials*, Business Center, Academic Society of Japan, Hiroshima, Japan, 1998

Kim Y., Hunt W. D., Hickernell F. S., and Higgins R., *J. Appl. Phys.* **75** (1994) 7299 (a)

Kim Y. J. and Kim H. J., *Materials Lett.* **21** (1994) 351 (b)

Kim K. H., Park K. C., and Ma D. Y., *J. Appl. Phys.* **81** (1997) 7764

Kim H.-K., Han S.-H., Seong T.-Y., and Chooi W.-K., *Appl. Phys. Lett.* **77** (2000) 1647

Kim S. Y., Jang H. W., Kim J. K., Jeon C. M., Park W. I., Yi G.-C., and Lee J.-L., *J. Electronic Mat.* **31** (2002) 868

Kino G. S. and Wagers R. S., *J. Appl. Phys.* **44** (1973) 1480

Kirchner C., Gruber Th., Reuβ F., Thonke K., Waag A., Gieβen Ch., and Heuken M., *J. Cryst. Growth* **248** (2003) 20

Knuyt G., Quaeyhaegens C., D'Haen J., and Stals L. M., *Thin Solid Films* **258** (1995) 159

Ko H. J., Chen Y. F., Hong S. K., Wenisch H., Yao T., and Look D. C., *Appl. Phys. Lett.* **77** (2000) 3761 (a)

Ko H. J., Chen Y., Hong S. K., and Yao T., *J. Cryst. Growth* **209** (2000) 816 (b)

Ko H. J., Chen Y. F., Yao T., Miyajima K., Yamamoto A., and Goto T., *Appl. Phys. Lett.* **77** (2000) 537 (c)

Kresse G., Dulub O., and Diebold U., *Phys. Rev. B* **68** (2003) 245409

Kroger F. A., *The Chemistry of Imperfect Crystals*, Wiley-Interscience, New York, 1964

Kumano H., Ashrafi A. A., Ueta A., Avramescu A., and Suemune I., *J. Cryst. Growth* **214/215** (2000) 280

Kumar V. and Sastry B. S. R., *Cryst. Res. Technol.* **36** (2001) 565

Kurtin S., McGill T.C., and Mead C. A., *Phys. Rev. Lett.* **22** (1969) 1433

Landolt-Bornstein, *Semiconductors*, Springer, Berlin, **17** (1982) 35

Lau C. K., Tiku S. K, and Lakin K. M., *J. Electrochem. Soc.* **127** (1980) 1843

Lee J.-H., Ko K.-H., and Park B.-O., *J. Cryst. Growth* **247** (2003) 119

Leroux M., Grandjean N., Beaumont B., Nataf G., Semond F., Massies J., and Gibart P., *J. Appl. Phys.* **86** (1999) 3721

Li S. S., *Semiconductor Physical Electronics*, Plenum, New York, 1993

Li B. S., Liu Y. C., Shen D. Z., Zhang J. Y., Lu Y. M., and X. W. Fan, *J. Cryst. Growth* **249** (2003) 179

Liang S., Sheng H., Liu Y., Huo Z., Lu Y., and Shen H., *J. Cryst. Growth* **225** (2001) 110

Lim W. T. and Lee C. H., *Thin Solid Films* **353** (1999) 12

Liu M., Kitai A. H., and Mascher P., *J. Lumin.* **54** (1992) 35

Liu Y., Gorla C. R., Liang S., Emanetoglu N., Lu Y., Shen H., and Wraback M., *J. Electronic Mat.* **29** (2000) 69

Look D. C., *Electrical Characterization of GaAs Materials and Devices*, Wiley:New York, 1989

Look D. C., Reynolds D. C., Sizelove J. R., Jones R. L., Litton C. W., Cantwell G., and Harsch W. C., *Solid State Comm.* **105** (1998) 399

Look D. C., Hemsky J.W., and Sizelove J. R., *Phys. Rev. Lett.* **82** (1999) 2552

Look D. C., *Mat. Sci. Eng. B* **80** (2001) 383

Look D. C., Reynolds D. C., Litton C. W., Jones R. L., Eason D. B., and Cantwell G., *Appl. Phys. Lett.* **81** (2002) 1830

Look D. C., Coskun C., Claflin B., and Farlow G. C., *Physica B* **340-342** (2003) 32

Lüpke G., *Surf. Sci. Rep.* **35** (1999) 75

Ma Y., Du G. T., Yang T. P., Qiu D. L., Zhang X., Yang J., Zhang Y. T., Zhao B. J., Yang X. T., and Liu D. L., *J. Cryst. Growth* **255** (2003) 303

Major S., Banerjee A., Chopra K. L., and Nagpal K. C., *Thin Solid Films* **143** (1986) 19

Makino T., Segawa Y., Kawasaki M., Ohtomo A., Shiroki R., Tamura K., Yasuda T., and Koinuma H., *Appl. Phys. Lett.* **78** (2001) 1237

Makino T., Tamura K., Chia C. H., Segawa Y., Kawasaki M., Ohtomo A., and Koinuma H., *J. Appl. Phys.* **92** (2002) 7157

Maniv S., Westwood W. D., and Colombini E., *J. Vac. Sci. Technol.* **20** (1982) 162

Miller A. and Abrahams E., *Phys. Rev.* **120** (1960) 745

Mohanty G. P. and Azaroff L. V., *J. Chem. Phys.* **35** (1961) 1268

Molnar R. J., Lei T., and Moustakas T. D., *Appl. Phys. Lett.* **62** (1993) 72

Morkoç H., *Nitride semiconductors and devices*, Springer-Verlag, 1999

Mott N. F., *Phil. Mag.* **19** (1969) 835

Mott N. F., *Metal Insulator Transitions*, Barnes and Noble Books, New York, 1974

Movchan B. A. and Demchishin A. V., *Fiz. Met. Metalloved.* **28** (1969) 653

Nan C.-W., Tschöpe A., Holten S., Kliem H., and Birringer R., *J. Appl. Phys.* **85** (1999) 7735

Natsume Y., Sakata H., Hirayama T., and Yanagida H., *J. Appl. Phys.* **72** (1992) 4203

Natsume Y., Sakata H., and Hirayama T., *Phys. Stat. Sol. (a)* **148** (1995) 485

Neumann U., Grunwald R., Griebner U., Steinmeyer G., and Seeber W., *Appl. Phys. Lett.* **84** (2004) 170

Ng H. T., Chen B., Li j., Han J., Meyyappan M., Wu J., Li S. X., and Haller E. E., *Appl. Phys. Lett.* **82** (2003) 2023

Ni H. Q., Lu Y. F., and Ren Z. M., *Jpn. J. Appl. Phys. Part 1* **40** (2001) 4103

Oda S., Tokunaga H., Kitajima N., Hanna J. -I., Shimizu I., and Kokado H., *Jpn. J. App. Phys.* **24** (1985) 1607

O'Donnel K. P. and Chen X., *Appl. Phys. Lett.* **58** (1991) 2924

Ogata K., Sakurai K., Fujita Sz., Fujita Sg., and Matsushige, *J. Cryst. Growth* **214/215** (2000) 312

Ogata K., Kawanishi T., Maejima K., Sakurai K., Fujita Sz., and Fujita Sg., *J. Cryst. Growth* **237 – 239** (2002) 553

Oleynik N., Adam M., Krtschil A., Bläsing J., Dadgar A., Bertram F., Forster D., Diez A., Greiling A., Seip M., Christen J., and A. Krost, *J. Cryst. Growth* **248** (2003) 14

Ohtomo A., Kawasaki M., Koida T., Masubuchi K., Koinuma H., Sakurai Y., Yoshida Y., Yasuda T., and Segawa Y., *Appl. Phys. Lett.* **72** (1998) 2466

Ong H. C., Zhu A. X. E., and Du G. T., *Appl. Phys. Lett.* **80** (2002) 941

Orton J. W. and Powell M. J., *Rep. Progr. Phys.* **43** (1980) 1263

Pankove J. I. and Aigrin P., *Phys. Rev.* **126** (1962) 956

Pankove J. I., *Phys. Rev.* **140** (1965) A2059

Pearton S. J., Norton D. P., Ip K., Heo Y. W., and Steiner T., *Superlattices and Microstructures* **34** (2003) 3

Pei Z. L., Sun C., Tan M. H., Xiao J. Q., Guan D. H., Huang R. F., and Wen L. S., *J. Appl. Phys.* **90** (2001) 3432

Pierret R. F., *Advanced Semiconductor Fundamentals, Volume VI: Modular Series on Solid State Devices, Addison-Westley Publishing Company Inc.*, 1987

Pikus G. E., *Sov. Phys. Solid State* **6** (1964) 261

Plachke D., Blohm G., Fischer Th., Khellaf A., Kruse O., Stoll H., and Carstanjen H. D., *Applications of Accelerators in Research and Industry-Sixteenth Int'l Conf.* (2001) 458

Ramamoorthy K., Sanjeeviraja C., Jayachandran M., Sankaranarayanan K., Bhattacharya P., and Kukreja L., *J. Cryst. Growth* **226** (2001) 281

Polyakov A. Y., Smirnov N. B., Kozhukhova E. A., Vdovin V. I., Ip K., Heo Y. W., Norton D. P., and Pearton S. J., *Appl. Phys. Lett.* **83** (2003) 1575

Redfield D., *Phys. Rev.* **130** (1963) 914

Reeber R. R., *J. Appl. Phys.* **41** (1970) 5063

Reynolds D. C., Litton C. W., and Collins T. C., *Phys. Stat. Sol.* **12** (1965) 3

Reynolds D. C., Look D. C., Jogai B., and Morkoç H., *Solid State Commun.* **101** (1997) 643

Reynolds D. C., Look D. C., Jogai B., Litton C. W., Collins T. C., Harsh W., and Cantwell G., *Phys. Rev. B.* **57** (1998) 12151

Rossinelli M., Blatter G., and Greuter F., *Electrical Ceramics*, British Ceramic Society, Stoke-on-Trent, 1985

Roth A. P., Webb J. B., and Williams D. F., *Solid State Commun.* **39** (1981) 1269 (a)

Roth A. P. and Williams D. F., *J. Appl. Phys.* **52** (1981) 6685 (b)

Roth A. P. and Williams D. F., *J. Electrochem. Soc.* **128** (1981) 2684 (c)

Rowe J. E., Cardona M., and Pollak F. H., *Solid State Commun.* **6** (1968) 239

Ryu Y. R., Zhu S., Look D. C., Wrobel J. M., Jeong H. M., and White H. W., *J. Cryst. Growth* **216** (2000) 330 (a)

Ryu Y. R., Zhu S., Budai J. D., Chandrasekhar H. R., Miceli P. F., and White H. W., *J. Appl. Phys.* **88** (2000) 201 (b)

Sallet V., Thiandoume C., Rommeluere J. F., Lusson A., Rivière A., Rivière J. P., Gorochov O., Triboulet R., and Muñoz-Sanjosé V., *Mat. Lett.* **53** (2002) 126

Scheidt T., Rohwer E. G., von Bergmann H. M., and Stafast H., *Phys. Stat. Sol. (c)* **1** (2004) 2243

Schroder D. K., *Semiconductor material and device characterization*, New York:Wiley, 1998

Schröer P., Krüger P., and Pollmann J., *Phys. Rev. B* **47** (1993) 6971

Schubert E. F., ECSE Department, Rensselaer Polytechnic Institute, online lecture notes

Schulz H. and Thiemann K. H., *Solid State Commun.* **32** (1979) 783

Scott J. F., *Phys. Rev. B* **2** (1970) 1209

Seager C. H. and Castner T. G., *J. Appl. Phys.* **49** (1978) 3879

Sernelius B. E., Berggren K. F., Jin Z. C., Hamberg I., and Granqvist C. G., *Phys. Rev. B* **37** (1988) 10244

Sheng H., Muthukumar S., Emanetoglu N. W., and Lu Y., *Appl. Phys. Lett.* **80** (2002) 2132

Shimizu M., Shiosaki T., and Kawabata A., *J. Cryst. Growth* **57** (1982) 94

Shockley W., *Electrons and Holes in Semiconductors*, Toronto:van Nostrand, p. 280, 1950

Sipe J. E., Moss D. J., and Van Driel H. M., *Phys. Rev. B* **35** (1987) 1129

Smith F. T. J., *Appl. Phys. Lett.* **43** (1983) 1108

Srikant V., PhD thesis, University of California, Santa Barbara, 1995 (a)

Srikant V., Sergo V., and Clarke D. R., *J. Am. Ceram. Soc.* **78** (1995) 1935 (b)

Srikant V. and Clarke D. R., *J. Appl. Phys.* **81** (1997) 6357

Srikant V. and Clarke D. R., *J. Appl. Phys.* **83** (1998) 5447

Studenikin S.A., Golego, N., and Cocivera, M., *J. App. Phys.* **84** (1998) 2287

Strhemechny Y. M., Nemergut J., Bae J., Look D. C., and Brillson L. J., *Mat. Res. Soc. Symp. Proc.* **744** (2003) M3.9.1

Stern F. and Talley R. M., *Phys. Rev.* **100** (1955) 1638

Stranski I. N. and Krastanov L., *Sitzungsber. Akad. Wissenschaft Wien* **146** (1938) 797

Studenikin S. A., Golego N., and Cocivera M., *J. Appl. Phys.* **84** (1998) 2287

Subramanyam T. K., Srinivasulu Naidu B., and Uthanna S., *Cryst. Res. Technol.* **35** (2000) 1193

Suscavage M., Harris M., Bliss D., Yip P., Wang S.Q., Schwall D., Bouthillette L., Bailey J., Callahan M., Look D.C., Reynolds D.C., Jones R.L., and Litton C.W., *J. Electron. Mater.* **4S1** (1999) 63

Swaminathan V. and Macrander A. T., *Materials Aspects of GaAs and InP based structures*, 319, Prentice-Hall, Englewood Cliffs, NJ, 1991,

Sze S. M., *Physics of semiconductor devices*, John Wiley & Sons Inc., New York, 1981

Tarsa E. J., De Graef M., Clarke D. R., Gossard A. C., and Speck J. S., *J. Appl. Phys.* **73** (1993) 3276

Thomas H., *Gallium arsenide for devices and integrated circuits, IEEE, Electrical and electronic materials and devices series 3*, 78, 1986

Tracy K. M., Hartlieb P. J., Einfeldt S., Davis R. F., Hurt E. H., and Nemanich R. J., *J. Appl. Phys.* **94** (2003) 3939

Tüzemen S., Dogan S., Ates A., Yidirim M., Xiong G., Wilkinson J., and Williams R. T., *Phys. Stat. Sol (a)* **195** (2003) 165

Uesugia K., Suzukia H., Nashikia H., Obinata T., Suemune I., Kumano H., and Nakahara J., *Appl. Surf. Sci.* **113/114** (1997) 371

Ursaki V. V., Tiginyanu I. M., Zalamai V. V., Masalov V. M., Samarov E. N., Emelchenko G. A., and Briones F., *Semicond. Sci. Technol.* **19** (2004) 851

Van de Walle C. G., *Physica B* **380-310** (2001) 899

van der Drift A., *Philips Res. Rep.* **22** (1967) 267

van der Pauw L. J., *Philips Res. Rept.* **13** (1958) 1

Vanheusden K., Seager C. H., Warren W, L., Tallant D. R., and Voigt J. A., *Appl. Phys. Lett.* **68** (1996) 403 (a)

Vanheusden K., Warren W. L., Seager C. H., Tallant D. R., Voigt J. A., and Gnade B. E., *Appl. Phys. Lett.* **79** (1996) 7983 (b)

Venables J. A., *Introduction to surface and thin film processes*, Cambridge University Press, 2000

Vincent R., *Phil. Mag.***19** (1969) 1127

Vogel D., Krüger P., and Pollmann J., *Phys. Rev. B* **52** (1995) R14316

Volmer M. and Weber A., *Z. Phys. Chem.* **119** (1926) 277

von Wenckstern H., Kaidashev E. M., Lorenz M., Hochmuth H., Biehne G., Lenzner J., Gottschalch V., Pickenhain R., and Grundmann M., *Appl. Phys. Lett.* **84** (2004) 79

Wang R., King L. L. H., and Sleight A. W., *J. Mater. Res.* **11** (1996) 1659

Wang X., Yang S., Yang X., Liu D., Zhang Y., Wang J., Yin J., Liu D., Ong H. C., and Du G., *J. Cryst. Growth* **243** (2002) 13

Wang L. and Giles N. C., *J. Appl. Phys.* **94** (2003) 973

Wang Z. L., *Materials Today* **7** (2004) 26

Weider H. H., *Thin Solid Films* **31** (1976) 123

Wemple S. H. and DiDomenico M. Jr, *Phys. Rev. B* **3** (1971) 1338

Williams D. B. and Carter C. B., *Transmission Electron Microscopy IV*, Plenum Press, New York, 1996

Wooten F., *Optical Properties of Solids*, Academic, New York, 1972

Wright P. J., Griffiths R. J. M., and Cockayne B., *J. Cryst. Growth* **66** (1984) 26

Wu H. Z., He K. M., Qiu D. J., and Huang D. M., *J. Cryst. Growth* **217** (2000) 131

Wu X. L., Siu G. G., Fu C. L., and Ong H. C., *Appl. Phys. Lett.* **78** (2001) 2285

Xiong G., Wilkinson J., Mischuck B., Tüzemen S., Ucer K. B., and Williams R. T., *Appl. Phys. Lett.* **80** (2002) 1195

Xu Y. -N. and Ching W. Y., *Phys. Rev. B* **48** (1993) 4335

Xu P.S., Sun Y. M., Shi C. S., Xu F. Q., and Pan H. B., *Nucl. Inst. Meth. Phys. Res. B* **199** (2003) 286

Yamamoto A., Miyajima K., Goto T., Ko H. J., and Yao T., *J. Appl. Phys.* **90** (2001) 4973

Yan J. F., Lu Y. M., Liu Y. C., Liang H. W., Li B. H., Shen D. Z., Zhang J. Y., and Fan X. W., *J. Cryst. Growth* **266** (2004) 505

Ye Z.-Z., Lu J.-G., Chen H.-H., Zhang Y.-Z., Wang L., Zhao B.H., and Huang J.-Y., *J. Cryst. Growth* **253** (2003) 258

Young D. L., Coutts T. J., Kaydanov V. I., Gilmore A. S., and W. P. Mulligan, *J. Vac. Sci. Technol. A* **18** (2000) 2978

Yu P. W., *J. Appl. Phys.* **48** (1977) 5043

Zhang X. T., Liu Y. C., Zhi Z. Z., Zhang J. Y., Lu Y. M., Shen D. Z., Xu W., Zhong G. Z., Fan X. W., and Kong X. G., *J. Phys. D: Appl. Phys.* **34** (2001) 3430

Zhang B. P., Binh N. T., SegawaY., Wakatsuki K., and Usami N., *Appl. Phys. Lett.* **83** (2003) 1635

Zhang Y., Du G., Yang X., Zhao B., Ma Y., Yang T., Ong H. C., Liu D., and Yang S., *Semicond. Sci. Technol.* **19** (2004) 755

Zhenguo J., Kun L., Chengxing Y., Ruixin F., and Zhizhen Y., *J. Cryst. Growth* **253** (2003) 246

APPENDIX

Table of ZnO constants

		Reference
Lattice constant a	3.2498 Å	ASTM
Lattice constant c	5.2066 Å	ASTM
Density, ρ	5.62 – 5.78 g/cm^3	Heiland *et al.*, 1959
Optical band gap, E_g	3.3 – 3.4 eV	Srikant and Clarke, 1998
Elastic moduli at 25 °C $C_{11}, C_{12}, C_{13}, C_{33}$	$2.097 \bullet 10^{12}$, $1.211 \bullet 10^{12}$, $1.051 \bullet 10^{12}$, $2.109 \bullet 10^{12}$ dyn/cm^2	Bateman, 1962
Electron effective mass, m_e	0.24	Pearton *et al.*, 2003
Hole effective mass, m_h	0.59	Pearton *et al.*, 2003
Dielectric constant, ε	8.5	Reynolds *et al.*, 1965
Conduction band density of states, n_C	$5.9 \bullet 10^{18}$ cm^{-3}	Roth *et al.*, 1981a
Linear thermal expansion coefficient at 300 K, α_L	$8.63 \bullet 10^{-6}$ /°C	Kumar and Sastry, 2001
Elastic stiffness c_{1133}, c_{3333}	105.1, 210.9 GPa	Landolt-Bornstein, 1982
Crystal field splitting, Δ_{cf}	42 meV	Pikus, 1964
Spin orbital splitting, Δ_{so}	-5 meV	Pikus, 1964
Deformation potentials C_1, C_2, C_3, C_4	-2.66, 2.82, -1.34, 1.0 eV	Rowe *et al.*, 1968
Effective Richardson constant, A^*	32 Acm^{-2}K^{-2}	Sze, 1981

List of publications

The following two articles originating from this work have been submitted, accepted for publication, and published:

- *Structural and optical characterization of MOCVD-grown ZnO thin films* O. Pagni, G. R. James, and A. W. R. Leitch, *Phys. Stat. Sol. (c)* **Vol. 1/4/2004**, p. 864

- *Influence of VI:II ratio on the properties of MOCVD-grown ZnO thin films* O. Pagni and A. W. R. Leitch, *Phys. Stat. Sol. (a)* **201** (2004) 2213